Mapping and Controlling Nucleation

Finlay Alexander Walton

BSc Hons. MSc

University of Glasgow

Submitted in fulfilment of the requirements for the Degree of Doctor of Philosophy

School of Chemistry

College of Science and Engineering

University of Glasgow

September 2019

University of Glasgow

Abstract

This thesis reports on an investigation of two non-trivial nucleation phenomena, with the goal that understanding these will enable greater understanding of nucleation generally.

Non-photochemical laser-induced nucleation (NPLIN) phenomena have been investigated for more than twenty years but lack a complete explanation. The laser-induced phase separation and nucleation (LIPSaN) phenomenon has been discovered and it is proposed as the mechanism behind NPLIN. A laser generates a potential which, when incident on a binary mixture in proximity to its critical point, causes the high-refractive index component to migrate to the focus. The effect bears a similarity to optical trapping of particles, as the trapped particle has a higher refractive index than the medium it is in. It has been shown that nucleation can be induced in metastable binary mixtures, which is analogous to the metastable supersaturated solutions which are typical in NPLIN experiments. It is proposed that NPLIN can only work if there is a hidden liquid-liquid critical point in the supersaturated regime.

The liquid-liquid transition (LLT) is a ubiquitous example of polyamorphism – the transition between one liquid state with no long-range ordering to another. There are several examples of LLTs, but none that are quite as fiercely debated as triphenyl phosphite (TPP). The debate can be summarised as two competing hypotheses: Hédoux – the second liquid does not exist; it is actually the untransformed liquid mixed with nano or micro scale crystals, or Tanaka – the second liquid state exists, but nano or micro crystals are also produced at higher LLT temperatures. It will be shown using a wide range of techniques that Tanaka is at least partially correct, but the two sides are two sides of the same coin. The second liquid state exists and there is a first order LLT, but the so-called nanocrystals are better described as locally favoured structures that are similar to the structure of the crystal. There are three crystal polymorphs of TPP and their distinct unit cells and conformers have been characterised with single crystal X-ray diffraction (XRD). There is a conformational change during the LLT which has been characterised using infrared, density functional theory (DFT) and XRD data. The LLT is associated by a flip of a phenoxy arm and change from parallel 'sandwich' to T-shaped π- π stacking.

Both avenues of investigation emphasise the importance of critical points and their influence in how nucleation proceeds. The work presented here sheds some light on two poorly understood nucleation phenomena and will hopefully aid in a more robust understanding of nucleation generally.

Contents

i. Acknowledgements

"El sueño de la razón produce monstrous"

– Francisco Goya

ii.   Author's Declaration

"I declare that, except where explicit reference is made to the contribution of others, this dissertation is the result of my own work and has not been submitted for any other degree at the University of Glasgow or any other institution."

Printed Name: Finlay Alexander Walton

Signature: _____

iii. List of Figures & Tables

vi. List of Abbreviations

Asym	Asymmetric
BF	Bright field
C1	Crystal 1 – monoclinic 1
C2	Crystal 2 - hexagonal
C3	Crystal 3 – monoclinic 2
CNT	Classical nucleation theory
CP	Crossed polarisers
CW	Continuous wave
DSC	Differential scanning calorimetry
EM	Electromagnetic
FLD	Frustration limited domain
FRET	Förster resonance energy transfer
FTIR	Fourier transform infrared
FWHM	Full width at half maximum
Hex	The C2 hexagonal (rhombohedral) triphenyl phosphite polymorph
IC	Internal conversion
IR	Infrared
ISC	Intersystem crossing
L1	Liquid 1 – untransformed liquid
L2	Liquid 2 – glacial phase
LCST	Lower critical solution temperature
LFS	Locally favoured structures
LIN	Laser-induced nucleation
LIPS	Laser-induced phase separation
LIPSaN	Laser-induced phase separation and nucleation
LLT	Liquid-liquid transition
Mon	The C3 monoclinic triphenyl phosphite polymorph
NDE	Nonlinear dielectric effect
NG	Nucleation and growth
NMR	Nuclear magnetic resonance
NPLIN	Non-photochemical laser-induced nucleation
OKE	Optical Kerr effect
OPD	Optical path difference

PC	Phase contrast
SANS	Small angle neutron scattering
SAXS	Small angle X-ray scattering
SD	Spinodal decomposition
Sym	Symmetric
$T_{Binodal}$	Binodal temperature
T_C	Critical temperature
T_G	Glass transition temperature
TPP	Triphenyl phosphite
T_Q	Quench temperature
T_{RC}	Recrystallisation temperature
T_{SD}	Spinodal decomposition temperature
UCST	Upper critical solution temperature
VH	Vertical horizontal
VV	Vertical vertical
WAXS	Wide angle X-Ray scattering
XRD	X-ray diffraction

1. General Introduction

1.1.1. Overview

This thesis fundamentally reports on an investigation into nucleation phenomena, with the goal of helping to build a clearer picture of nucleation and its inhibition more generally. The two phenomena which have been investigated are non-photochemical laser-induced nucleation (NPLIN) and the liquid-liquid transition (LLT) in triphenyl phosphite (TPP). These two specific areas could well have broad implications in terms of understanding the behaviour of pure liquids, liquid mixtures and how nucleation proceeds.

This introductory chapter will focus on subjects that are shared between the two themes of this thesis. Thermodynamics, nucleation theory and critical points will be discussed, followed by the fundamental properties of light and the optical microscopy techniques used in this work.

1.2. The Thermodynamics of Phase Transitions

In order to under understand nucleation theory, it is essential to understand some basic thermodynamics and how different types of phase transition occur.

1.2.1. Entropy

Entropy S can be defined as the amount of possible microscopic variations in a system, which are hidden macroscopically. Entropy can be defined as

$$S = k \ln \Omega \tag{1.1}$$

where k is the Boltzmann constant (with units J K^{-1}, which S shares) and Ω is the number of possible microscopic states of the system.[1] Equation (1.1) only holds true if the probability of occupying each microstate is the same – like in an ideal gas. In many systems however, the probability of the occupation of each microstate can vary and must be taken into account and summed. Entropy is a measure of disorder, and the second law of thermodynamics states that for an isolated system, entropy increases over time as all possible processes occur, such that

$$\frac{dS}{dt} \geq 0 \, . \tag{1.2}$$

In an isolated system, i.e. with no involvement of the surrounding environment, spontaneous processes cannot proceed at equilibrium, thus it is not possible to increase S. This implies that entropy maximises at equilibrium. Thus, entropy can be thought of as a driving force to achieve equilibrium.

1.2.2.   Free Energy

If Equation (1.2) is combined with an expression for the first law of thermodynamics (the conservation of energy)

$$dU = TdS - PdV + \sum_i \mu_i dN_i \tag{1.3}$$

then the result is a form of the Clausius inequality

$$dU - TdS + PdV - \sum_i \mu_i dN_i \leq 0 \tag{1.4}$$

where U is the internal energy, T is the temperature, P is the pressure, V is the volume, μ_i is the chemical potential and N_i is the change in the number of molecules. The inequality sign means that for irreversible processes there can be a 'free' energy associated with the process. A general expression for an infinitesimal change in free energy $d\varphi$ can therefore be written as

$$d\varphi = dU - TdS + PdV - \sum_i \mu_i dN_i \tag{1.5}$$

where when a single molecule or particle dN_i added, it will contribute a change in internal energy dU, entropy dS, volume dV and chemical potential μ_i. As equilibrium is approached, entropy tends to maximise but free energy tends to minimise – this is easy to see in equation (1.4) as the entropic term is negative. From this, an expression for the free energy at constant temperature and pressure – the Gibbs free energy – which is the most appropriate for describing liquids, can be derived. If only work and heat are exchanged with the environment, $dN_i = 0$ so it can be written that

$$dG = dU - T_0 dS + P_0 dV \tag{1.6}$$

where dG is the infinitesimal change in the Gibbs free energy. (1.6) can then be integrated to give

$$G = U - T_0 S + P_0 V \ . \tag{1.7}$$

Calculating an exact value for G is not practical, but it is very useful to consider ΔG for a given transition or reaction, as the sign indicates whether it will be spontaneous or not. A negative value of ΔG indicates that the product or final state has a lower Gibbs free energy than the reactant or initial state, meaning that there is 'free' energy available to do work and allow the reaction or transition to proceed. The enthalpy $H = U + P_0V$, so the change in Gibbs free energy can be written as

$$\Delta G = \Delta H - T\Delta S .$$
<div align="right">(1.8)</div>

Equation (1.8) is ubiquitous in chemistry and very useful, as values of the change in enthalpy ΔH and absolute entropy S can be experimentally determined using a calorimeter. Consequently, there is a large amount of standard entropy and enthalpy data available for use in a simple calculation for predicting how a new reaction or transition will proceed. If ΔG is positive, a reaction is not thermodynamically favourable and will not occur spontaneously. If ΔG is negative, the reaction is favourable and can occur spontaneously – this says nothing about the rate of reaction, however. Kinetic factors may cause the rate of reaction of a transition to be slow to the point of being negligible. For example, ΔG < 0 for the transition between the carbon allotropes diamond and graphite, but the enormous energy barrier between them caused by the need to break multiple C-C bonds, means that diamond is stable even on geological timescales.

1.2.3.   Phase Transitions

Qualitatively, a phase transition can be defined as a change from one distinct state of matter to another, but what defines a 'state' is not a trivial question. Classically the three states of matter are solid, liquid and gas for a pure substance, which can be defined as condensed immobile, condensed fluid and dispersed fluid. In recent times a fourth state known as plasma (a conductive ionised gas with free electrons, such as lightning or sparks) has been included in that category, but there are also states which only exist in extreme conditions relative to those seen on earth like Bose-Einstein condensates and new categories such as ferromagnetism. Lines can be drawn in a phase diagram to represent the points at which a system undergoes a transition, often in terms of pressure and temperature. A simplified phase diagram for water is shown in Figure 1. These phase equilibrium lines represent the temperatures and pressures at which the two adjoining phases can coexist at equilibrium. Two common features of phase diagrams are triple points and critical points. The triple point in Figure 1 for instance, is the point at which solid, liquid and

gas phases have the same free energy and so can coexist at equilibrium. A critical point is an extremity of a phase equilibrium line (often gas-liquid), after which the two phases become difficult to distinguish and in the gas-liquid case are referred to collectively as a supercritical fluid. Although there is no latent heat beyond the critical point, there still exists two zones which resemble the two phases, separated by what is known as the Widom line.[2]
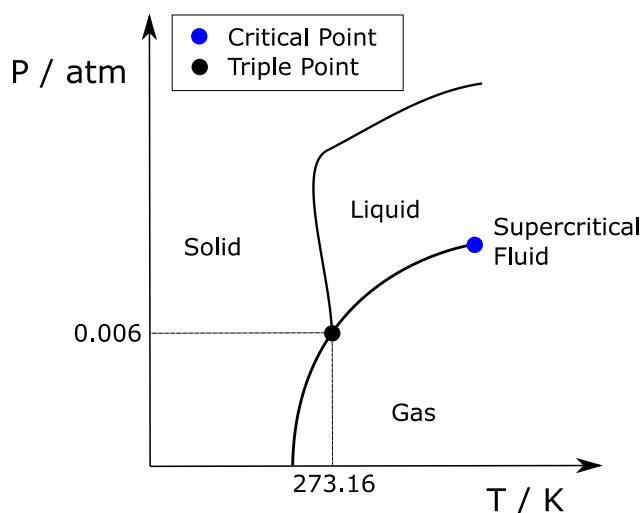
Figure 1 – Simplified phase diagram of water. The triple point is the pressure and temperature at which all three phases can coexist and the (gas-liquid) critical point marks the final point at which gas and liquid phases can coexist and distinguished. At higher temperatures and pressures water exists as a single, supercritical fluid phase.

Phase transitions are often identified by Ehrenfest classification; if a transition is discontinuous in some quantity which is the first derivative of a free energy with respect to a variable of state – it is said to be a first order transition. In solid-liquid-gas transitions for example, there is a change in density which is discontinuous. Density is the inverse of the first derivative of the free energy with respect to pressure, so the transition is first order. Density in this case is referred to as the order parameter, which as its name suggests is also a measure of order. Second order transitions are continuous in the first derivative, but show a discontinuity in the second derivative, e.g. magnetisation in a ferromagnet as it rises above the Curie temperature. For the most part, the modern way to classify phase transitions groups them together in the same way as Ehrenfest – first order transitions possess a latent heat, which is generally detectable using differential scanning calorimetry (DSC). Second order transitions are continuous and have no latent heat. Ehrenfest does not take into account transitions where an order parameter tends to infinity rather than having a discontinuity. This is quite common however, such as in the case of

4

liquid-liquid critical points which will be described in more detail after introducing nucleation theory.

When a phase boundary is crossed, the free energy of the new phase is lower than that of the old phase, so ΔG < 0 and the transition is thermodynamically favourable. This doesn't mean that the transition will proceed however, as it may be hindered kinetically by an energy barrier. The energy barrier typically originates from the need to form an interface between the two phases. This type of kinetics is referred to as nucleation and growth, and will now be discussed in more detail.

1.3. Nucleation Theory

Nucleation is the first stage of the formation of a new thermodynamic phase or structure. It applies to a variety of transitions from crystallisation and condensation to the self-assembly of polyoxometalates or amyloid fibrils. Once a phase has nucleated it can then grow until either the solute has run out, or the whole sample has transformed. The original, simple model of nucleation which is known as classical nucleation theory (CNT) or Gibbs theory will now be described.

1.3.1.   Classical Nucleation Theory

The relative free energies of two phases can be used as measure of which of the two is more thermodynamically stable, so if a new phase has a lower free energy than the current phase, the transition can proceed spontaneously. The difference in Gibbs free energy between the two states is the maximum amount of non-volume work that the system can perform, so it is the more physically relevant parameter. When ΔG is negative, the transition is favourable. In order for a new phase to nucleate and grow, an interface must form between the first and second phases. The molecules or particles at the interface will inevitably be in a higher energy arrangement than in either bulk phases, which means an energy cost. The formation free energy of a nucleating droplet can be written as

$$\Delta\varphi = \sum \Delta\mu_i N_i + \sigma A \qquad (1.9)$$

where $\Delta\varphi$ is the formation free energy, $\Delta\mu_i$ is the change in chemical potential when a molecule is added, N_i is the number of molecules in the droplet, σ is the interfacial tension, with units of J m^{-2} and A is the surface area of the droplet.[3] It can be more convenient to express this equation in terms of the radius of an ideal spherical nucleus, rather than individual molecules, so this will now be derived. At constant

temperature and pressure for a single component system, the sum of changes in chemical potential are equal to the Gibbs free energy, which can be written per unit volume as

$$\sum \Delta \mu_i N_i = \Delta G_V \frac{4}{3} \pi r^3 \qquad (1.10)$$

where ΔG_V is the Gibbs free energy per unit volume and r is the radius of the nucleus. The formation free energy can then be written as

$$\Delta \varphi = \Delta G_V \frac{4}{3} \pi r^3 + 4 \sigma \pi r^2. \qquad (1.11)$$

The two terms in equation (1.11) can be referred to as the bulk and surface terms respectively. Since the bulk term has a cubic dependence on r and the surface is a square dependence, for low values of r, ΔG_{Total} > 0 so nucleation is unfavourable. As r increases however, $\Delta \varphi$ maximises, which is referred to as the critical nucleus size r_C which is the peak of the blue curve in Figure 2. At r_C, the total energy of the droplet is at a maximum, but there is now a finite probability that the new phase will nucleate. Above this radius, the bulk energy term decreases faster than the surface term increases, eventually giving $\Delta \varphi$ < 0, so the growth of the nucleus is now thermodynamically favourable. At r_C the probability of nucleation is still low, which increases with the radius. The probability of nucleation can be expressed as a rate of nucleation J for a critical cluster in the form

$$J = Z \beta C_1^e e^{\frac{-\Delta \varphi}{kT}} \qquad (1.12)$$

where Z is the Zeldovich non-equilibrium factor, β is growth rate of nuclei and C_1^e is the concentration of nuclei at equilibrium. The Zeldovich factor is a combination of several other constants including the surface tension, partial molecular volume and degree of supersaturation. It is worth noting that Z varies with the exponential of the degree of supersaturation, so small changes in temperature or concentration can have large effects on the nucleation rate. The equation cannot be used to calculate steady state concentrations, but it takes into account the growth of the nucleus above the critical radius and 'evaporation' from the nucleus to form smaller clusters elsewhere.
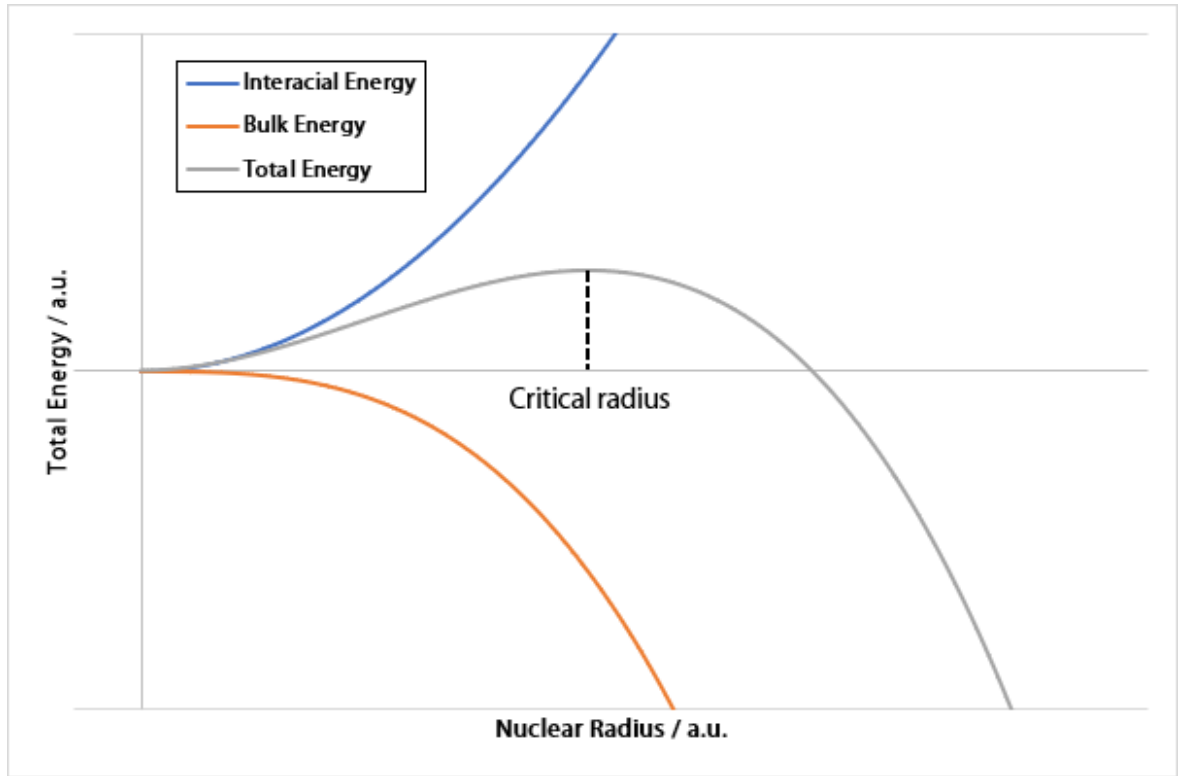
Figure 2 – Below the critical radius of a nucleus (the maximum turning point of the total energy – the grey curve), the energy associated with the interface between the nucleus and bulk dominates. Above the critical radius, the bulk energy decreases more rapidly than the surface term increases. The blue curve represents the total free energy of the nucleus – the energy maximum occurs at the critical radius.

Classical nucleation theory is simplistic interpretation of homogeneous nucleation, which means nucleation in the bulk liquid. However, nucleation often proceeds heterogeneously, i.e. nucleation on the surface of another phase, like the walls of the container or an impurity. A classical interpretation of this is that the contact angle the nucleus makes with the surface means that there is less interface per unit volume than there would have been in the bulk.

The extent to which a transition has been completed as a function of time can be described by the Avrami equation

$$x = 1 - e^{-kt^n} \tag{1.13}$$

where x is the fraction completed, k is a time constant and n is a constant which depends on the number of dimensions of growth. Often n = dimensions + 1 is used but other derivations come to different definitions of n.[4]

If a phase is cooled to a temperature where its free energy is slightly higher than a second phase, a transition is thermodynamically favourable but the nucleation rate may be very low. As the system is cooled, the nucleation rate will increase and the transition may proceed quickly with a rapid growth rate. This is accompanied by an

increase in viscosity, so the result is a competition between the increasing thermodynamic driving force and decreasing kinetics. Figure 3 shows curves which represent the progress in time of a transition at 0, 50 and 90%. The curves show a minimum time for transition progression at an 'optimum' temperature.
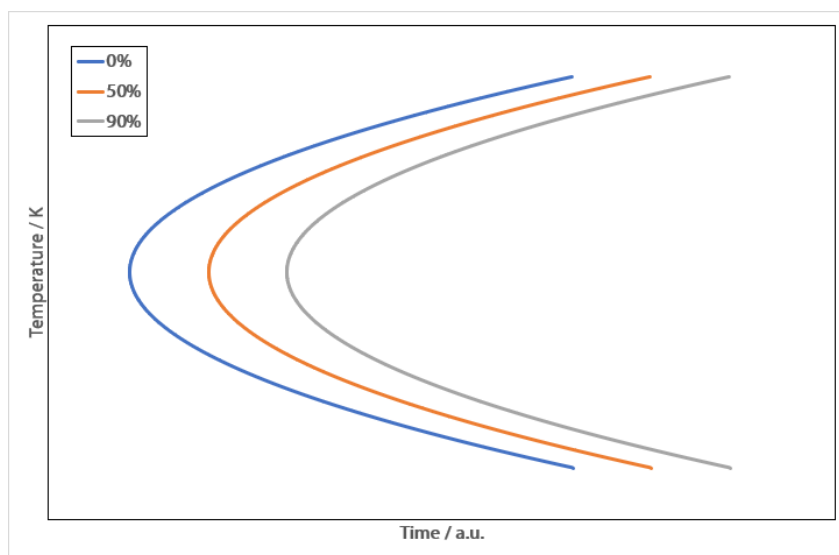
Figure 3 – The time required for a certain percentage of a sample to transform as a function of temperature. As temperature decreases, the nucleation rate increases. As temperature decreases the viscosity also increases. The result is a minimum time for the transition to be complete.

This behaviour can be observed in supercooled triphenyl phosphite, which will be detailed in Chapter 0.

1.3.2.   Non-Classical Nucleation Models

Nucleation is a complex phenomenon, and classical nucleation theory for the most part, acts as a starting point for refinement of nucleation models. Homogeneous nucleation simulations carried out by Sanz and co-workers[5] for water predict that it is practically impossible for homogeneous nucleation to occur above -20 °C. The nucleation rate predicted at -19.5 °C was $J = 10^{-83}$ m^{-3} s^{-1}, which corresponds to one critical ice nucleus in a cubic metre every 10^{75} years. Clearly this is not what is observed in reality as small volumes of water tend to freeze a few degrees below the melting point at 0 ° C. Their models neglect heterogenous nucleation, i.e. when nucleation occurs on container walls, contaminant particles or intentionally placed nucleation sites like boiling stones or seed crystals. Models have attempted to take this in to account by adjusting the surface term in (1.11) to be less than $4\pi r^2$, depending on factors like surface angle and contact angle. Models can further be refined by giving the interface a characteristic thickness, correcting the surface tension for its dependence on curvature (as the nucleus grows, the interface

flattens) and factoring in the contributions of degrees of freedom to the bulk free energy term[3].

CNT assumes the monomeric addition of molecules or particles. This has shown not always to be the case, as pre-nucleation clusters may form[6], indicating a two-step nucleation model. These are thermodynamically stable clusters on the sub-nanometre scale which can aggregate reversibly to form assemblies. Depending on the type of transition, these clusters may go on directly to form a crystal as CNT describes, but form liquid-like domains and/or amorphous phases as alternative routes to the more thermodynamically stable crystal. This ties in with the Ostwald step rule, which is the principle that less stable phases will form first, on the route from an unstructured liquid to a highly ordered and stable crystal. There have been several observations of pre-nucleation clusters, including in calcium phosphate[7], calcium carbonate[8] iron oxide[9] and small organic molecules like amino acids[10], using x-ray techniques, infrared spectroscopy and cryo-transmission electron microscopy. Dense liquid domains which are hundreds of nanometres in size have been observed during calcium carbonate (vaterite) nucleation[11] in an aqueous solution. The domains resulted from density fluctuations, which led to crystal nucleation in the dense domains. A schematic showing pre-nucleation clusters and a dense liquid intermediate as an alternative route to nucleation is shown below in Figure 4.
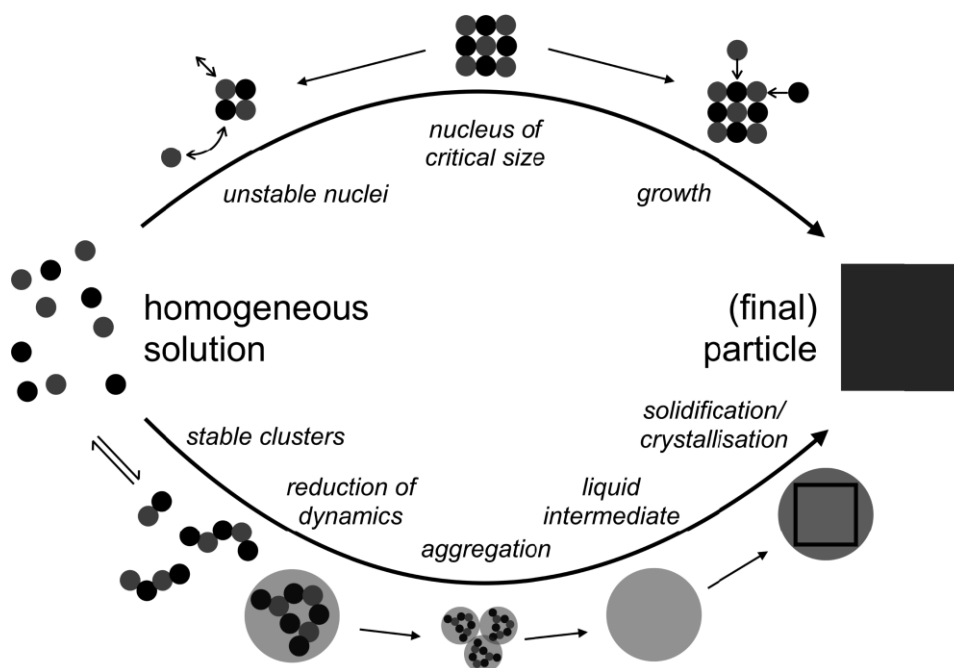
Figure 4 – From Gebauer et al[6]. The classical route to nucleation (top) and the non-classical pre-nucleation cluster route (bottom), including the aggregation of pre-nucleation clusters and liquid/amorphous solid intermediates.

1.3.3. Geometric Frustration

According to CNT, as the temperature of a solution decreases and supersaturation ratio increases, the probability of nucleation increases. The same holds true for pure, supercooled liquids. Consequently, the nucleation rate increases, but the rate varies wildly between different chemicals and mixtures. Some crystallise or precipitate immediately after entering a metastable supersaturated or supercooled state, whereas others can remain metastable seemingly indefinitely and easily form glasses. An explanation for this is the idea of geometric frustration. The most energetically favourable local configuration of monomers may not lend itself to the formation of the crystal. If a central atom is co-ordinated to 12 other atoms – which is common in metals[12] - is a regular dodecahedron with the atoms on the faces (or an icosahedron with the atoms at the vertices). Regular dodecahedra have five-fold symmetry which does not allow periodic tiling of three-dimensional space. It should be noted that there are arguably some exceptions to this, like pyrite (iron disulphide) which under certain conditions has a pyritohedral geometry, that is similar to a regular dodecahedron.[13] Frank famously calculated using Lennard-Jones potentials that the regular dodecahedra were energetically favoured over face-centred cubic and hexagonal close packing lattices with the same number of atoms.[14] This would mean that locally favoured dodecahedra would form instead of periodic structures, frustrating crystallisation.

If a frustrated liquid is cooled well below its melting point, it may form an amorphous glass rather than crystallising. Glass formation is common and is accompanied by a glass transition temperature T_G. The nature of the glass transition is controversial, as some consider it not to be a transition at all, merely a slow-down of dynamics relative to normal timescales. Glass transitions have a latent heat associated with them and are easily identifiable using DSC.

The Frank model is simple and based on atoms as hard spheres, but clearly multi-atom molecules can form many more geometries than the three listed above. The concept can be generalised as locally favoured structures (LFS) which lower the free energy locally but cannot tile space and thus frustrate the formation crystal phases by means of an energy barrier. LFS have been measured experimentally in glassy triphenyl phosphite using x-ray scattering and have a size of approximately 3 nm, which corresponds to a couple of molecules.[15]

1.4. Liquid-Liquid Phase Separation in a Binary Mixture

Liquid-liquid phase separation in a binary mixture will now be described, as it is crucial component of Chapter 2. In principle, at constant pressure all binary mixtures will mix and demix at some point. Mixtures like hexane with heptane may demix at an inaccessibly low temperature, and oil and water will mix at a hypothetical temperature above their boiling points. Poorly mixing liquids like nitrobenzene and decane exhibit an accessible phase equilibrium curve, which is depicted in Figure 5. The peak of the upper (red) curve is called the binodal and is peaked by the critical point, or upper critical solution temperature (UCST).

Phase separation in a binary mixture is in a sense difficult to classify as a continuous or a first order transition, as it proceeds differently, depending on whether the sample is critical or not. If the sample is of the critical composition, you see characteristic concentration fluctuations and an increase in viscosity as the critical point is approached and an instantaneous transition – so it is continuous. If the sample is not critical, there is a temperature gap between the binodal and spinodal lines, meaning that between those lines, the mixed state is metastable to the demixed state. As such, there can then be a latent heat associated with the transition – so it can be classified as first order. If you take two poorly mixing liquids and plot temperature against mole fraction, there exists a region which they are miscible, or immiscible where they decompose into two phases. Figure 5 shows these regions, which are separated by two curves, the binodal and spinodal. Above the binodal (also known as the co-existence curve) the liquids are miscible, i.e. they are mixed. Below the spinodal, the liquids separate in to two phases which are each typically rich in one of the pure components; if the binodal and spinodal are known, the Lever rule can be used to calculate the composition of the two phases. Between the two curves, a metastable region exists where the transition to the phase separated state is spontaneous, but there is an energy barrier associated with forming an interface which must be overcome. The peak of the curves where they overlap is called the critical point, or the upper critical solution temperature (UCST) or the upper consulate point. If a mixture of critical composition crosses from the single-phase region to the two-phase region, the transition proceeds immediately by spinodal decomposition. UCSTs are common, but it is also possible to have a lower critical

solution temperature (LCST) or indeed both in different regions of the phase diagram.
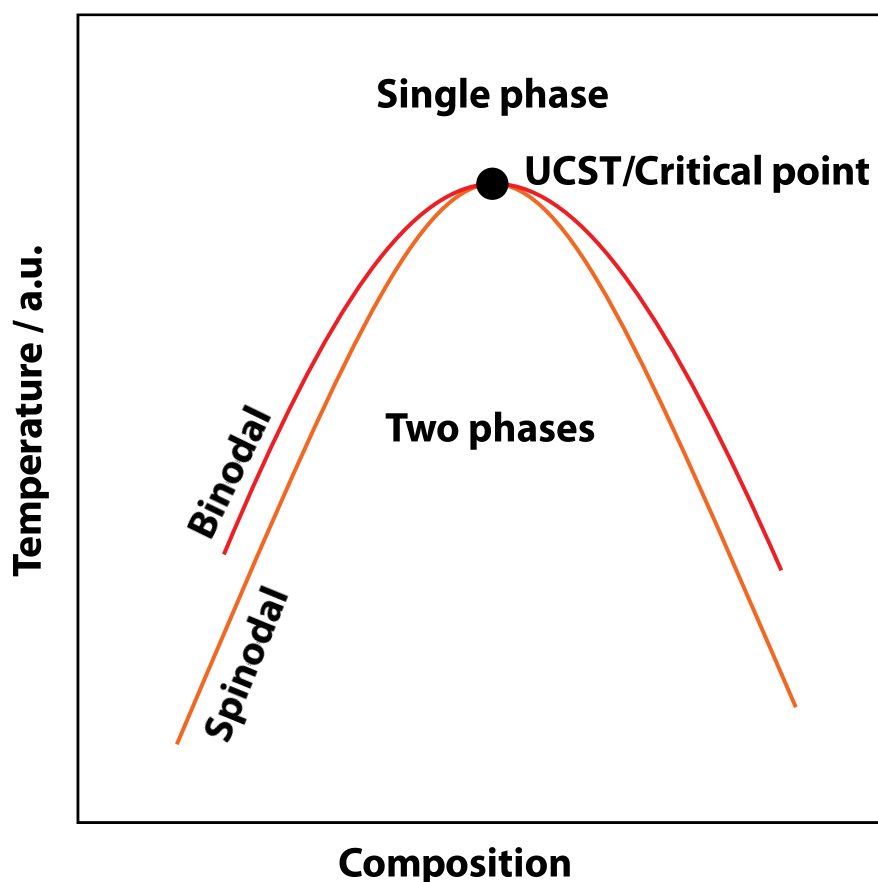
Figure 5 – Phase diagram showing a typical upper critical solution temperature (UCST) with binodal and spinodal lines. Above the binodal a single phase exists and below the spinodal two phases exist. The two lines enclose a metastable region where the phase separated state is thermodynamically favourable but there is an energy barrier which must be overcome for nucleation to occur.

1.4.1.   Hidden Liquid-Liquid Critical Points

Ten Wolde and Frenkel[16] proposed the existence of a hidden liquid-liquid critical point which drastically increases the nucleation rate and altered the *route* to the nucleation of stable crystal. The authors simulated a colloidal solution of particles which interact weakly through Lennard-Jones potentials, which are a class of mathematically simple interatomic potentials. If the interaction length of the potential is long (which models weak interactions like in noble gases well), an accessible critical point at some temperature T_C occurs (Figure 6 (a)). Above this point, the solution is a homogenous fluid and below it (or rather enclosed by the binodal line) the solution decomposes in two phases – vapour and liquid. It should be noted that the labels vapour, liquid and solid correspond to dilute fluid, condensed fluid, and condensed static phases in the solution. This is analogous to the phase diagram of a binary mixture where a mixed phase decomposes into the two components - an

example of this is shown later in Figure 5. If the interaction length is short relative to the particle size however, the critical point moves below the liquidus line (between fluid-fluid and fluid-solid regions) as shown in Figure 6 (b).
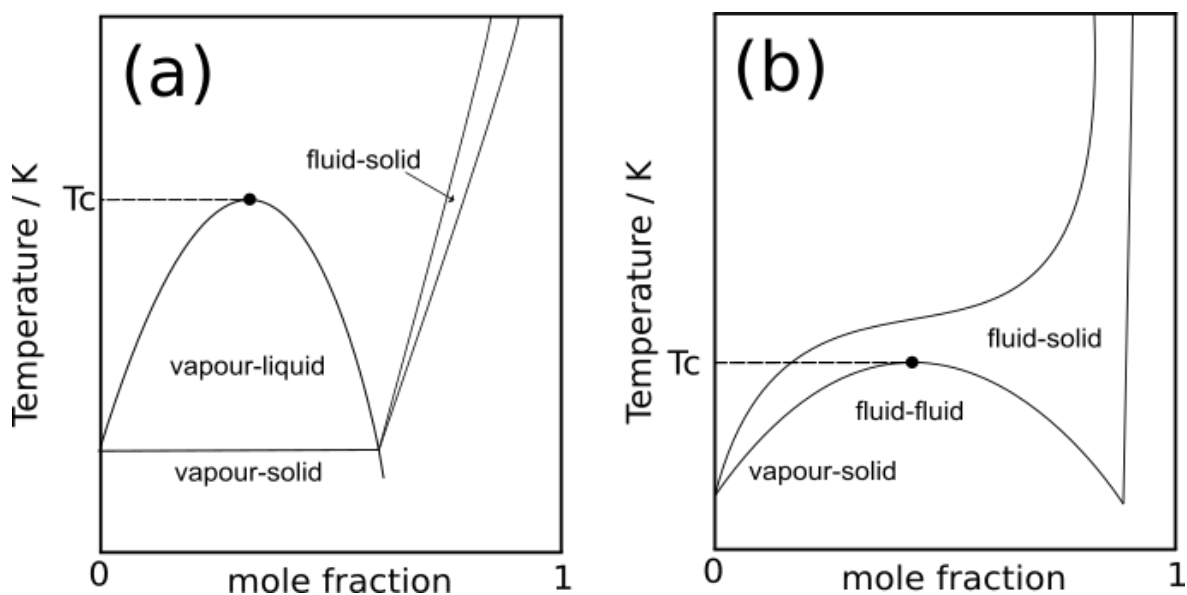
Figure 6 – Reproduced phase diagrams inspired by those from Frenkel and ten Wolde's paper[16] which depicts solutions of spheres which interact via Lennard-Jones potentials over (a) a long-range relative to the particle radius and (b) a short range. (a) shows a binodal and critical point at T_C which mirrors the phase diagram of badly mixing binary mixtures. When the interaction length is reduced in (b), the critical point moves below the liquidus (in this case, the line between the fluid-fluid and fluid-solid regions).

Frenkel and ten Wolde mapped the free energy barrier landscape at various points around the fluid-fluid critical point in Figure 6 (b) – the maps far from and close to the critical point are shown in Figure 7 A and B respectively. The landscapes are a function of N_{Cryst} and N_p which are the number of solid-like particles (if the surrounding particles show symmetry, they are designated solid-like) and the number of connected particles (liquid-like or solid-like) respectively. There are two important take-away from these diagrams. The first is that the saddle point in the free energy landscape shown in B is significantly lower than that of A, indicating an increased nucleation rate – which the authors quote to be a factor of 10^{13} higher than A. The second is the optimal pathway through the landscape to summit the saddle point. B indicates that many particles connect without forming solids – instead there are dense regions where nucleation is more probable. The work indicates that hidden critical points play an important role in direction of and the rate of nucleation.
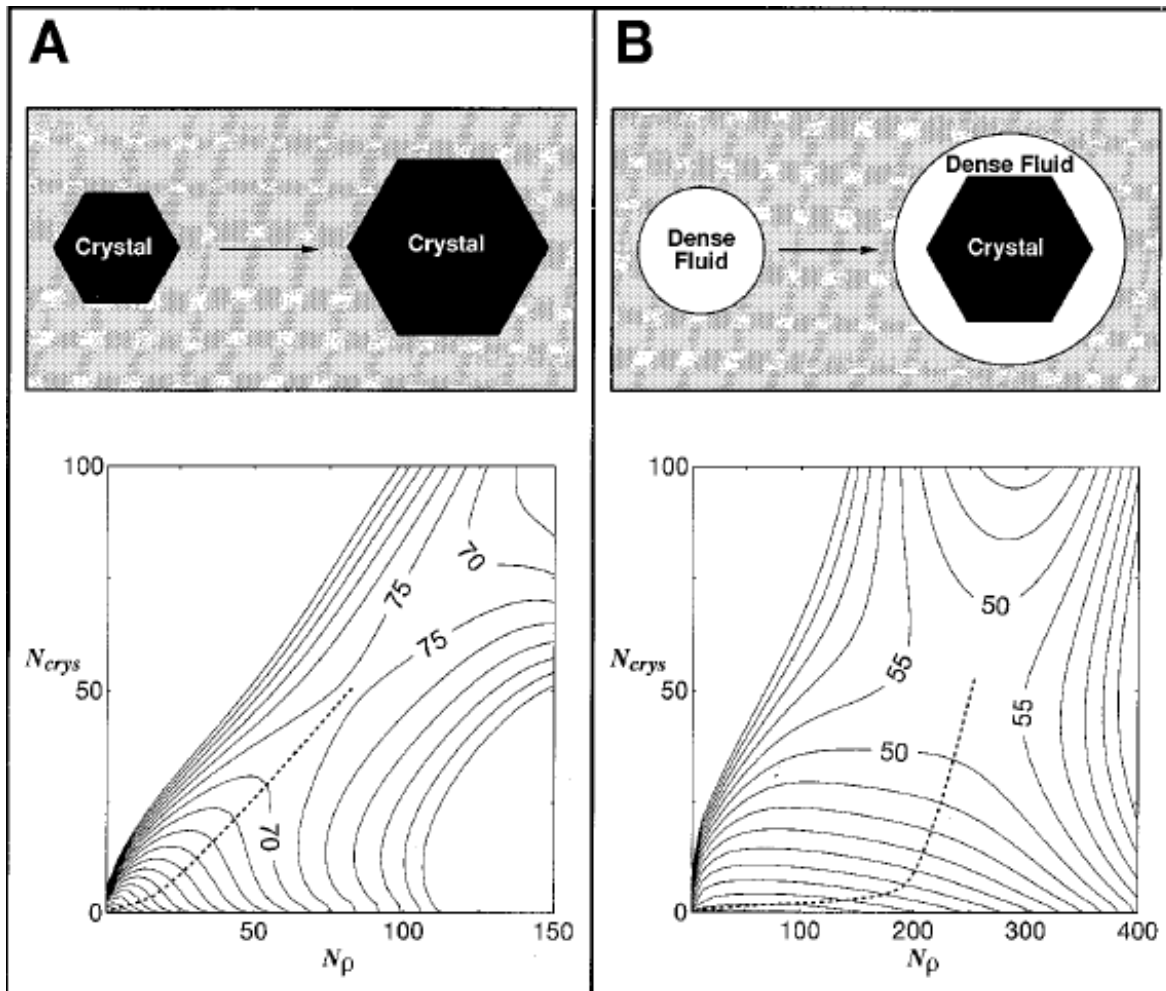
Figure 7 – Two different routes nucleation pathways for protein solutions from Frenkel and ten Wolde.[16] The graph axes N_{Cryst} and N_ρ are the number of solid-like particles and number of connected particles respectively. The contour lines represent energy, and form saddles shapes. A shows a classical nucleation route where any connected particles are part of a solid – so they are roughly proportional. B shows a big increase in the number of connected particles - which can be a liquid – with next to no increase in the quantity of solid.

Much of this thesis involves how light interacts with matter, specifically for microscopy, spectroscopy, diffraction and LIPSaN. As such it is essential to describe the fundamental properties of light.

1.5. Properties of Light

Classically, electromagnetic (EM) radiation (light) has wave-like properties.[17] Light is massless and therefore carries no momentum. Light can be described as an oscillating electric field with an oscillating magnetic field perpendicular to it. Both fields are perpendicular, or transverse to the direction of propagation. Light travels at a constant velocity in a given medium of refractive index n, where the velocity is given by

$$v_n = \frac{c}{n} \qquad (1.14)$$

14

where the speed of light in a vacuum c = 2.998×10⁸ m s⁻¹. Two sources of light with the general equation

$$y(x,t) = y_0 \cos(kx - \omega t + \phi)$$ (1.15)

can interfere either constructively or destructively, where y_0 is the amplitude, k is the wavevector, ω is the angular frequency and φ is the phase. If it is assumed the two sources of light are coherent, i.e. have the same frequency, direction of propagation and phase, the resultant amplitude will simply be 2y (Figure 8 (left)). If one source experiences a delay or scatters from an object, a phase shift occurs and the resultant amplitude will be 0 < y(x, t) < 2y. If the phase shift is exactly φ = π radians, the two sources will interfere destructively and the amplitude will be zero(Figure 8 (right)).
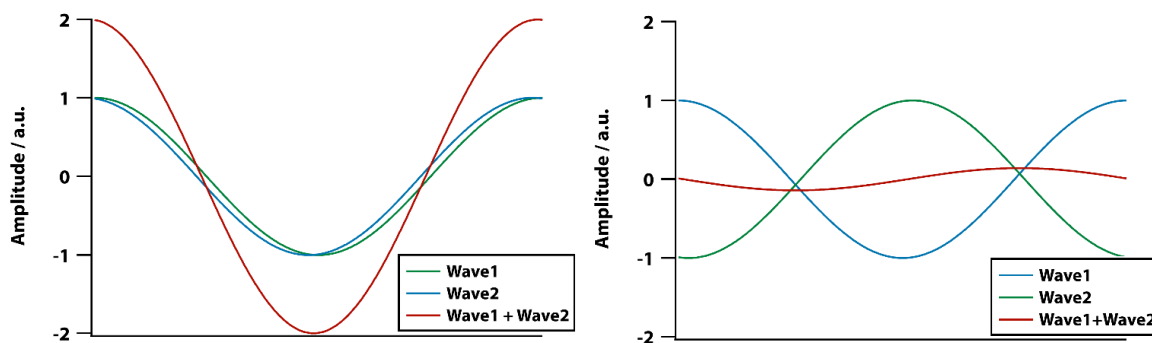
Figure 8 – Superposition of two cosine waves when the phase difference is (left) ~0 radians and (right) ~180 radians. There is a slight offset so that all curves are easier to distinguish.

One of the characteristic effects of light is diffraction, which refers to phenomena that occur when light meets an object or a slit. Diffraction is only noticeable when the wavelength of the light is similar to the size of the object or slit. An example of diffraction is what happens when a beam of light is incident on a single slit. Light deviates from simply propagating forwards as according the Huygens' principle, each point on the wavefront can be regarded as a new source of wavelets, emanating in all directions from that point. The resulting pattern in the far-field limit is a sinc² function which is depicted in red in Figure 9. The positions of the minima can be given by

$$d \sin \theta = m\lambda$$ (1.16)

where d is the slit width, m is the minimum number and θ is the angle relative to the original propagation direction before the slit. The intensity pattern seen on the screen - a sinc^2 function - is the square of the Fourier transform of the profile of the slit. If the slit is regarded as being infinitely long (into the page), it is effectively two dimensional. So, a 2D slit gives rise to sinc^2 function.
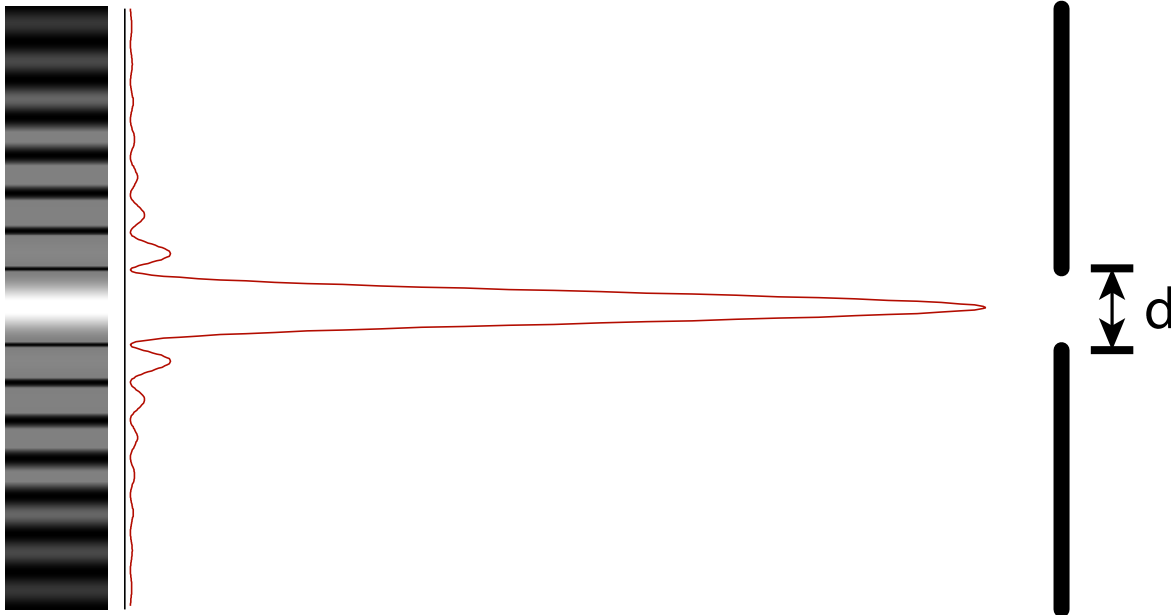
Figure 9 – Diffraction of light through a single slit results in a sinc pattern, with a large central maximum, and more minima and maxima at higher deflection angles.

A light source can be split into n coherent sources by passing it through n slits. The coherent sources interfere in the way depicted in Figure 8 and this results in a series of minima and maxima. The more slits there are, the sharper the spots become. As will be explained in X-ray diffraction section in Chapter 3, the interference of waves can be expressed by Bragg's law

$$S \sin \theta = n\lambda \qquad (1.17)$$

where S is the slit spacing and n is the maxima number, n = 0, 1, 2 etc.
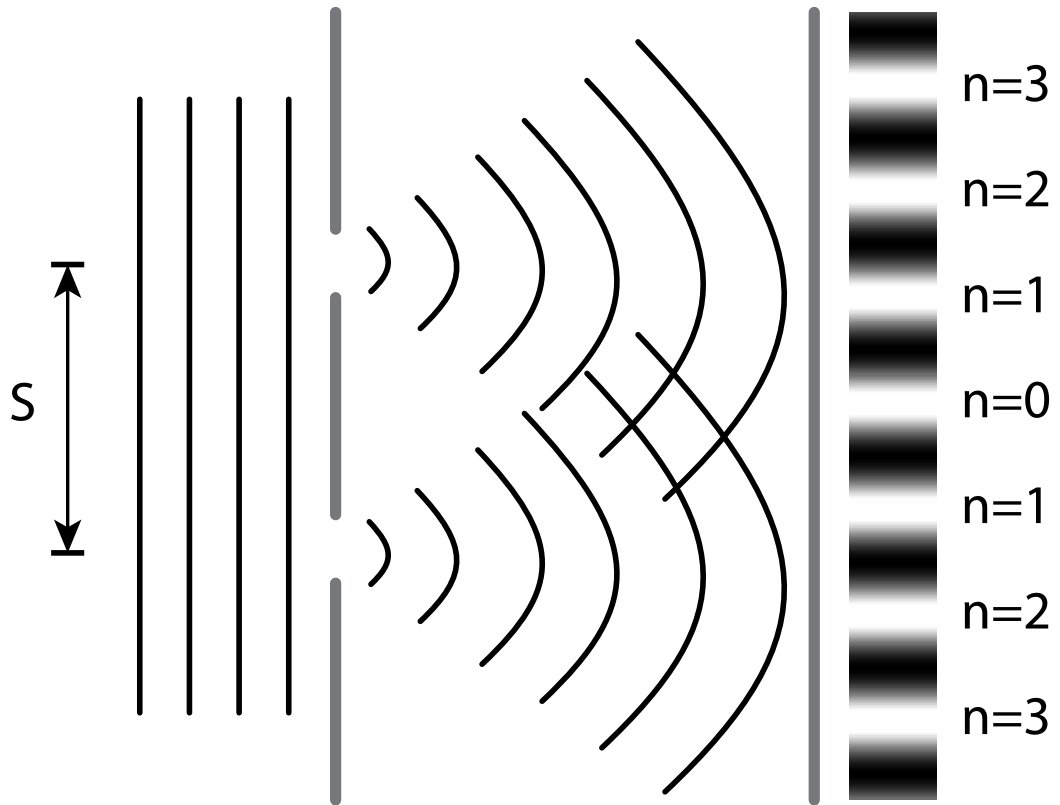
Figure 10 – A double slit example of the pattern produced by a grating - i.e. multiple sources of coherent light with even spacing S.

The diffraction limit relates to the wavelength of light. It is often referred to as the Rayleigh criterion for trying to resolve two-point sources where their radius must be farther apart than the radius of the airy disk. For a circular aperture,

$$\sin\theta_r = 1.22\frac{\lambda}{d} \tag{1.18}$$

Where θ_r is the angular resolution, λ is the wavelength of light and d is the diameter of lens aperture. An Airy disc is a 2D equivalent of a sinc function for a circular aperture as opposed to a 1D slit. For an optical microscope system specifically, (1.18) can be rearranged in terms of distance D, to what is often referred to as Abbe's limit

$$D = \frac{0.61\lambda}{NA} \tag{1.19}$$

where NA is the numerical aperture of the objective lens. Practically, normal (air) objective lenses are limited to about NA = 0.95 for a very short working distance (the distance from lens to sample). The limit can be extended by using an objective lens which is immersed in a high refractive index liquid such as certain oils.

Now that the wave properties of EM radiation have been discussed, the next section will describe how light can act like a particle which has mass, and therefore can possess momentum.

1.5.1. Wave-Particle Duality – Particulate Properties of Light

EM radiation can exhibit particulate properties, and particles likewise act like waves. Beams of particles with low mass like electrons can interfere to produce diffraction patterns just like light. Electron microscopes can also be used to overcome Abbe's limit to obtain even sub-atomic resolution. The particulate nature of EM radiation will now be described. When developing his theory of blackbody radiation, Max Planck made the assumption that atoms acted as quantised oscillators – making the energy they emitted in the form of light quantised as well. Albert Einstein later explained this – as well as famously the photoelectric effect – by postulating that the light itself existed as discrete quanta with energy

$$E = hf \qquad (1.20)$$

where f is frequency and the Planck constant h = 6.626 × 10^{-34} J s. The photoelectric effect can be explained with the following example. A quantity Q of low energy light is incident on a metal surface which results in the ejection of one electron with kinetic energy E_K. One may suppose that shining a quantity 100Q will result in electrons with a higher kinetic energy, but instead 100 electrons of kinetic energy E_K are emitted. However, a quantity Q of light with a shorter wavelength will result in an electron with a higher kinetic energy. Of course, it is also the case that certain optically non-linear materials like quartz can absorb two photons of energy E/2 and emit a single photon of energy E. This is referred to as frequency doubling (also known as second harmonic generation), but it only occurs at very high light intensities.

One quantum mechanical interpretation of the photoelectric effect involves photon having momentum **p**, which relates to the wave vector **k** according to

$$p = \hbar k \qquad (1.21)$$

where ħ = h/2π is the reduced Planck constant. During reflection or refraction there will be a change in the photon wave vector and corresponding change in momentum, meaning momentum will be transferred. The phenomenon is often referred to as radiation pressure. Solar radiation pressure has a significant effect on

satellite orbits, and strong light beams such as lasers can use radiation pressure to push around microscopic objects, which is related to the technique of optical trapping.

1.5.2. Optical Trapping

Optical trapping (or optical tweezing) involves using a highly focussed laser beam to either attract or repel microscopic particles such as glass beads. The force is attractive if the refractive index of the particle is greater than that of the surrounding medium, and repulsive if the opposite is true. The ray optics interpretation of optical trapping is depicted in Figure 11 and can be described as follows: In the focus of a laser there are large gradients of light intensity. As light enters say, a dielectric glass bead, it refracts which causes a change in the momentum vector. The transferred momentum is directed away from the direction that the light refracted towards. If considerably more photons refract through one side of the bead, there will be a net force towards the region of highest intensity. This effect works transverse to the direction of propagation, but also vertically which could be described as a tractor beam – particularly if the cone of light is at a very high angle, creating a high field gradient in the vertical axis. In order to draw the bead towards the source of light, it must also overcome radiation pressure arising from absorption and reflection. If the object is a black body, the incident pressure will be

$$P_{Incident} = I / c \qquad (1.22)$$

where I is the intensity in W m^{-2} and c is the speed of light. In the case of reflection, there is momentum transferred during absorption *and* emission, so it is double that of a black body.
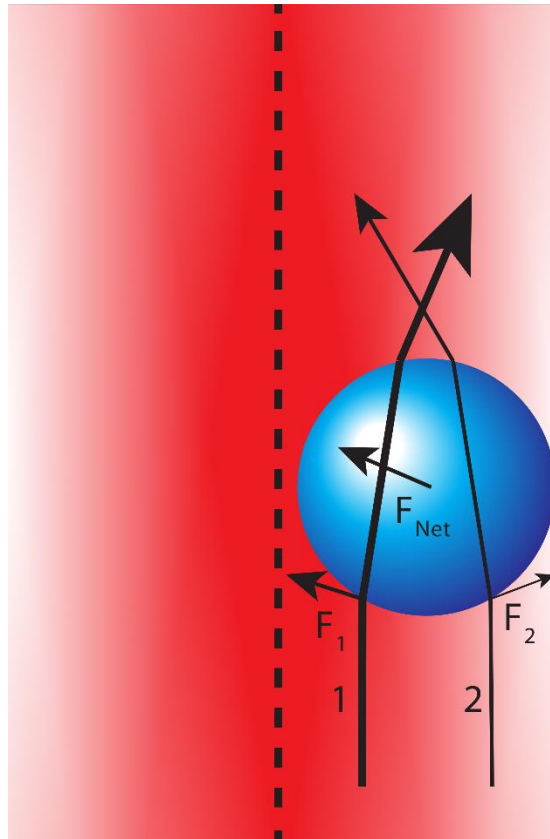
Figure 11 – Diagram depicting the ray optics interpretation of optical trapping. Two parts of a laser beam 1 and 2 refract on opposite sides of a transparent, spherical particle. Due to Newton's third law, the energy required to change the vector of the light beam results in a force, which are F_1 and F_2 for the two parts of the beam. Since the light intensity at 1 is larger than 2, the net force F_{Net} points towards the region of highest electric field intensity.

1.5.3. Microscopy

Basic ray optics and lenses will now be described, followed by the elements of an upright optical microscope and microscopy techniques which are applicable to this work.

1.5.4. Ray Optics

If a light ray enters some medium of refractive index n from air (which for simplicity n = 1 will be assumed) normal to the surface, two things happen. Light slows down to a velocity which relates to n by equation (1.14), and as a consequence the wavelength lengthens according to

$$v = f\lambda \tag{1.23}$$

where the frequency f stays constant. If light enters at angle of incidence θ_i with respect to the normal (dashed line in Figure 12), in to a medium refractive index n_2 > n_1, the ray will bend towards the normal. Where n_2 < n_1, the opposite will happen

20

– light will bend away from the normal. The equation which describes the relationship is Snell's law,

$$n_1 \sin \theta_i = n_2 \sin \theta_r \qquad (1.24)$$

where n_1 and n_2 are the refractive indices of the two media and θ_i and θ_r are the angles of incidence and refraction respectively. Figure 12 also depicts reflection, where the angle of incidence θ_i equals the angle of reflection θ_m.
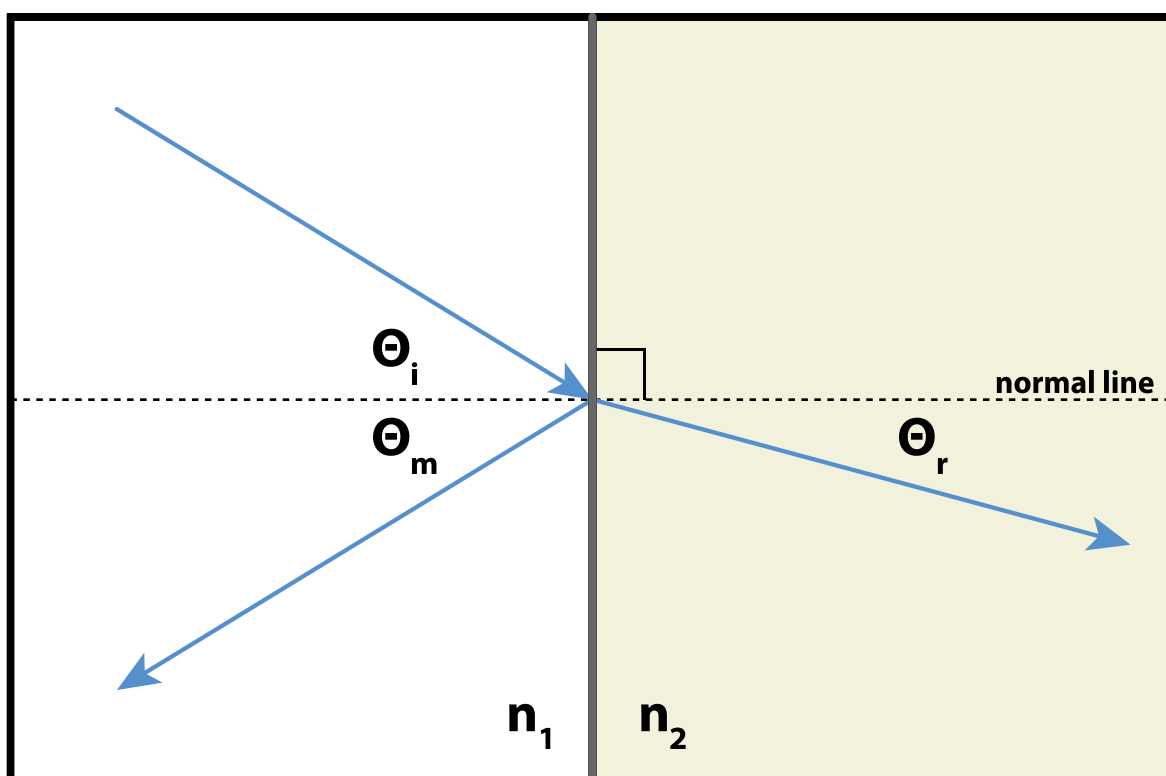
Figure 12 – Ray optics diagram illustrating reflection and refraction, the latter of which is described by Snell's law, the relationship between relative refractive indices and the bending of a light ray when entering or leaving media.

Lenses which bulge outwards are referred to as convex whereas those which bend inwards are concave. Figure 13 depicts how a bi-convex (double sided) lens can be used to increase the size of the image of an object relative to the original size. The magnification of the lens M is the both the ratio of the heights of the image (h') and object (h) and the distance from the image (s') and object (s) to the lens, where

$$M = \frac{s'}{s} = \frac{h'}{h}. \qquad (1.25)$$
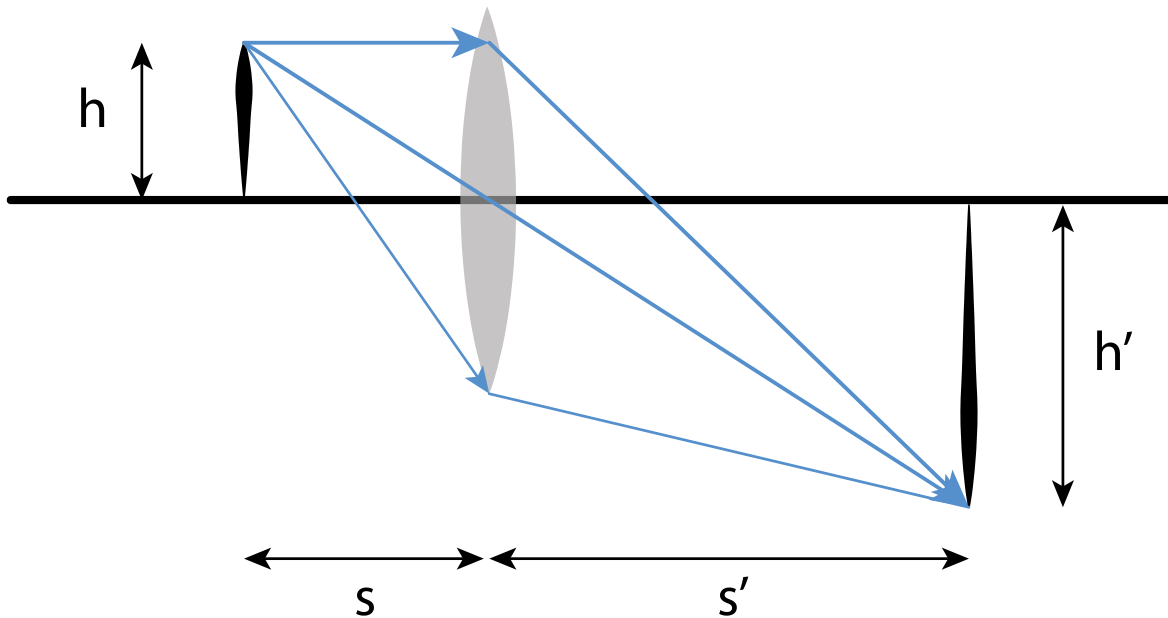
Figure 13 – Ray optics of a convex lens. The magnification of the lens is both the ratio of the distances s and heights of the image (left) and object (right).

The thin lens equation relates the focal length of a lens with the distances to the object and image as follows:

$$\frac{1}{s} + \frac{1}{s'} = \frac{1}{f}.$$

(1.26)

Multiple lenses with specific purposes can be used in combination to produce high quality and high magnification images in the form of an optical microscope.

1.5.5.   Upright Optical Microscope

Optical microscopes can be upright, with the light source at the base and camera/binoculars at the top or inverted where they are reversed. An upright microscope in transmission mode is used for the majority of experiments in this thesis. The diagram shown in Figure 14 shows the essential elements of an upright, transmission mode optical microscope, including the components used for polarisation and phase contrast modes. Light from a lamp is directed to the condenser lens, which focusses the light in the sample plane. The light is collected by the objective lens which it focusses to produce a real image on the camera. This fundamental mode of microscopy is referred to as bright field (BF).

Camera

Analyser

Phase shift ring

Objective

Sample

Condenser

Polariser

Phase contrast annulus

Condenser diaphragm

Lamp
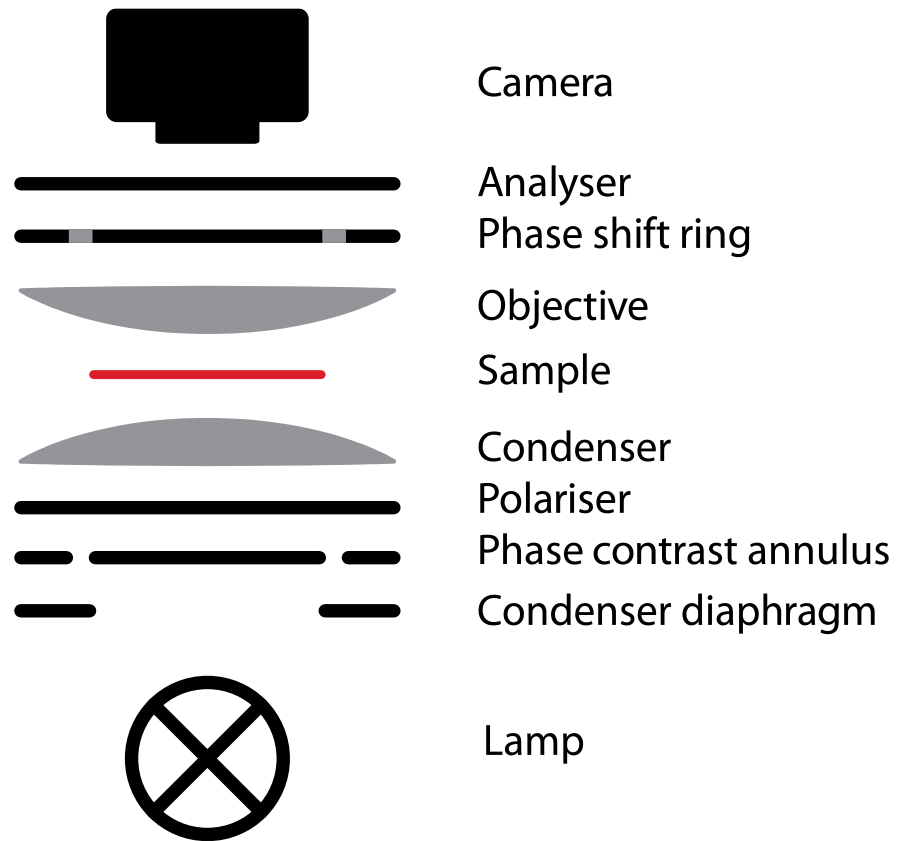
Figure 14 – Block diagram of the components of an optical microscope with polarisation and phase contrast capabilities. Binoculars have been omitted as the setup used in experiments does not feature them due to risk management and laser safety.

Optimising an image using Kohler illumination, followed by polarisation and phase contrast modes will now be described.

1.5.6. Kohler Illumination

Kohler illumination is a state where the image of the light source is at its most defocussed, and the sample is illuminated uniformly. Basically, this is achieved by contracting the condenser diaphragm (refer to Figure 14), centring it, then adjusting the position of the condenser lens until the diaphragm comes in to focus. The aperture is then opened so that the whole field of view is unobstructed, but no farther. The condenser diaphragm acts in the same way as the aperture in a handheld camera. Opening the aperture lets more light in but reduces the depth of field. The positioning of the condenser and the diameter of the aperture also defocus the image of the light source in the sample plane, for more uniform illumination. All microscope images in this thesis have been optimised using Kohler illumination prior to experiments.

1.5.7. Polarisation microscopy

'Crossed' polarisers are placed above and below the sample (see Analyser and Polariser in Figure 14), oriented almost perpendicular to each other. This means that on the whole, only parts of the sample which cause the light polarisation to rotate will be transmitted to the camera. There is often a slight angular offset, in order to give contrast between light which has been rotated clockwise and anti-clockwise. Figure 15 shows a chiral liquid crystal which has been imaged using crossed polarisers with slight positive and negative angular offsets. The dark spots become bright, and the bright background becomes dark.
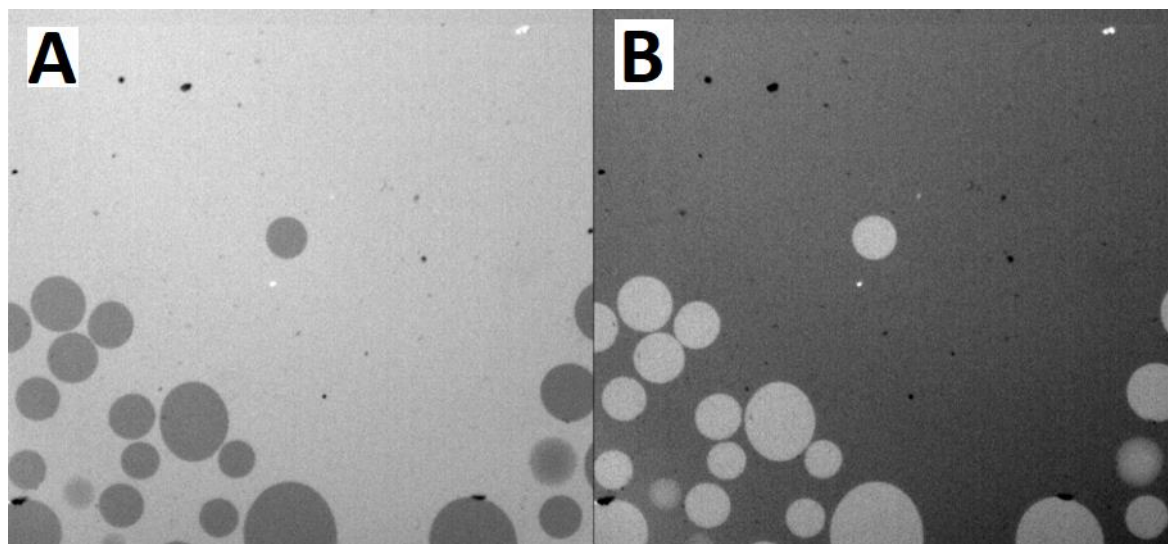
Figure 15 – A chiral liquid crystal phase which has been imaged using polarisation microscopy. In the left image the first polariser has an angular offset of roughly 5° (clockwise) and in the right, roughly -5° (anticlockwise). The levorotary (left-handed) chiral phase rotates light the opposite way from the dextrorotary (right-handed) phase. This creates dark and light contrast which depends on the sign of the angular offset.

When light experiences different refractive indices for different linear polarisation directions, the medium is said to be birefringent. Birefringent crystals such as calcite and triphenyl phosphite (TPP) rotate linearly polarised light, so they can be viewed using crossed polarisers. TPP spherulites (crystals which grow radially) for example, show Maltese crosses when viewed using crossed polarisers (images in Chapter 3).
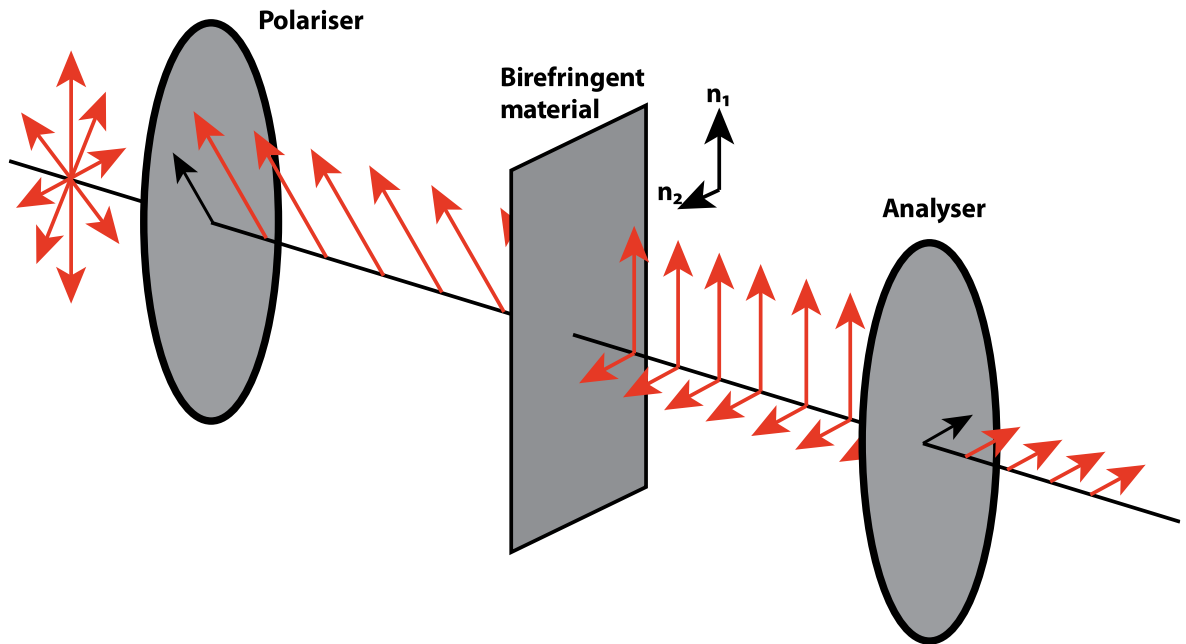
Figure 16 – Illustration of how birefringent crystals lead to light being transmitted through crossed polarisers by rotating the light from the first polariser.

1.5.8.   Phase Contrast Microscopy

Phase contrast (PC) microscopy converts phase shifts into differences in intensity, in order to enhance contrast. It is particularly useful for viewing sub-cellular detail - cells appear practically transparent using bright field microscopy. The PC technique can be used to easily resolve glass beads and droplets in water. For negative PC mode, high refractive objects which cause a phase shift and appear brighter. Likewise, objects with a lower refractive index than the bulk appear darker. This effect works very well for small objects on the micron scale, but larger objects are subject to the shade off effect. The shade-off effect causes the centre of large objects to have the same intensity as the bulk, but you can still tell whether a large droplet for example has a higher refractive index by the intensity profile at the edges (See Appendix 5.1). The diagram below illustrates the working principle of phase contrast microscope.
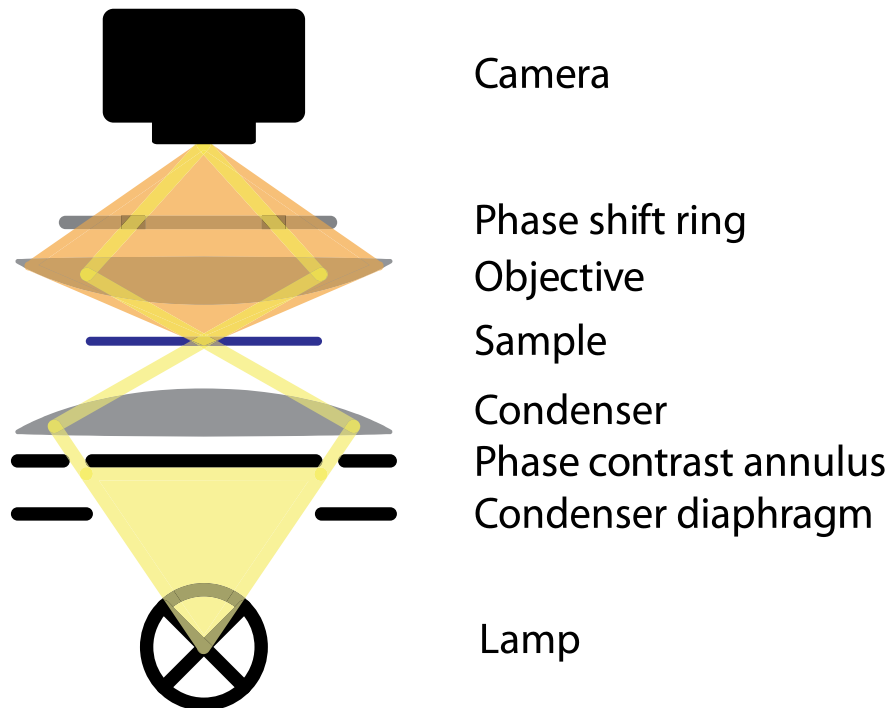
Figure 17 – Elements of a phase contrast microscope. Typically, a standard halogen lamp illuminates the sample, but passes through a phase contrast annulus which only allows high angle light to transmit. Some of the light passes through the sample plane without interaction, the yellow S-wave. Some interacts with the sample and experiences a phase shift, the orange D-wave. Both waves pass through a phase shift ring, that for negative PC mode, applies a phase shift equivalent to ¼ of the wavelength of green light to most of the D-wave. The S-wave passes through the ring without a phase shift. The phase shift ring normally also attenuates the S-wave enough to bring it to a similar intensity to the D-wave, which gives the image far better contrast. The two waves constructively interfere to produce the P-wave which is incident on the camera. Parts of the sample that produce a greater phase shift result in a brighter interference pattern on the camera.

Typically, a standard halogen lamp illuminates the sample, but passes through a phase contrast annulus which only allows high angle light to transmit. Some of the light passes through the sample plane without interaction, shown as the yellow S-wave in Figure 17. Some interacts with the sample and experiences a phase shift, which is shown as the orange D-wave. Both waves pass through a phase shift ring, that for negative PC mode, applies a phase shift equivalent to ¼ of the wavelength of green light to most of the D-wave. The S-wave passes through the ring without a phase shift. The phase shift ring normally also attenuates the S-wave enough to bring it to a similar intensity to the D-wave, which gives the image far better contrast. The two waves constructively interfere to produce the P-wave which is incident on the camera. Parts of the sample that produce a greater phase shift result in a higher amplitude interference pattern and brighter intensity on the camera.

1.5.9. Fluorescence Microscopy

Optical microscopes can be adapted to include an extra fluorescence module which is placed between the objective lens and the camera/detector. The module contains cubes which contain excitation and emission filters and a dichroic mirror which transmits long wavelength light and reflects short wavelength light. The light source can take the form of a broadband lamp, light-emitting diodes or even lasers in confocal fluorescence microscopes. The light is first directed perpendicular to the microscope column, through the excitation filter, to isolate the wavelength that the chosen fluorophore absorbs at. The shorter wavelength excitation light reflects off the dichroic, through the objective lens and to the sample. The sample absorbs the light and emits it at a longer wavelength via fluorescence. The emission light transmits through the dichroic mirror and is isolated using the emission filter before hitting the camera or detector.
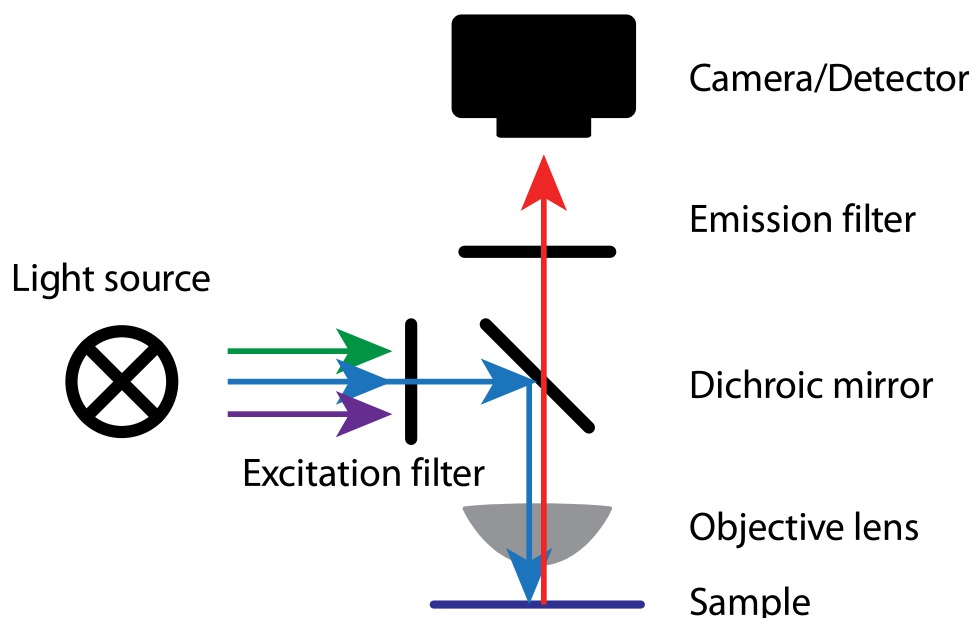
Figure 18 – Beam diagram of the essential components of a fluorescence module for an optical microscope. Broadband light passes through an excitation filter to isolate the desired wavelength that the fluorophore absorbs at. The light is reflected off a dichroic mirror and through the objective lens to the sample. The sample absorbs the light and fluoresces at a Stokes shifted, longer wavelength. The dichroic mirror is chosen such that the excitation wavelength reflects but the emission wavelength transmits. The emission light transmits through the dichroic and is then filtered using the emission filter, to discard any stray light heading for the camera or detector.

Fundamentally, fluorescence is a form of luminescence where a singlet state in a molecule relaxes to a singlet ground state and emits a photon. A singlet state has a spin multiplicity or quantum number $S = 0$, whereas triplet states have $S = 1$. Transitions between excited singlet and triplet states are known as intersystem crossings (ISC) and are forbidden since spin is not conserved. The transition can

be weakly allowed however, as spin orbit coupling makes the total angular momentum the sum of spin and orbital angular momentum. Figure 19 illustrates how an electron which has been promoted to an exited singlet state S1 can sometimes cross by ISC to an excited triplet state, which then drops through phosphorescence to a singlet ground state. Phosphorescence is also forbidden due to lack of spin conservation. Fluorescence is a fairly rapid process, with the excited state lifetime of 1 – 10 ns. Since after an ISC the excited triplet state can only relax via a forbidden transition it has a much longer lifetime – anything from 10 ms to hours. In both cases, excited states can also drop down vibrational or rotational states via internal conversion (IC), which occurs over 1-100 ps. Since IC is a faster process than fluorescence or phosphorescence, the majority of luminescent photons have a lower energy and longer wavelength. The difference in energy between the absorption and emission peaks is known as the Stokes shift.
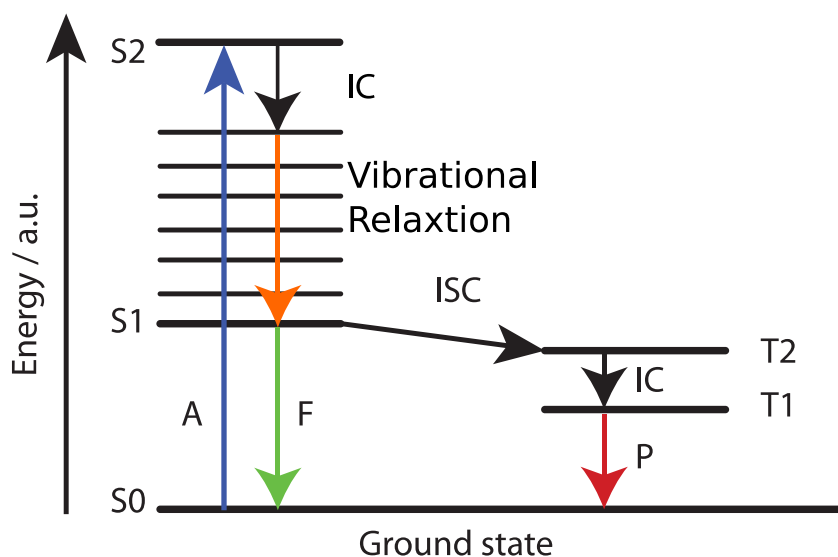
Figure 19 – Jablonski diagram illustrating luminescence processes. A photon is absorbed which promotes the ground electronic state to an excited singlet state S2. The system undergoes a non-radiative internal conversion (IC) to an S1 level, followed by vibrational relaxation, which generates heat. The system either proceeds by fluorescence and the emission of a lower energy photon, or a forbidden intersystem crossing to a triplet state T2. An internal conversion is depicted between the T2 and T1 levels, followed by phosphorescence and the emission of a photon (which is also forbidden) to the ground state.

The processes shown on the Jablonski diagram in Figure 19 can happen intermolecularly as well as intramolecularly. Fluorescent molecules are said to be *quenched* if energy is transferred to another molecule. Quenching typically occurs by at least one of two processes: Förster resonance energy transfer (FRET) and Dexter electron transfer. FRET is a form of non-radiative energy transfer, where the energy of a *virtual photon* from a donor molecule is instead transferred to promote

an electron in an accepter molecule. FRET often occurs between two fluorophores, so fluorescence emission can still occur in the acceptor molecule, but often at a longer wavelength than the donor. Dexter electron transfer requires the overlap of the wavefunctions of particular molecular orbitals of the donor and accepter and occurs in electron deficient quenchers like compounds with nitro groups.[18]

The two quenching mechanisms can be discriminated by measuring their quenching rate as a function of intermolecular separation. Since Dexter requires wavefunction overlap, it requires shorter separation, and the rate varies linearly with distance. FRET on the other hand can operate over longer distances since it is a dipole-dipole interaction and the quenching rate has a dependence on separation to the sixth power.

The topics which are common to both results chapter 2 and 3 have been introduced, so the chapters will now be presented individually, with chapter specific introductory topics.

2. Control over phase separation and nucleation near a liquid-liquid critical point using the electric potential of a laser

2.1. Summary

Gaining control over the nucleation of new phases is advantageous but has been hard to achieve. Despite there being a long period of crystallization engineering by varying physical and chemical parameters, controlling which polymorph crystallizes or whether a molecule crystallises or forms an amorphous glass is still something to be desired. In the last few decades several examples of control using laser-induced nucleation have surfaced, however the absence of a complete physical understanding is preventing the field from advancing. In this chapter, it will be demonstrated that the proximity to a liquid-liquid critical point on a binodal line allows the electric potential of a laser beam to induce concentration gradients in binary mixtures. In the metastable region between binodal and spinodal lines and near the critical point, the nucleation of a phase separated state can be induced. A simple theoretical model explains why this phenomenon is well within the laws of physics and bears a similarity to optical tweezers. The electric field of a laser produces a potential that lowers the free energy of the phase separated state with respect to the mixed state of a binary mixture of badly mixing liquids. Laser-induced phase separation and nucleation (LIPSaN) explains the physics behind non-photochemical nucleation phenomena and presents a new technique for the optical manipulation of matter.

2.2. Introduction

The nucleation and growth of phases, particularly crystals from solution, is critical to understand if scientists and engineers are to be able to produce the pharmaceuticals, coatings, electronics and other chemicals of the future. A significant proportion of pharmaceutical products and speciality chemical products are produced in crystalline form. Products include aspirin, paracetamol and other common drugs, paint pigments and silicon wafers. The fundamental process of nucleation is spontaneous, messy and is also badly understood. Classical nucleation theory, or Gibbs theory, has already been described in Chapter 1, along

with hidden liquid-liquid critical points[16] and pre-nucleation clusters[8] which can influence nucleation rate and the route to stable phases. A deeper understanding of nucleation is highly desirable, so it is hoped that this chapter can contribute to the picture by tackling the recently discovered phenomenon of non-photochemical laser-induced nucleation. But first, it is important to explain some of properties of lasers before the NPLIN experiments which use them are discussed.

2.2.1.   Lasers

Laser beams have certain properties which are highly desirable for telecommunications, data storage, spectroscopy, metrology and medicine. Laser stands for 'Light Amplification by Stimulated Emission of Radiation'. Laser beams are highly spatially and temporally coherent, so the photons are in phase and the beam tends to have a narrow linewidth, i.e. is monochromatic (except when pulse lengths are very short). As the acronym suggests, lasers achieve coherence by a phenomenon called stimulated emission which is depicted in Figure 20. Normally after a photon has been absorbed and has promoted an electron to some excited state E2 from ground state E1, a photon with be emitted spontaneously during decay back to E1. In stimulated emission, a second photon with energy hv interacts with the excited electron and triggers the emission of two photons, which are now spatially and temporally coherent. After many iterations, the result is a collection of photons of which a high proportion are coherent.
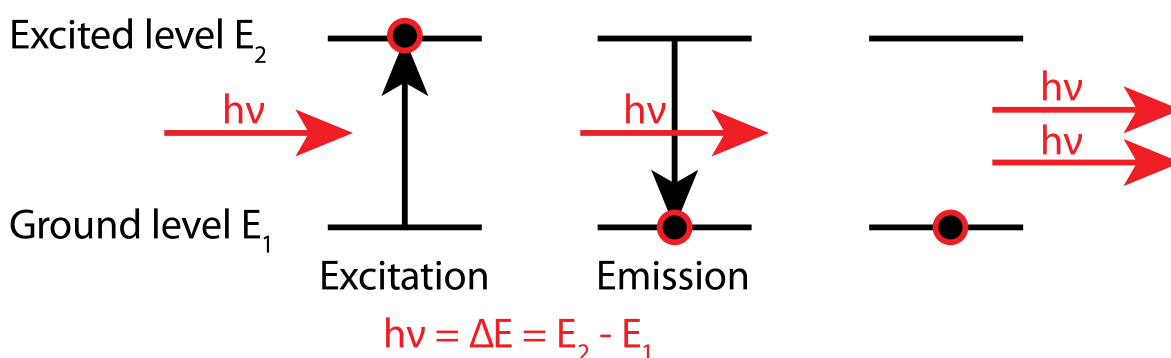
Figure 20 – Depiction of stimulated emission. An electron is excited from E1 to E2 by a photon of energy E = hv. If a second photon interacts with the excited electron before it decays spontaneously, the emission is instead stimulated by the photon, and two coherent photons are emitted.

In most materials the standard absorption of a photon is much more probable than stimulated emission, so they must be designed in a way which reverses this. The chief way that this is achieved is by population inversion, i.e. the majority of electrons remain in an excited state rather than the ground state. So,

$$\frac{N_{E_2}}{N_{E_1}} >> 1 \qquad\qquad (2.1)$$

where N is the number of photons occupying a given energy level. Population inversion is achieved by designing a material which can act as a *gain medium*, e.g. titanium doped sapphire (Ti:Al$_2$O$_3$) which has four energy levels with specific energies and lifetimes (Figure 21). The gain medium is pumped with photons from a higher energy light source (often another laser such as a diode laser) which excites electrons from the ground state level 1 to level 4. This is followed by a relatively fast transition to level 3, so that level 4 continues to be free for other level 1 electrons to be promoted to. The transition from level 3 to level 2 determines the energy E = hv of emitted photons and is relatively slow, which acts in a sense like a bottleneck, so that excited electrons pile up in level 3. Level 2 to the ground state level 1 is relatively fast, which means that electrons do not remain there for long. Once equilibrium has been established, the number of photons in level 3 greatly outnumbers level 2, so population inversion has been achieved and stimulated emission becomes more probable.
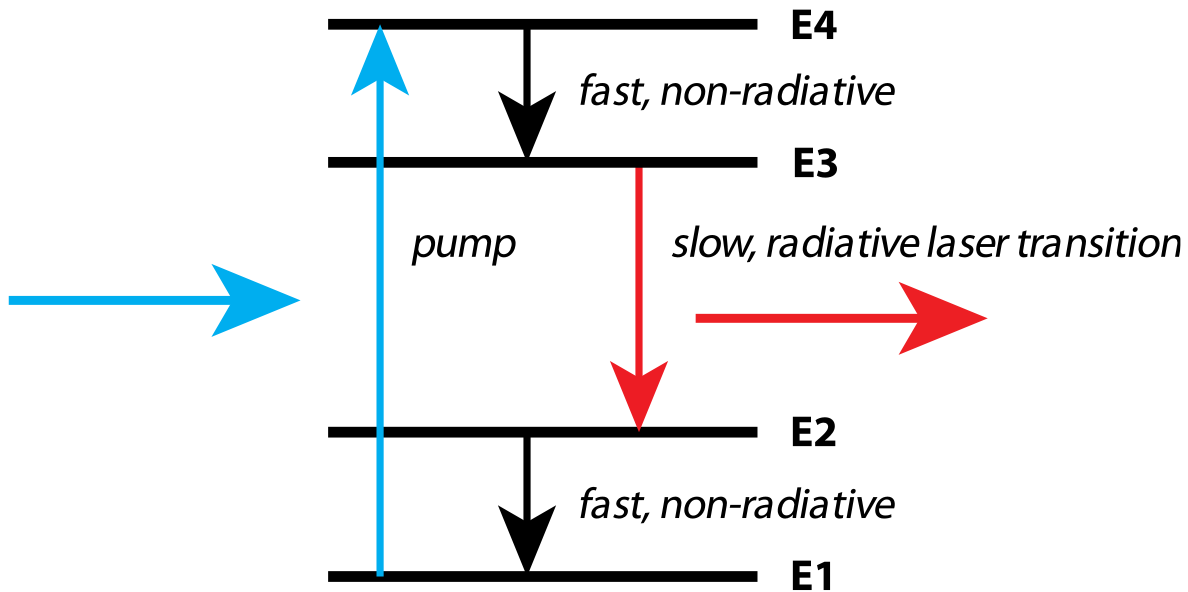
Figure 21 – Depiction of a four-level system which can achieve the population inversion requiring for lasing. A slow lasing transition and fast transitions from E4-E3 and E2-E1 maintain a high number of excited electrons in the E3 state and a small number in the E2 state.

Laser gain media are typically housed inside an optical cavity with two plane parallel mirrors. If the two mirrors have similar reflectivity, the cavity is referred to as Fabry-Pérot, but if one is more reflective than the other, it more like a Gires-Tournois cavity – both are used in different types of lasers. At least one of the mirrors has to be

partially reflective, in order for photons to leave the cavity. Housing the gain medium in a reflective cavity like this ensures a high density of photons and makes sure stimulated emission is undergone frequently enough to maintain beam coherence. The length of the cavity also affects which frequencies are amplified, as it acts as a resonator. Transverse and longitudinal standing waves form in the laser cavity with a wavelength

$$\lambda_0 = 2nL/m \qquad (2.2)$$

where L is the length of the cavity, n is the refractive index of the gain medium and m is the mode number. As the equation describes, harmonics of the desired wavelength are produced, so these need to be filtered out. It should be noted that this equation is simplified – as many lasers have a longer cavity length than the length of the gain medium.

What has been described so far roughly corresponds to a continuous wave (CW) laser which emits a constant beam of constant power. Lasers can be designed to emit trains of pulses, some of which can be < 100 attoseconds (10^{-16} s) in length.[19] Due to the Heisenberg uncertainty principle, as the pulse length gets very low, the spread of frequencies must rise. As a result, ultrafast pulsed lasers are not monochromatic, but cover a broad range of wavelengths. Pulses are typically generated through a process called mode locking, which involves using some method to force a fixed phase relationship between the cavity modes ω_n. If adjacent modes have a random phase relationship, the amplitude of the laser will oscillate randomly. If the modes are fixed to oscillate with a phase shift equal to the spacing between the modes $\Delta\omega = \omega_{n+1} - \omega_n$ then the sum will produce a short pulse, which is depicted in Figure 22. The more modes that are used, the shorter the pulse can become, which is of course at the cost of how narrow the spread of frequency is.
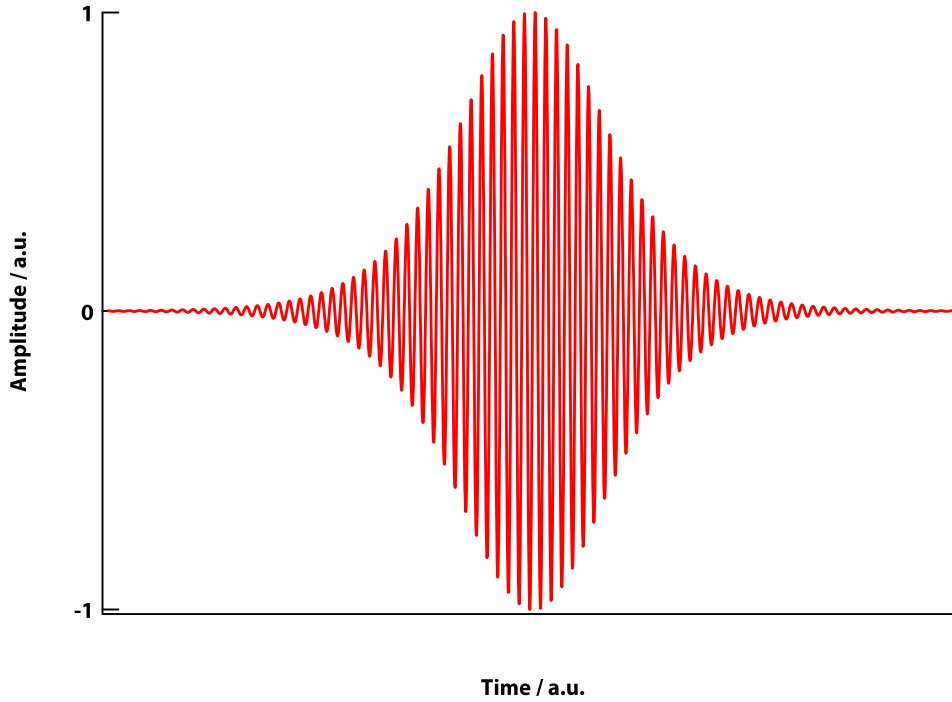
Figure 22 – Example of an ultrafast laser pulse. The envelope in this case is a squared hyperbolic secant function.

If the simplification of a square pulse is made, the peak power of a laser pulse is given by

$$P_{peak} = \frac{E_{pulse}}{\Delta t} \qquad (2.3)$$

where E_{pulse} is the pulse energy and Δt is the pulse width. The width of a laser pulse like the example in Figure 22 will be defined at the full width half maximum (FWHM).

The peak power density, for which the Greek letter zeta (ζ) will be assigned, follows the relation

$$\zeta_{Peak} = \frac{E_{Pulse}}{\pi(d/2)^2 \Delta t} = \frac{P_{Peak}}{A} \qquad (2.4)$$

where d is the diameter of the beam at the waist (1/e of maximum) and A is the area of the beam. Pulsed lasers possess a repetition rate, or rep rate, which can vary from several Hz to MHz. Based on the repetition rate and pulse length, it is easy to calculate the fraction of time that the beam is in the 'on' state for

$$\frac{t_{On}}{t_{Total}} = \frac{R_{Repetition}\Delta t}{1} . \qquad (2.5)$$

34

For the pulsed laser used for a typical experiment in this work, $R_{Repetition}$ = 1 MHz and Δt = 1 ps so the on/off fraction is 10^{-6}.

The optical setup which integrates two lasers – one CW and one pulsed – and is used for majority of experiments in this chapter will now be described.

2.2.2. Optical Setup

The optical setup used consists of an upright optical microscope with phase contrast and polarisation capabilities, a fluorescence module and two laser sources which are directed into the microscope column using a periscope and dichroic mirror. Figure 23 shows a plan view of the optical bench which in short, consists of two lasers which are along the same beam path towards the periscope, and can be alternated using the flip mirror M4.
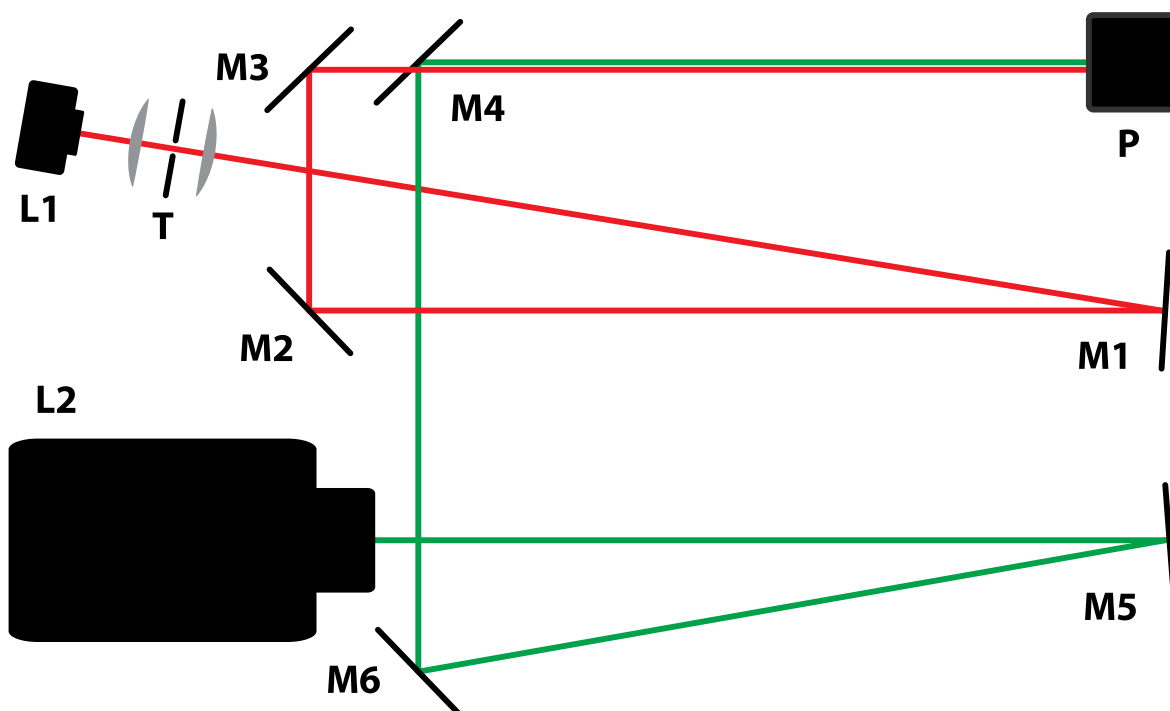
Figure 23 – Plan view diagram of the main elements of the laser bench setup. Lasers L1 and L2 are a 785 nm, CW, 250 mW diode laser and a 1040 nm, 350 fs - 4 ps, 1 MHz/100 kHz 8.5 W pulsed laser respectively. Mirrors M1, M2 and M3 are used for alignment L1, and M5 and M6 are used to align L2. M4 is a flip mirror which can direct either L1 (red beam) or L2 (green beam) towards the periscope P. T is a telescope which featured a spatial filter aperture and expands the beam diameter to better fill the back of the objective lens prior to reaching the sample. It should be noted that L1 contained an aspheric lens within its housing for collimation, which has not been illustrated or labelled.

A periscope is used to raise the beam to the height of the custom module for the microscope which contains a dichroic mirror. A series of apertures are placed before, within and after the periscope for alignment. Figure 24 depicts an elevation view of the microscope column which features a custom built module containing a

dichroic mirror for laser entry, a fluorescence module, positions for polarisers (labelled analyser, above the sample), a wheel of annuluses for phase contrast, and annuluses built in to the 10x and 20x objective lenses. There is also a 50x non-phase contrast objective. As long the fluorescence emission filter is placed above the laser dichroic in the column, it is possible to carry out epifluorescence while simultaneously irradiating the sample with the laser. If the emission filter was placed within the filter cube of the fluorescence module, it would attenuate the laser significantly.
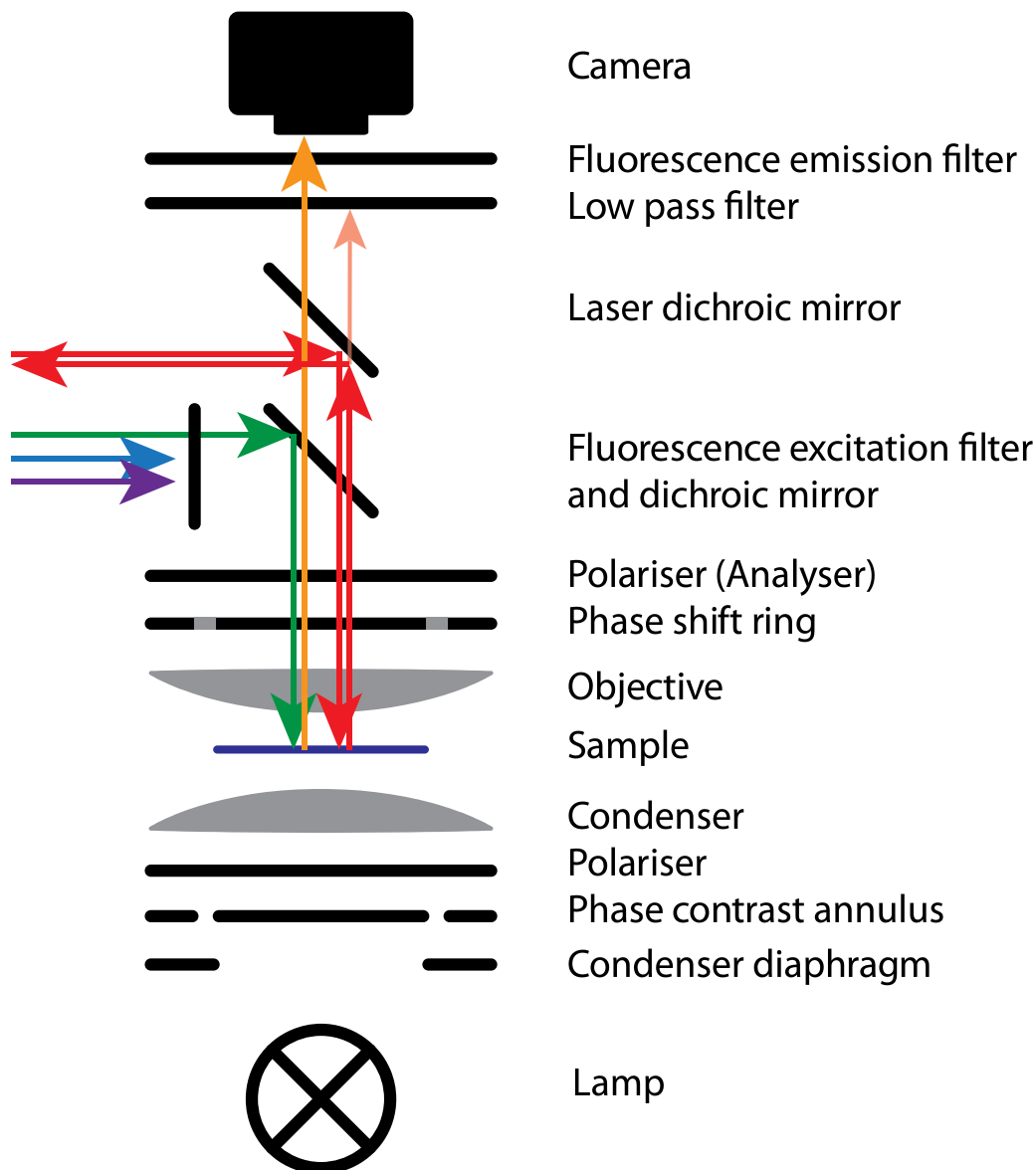
Figure 24 – Elevation view of the microscope used for the majority of experiments. The microscope can be used in phase contrast mode if the phase contrast annulus is equipped. Polarisers can be inserted for polarisation microscopy (crossed polarisers). There are an array of filter cubes for epi-fluorescence. As the custom laser module is above the fluorescence module, the emission filter would block the laser if unmodified. To rectify this, the filter has been placed above the laser module. Despite there being a laser dichroic mirror, it was still essential to use a low pass filter to attentuate the transmitted laser light to an acceptable level for low light experiments.

Now that lasers and the optical setup used has been outlined, the literature surrounding the non-photochemical laser-induced nucleation (NPLIN) phenomenon will now be summarised.

2.2.3. Non-Photochemical Laser-Induced Nucleation

The principle of non-photochemical laser-induced nucleation (NPLIN) is simple – direct a laser at a metastable solution and trigger nucleation – through a mechanism which does not involve heat. There are numerous examples of nucleation where heating produces cavitation bubbles[20], or causes a photochemical reaction.[21] The majority of the examples of NPLIN use nanosecond pulsed lasers with fairly high peak power densities in the range 10-100 MW cm^{-2}. The first example of NPLIN was demonstrated by Garetz and co-workers who used a 20 ns 1064 nm laser Nd:YAG laser to nucleate urea crystals from a supersaturated solution.[22] The amplified pulse energy was 0.1 J and the beam area was ~2 mm^2, resulting in a power density of 250 MW cm^{-2}. They conclude that since there are no vibrational bands in urea near 1064 nm and at the power density used, multiphoton absorption is insignificant, the mechanism must be non-photochemical. Garetz proposed a mechanism based on the optical Kerr effect (OKE) causing molecules to align with the electric field, partly because the needle-like urea crystals tended to align with the field. This is puzzling as the peak power of the laser Garetz used (using equation (2.3) is 5 MW and the peak power required for the OKE to be significant tends to be ~10 GW.[23] Garetz revisited NPLIN four years later and demonstrated the same effect with supersaturated solutions of the amino acid glycine.[24] The thermodynamically more stable γ polymorph of glycine[25] was unexpectedly produced during NPLIN experiments, with only the kinetically favoured α polymorph being produced in control experiments with the laser off. This led to a more thorough study using 41 samples, where the nucleated polymorph was controlled with 100 % success – linearly polarised light produced γ and circularly polarised light produced α.[26] The authors reported an increase in nucleation probability with laser power and implicitly rule out an OKE mechanism by calculation (although they use the OKE as a mechanism in subsequent publications). Since laser polarisation appears to have such an influence, the authors argue that this is further evidence that NPLIN is not a heat or photochemical effect. Since then, NPLIN has been reported to occur in solutions of phenylalanine[27], L-histidine, hen egg lysozyme[28], CO2[29,30], potassium halides[31], sodium chlorate[32], sulfathiozole[33], carbamazapine[34], pure acetic acid[35]

and a liquid crystal.[36] Simulations carried out by Knott and co-workers cast further doubt on the OKE mechanism.[37] Alexander and co-workers published a number of articles which repeated older experiments and cast doubt on some NPLIN claims.[30,38,39] Their data shows no statistically significant relationship between linear polarisation direction and urea crystal orientation – casting further doubt on the OKE mechanism. They conclude that CO_2 bubble nucleation in sucrose solutions is due a heating effect. Along with Clair and co-workers[40], they doubt Garetz's claim of 100% polarisation switching of glycine polymorphs, saying that although control was possible, it was only achievable over a very narrow range of supersaturation ratios. In addition, they propose that NPLIN in glycine is caused by cavitation bubbles from impurity nanoparticle heating, which result in a local increase in supersaturation. Eral and co-workers come to the conclusion that the mechanism behind NPLIN is a pressure wave generated by the laser.[41] Most recently, Alexander and Camp described the evidence for polarisation selection using NPLIN to be "patchy", and the exact mechanism behind NPLIN to be uncertain.[42]

Laser-induced nucleation experiments performed by Masuhara and co-workers using focussed CW lasers have reliably shown polarization control over polymorph selection, however only at the air-solution interface.[43] This suggests that heating, evaporation, convection or Marangoni effects may play critical roles[44], which would also explain why the method works in under-saturated solutions. However, interestingly, these experiments have also demonstrated polymorph selection.

At this stage, NPLIN has a range of potential mechanisms ranging from the optical Kerr effect or some other electric field based mechanism, to pressure waves, cavitation bubbles and impurity heating. OKE has effectively been ruled out; a more plausible mechanism as suggested by Knott and co-workers[45] is an Isard type – the growing nucleus has a higher refractive index than the surrounding liquid and is therefore stabilised by the field. One feature of NPLIN phenomena which has somewhat slipped under the radar is the rather small selection of solutions that it occurs in. If it is something as generic as the mechanisms outlined so far, why is NPLIN not observed more broadly? The mechanism which will be advanced here involves the influence of a liquid-liquid critical point like that which was described by Frenkel and ten Wolde[16], which is hidden behind the curtain of crystallisation.

Before moving on to discuss theory, a brief mention will be given to the related non-linear dielectric effect (NDE).

2.2.4. The Non-Linear Dielectric Effect

The non-linear dielectric effect (NDE) is a bit of a tangent, but it is worth discussing due to its similarities with the LIPS effect.

In 1965, Debye and Kleboth published a paper which showed the unusual dielectric behaviour of a mixture of nitrobenzene/2,2,4-trimethylpentane, when near the critical point T_C of demixing.[46] They reported that when a DC electric field is applied to the mixture, T_C decreased slightly. They determined the size of the shift by comparing critical opalescence data at different electric field strengths. Critical opalescence is the exponential rise in opacity that is often seen during continuous phase transitions like demixing by spinodal decomposition. The authors found a depression in T_C of 0.015 °C for a field intensity of 45,000 V cm^{-1}. Ziolo and co-workers carried out a similar experiment and made several observations: there was a greater change in T_C for liquids that had a greater difference in dielectric constant, the effect was also greater for the liquid crystal N-(4-Methoxybenzylidene)-4-butylaniline than for the molecular liquids, and the liquid with the higher dielectric constant was attracted preferentially to areas of high field.[47]

There is a similarity between LIPSaN and the NDE. In both cases, mixtures with a difference in relative permittivity ε_r can be separated using high electric fields – the higher ε_r component being drawn to the high field region. Of course at zero frequency $\varepsilon_r = \varepsilon_0$, the dielectric constant, and at visible frequencies $\varepsilon_r \approx n^2$. The interpretation of the NDE is different from the interpretation of LIPSaN described in this chapter. NDE is interpreted as a shift of a critical point (or the whole binodal), but LIPSaN is interpreted in this chapter either as the lowering of free energy by the high refractive index component occupying the laser focus, or as an analogue of optical trapping.

2.3. Theory

In this theory section the fundamental physical principles behind what will be termed the LIPSaN phenomenon will be laid out and some predictions will be made which will be compared to experiment in the results and discussion sections. Much of this section was recently published by us.[48–50] The regular solution model in the next section will be amended to include a term to factor in the effect of the laser. This will be used to calculate the mole fraction in the focus and predict the effect of moving away from the critical point in terms of temperature. The steady-state heating in the

focal volume will be solved analytically in one dimension and the effect of thermophoresis (the Soret effect) will be estimated.

2.3.1.   Regular Solution Model of Mixing

In order to model the free energy associated with the mixing/demixing of two liquids, the regular solution model as it is presented by Jones[51] will be used as a starting point. The regular solution model builds on the ideal model of a mixture by factoring in an enthalpy of mixing as well as entropy. The enthalpic term is asymmetric with respect to mole fraction, however deviations from ideality are often asymmetric and so are not fully accounted for. A mixture can be defined with mole fractions of molecules A and B which are given by x_0 and x_B respectively, such that $x_B = 1 - x_0$. The regular solution model defines the energy of the interaction between A and B relative to their self-interaction by introducing the variable χ which is defined as

$$\chi = \frac{z}{2}(2\varepsilon_{AB} - \varepsilon_{AA} - \varepsilon_{BB}) \qquad (2.6)$$

where z is the number of nearest neighbours of a given molecule in the mixture and ε is the molar interaction energy for each pairing. The term for the total molar free energy of mixing is then given by

$$F_{mix} = (x_0, T, \chi) = RT(x_0 \ln x_0 + x_B \ln x_B) + \chi x_0 x_B \qquad (2.7)$$

Here $z\varepsilon_{AA}$ is approximately equal to the heat of vaporisation, which ranges from zero (at the gas/liquid critical point) to ~40 kJ mol^{-1}. This means that χ is positive on the order of a few kJ mol^{-1} for poorly mixing liquids. This equation can be used to calculate the free energy of mixing using a sensible choice of parameters, which is shown in Figure 25.
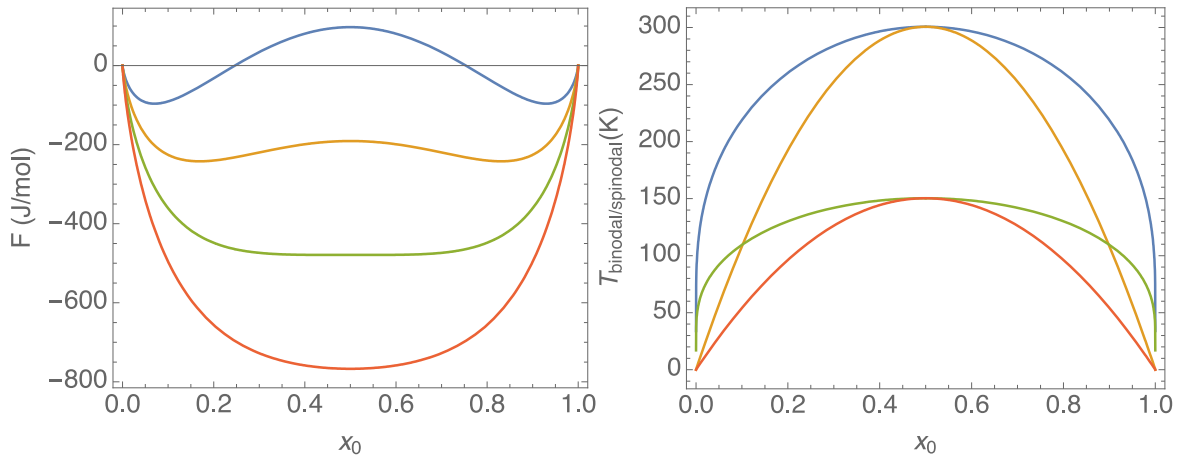
Figure 25 – (left) Free energy of mixing (defined in equation (2.7))for χ = 5 kJ mol⁻¹ and T = 200, 250, 300 and 350 K (top to bottom). At high temperature there is one minimum at a mole fraction of 0.5. At low temperature there are two minima at either side, as the mixture separates in to two phases. (right) Binodal and spinodal lines for (lower curves) χ = 2.5 and (upper curves) 5 kJ mol⁻¹.

The co-existence curve (binodal) is at $dF_{mix}/dx = 0$ and the spinodal at $d^2F_{mix}/dx^2 = 0$, which can be solved for T to give

$$T_{Binodal} = \frac{\chi(1-2x_0)R^{-1}}{\ln(1-x_0) - \ln(x_0)} \tag{2.8}$$

and

$$T_{Spinodal} = 2x_0 \chi(1-x_0)R^{-1}. \tag{2.9}$$

As it can be seen in Figure 25, when χ = 5 kJ mol⁻¹ gives a reasonable approximation for the binodal of a nitrobenzene-decane mixture which has T_C = 295.96 K and x_C = 0.575 and will be used for the majority of the experiments described in this chapter. Like many examples of binary mixtures, the experimental binodal of nitrobenzene-decane shows slight asymmetry (Figure 31), but a symmetric approximation will be sufficient for the model.

The effect of free energy changes in a small volume caused by spontaneous concentration fluctuations now need to be considered. V_0 is defined as the total volume of the sample and x_0 as the mole fraction of the initial mixture in terms of A. Now a microscopic volume V_{laser} is defined which will be the focal volume of the laser later on. If the mole fraction of the focal volume x_{laser} changes, so must the remaining x_{rest} so that the total amounts of A and B are conserved. This implies

$$x_{rest} = \frac{x_0 V_0 - x_{laser} V_{laser}}{V_0 - V_{laser}} \tag{2.10}$$

and so, the free energy in total of the system in a phase separated state is

$$F_{sep}(x_{laser}) = \frac{V_{laser}}{V_0} F_{mix}(x_{laser}) + \frac{V_{rest}}{V_0} F_{mix}(x_{rest}). \tag{2.11}$$

The diagram in Figure 26 shows the change in free energy in a small volume V_{laser} $\Delta F = F_{sep} - F(x_0)$ which is associated with a change in mole fraction in said volume for different initial mole fractions which are 0.3 (blue), 0.5 (orange) and 0.7 (green). The temperature is set a few K above the critical temperature at 301 K. As expected, the free energy increases when the concentration in V_{Laser} changes. Near the critical concentration, the free-energy potential (orange) is fairly flat which results in large concentration fluctuations away from the equilibrium concentration.
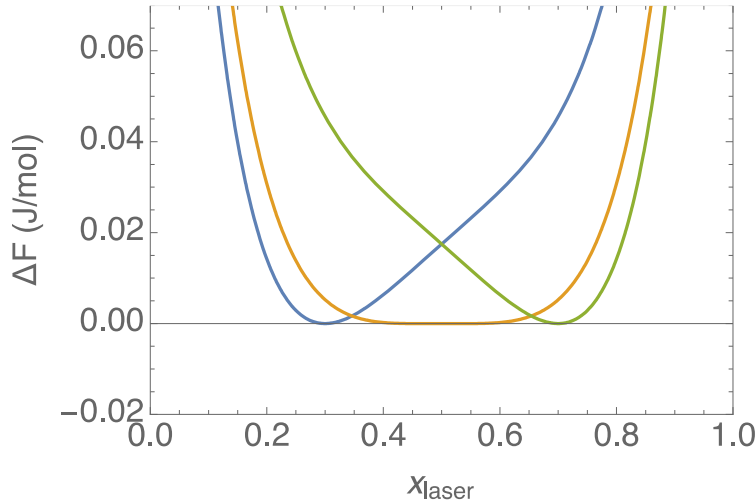
Figure 26 – The change in the free energy of mixing (ΔF) when the mole fraction of a small volume V_{laser} is varied. Chosen parameters are χ = 5 kJ mol⁻¹, V_{laser} = 10⁻³×V_0 and T = 301 K. The initial mole fractions are set to x_0 = 0.3 (blue), 0.5 (orange) and 0.7 (green).

2.3.2.   The Effect of the Laser

The assumption will be made that the refractive index of a mixture is the average of that of the two components, factoring in mole fraction such that

$$n(x) = xn_A + (1-x)n_B \tag{2.12}$$

where n_A and n_B are the refractive indices of the components A and B respectively. This is a modified version of the Gladstone-Dale relation, which fits experimental data well for binary liquid mixtures.[52,53] Since the molecular scale (10^{-10}-10^{-9} m) is

much smaller than the scale of the wavelength of visible and near-IR light (10^{-8}-10^{-7} m), the dipole approximation can be used to calculate the stored electromagnetic energy in the field of the laser. The dipole approximation is given by

$$U_{dip} = -\varepsilon_0 n^2 E^2 \qquad (2.13)$$

where U_{dip} has dimensions energy per unit volume. The energy stored in the field in the small volume in Joules is

$$U_{laser} = -\varepsilon_0 n^2 (x_{laser}) E^2 V_{laser} . \qquad (2.14)$$

The total free energy change is then given by

$$\Delta F_{sep,laser}(x_{laser}) = F_{sep}(x_{laser}) - F_{mix}(x_0) - [n^2(x_{laser}) - n^2(x_0)]\varepsilon_0 E^2 V_{laser} . \qquad (2.15)$$

Here the laser intensity I can be defined as

$$I = \varepsilon_0 E^2 = \frac{U_{laser,ext}}{Ac} \qquad (2.16)$$

where A is the area of the laser focus, c is the speed of light and $U_{Laser, ext}$ is the energy flux of the laser beam with units of Watts. For example, a laser with an optical power of 50 mW which is focussed to a spot of diameter 1.7 µm at the beam waist gives an intensity I ≈ 1 kJ m^{-3}.

Figure 27 shows the free energy change ΔF by the optical-tweezing effect of the laser when the assumption is made that component B has a higher refractive index. Switching on the optical-tweezing potential biases the potential minimum towards the right (larger x) and therefore the laser volume is expected to become enriched with the high refractive index liquid. This process will be referred to as laser-induced phase separation (LIPS)[48–50]. In the metastable case, switching on the laser causes the system to tip from metastable (two minima separated by a barrier) to unstable (single minimum determined by the tweezing laser) at sufficient laser power, thereby triggering phase separation.
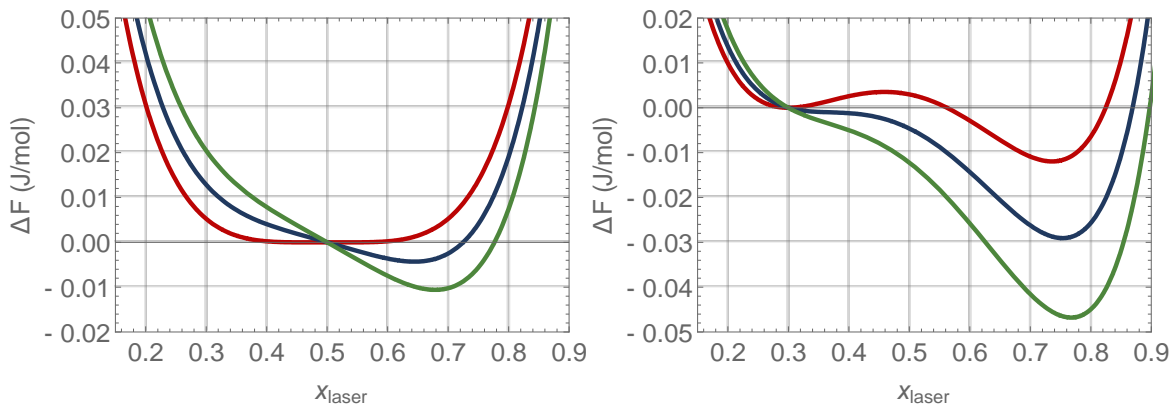
Figure 27 – Plots of the free energy change ΔF in a mixture of nitrobenzene-decane with mole fraction x_0 of nitrobenzene when the mole fraction is changed to x_{laser} in a small volume. Here the initial nitrobenzene mole fraction is $x_0 = 0.5$ (left)) and $x_0 = 0.7$ (right), the laser intensity is $I = 0$ (red), 100 (blue), and 200 (green) J/m^3, $\chi = 5$ kJ mol⁻¹, and (left) $T = 301$ and (right) 280 K. The refractive indices are set to $n_{decane} = 1.41$ and $n_{nitrobenzene} = 1.54$. The left panel represents a stable critical mixture undergoing LIPS – the free energy minimum for the laser volume moves to a higher mole fraction. The right panel represents a metastable sample where the global free energy minimum of the laser volume is at a high mole fraction, but it is stuck in a local minimum at the bulk mole fraction of 0.3. The effect of the laser is to remove the barrier between the two states, triggering nucleation.

In the high temperature regime, the free-energy difference curve from equation (2.15), has only a single minimum. Thus, in principle, one could find this stable minimum by determining $d\Delta F_{sep,laser}/d\phi = 0$, however, this does not have a simple analytical solution. Instead, the minimum of the free energy difference using a numerical algorithm will be determined. In the low temperature limit (below the spinodal), the free energy difference also has single minimum. However, for temperatures between the binodal and spinodal, the free energy difference has two minima. The numerical approach outlined here implies that the metastable minimum will be missed and only the stable minimum will be found.

The experiments will be carried out by using PC microscopy, which is sensitive to changes in refractive index. Since the refractive index is linearly proportional to the volume fraction in the model (equation (2.12)) the volume fraction can be used as a proxy for the signal measured in the experiments. This can only be done for small objects, as for larger ones the shade-off effect renders the signal from the centre of the object the same as homogenous sample around the object – this will be demonstrated later.

Figure 28 shows the predicted phase contrast signal calculated by finding the mole fraction φ that minimises the free-energy difference numerically and subtracting off the original volume fraction. The curves are a function of temperature – as the

44

temperature rises and system moves away from the critical point, the signal dies away. At higher laser intensities the LIPS effect extends to higher temperatures but is fairly consistent at temperatures very close to T_C. The LIPS effect extends to higher temperatures when the mixture is closer to the critical mixture x_C. The discontinuities which appear in both graphs in the blue and orange curves may be anomalies of the numerical method.
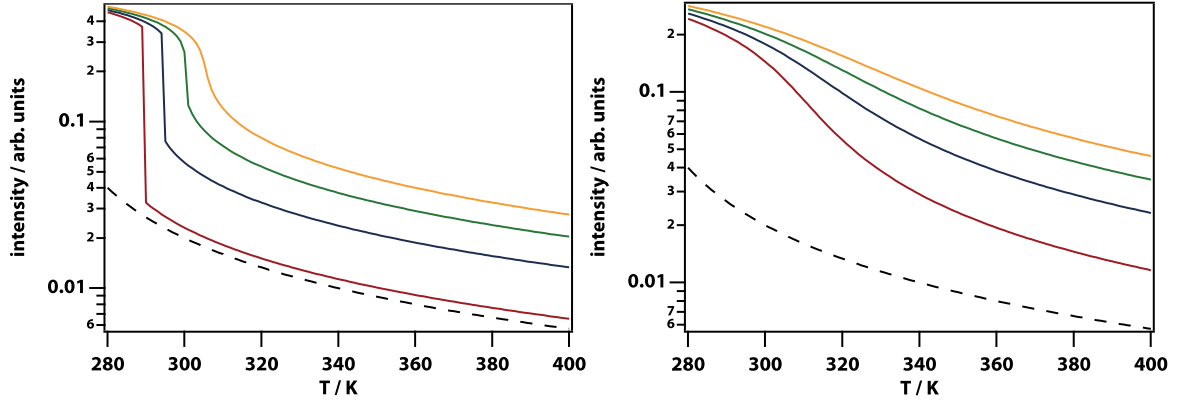
Figure 28 – Plots of predicted phase contrast signal, calculated by finding the mole fraction φ that minimises the free-energy difference numerically and subtracting off the original volume fraction. The initial mole fractions are $x_0 = 0.3$ (left) and 0.5 (right). The coloured curves represent different values of laser intensity: I = 100 (red), 200 (blue). 300 (green) and 400 (yellow) J m^{-3}. Also plotted is the power law $0.8 \times (T-260)^{-1}$ (black dashed line). As the mole fraction moves towards the critical mole fraction x_C, the effect operates to higher temperatures. The signal is predicted to be stronger at temperatures very close to T_C, but this may be an anomaly of the method – the discontinuities in the orange and blue curves in both graphs are unusual.

2.3.3.   The Kramers Equation for Diffusion

The free-energy potentials derived above the basis for a calculation of the kinetics of LIPS. The liquid diffusion can be modelled by a Fokker-Planck equation, describing the evolution of the probability distribution function p(x, t) of a random variable x as

$$\frac{\partial}{\partial t} p(x,t) = -\frac{\partial}{\partial x}[v(x,t)p(x,t)] + \frac{\partial^2}{\partial x^2}[D(x,t)p(x,t)] \qquad (2.17)$$

where v(x, t) is the drift velocity and D(x, t) the diffusion coefficient. In this case, the diffusion coefficient can be taken as constant and so $v(x) = -\mu \partial U(x)/\partial x$ can be substituted since the drift velocity scales with the gradient of the free-energy potential. The Stokes-Einstein equation states that

$$\mu = \frac{1}{6\pi\eta r}, D = \frac{k_B T}{6\pi\eta r} \qquad (2.18)$$

where μ is the mobility, η is the viscosity, r is the radius of the diffusing particle (molecule) and the Boltzmann constant $k_B = 1.380 \times 10^{-23}$ J K^{-1}. It then follows that

$$\frac{\partial}{\partial t} p(x,t) = \frac{D}{k_B T} \frac{\partial}{\partial x}\left[p(x,t)\frac{\partial U(x)}{\partial x} \right] + D\frac{\partial^2}{\partial^2 x} p(x,t) \qquad (2.19)$$

which has been derived previously for the case of solvent-driven electron transfer.[54] When the potential U(x) is set to zero everywhere, the Green's function of this Fokker-Planck equation can be derived, which is given by

$$p(x,t) = \frac{1}{\sqrt{4\pi Dt}} e^{-x^2/4Dt}. \qquad (2.20)$$

Thus, in the absence of a potential, in one dimension and where the initial distribution is a delta function, the standard deviation of the distribution varies eith time as $\sigma = \sqrt{2Dt}$.

The diffusion coefficient D can be approximation using the Stokes-Einstein expression in equation (2.18) where the diffusion coefficient has units m^2 s^{-1}. If this equation is applied to nitrobenzene (parameters: molar mass 123.06 g mol^{-1}, density 1.199 g cm^{-3}, viscosity = 2.03 cP, so R = 3.44 nm) it is found that $D_{trans} = 3.1 \times 10^{-10}$ m^2 s^{-1}. The thermal diffusivity for nitrobenzene $\alpha = 0.94 \times 10^{-7}$ $m^2 s^{-1}$.[55] Roughly speaking, the thermal diffusivity $\alpha \approx D \times 1000$, which indicates that heat travels $\approx$ 30× farther in the same amount of time. As such, the assumption will be made that thermal equilibrium is achieved significantly more quickly than concentration equilibrium.

In the case of a focussed laser with a Gaussian beam profile of width w, the trapping potential is simply

$$U(x) \propto e^{-x^2/2w^2} \qquad (2.21)$$

and the width is typically a couple of mm in my experiments (since long working distance objectives had to be used). The diffusion equation (2.19) with the trapping potential equation (2.21) was solved numerically using a 2nd-order Runge–Kutta method on a spatial grid. Typical results are shown in Figure 29 with parameters chosen to be relevant to the mixture nitrobenzene–hexadecane . The trapping laser draws nitrobenzene into the focus leaving behind a depletion region that gradually fills in over time. The peak of the distribution grows on a timescale of roughly 0.5 s, determined by the diffusion coefficient D.
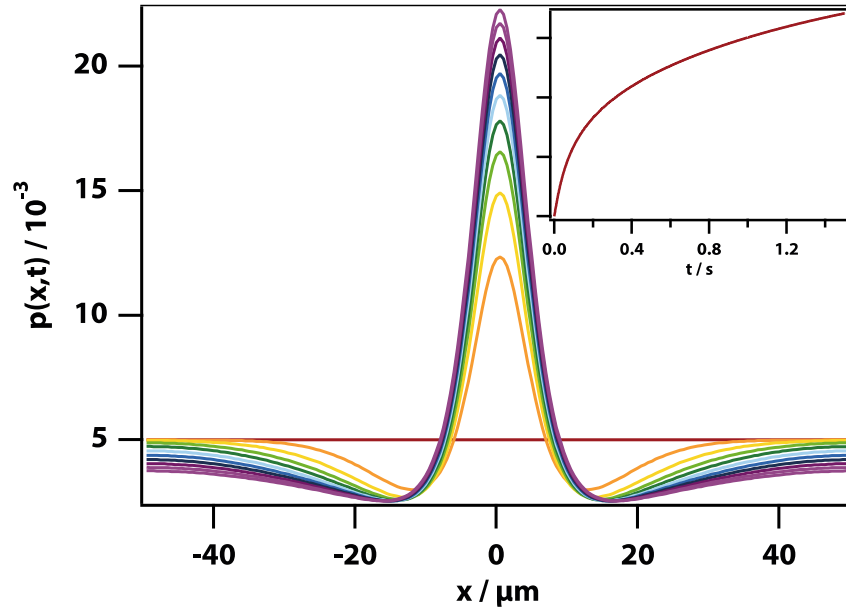
Figure 29 – Simulation of the evolution of the concentration of the high refractive index substance under the influence of an optical trapping force. Box length 100 µm, 1-ms time step in simulation, 200 grid steps, D_{trans} = 3.1×10⁻¹⁰ m²s⁻¹, T = 300 K, w = 6 µm. (inset) The value of the peak as a function of time in seconds.

2.3.4.   Heat Diffusion

The equation described by Schmidt and co-workers[56] for heating in optical traps can be used to obtain a steady state change in temperature in the focus of 0.50 K for decane and 0.57 for nitrobenzene. However, given the limited testing of the model, a new expression for steady-state heating in the focal volume was derived from scratch.

The one-dimensional heat equation is[57]

$$\frac{\partial u}{\partial t} = \frac{k}{c_p \rho}\left(\frac{\partial^2 u}{\partial x^2}\right) \equiv \alpha\left(\frac{\partial^2 u}{\partial x^2}\right)$$

(2.22)

where u is the temperature field, k is the thermal conductivity, c_p is the specific heat capacity, ρ is the mass density and α is the thermal diffusivity in m² s⁻¹. α has the same units and behaviour as the diffusion coefficient D. Adding a term for internal heat generation gives

$$\frac{\partial u}{\partial t} = \alpha\left(\frac{\partial^2 u}{\partial x^2}\right) + \frac{q}{c_p \rho}$$

(2.23)

where q is the heat generated per unit volume in W m⁻³. In reality the heat source is a laser, so it has an approximately 2D Gaussian profile, but this will be simplified to a delta function in order to find a steady state solution. Such a solution is only possible if a constant temperature is maintained, so a source of cooling is needed,

47

which in this case is temperature controlled Linkam THMS600 stage in experiments. Factoring in both of those changes,

$$\frac{\partial u}{\partial t} = \alpha \left(\frac{\partial^2 u}{\partial x^2} \right) + \frac{Q}{c_p \rho} \delta(x) - \beta(u - T_0) = 0 \tag{2.24}$$

where $\delta(x)$ is the Dirac delta function with units m^{-1}, Q is the magnitude of the CW heat source with units $W\ m^{-2}$, β is the rate of heat transfer and T_0 is the set temperature of the sample stage.

This differential equation is soluble using complex contour integration. To begin with, a Fourier transform gives

$$-\alpha k^2 \tilde{u} + \frac{Q}{c_p \rho} - \beta(\tilde{u} - T_0 2\pi \delta(k)) = 0 \tag{2.25}$$

which can be rearranged in terms of $\tilde{u}$ to give

$$\tilde{u} = \frac{\dfrac{Q}{c_p \rho} + \beta T_0 2\pi \delta(k)}{\alpha k^2 + \beta}. \tag{2.26}$$

Equation (2.26) has poles at $k = \pm i \sqrt{\beta / \alpha}$, so the inverse Fourier transform is

$$u = \frac{1}{2\pi} \int_{-\infty}^{\infty} dk \tilde{u} e^{+ikx} = \frac{1}{2\pi} \frac{Q}{c_p \rho} \int_{-\infty}^{\infty} dk \frac{1}{\alpha} \frac{e^{+ikx}}{(k + i\sqrt{\beta/\alpha})(k - i\sqrt{\beta/\alpha})} + \frac{1}{2\pi} \beta T_0 \int_{-\infty}^{\infty} dk 2\pi \delta(k) \frac{e^{+ikx}}{\alpha k^2 + \beta} \tag{2.27}$$

which can be solved for x > 0 by closing the contour in the upper half plane. Using the residue theorem,

$$u(x > 0) = T_0 + \left(\frac{Q}{c_p \rho} \right) i \frac{1}{\alpha} \frac{e^{\sqrt{\beta/\alpha}x}}{2i\sqrt{\beta/\alpha}} = T_0 + \frac{1}{2} \sqrt{\frac{1}{\alpha\beta}} \left(\frac{Q}{c_p \rho} \right) e^{-x/\sqrt{\alpha/\beta}}. \tag{2.28}$$

For x < 0 the sign of the exponential term changes from negative to positive, so for all x

$$u(x) = T_0 + \Delta T e^{-|x|\sqrt{\alpha/\beta}} \tag{2.29}$$

where

$$\Delta T = \frac{1}{2}\sqrt{\frac{1}{\alpha\beta}\left(\frac{Q}{c_p\rho}\right)}.$$ (2.30)

The characteristic width of the heating spot, which obviously takes the form of a Gaussian function, is approximately $\sqrt{\alpha/\beta}$. Fourier's law of heat flow can be used to estimate β, so

$$q = -\kappa_{glass}\frac{\Delta T}{d_{glass}}$$ (2.31)

where ΔT is the temperature differential between the sample and the stage, d_{glass} is the thickness of the glass/mica windows used and κ_{glass} the thermal conductivity. Thus, a logical differential equation for the change in liquid sample temperature with time is

$$\frac{dT_{liquid}}{dt} = \frac{-q}{c_{p,liquid}\rho d_{liquid}} = \frac{-\kappa_{glass}}{c_{p,liquid}\rho d_{liquid}d_{glass}}(T_{liquid}-T_0)$$ (2.32)

so

$$\beta = \frac{-\kappa_{glass}}{c_{p,liquid}\rho d_{liquid}d_{glass}}.$$ (2.33)

Using the values shown in Table 1, β = 507 s^{-1} is obtained.

Now, using equation (2.29) the diameter of the heated spot at e^{-1} of the maximum and the temperature change at that point can be calculated. For borosilicate glass windows the diameter is 13 μm and the maximum temperature change is 1.6 K. For this calculation the extinction coefficients of nitrobenzene and decane were determined experimentally using UV-Vis spectroscopy – the data is shown in Figure 91 and Figure 92 in the Appendix, section 5.3. It was found that 1.5 μW out of a 200 mW incident optical power was absorbed.

Specific heat capacity nitrobenzene	$c_{p, \text{nitrobenzene}}$ = 1400 J kg^{-1} K^{-1}
Mass density nitrobenzene	$\rho_{\text{nitrobenzene}}$ = 1175 kg/m^3
Thermal diffusivity of nitrobenzene[55]	$\alpha_{\text{nitrobenzene}}$ = 0.94 10^{-7} m^2/s
Thermal conductivity glass	$\kappa_{\text{glass}} \approx$ 1 W m^{-1} K^{-1}.
Thermal conductivity mica	$\kappa_{\text{mica}} \approx$ 0.71 W m^{-1} K^{-1}
Thickness window glass	d_{glass} = 80 μm
Thickness window mica	d_{mica} = 100 μm

Table 1 – Parameters used the heating calculation

2.3.5. Thermophoresis

It is essential to consider all possible mechanisms for the LIPS effect – so the change in concentration due to thermophoresis (the Soret effect) has been calculated. Thermophoresis can be described as the preference of one component to reside in a hot or cold region relative to the other component and can be described by

$$\frac{\partial \chi}{\partial t} = \nabla \bullet (D \nabla \chi + D_T \chi (1 - \chi) \nabla T) \tag{2.34}$$

where χ is mole fraction, D is the diffusion coefficient and D_T is the thermodiffusion coefficient. In one dimension

$$\frac{\partial \chi}{\partial t} = D \frac{\partial^2}{\partial x^2} \chi + D_T \frac{\partial}{\partial x} \chi (1 - \chi) \frac{\partial}{\partial x} T, \tag{2.35}$$

which can be amended by substituting the derivative of equation (2.29) with respect to x

$$\frac{\partial}{\partial x} T = \frac{-x}{|x|} \frac{\Delta T}{\sqrt{\alpha / \beta}} e^{-|x|/\sqrt{\alpha/\beta}}, \tag{2.36}$$

assuming equilibrium conditions so $d\chi/dt = 0$ and the Soret coefficient S = D_T/D the equation changes to

$$\frac{\partial}{\partial x} \chi = \frac{S \Delta T}{\sqrt{\alpha / \beta}} \chi (1 - \chi) e^{-|x|/\sqrt{\alpha/\beta}}. \tag{2.37}$$

If a few substitutions are made $(A = (S/2\alpha)(Q/c_p\rho)$ and $B = \sqrt{\alpha / \beta})$ the equation simplifies to

$$\frac{\partial}{\partial x}\chi = A\chi(1-\chi)e^{-x/B}$$ (2.38)

which solves to give

$$\chi(x) = \frac{c_0\exp(ABe^{-x/B})}{c_0\exp(ABe^{-x/B})+1-c_0}.$$ (2.39)

(2.39) tends to c_0 when x goes to infinity. By substituting (2.30) AB can be simplified as

$$AB = \frac{S}{2}\sqrt{\frac{1}{\alpha\beta}}\left(\frac{Q}{c_p\rho}\right) = S\Delta T,$$ (2.40)

so, the concentration profile due to thermophoresis can finally be given as

$$\chi(x) = \frac{c_0\exp(S\Delta Te^{-x/\sqrt{\alpha/\beta}})}{c_0\exp(S\Delta Te^{-x/\sqrt{\alpha/\beta}})+1-c_0}.$$ (2.41)

Picking different orders of magnitude of the Soret coefficient gives rise to different effects on the mixture (Figure 30). S = 10 has a large effect, resulting in a region of one pure component. S = 10^{-3} however has an almost negligible effect – a change of a few ten thousandths in terms of mole fraction. Since the values of S which were determined by Wiegand and co-workers[58] for various binary mixtures are of the order of 10^{-3}, thermophoresis plays a negligible role for the samples used in this chapter.
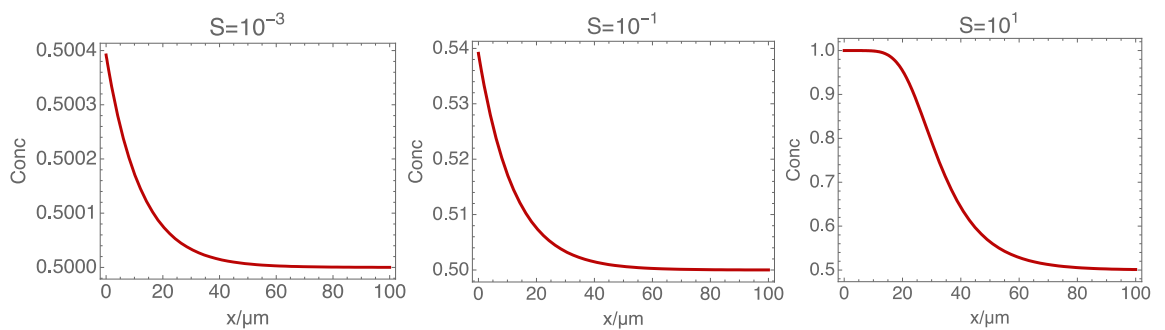
Figure 30 – Different values of the Soret coefficient S and the thermophoretic effect on a mixture like nitrobenzene-decane where ΔT = 1.57 K and √α/β = 12.2 μm.

2.4. Methods

2.4.1.　　Materials

Experiments were carried out on nitrobenzene, aniline, decane, hexadecane, cyclohexane and methylene blue (Sigma Aldrich) and used as supplied. All samples were filtered before use using 0.2 μm hydrophilic polytetrafluoroethylene filters (Millipore) to remove dust. For all microscopy experiments, a sample thickness of 11.58 ± 0.19 μm was used, controlled by dispersing a low concentration of glass monodisperse particle standards (Whitehouse Scientific). Mixtures were sandwiched between borosilicate glass (VWR) and ruby mica discs, which were cleaned by rinsing in acetone, isopropyl alcohol and distilled water, followed by drying in an oven at 423 K for 30 mins. The sample temperature was controlled to ± 0.1 K using a Linkam THMS600 microscopy stage. In the experiments, the samples were prepared above the critical temperature or binodal of the mixture, then cooled and held at the desired temperature to maintain a homogeneous mixture.

2.4.2. Microscopy and Laser Setup

Microscopy was carried out using an Olympus BX53 light microscope that features modular units for phase-contrast (PC) and fluorescence microscopy, and a custom unit allowing for simultaneous laser irradiation and microscopy. The light source for fluorescence was a CooLED pE-300 and filter set used was TXRED (centre wavelengths of 559 and 630 nm for excitation and emission respectively). The primary laser used was a 785-nm diode laser (Thorlabs) producing a maximum power incident on the sample of 200 mW with an elliptical mode with a mean beam radius (at half height) of 1.7 and 2.4 μm when using a 10× and 20× objective respectively. The laser used for pulsed experiments was a 1040 nm Newport Spectra Physics Spirit One, which produces an average power of up to 8.5 W and produces a TEM_{00} mode with $M^2 < 1.1$. Phase-contrast microscopy converts small differences in optical path length into intensity, therefore it can be used as a measure of refractive index. Negative phase contrast (PC) has been used here and results in intensity scaling with refractive index for objects on the micrometre scale. Nitrobenzene strongly quenches many fluorescent dyes, but the dye methylene blue is quenched relatively weakly. This produces contrast between the nitrobenzene-rich and decane-rich phases in fluorescence microscopy.

2.4.3. Data Analysis

Image data were captured using the ImageJ add-on Micro Manager and analysed primarily using ImageJ. IGOR was used to fit data. Most of the LIPS intensity data

was processed by fitting a Gaussian function to radial distributions of the LIPS droplets and taking the area under the curve. In general, there was little difference between the data obtained via this method, and simply taking the average intensity of the centre of the LIPS droplet. The latter method was only used when collecting formation and decay data as the number of data points would make the former method very time consuming with little if any benefit.

2.5. Results

This results section will be broken down in to two parts which correspond to experiments involving laser-induced phase separation (LIPS), and laser-induced nucleation (LIN) in the metastable region between the binodal and spinodal lines.

2.6. Laser-Induced Phase Separation

The mixture that was chosen for the majority of the experiments described in this chapter was nitrobenzene-decane. Many nitrobenzene-alkane mixtures show UCSTs, but decane has a lower vapour pressure than shorter alkanes like hexane and octane, which was helpful for sample preparation and sample longevity. Nitrobenzene-decane mixtures have critical parameters $x_C = 0.575$ and $T_C = 295.96$ K in the literature.[59] x_C was determined experimentally to be 0.575 but T_C was found to be 296.8 ± 0.1 K. The slight difference in T_C could be a confinement effect as the samples are sandwiched between glass or mica slides with a separation of 11 μm, however a study which investigated the effect of confinement on the binodal of nitrobenzene-hexane mixtures showed little difference when confined in 100 nm pores[60]. Alternatively, the difference may be down to chemical purity, as no further purification was carried out after purchase. The binodal of nitrobenzene-decane is shown in Figure 31, and has been fitted with a fourth order polynomial rather than a parabola to better illustrate the plateaued top of the experimental binodal. The binodal data were determined by gradually warming the mixture from a phase separated state to a homogeneous one. If the mixture were to be cooled from a mixed state, it would be possible to cross the binodal for non-critical mixtures. As was stated earlier, within the binodal the phase separated or demixed state is thermodynamically favoured and outside it, the mixed state is favoured.
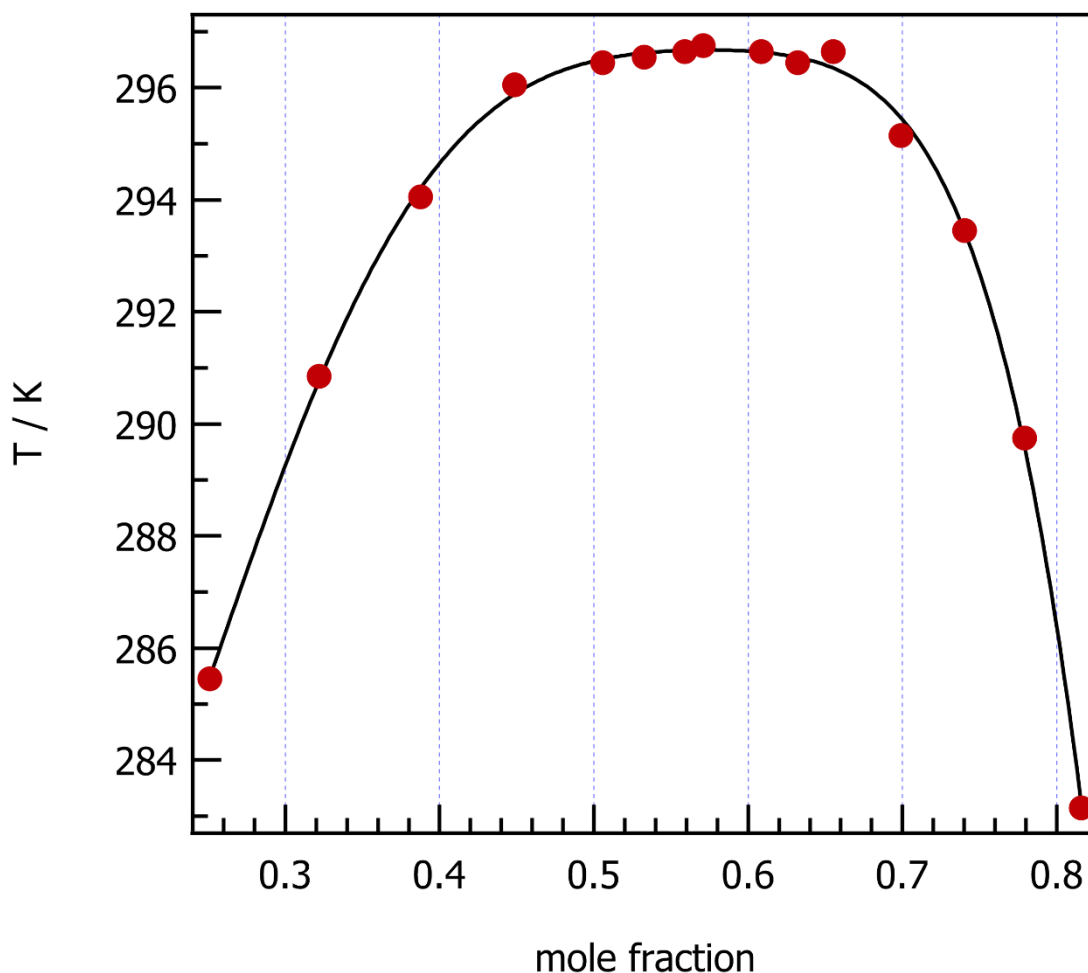
Figure 31 – Phase diagram showing the binodal or co-existence curve of a nitrobenzene-decane mixture when sandwiched between two borosilicate glass slides with a thickness of 11 μm. The peak, or critical point, is at T_C = 296.8 K and x_C = 0.575. The experimental data matches the literature value of x_C, but is a touch higher than the literature value for T_C of 295.96 K.[59] This effect is likely due to confinement, pushing up the critical point.

Using a critical mixture, the temperature was held 0.1 K above the binodal, and the sample was irradiated with a focussed 785 nm CW laser at 200 mW. When viewed with phase contrast microscopy, a diffuse bright spot is visible in the laser focus (Figure 32). Since negative phase contrast was used, a bright object indicates a phase delay, so it can be deduced that the object has a higher refractive index. The mixture was chosen carefully so that components had a large difference in refractive index. Nitrobenzene has n = 1.54 and decane n = 1.41. Thus, the bright spot indicates a higher fraction of nitrobenzene. Based on the intensity using phase contrast of phase separated droplets and the lever rule, the refractive index and composition of the droplet can be estimated (See Appendix 5.1 for a more complete description of the method). The change in refractive index between the droplet and the surrounding bulk is Δn = 0.002, and the mole fraction of nitrobenzene in the droplet is 0.589 compared to 0.575 in the bulk.
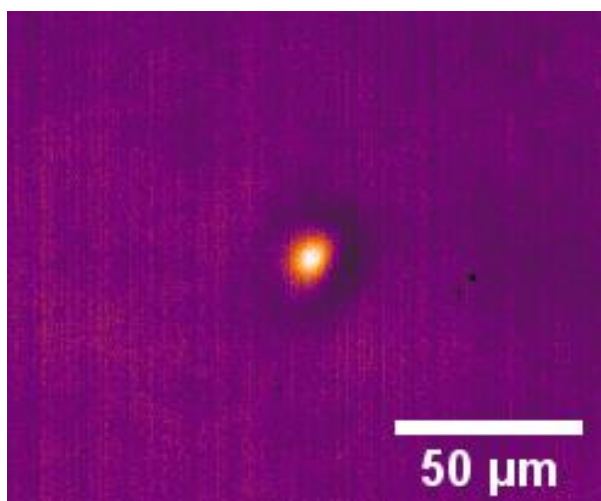
Figure 32 – False coloured PC image of the LIPS effect in a nitrobenzene-decane mixture.[48] The image shows a bright spot - indicating an object with a higher refractive index than its surroundings. In the nitrobenzene-decane case, this is nitrobenzene-rich, as nitrobenzene has a higher refractive index. A 785 nm laser with a 200 mW optical power was used.

A radial distribution function of the LIPS droplet shown in Figure 33 reveals that it has a FWHM diameter of 2.4 μm when using a 10× objective, which is larger than the 1.7 μm beam waist of the laser (since the diode laser profile is elliptical, the long axis has been chosen). Figure 33 shows a dip in phase contrast intensity surrounding the central droplet at a radius of ~7 μm which goes away over time and moves farther away (~9 μm at 25.8s). PC microscopy is an interference-based technique which naturally produces dark fringes around bright objects and vice versa. Based on that alone, mole fraction cannot be determined accurately, but the fact that the minimum in PC intensity moves tells us that there is a non-equilibrium dip in nitrobenzene concentration around the LIPS droplet which fades over time as equilibrium is reached.
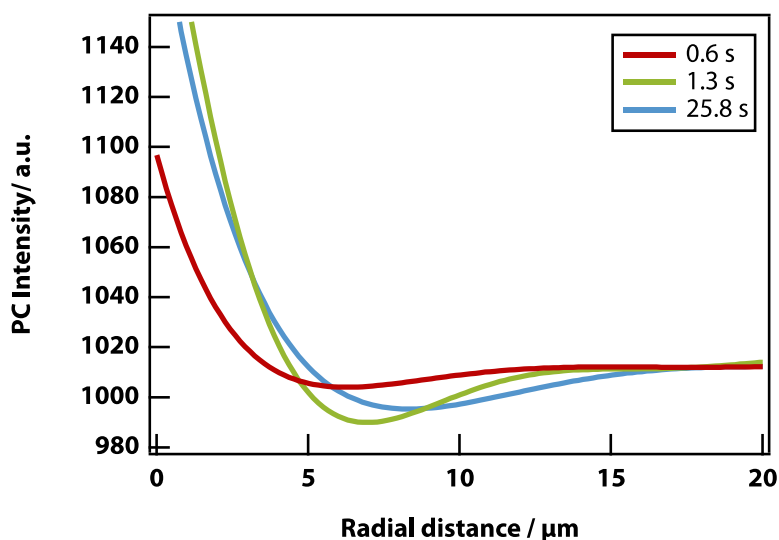
Figure 33 – Radial distribution function of the LIPS droplet in nitrobenzene-decane. It reveals a steady-state droplet diameter of 2.4 µm at FWHM.

In order to make completely sure that the LIPS droplet contains a higher fraction of nitrobenzene as the PC microscopy indicates, fluorescence microscopy was used. Nitrobenzene strongly quenches fluorescent dyes via the Dexter mechanism[18], which can be used to generate contrast between nitrobenzene-rich and poor regions. Initially, solvatochromic dyes like Coumarin 153 were used in an attempt to determine composition, but nitrobenzene proved too strong a quencher to get a reliable signal using the microscope or even a sensitive fluorimeter. The dye Methylene blue was chosen as it has a relatively low quenching constant when dissolved in nitrobenzene.[61] Methylene blue has an excitation λ_{MAX} at 665 nm and emission λ_{MAX} at 716.9 nm. Due to limited availability of filter sets, a Texas red set was used (ex 559 nm, em 630 nm), but this proved to be satisfactory. Figure 34 shows a fluorescence microscopy image of methylene blue dissolved in a critical nitrobenzene-decane mixture. There was a degree of overlap between the tail of the laser light and the emission filter, and since the laser is obviously many orders of magnitude brighter, it obscured the LIPS droplet. To get around this, the laser was repeatedly switched on and off, recording at as fast a frame rate as was practical. Twenty of the first frames following the laser being switched off were averaged to give the final image in Figure 34. Clearly there is a dark spot visible where the laser previously was, which corroborates the finding that the LIPS droplet is nitrobenzene-rich. As a control, the same experiment was carried out using a non-critical sample where the LIPS effect was not observed, and no dark spot was resolvable.
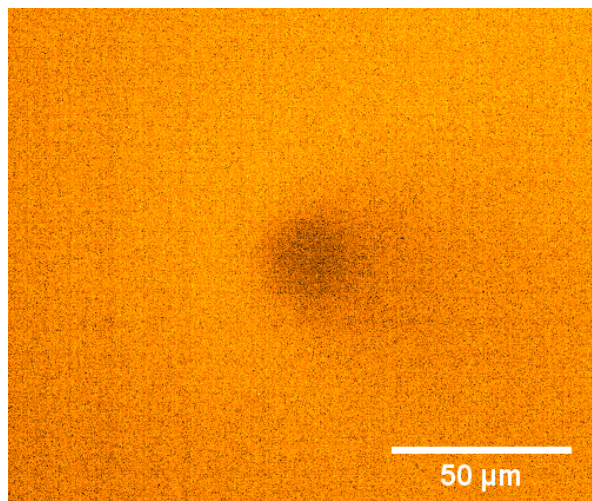
Figure 34 – Fluorescence microscopy image of a LIPS droplet in a mixture of nitrobenzene and decane, using the dye methylene blue. Nitrobenzene quenches the fluorescence of the dye, creating a dark spot in the focus where the fraction of nitrobenzene is the highest.

Figure 35 shows a range of critical mixtures which show the LIPS effect at a temperature of 0.1 K above their respective critical points. The LIPS effect was observed most strongly in benzene derivatives mixed with alkanes, but also nitromethane and n-octanol.
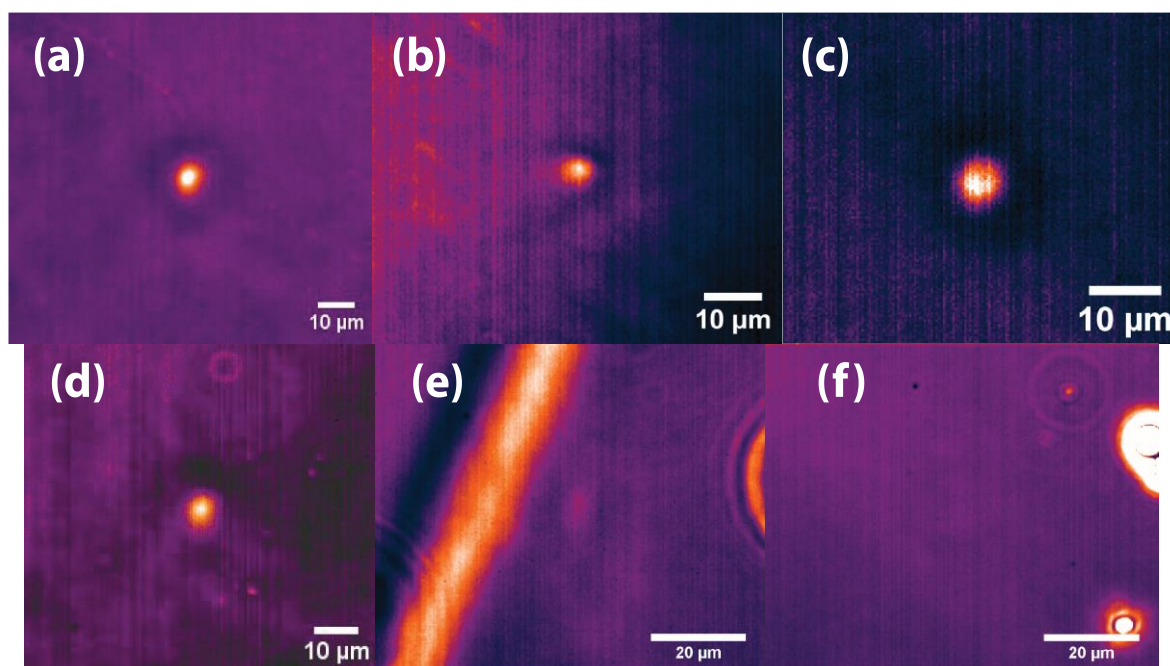
Figure 35 – Six of the mixtures that were tested for the LIPS effect. The LIPS effect was observed for (a) nitrobenzene-decane, (b) nitrobenzene-hexadecane, (c) aniline-cyclohexane, (d) phenol-decane and faintly in (e) nitromethane-1-octanol. The effect was not observed for (f) nitromethane-1-butanol, likely for two reasons: they have a very similar refractive index, so the LIPS effect should be very weak, but objects with the same refractive index show the same signal in phase contrast, so it may not be visible even if the LIPS effect took place. It should be noted that the bright line in (e) is a phase boundary due to critical fluctuations.

Mixture	T_C (K)	x_C	Δn
Nitrobenzene-Hexane	293.6 [59]	0.430	0.1812
Nitrobenzene-Octane	293.2 [59]	0.51	0.1430
Nitrobenzene-Decane	296.0 [59]	0.575	0.1452
Nitrobenzene-Dodecane	300.4 [59]	0.630	0.116
Nitrobenzene-Hexadecane	309.6 [62]	0.716	0.1107
Nitromethane-n-Octanol	322.2 [59]	0.664	0.0355
Nitromethane-n-Butanol	290.4 [63]	0.582	0.0055
Aniline-cyclohexane	302.9 [64]	0.44	0.1594
Phenol-Decane	340.6 [59]	0.671	0.1190

Table 2 – Mixtures used in this chapter and their literature critical parameters to four significant figures.

In the case of the nitromethane mixtures (e) and (f), the difference in refractive index is small, particularly in the case of n-butanol (0.0055 compared to 0.1812 for nitrobenzene-hexane). The effect in (e) is very faint, but visible. (f) does not show an effect, for two possible reasons. The most likely reason is that in the dipole approximation (2.13) the energy stored in the field U_{dip} increases with the square of the refractive index n, so is not much of a thermodynamic drive for LIPS. The second possibility is that the droplet is simply invisible because PC microscopy turns phase delays from refractive index differences into intensity. The two possibilities can be tested by plotting the LIPS intensities of the mixtures as a function of refractive index difference, shown in Figure 36. A straight-line fit would indicate that the droplets are only more intense because of the microscopy and a cubic fit would show that the dipole approximation is valid and both are contributing to the increased intensity. The data clearly have a non-linear relationship and fit a cubic function with a lower R^2 value than that of a quadratic function. Fitting the data to a function of the form ax^n gave n = 3.001. As such, the lack of a LIPS droplet in n-butanol is due in part to less energy being stored in the field because of the small difference in refractive index. This result validates the hypothesis that the effect relates to energy being stored in the field according to the dipole approximation.
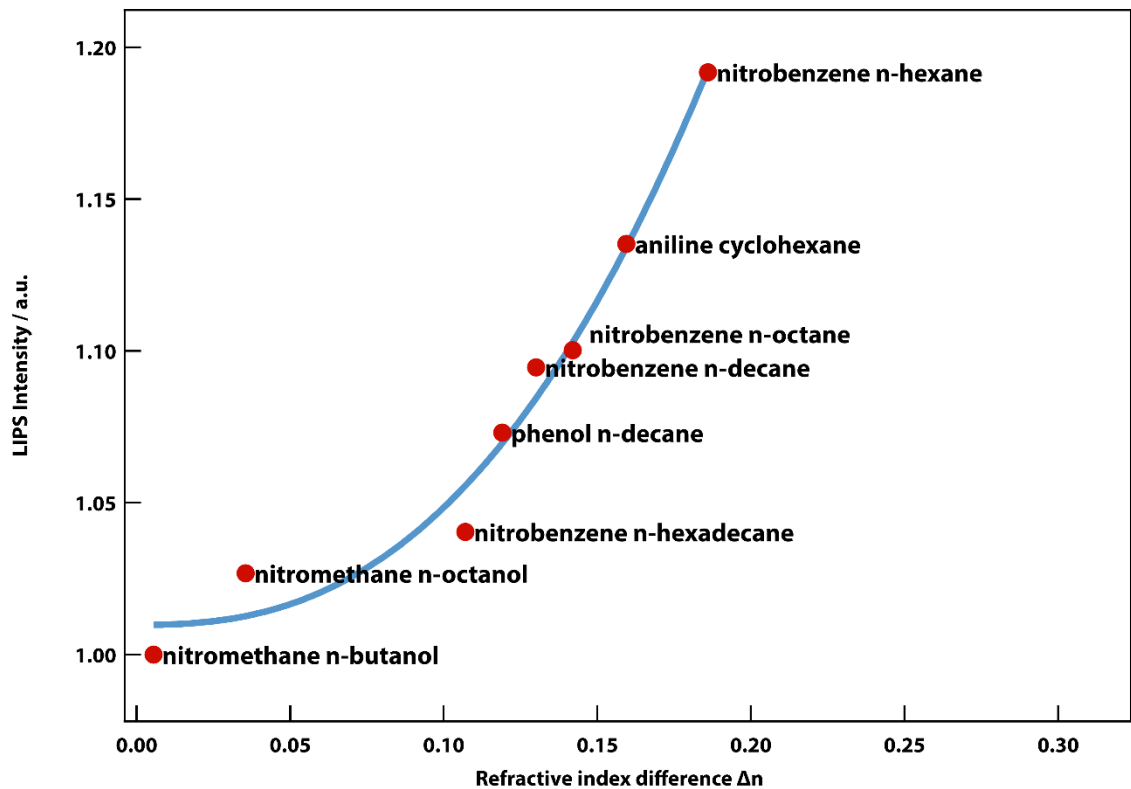
Figure 36 – LIPS Intensity of a LIPS droplet 0.1 K above the critical point of various critical mixtures as a function of refractive index difference.

The intensity of LIPS droplets in nitrobenzene-decane mixtures were measured as a function of mole fraction. The intensity was at its highest at the critical mole fraction (0.575) and faded away as the mixtures became dominated by one component.
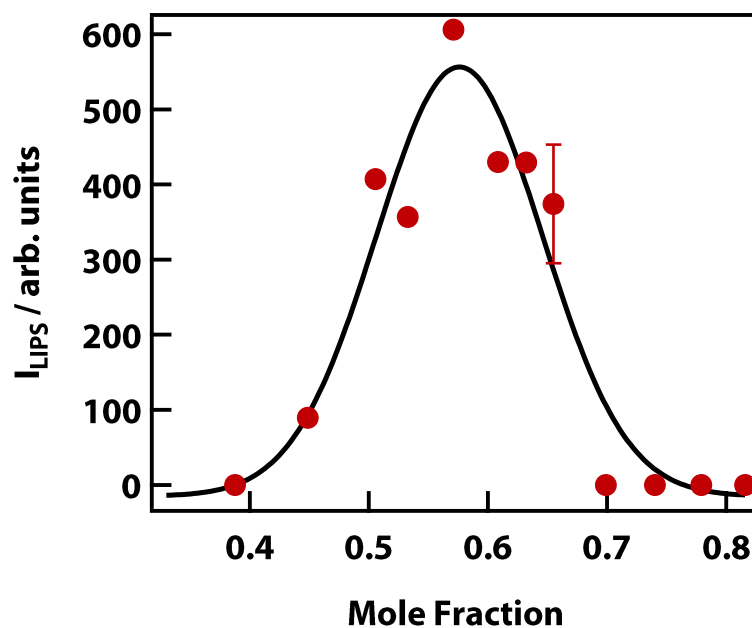
Figure 37 – Mole fraction dependence of the magnitude of the LIPS effect. There is clearly a relationship between proximity to the critical point and the effect.[48] The single error bar represents the standard error when multiple measurements were taken at different points on the sample.

The effect of proximity to critical points can be tested by carrying out temperature dependences on critical mixtures. Figure 38 shows temperature dependences at P = 70 mW for nitrobenzene mixed with octane, hexadecane and decane from left to right. They all show good fits with power laws of the form $a(T-T_0)^{-n}$ where the exponent n is 1, 2.4 and 1 respectively. The effect is weak, but present for quite a large range of temperatures. The power laws diverge to asymptotes at a temperature T_0 which is a lower than the critical points of the mixtures, so no data could be collected between those two temperatures as the mixture was demixed. For example, nitrobenzene-decane gave T_0 = 21.8 °C but has T_C = 23.6 °C.
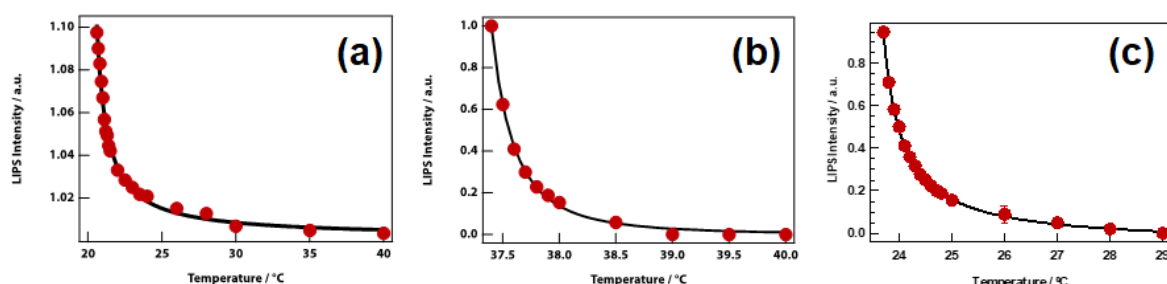
Figure 38 – Temperature dependences of the LIPS effect for the following critical mixtures: (a) Nitrobenzene-Octane, (b) Nitrobenzene-Hexadecane and (c) Nitrobenzene-Decane. As the mixtures cool towards their respective critical points, the magnitude of the LIPS effect rises according to a power law of the form ax^{-n} where the exponents n are 1, 2.4 and 1 respectively.

Power dependences in Figure 39 of the same mixtures as Figure 38 show a trivial linear relationship between laser power and LIPS intensity (N.B. the first point in Figure 39 (a) is below the lasing threshold). The intensity appears to saturate due to the shade-off effect which is inherent in phase-contrast microscopy (See Appendix).
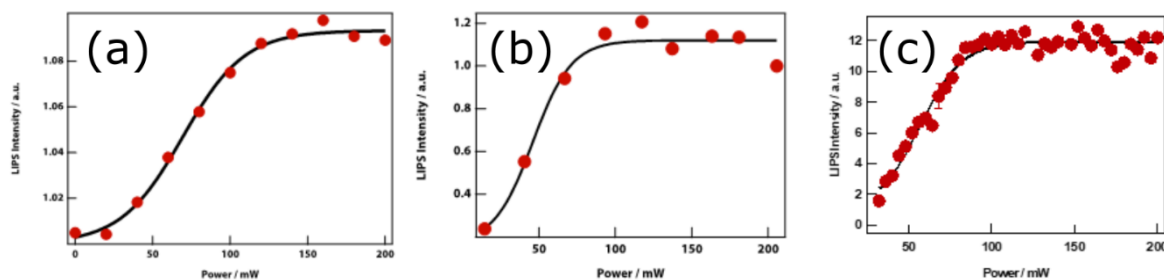
Figure 39 – Power dependences of the LIPS effect for the follow critical mixtures: (a) Nitrobenzene-Octane, (b) Nitrobenzene-Hexadecane and (c) Nitrobenzene-Decane. The data has been fitted to sigmoid functions to illustrate the saturation above 110 mW for (a) and 70 mW for (b) and (c).

Temperature dependences were carried out on a critical mixture of nitrobenzene-decane at a range of powers from 46.9 – 75 mW, to determine whether there is a relationship between power, and the temperature asymptote T_0 when plotted in the

60

form $a/(T-T_0)^n$. Looking at the data in Figure 40 it is clear that, as would be expected, the temperature dependence fits rise in intensity with increased laser power. The asymptotes are plotted in Figure 41, and there appears to be no relationship between the temperature asymptote and laser power, within the chosen range of powers.
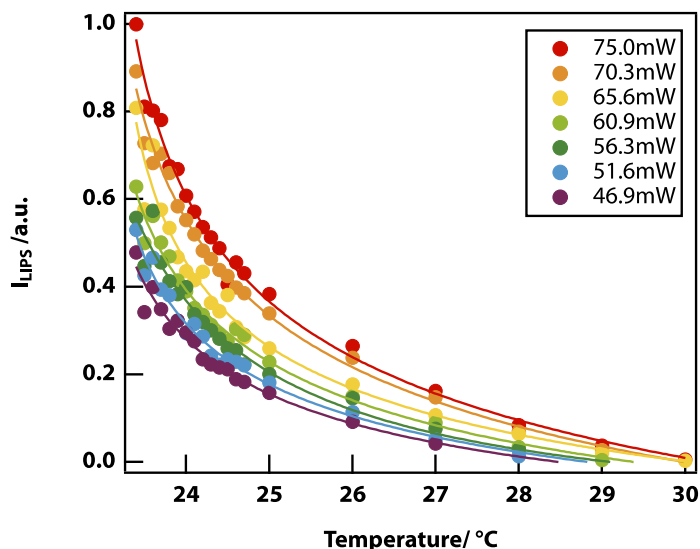
Figure 40 – Temperature dependences at a range of laser powers. There is a rise in the LIPS intensity of the fits as the laser power is increased.
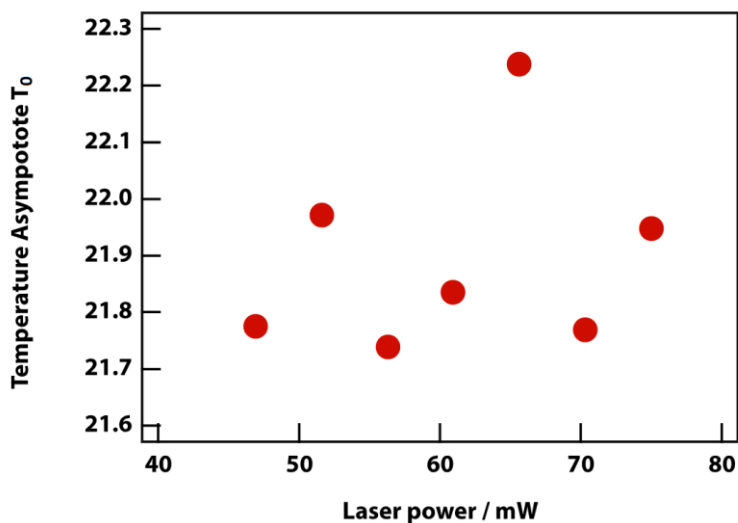
Figure 41 – Asymptotes from the temperature dependences in Figure 40 as a function of laser power. There does not appear to be any correlation between the two.

LIPS droplets do not appear instantaneously as the formation and decay processes are limited by the diffusion of molecules. Figure 42 shows the formation and decay of three nitrobenzene based critical mixtures with alkanes of different chain length. The data are fitted to exponential functions, and the formation and decay times are the time taken to reach e^{-1} of the maximum LIPS intensity (listed in Table 3). From

61

the limited sample of three, a relationship between chain length and formation or decay time cannot be determined. Since the viscosity of the alkane increases with chain length, it may be expected that the formation and decay would take longer. As chain length increases however, the refractive index also rises, so the refractive index difference Δn reduces. It may be the case that an increase in viscosity leading to longer times is offset by LIPS effect being reduced and the droplet having a mole fraction which is less different from the bulk.
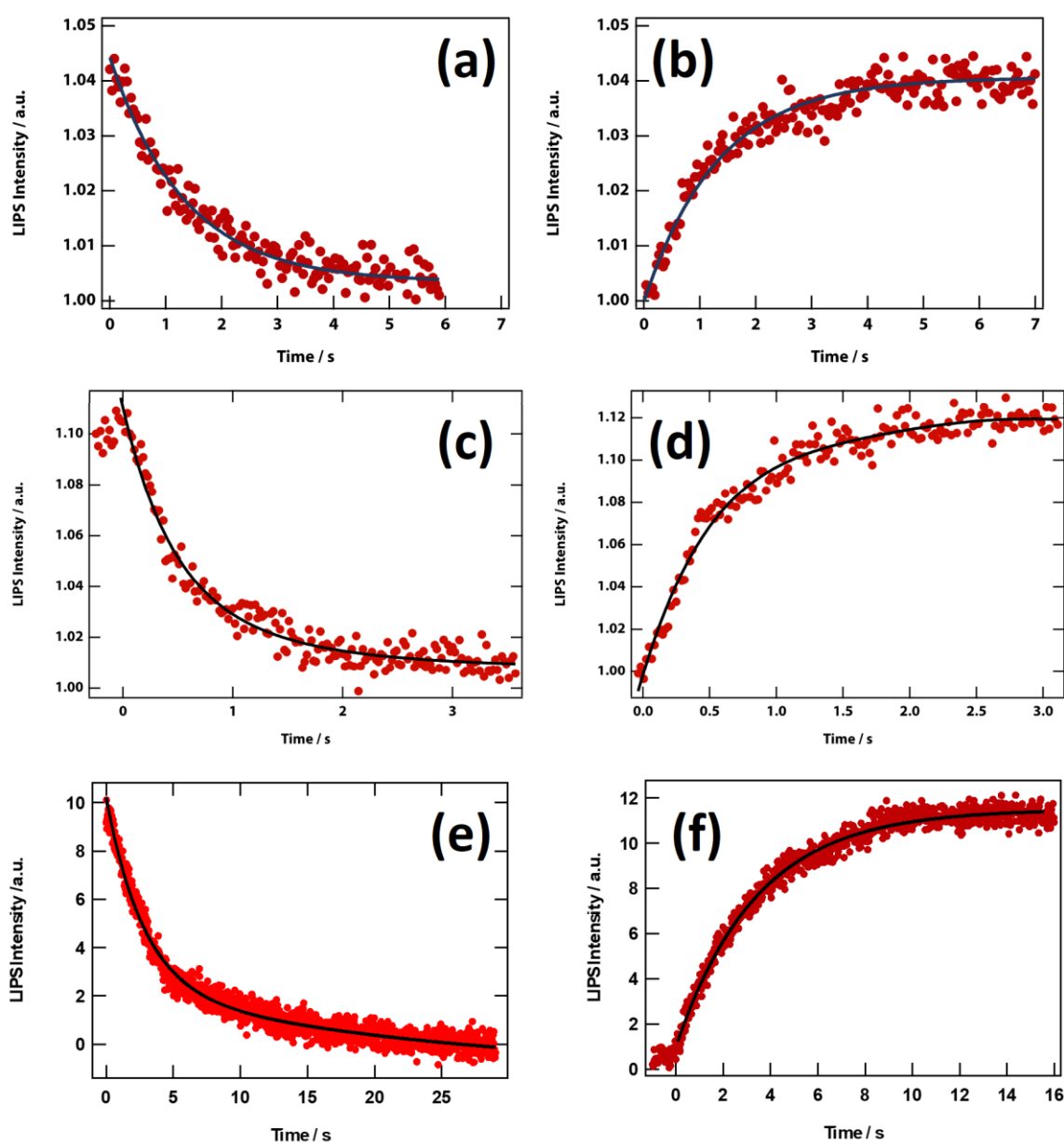
Figure 42 – Formation and decay curves of LIPS droplets in the following mixtures: (a), (b) Nitrobenzene-Octane, (c), (d) Nitrobenzene-Hexadecane and (e), (f) Nitrobenzene-Decane. The data are fitted to exponential functions for illustration.

Component 1	Component 2	Viscosity (cP)	Formation (s)	Decay (s)
Nitrobenzene	Octane	1.10	0.60	0.87
Nitrobenzene	Decane	1.31	1.31	1.68
Nitrobenzene	Hexadecane	2.48	1.19	1.11

Table 3 – Formation and decay times of critical nitrobenzene mixtures with alkanes of different chain lengths. Given the limited data, a link cannot be established between alkane chain length and formation and decay times.

The LIPS effect also works when an ultrafast pulsed laser is used in place of a CW laser. The LIPS intensity produced was similar when the average power was the same as the power of the CW laser. The pulsed laser used here has a wavelength of 1040 nm the base repetition rate used was 1 MHz. The pulse length of the laser can be varied between 350 fs and 4 ps, so a pulse length dependence was carried out. A random number generator was used to choose between five pulse lengths and 52 measurements were made in total. The intensity of the LIPS effect dropped slightly over the course of the experiment, so LIPS Intensity was measured as a function of time in a control experiment so that the data in Figure 43 was detrended before it was fitted to a straight line Using linear regression, a p-value of 0.02 was calculated, so as it below the 0.05 significance threshold, the null hypothesis can be rejected. The null hypothesis in this case was that there is no relationship between pulse length and LIPS intensity. As such, laser pulse length has a subtle effect on magnitude of the LIPS effect within the range 350 fs – 4 ps.
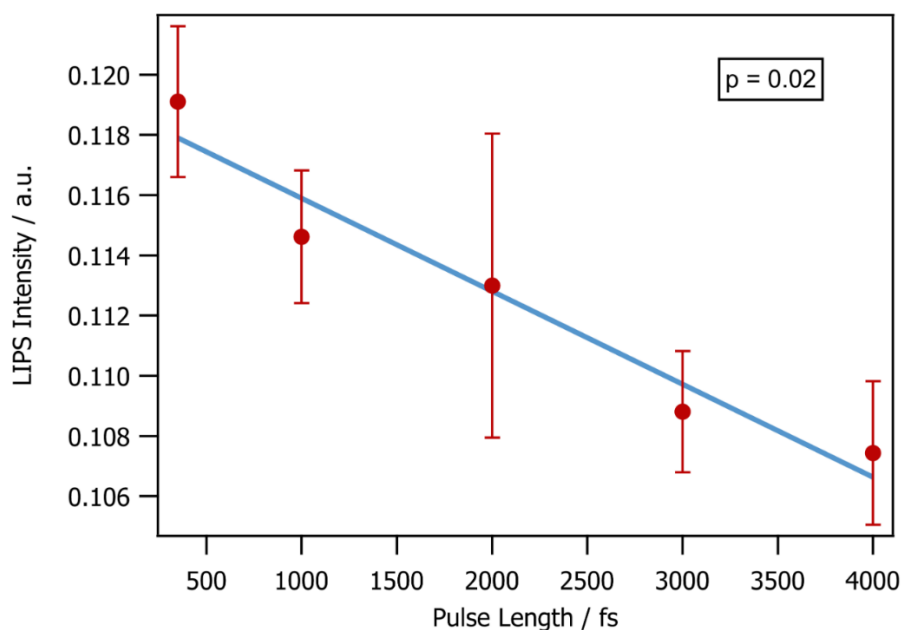
Figure 43 – The average intensity of the LIPS effect as a function of pulse length. The p-value of 0.02 refutes the null hypothesis, so there is an inverse relationship between the pulse length and the intensity of the LIPS effect.

This section has demonstrated how the LIPS effect manifests itself in, for the most part, critical mixtures. The next section will move on to using non-critical, metastable samples in or near the gap between the binodal and spinodal to induce nucleation using the LIPS effect.

2.6.1.   Laser-Induced Nucleation

Given that NPLIN has been extensively demonstrated in the last twenty years, it was essential that the model was backed up by nucleation experiments. Lased-induced nucleation (LIN) was achieved by irradiating the sample for between 1 and 60 seconds using non-critical mixtures of nitrobenzene and decane. It was initially predicted (Figure 27 left) that LIN would only be viable in samples with a lower-than-critical mole fraction of nitrobenzene, but the opposite was found to be case in the samples that were tried. A small range of mixtures in the interval $0.62 < x < 0.69$ exhibited LIN – the most pronounced being at the lower end of the interval. Figure 44 shows frames from a video made of a metastable mixture of mole fraction 0.632 at 297.1 K (which is on or slightly below the binodal when mica slides are used), which was irradiated for 30s. At first, the LIPS effect manifests itself normally (a), but only once the laser is switched off does nucleation occur (b-d), forming well-defined droplets (unlike the diffuse edged droplets seen in LIPS). The droplets were stable for tens of minutes, after which the properties of the sample generally begin to appreciably change, since the samples used here are not sealed at the edges of the glass slides.
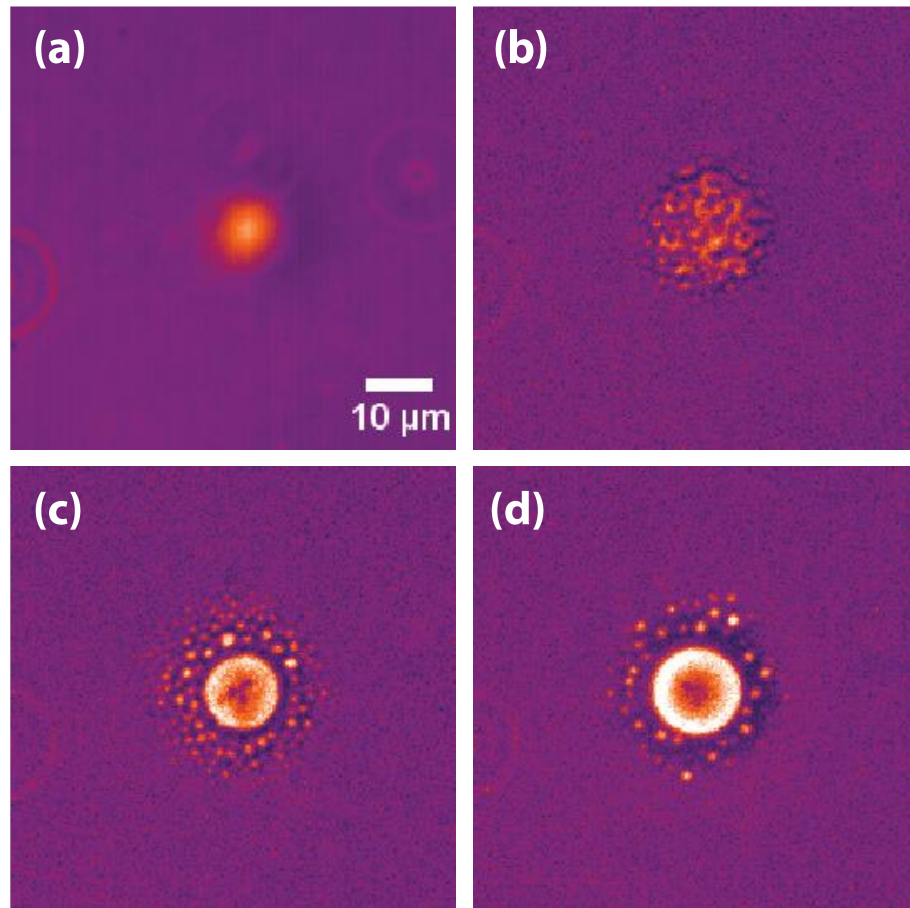
Figure 44 – Progression of a laser-induced nucleation experiment in a metastable nitrobenzene-decane mixture, conducted at x = 0.632 and T = 297.1 K with a laser power of 100 mW which was on for 30 s. (a) The laser is switched on and a LIPS droplet forms from a visibly homogenous mixture, causing a few degrees of heating. (b) Once the laser is switched off, the temperature equilibrates faster than the concentration, so the mixture drops down under the spinodal line, triggering the nucleation of the phase-separated state. (c), (d) After a second or so, a droplet with a defined interface forms through Ostwald ripening (competition between droplets mean that large ones get larger and small ones are consumed by the larger ones), which is stable for tens of minutes at least.

The LIN effect manifests itself differently at different mole fractions. At the highest mole fraction where an effect is visible (Figure 45 (a)), an array of droplets which are ~1 µm in size form. As the mole fraction is reduced, the sample is closer to the critical point, strengthening the LIPS effect. At x = 0.63, a large and defined droplet forms. The closer the sample gets to the critical point however, the narrower the metastable region becomes, so eventually no effect can be observed with the apparatus used, suggesting the metastable region (the temperature interval between binodal and spinodal lines) is < 0.1 K thick.
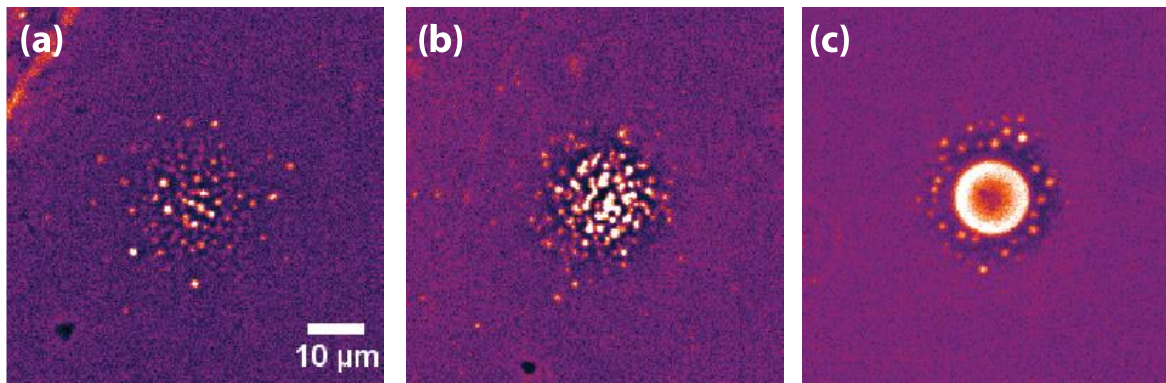
Figure 45 – The LIN effect at different mole fractions. (a) x = 0.675 (b) x = 0.957 and (c) x = 0.632. Higher mole fractions are farther away from the critical point, reducing the magnitude of the effect.

For x = 0.632 samples, there is in increase in the mean size of the central droplet as the exposure time increases (Figure 46 (a)). Although no quantifiable data to back this observation up is presented here, the droplets appear fainter as the exposure time rises. Droplet diameter also increases with laser power (b).
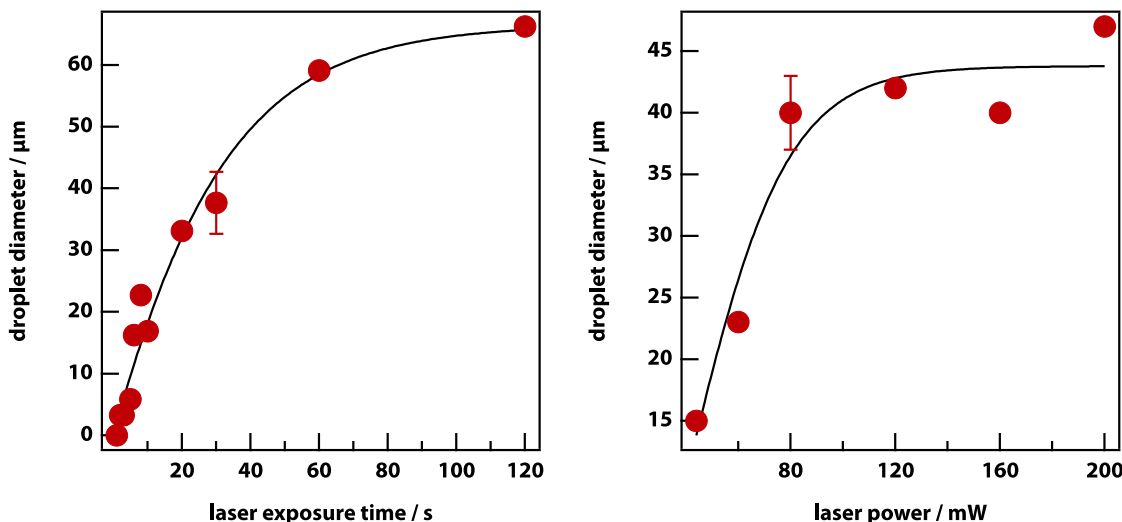
Figure 46 – The diameter of the droplet induced by LIN effect (before Ostwald ripening), as a function of (left) laser exposure time and (right) laser power[48]. Droplet diameter increases with both.

2.7. Discussion

The mechanism in the case of metastable binary mixtures is slightly different from that of supersaturated solutions and NPLIN. NPLIN samples are typically far into the supersaturated regime, so a small degree of heating does not have much of an effect. In the case of LIN, even a degree or two can lift the sample above the binodal. As such, nucleation is not triggered immediately as heating proceeds faster to equilibrium than diffusion by a factor of (~30 as was shown in 2.3.3) Figure 47 depicts the complete mechanism which proceeds as follows. Heating of a few degrees (this is estimated to be of 1.6 K at e^{-1} of the peak of the Gaussian heat

profile) lifts the state of the sample of out of the metastable regime (a) and the sample undergoes the LIPS effect – splitting in to an 'enriched' zone in the laser volume and a depleted region around it (b). The laser is then switched off, cooling the sample (c) but the enriched and depleted regions remain for longer (d). If this process is carried out with a critical mixture (e) a typical LIPS effect is observed. If it carried out at a higher mole fraction of nitrobenzene (or any high refractive index component), the depleted region moves within the binodal if the initial mole fraction and temperature are chosen correctly, triggering nucleation in that region (f). In the case of (g), only the much smaller enriched region will breach the binodal, which should phase separate according to the lever rule, only it is constantly acting against diffusion to deplete the volume, rending it unstable and unobservable. This interpretation fits with the observation that LIN only works at higher volume fractions. LIN also operates over much larger distances than the size of the LIPS droplet (60 µm as opposed to 2.4 µm), which mirrors what is seen by Sugiyama and Masuhara with NPLIN of phenylalanine crystals.[65] This cannot be explained by only the laser volume moving in to the binodal. As the exposure time increases, the depletion region which is affected by the laser electric potential will increase and move closer to the mole fraction of the bulk. The depleted volume moving below the binodal fits with this picture.
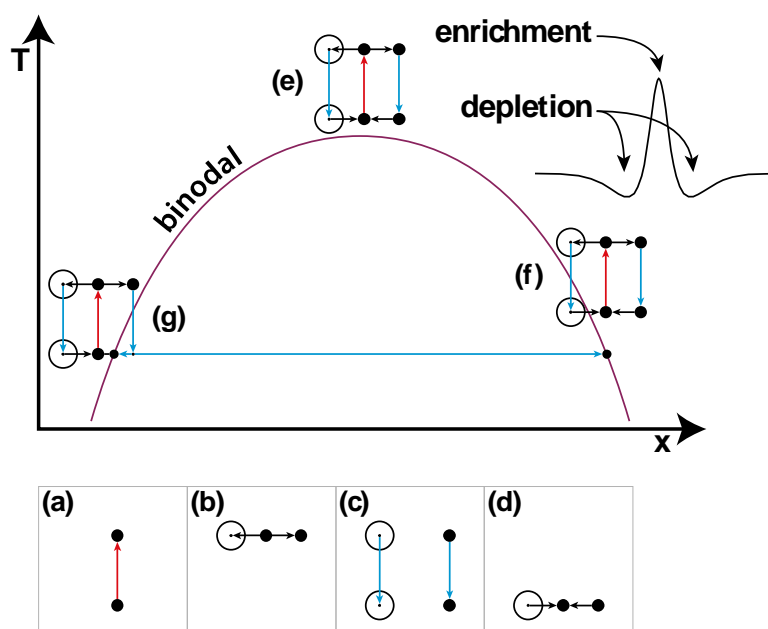
Figure 47 – Depiction of mechanism behind laser-induced nucleation (LIN)[48]. (a) The small degree of heating in the laser focus lifts the sample state above the binodal so that nucleation cannot occur and (b) but the LIPS effect still manifested itself. After the laser is switched off, (c) the temperature drops faster than (d) the mixture can equilibrate. This leads to the large depleted volume dropping below the binodal and triggering nucleation in a wide area.

Photothermal separation has been documented in binary mixtures of molecular liquids[66] and polymers[67], but relies on the system in question having a lower critical solution temperature (LCST), the opposite of the UCST present in the mixtures that are used here. Bunkin and co-workers used such an LCST mixture and using a model based on the Navier-Stokes equation concluded that heat-induced barodiffusion (diffusion due to pressure) was the dominant mechanism[68]. Any heating in an LCST system forces the mixture into the separated state, whereas heating in a UCST mixture moves further into the mixed regime. As such, the mechanism of the LIPS effect cannot be due to a direct heating effect. One of the main mixtures used here - nitrobenzene-decane - has no absorption bands at the diode laser wavelength of 785 nm (see Appendix 5.3) so the mechanism of resonant trapping of fluorescent molecules can be ruled out.[69] Thermophoresis, or the Soret effect, is the diffusion of molecules in a mixture due to their preference to be in a region of high or low temperature, lowering the overall free energy. Typically, the larger or heavier particle will experience positive thermophoretic behaviour, i.e it will move from hot to cold. Thermal conductivity, absorption coefficient and the thermal gradient all play a role however, making the sign hard to predict. The differential equation which describes thermophoresis has been solved (see 2.3.5 in the Introduction), and using the steady-state focal heating calculation, and values of the approximate Soret coefficient from Wiegand[58], it can be concluded that the change in mole fraction is negligible relative to change due to the LIPS effect.

The LIPS effect bears a striking similarity to optically trapping of particles such as glass beads where, due to refraction within the particle, there is a small transfer of momentum which leads to a net restoring force towards the region of highest electric field. In optical trapping there is a second force at play however, the scattering force, which is collinear with the beam. In order to trap particles in bulk liquid for example, the restoring force must be greater than or equal to the scattering force, which requires an objective lens with a numerical aperture >~ 1.[70] The experimental setup used here requires a high working distance lens, which has a much lower numerical aperture of 0.3. As such in the experiments, the LIPS effect droplet is only observed against the lower cover slip.

The LIPS effect detailed here does not depend on the presence of pre-nucleation clusters that can be trapped and aggregated by the laser. Rather the laser generates an electric potential which lowers the free energy of the phase separated state. The mixtures that were used were chosen because their critical points are easily

accessible and not hidden below a liquidus or above the boiling points of the components. Ultimately, this is a generic effect which applies to all mixtures and not simply those which mix poorly.

The LIPS effect was not observed using PC microscopy for mixtures with small differences in refractive index, however this does not prove conclusively that there is no droplet there. A diffuse droplet with the same refractive index as its medium would be effectively transparent under phase contrast since there would be no phase shift. One would expect an approximately linear relationship between the PC signal intensity and refractive index of the object, but the data in Figure 36 show that the data fits a higher order function. Equation 9 predicts that there will be a quadratic contribution to the PC signal from the greater electric potential generated by the laser – resulting in a cubic relationship overall. Fitting the data to a function of the form ax^n gave n = 3.001 and cubic fits gave better R^2 values than quadratic fits. This result validates the model described earlier which includes a quadratic contribution from the dipole approximation.

The LIPS effect is likely to be related to the laser-induced nucleation of amino acid crystals observed by Masuhara *et al.*[43] although the experiments could only be carried out at air-solution interfaces, implying that evaporation of Marangoni effects may play a role. A repeat of these experiments in the bulk would be worthwhile, bearing in mind the possibility of a hidden liquid-liquid critical point enhancing concentration fluctuations. Bulk NPLIN phenomena described by Garetz[22,26], Alexander[38,42] and others[65] fit with the narrative outlined here as the final states have higher refractive indices than their precursor mixtures. There are two potential exceptions to this picture, the first being carbon dioxide (CO_2) bubbles. Peters and co-workers reported NPLIN of CO_2 bubbles from solutions of CO_2 in water.[29] As a gas, CO_2 has a much lower n than water, so this does not fit with the theory presented here. The threshold pulse energy of the effect was reported to be independent of wavelength and purity of the chemicals – suggesting heating does not play a role - but due to small sample sizes and a lack of error bars, this claim may not be valid. Alexander and co-workers ran similar experiments and found that filtering their solutions, or thoroughly cleaning glassware in acid increased the threshold and decreased the lability (number of nucleation events).[30] In any case, since experiments show a depletion region which has a higher fraction of the low n component, this may be responsible for lowering the energy barrier to CO_2 nucleation. The second potential exception to this rule is NPLIN of glacial acetic

acid[35], as it is a pure liquid rather than a solution or mixture. It is well established that pure liquids can exhibit liquid-liquid critical points, such as triphenyl phosphite[71], n-butanol[72] and d-mannitol.[73] It may be the case that acetic acid exhibits a yet undocumented liquid-liquid critical point.

2.8. Conclusion

At a phase boundary the free energies of the two phases are identical and fluctuations in concentration or densities can be observed, particularly in the absence of an energy barrier between them. Fluctuations are strongest in proximity to critical points, such as the UCST seen in the binary mixtures in this thesis. It has been demonstrated that these fluctuations can be harnessed using a laser, which generates an electric potential that draws the high refractive index component of the mixture into the focus. In critical and near-critical mixed samples which are within ~1 K of the critical point, the electric potential drives phase separation (Figure 32). In metastable samples, the laser electric potential lowers the energy barrier to the separated state and can trigger nucleation (Figure 44).

It has been shown that an inexpensive laser-diode can be used to induce phase separation and nucleation in critical binary liquid mixtures. The effect depends on both a difference in refractive index, and more importantly proximity to a liquid-liquid critical point. The theory presented here applies to laser-induced crystal nucleation and provides a framework for future research on the subject.

Thus, LIPS effectively harnesses critical concentration fluctuations to drive the system towards the phase separated state. It can explain all the laser-induced nucleation experiments even in the absence of an obvious critical point (that is, it may be hidden in a metastable region such as below the liquidus).

The Liquid-Liquid Transition in Triphenyl Phosphite

2.9. Summary

Debate has been raging for decades about the nature of a possible second liquid phase (A.K.A the glacial phase) of triphenyl phosphite and the validity of having more than one liquid phase more generally. One hypothesis which is proposed by Hajime Tanaka principally is that the glacial phase is a second liquid state, which differs from the original liquid by forming locally favoured structures (LFS) of a few molecules.[74] The second hypothesis – of which the main proponent is Alain Hédoux - is that the elusive phase is nothing but a mixture of the original liquid and micro/nanocrystallites which have *aborted crystallisation.*[75] A review of the literature surrounding TPP tends to favour the Tanaka hypothesis, but the Hédoux hypothesis is also supported by a large body of evidence. Both maintain the existence of nanocrystals, but the evidence for this is weak. A variety of techniques have been used to elucidate the nature of the glacial phase (which will be referred to as L2) of TPP.

2.10.   Introduction

To begin with, the techniques and background literature which are relevant only to this chapter will be introduced. Techniques will be discussed first, followed by a literature review about liquid-liquid transition, with an emphasis on triphenyl phosphite.

2.10.1.   Infrared Spectroscopy

Infrared (IR) spectroscopy involves measuring light absorption in the infrared region, which typically corresponds to molecular vibrations, rotations and translations. The fingerprint region in the mid-IR (4000 - 400 cm^{-1}) is particularly useful in identifying compounds or their chemical and physical properties, as the vibrations produce intense and distinct lines, in contrast to the broad peaks of the far-IR. The gross selection rule for absorption by a particular molecular vibration is that there must be a change in the dipole moment vector. This does not mean that molecules that have a permanent dipole moment have vibrations that are always IR active and vice versa. For example, Figure 48 depicts the symmetric and anti-symmetric stretch modes of CO_2, which are IR inactive and active respectively. The symmetric stretch

has no net dipole moment at any point of its oscillation, but the dipole moment vector of its antisymmetric counterpart oscillates between pointing at either oxygen.
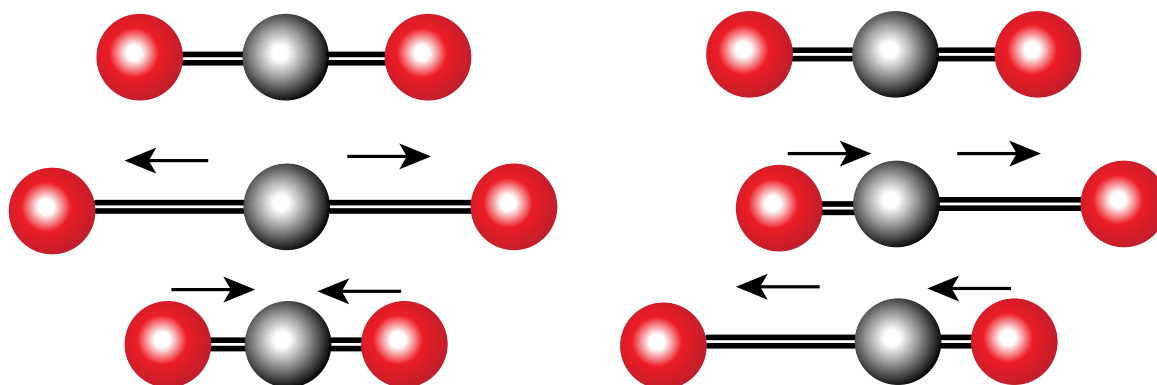
Figure 48 – Depiction of CO2 at rest and undergoing (a) symmetric and (b) asymmetric stretches. The symmetric stretch has no net dipole moment at any point during the vibrations since the partial negative charges on the oxygens cancel out, making it IR inactive. The asymmetric stretch dipole moment vector varies from side to side during the vibration, so it is IR active.

In terms of quantum mechanics, the transient dipole moment can be expressed as the transition dipole moment $\boldsymbol{\mu}_{fi}$ between initial and final vibrational states ψ_i and ψ_f. *So*

$$\boldsymbol{\mu}_{fi} = \int \psi_f \hat{\boldsymbol{\mu}} \psi_i d\tau \tag{3.1}$$

where $\hat{\boldsymbol{\mu}}$ is the transition dipole moment operator. So, the gross selection rule is therefore

$$\boldsymbol{\mu}_{fi} \neq 0. \tag{3.2}$$

The magnitude of IR absorption increases with the square of the transition dipole moment, where Einstein's coefficient of stimulated absorption

$$B_{fi} = \frac{|\boldsymbol{\mu}_{fi}|^2}{6\varepsilon_0\hbar^2}, \tag{3.3}$$

ε_0 is the dielectric constant and $\hbar$ is the reduced Planck constant.[76]

Older IR spectrometers are dispersive, which means they measure absorption a few wavelengths at a time sequentially. Modern spectrometers are often Fourier Transform Infrared Spectrometers (FTIRs) which record absorption as a function of the position of a mirror, which is then converted to spatial frequency (i.e. wavenumber) using a Fourier transform. This is possible because length (m) and

spatial frequency (m^{-1}) are conjugate variables. FTIRs possess what are basically Michelson interferometers (Figure 49 (a)). A coherent and broadband beam of infrared light passes through a 50/50 beamsplitter to produce two identical and perpendicular beams. The beams reflect off two mirrors, one of which moves on a translation stage. The optical path difference (OPD) due to moving the mirror generates a phase difference. The phase difference gives rise to an interference pattern on the detector as a function of mirror position as shown in Figure 49 (b). The beam interacts with the sample, whether the FTIR is in reflectance, transmission or attenuated total reflectance mode, and heads to the detector. Each frequency of IR light will produce minima and maxima at different mirror positions for the same phase difference – the frequencies can be extracted out using a Fourier transform. A background spectrum measurement is obviously necessary in order to factor in any changes due to sample container, air, moisture and optics.
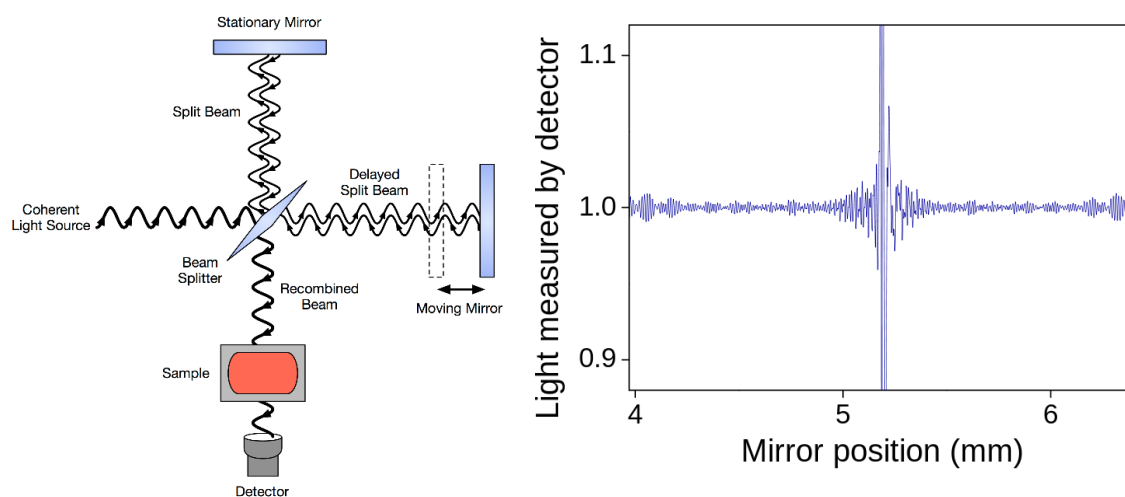
Figure 49 – (left) A Michelson interferometer which is configured for an FTIR. A coherent, broadband beam of IR light is split in to two, and a phase delay is introduced by moving one of the mirrors. The beam recombined with an interference pattern shown in (right) as a function of mirror position. The Fourier transform of the pattern is a standard IR absorption spectrum.[CCO, public domain]

The resolution of a dispersive spectrometer is limited by the width of a slit, as all frequencies are dispersed by a grating at different angles. A thinner slit means higher resolution, but at the cost of brightness which leads to longer acquisition times and a larger number of grating positions needing measured. The FTIR has a throughput advantage as it irradiates the sample with all frequencies at once, which can be easily decomposed computationally using a Fourier transform. The resolution is limited by the length of the mirror arm, i.e. the maximum OPD possible. The resolution scales with the inverse of the OPD, so four times smaller (better) resolution requires an OPD (or mirror arm) that is four times longer. An FTIR in

transmission mode will be used for all IR experiments which are detailed in this thesis, at a resolution of 2 or 4 cm^{-1}.

2.10.2.   Infrared Imaging

Since IR light has a longer wavelength than visible light, attempts at high resolution microscopy will be hampered due to Abbe's limit. IR microscope resolution is limited to roughly the wavelength, providing that a bright, highly spatially coherent source is used such as from a synchrotron.[77] Light with wavenumber v = 1200 cm^{-1} (which is the roughly the main wavenumber of interest in this work) corresponds to a wavelength of λ = 8.3 μm, so that is roughly the resolution limit. One way of carrying out infrared imaging is to use pass IR light from a synchrotron in to an FTIR to shine a broadband beam through a square aperture of, for example 10 by 10 μm and raster scan a pre-determined field of interest by moving the sample stage. The result is a spectrum for every 'pixel', which is also known as hyperspectral imaging. A smaller aperture, while in principle providing better resolution, is not practically viable due to significant beam attenuation. IR spectroscopy is traditionally a bulk technique, so for samples with multiple phases present, IR imaging can be very useful for picking out what phases give rise to particular spectra.

2.10.3.   X-Ray Diffraction

X-rays correspond to a region of the EM spectrum with wavelength λ = 0.01 – 10 nm, or energy E = 100 eV – 100 keV. The low wavelength means that they can be used to probe sub-atomic length scales, which are the order of 0.1 nm. In a laboratory, X-rays tend to be produced by accelerating electrons to strike a metal surface like tungsten, molybdenum or copper. An incident electron can eject an inner shell electron from a metal atom, causing an outer electron to drop to fill the vacancy and the emission of a photon corresponding to the difference in energy between the two states. Naturally this means that different metals have different x-ray energies, which means different scattering angles (λ varies with θ in (3.4)), so laboratories tend to have multiple sources to maximise the range of sizes that can be probed. X-rays and other regions of the EM spectrum can also be produced in the form of synchrotron radiation, where electrons are accelerated to a high velocity and deflected using magnetic fields, where the wavelength of the radiation depends on the velocity and the radius of the path of the electron. Like all waves, X-rays can interfere and form diffraction patterns with maxima and minima. Since X-rays can have shorter wavelengths than the spacing between atoms in a lattice, the positions

of the maxima can be used to determine the distances between lattice planes in crystals, and even angles if the sample is a single crystal. The Bragg condition is

$$2d \sin \theta = n\lambda \tag{3.4}$$

where d is the spacing between lattice planes, θ is the incident angle of the x-rays (90° being normal to the plane), n is the integer maximum number and λ is the wavelength. The Bragg condition is illustrated in Figure 50.
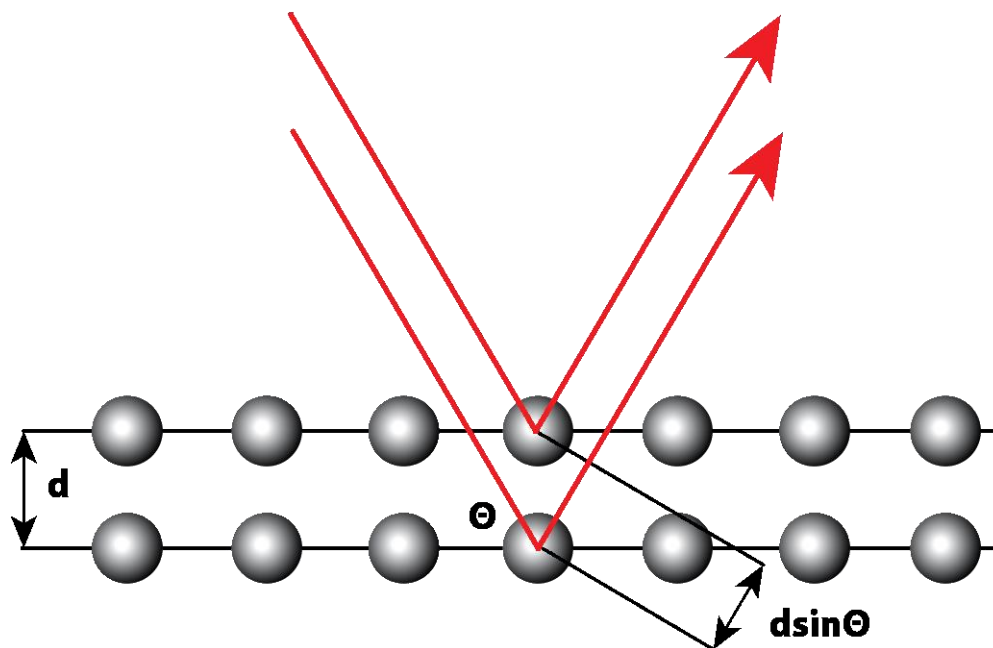
Figure 50 – Depiction of the Bragg law, showing coherent x-rays beams reflecting off successive lattice planes, with a phase difference equal to dsinθ.

Powder or polycrystalline samples can have lattice planes in any orientation, so some information is lost and a ringed pattern show in Figure 51 (b). Typically, a radial distribution function is taken of the powder rings so that they are presented as peaks, where the x-axis is the angle 2θ. Bragg's law is then used to convert 2θ to d-spacing, which is the distance between any two repeating units. Knowing d-spacings is helpful, but it does not tell you about the orientation of the planes with respect to each other or which d-spacing corresponds to the unit cell, so determining a unit cell can be difficult if this is the first time a crystal has been analysed. Crystallographic lattice planes can be classified using Miller indices (h, k and l), which are integer coefficients of the basis set of three direct lattice vectors a_1, a_2 and a_3. The unit cell of a crystal corresponds to the planes [100], [010] and [001].

A given lattice plane of a single crystal has a single orientation, and so light scattered from a single crystal has a single direction and produces a spot Figure 51 (a). Single crystal samples can then be rotated to get a full three-dimensional crystal structure.

75
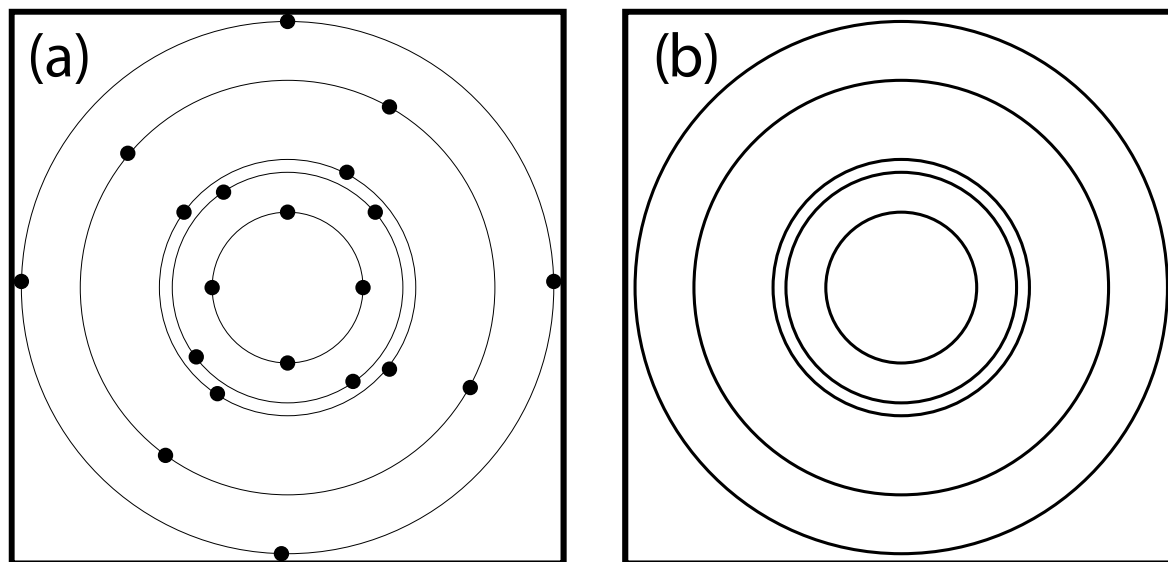
Figure 51 – Examples of diffraction patterns for (a) a single crystal and (b) a powder or polycrystalline sample. The latter have crystals in random orientations, so discrete spots build up to form rings.

Talking in terms of lattice planes is a simplification of x-ray diffraction. Fundamentally, the x-rays scatter elastically (Rayleigh scattering) from repeating patterns of electron density. As such, XRD can not only determine the spacings and orientations of planes, but the relative positions of individual atoms. Modern crystallography software can practically instantly determine molecular structure, the time-limiting step being the rotation of the detector to record patterns every 0.5 ° for example. It is not impossible to determine molecular structure from powder patterns, but bright, high quality beams and long exposure times can make it easier to determine molecular structure through Rietveld refinement – which is a least squares method of fitting experimental patterns to known patterns.

2.10.4. Density Functional Theory

Density functional theory (DFT) is a quantum mechanical method of modelling electronic structure in multiple-body structures such as molecules. Simple systems like a hydrogen atom can be solved easily using the Schrödinger equation in terms of wavefunctions, but two electron atoms for example do not have exact solutions and thus require approximation methods like DFT. Energy is a function of electron density, and electron density is a function of position – this function of another function is referred to as a functional. Wavefunction based approximations like Hartree-Fock have 3N degrees of freedom (where N is the number of atoms) and so 3N variables (111 for TPP). Electron density is only a function of position in 3D space, so only x, y and z – this is part of Hohenberg-Kohn theorems, which form the

basis of DFT. The total energy of the system tends to be approximated by the sum of five potentials in the Kohn-Sham equations

$$\{h_1 + j_0 \int \frac{\rho(2)}{r_{12}} d\tau_2 + V_{XC}(1)\}\psi_m(1) = \varepsilon_m \psi_m(1) \qquad (3.5)$$

where ion-electron potential energy, ion-ion potential energy, electron-electron potential energy and kinetic energy are expressed by the first two terms and V_{XC} is the exchange-correlation energy. The latter is difficult to calculate, as it originates from the abstract Pauli exclusion principle which states that in a quantum system like a molecule, no two fermions (including electrons) can be in the same quantum state. The choice of functional often translates to how the exchange-correlation energy is calculated. The Hartree-Fock method calculates an exact electron correlation energy based on the interaction between an electron and a mean field around it. It does not take in to account individual correlations between all the electrons – which would make it a ludicrously more computationally intensive calculation. One selling point of DFT is that it combines exchange and correlation energies and approximates it as the exchange-correlation energy V_{XC}. The common B3LYP hybrid functional mixes the exact calculation of the correlation energy of Hartree-Fock with the approximate method of DFT and is often referred to as a hybrid functional.

Typically, a basis set and a method are chosen which lend themselves to a particular problem. A basis set is a fundamental set of vectors that can be used to describe a space, for example i, j and k for 3D Cartesian space. In chemistry the vectors represent atomic or molecular orbitals. A carbon atom for example, has electronic structure $1s^2\ 2s^2\ 2p^2$, and since s orbitals are spherically symmetric, the unique orbitals are 1s, 2s, $2p_x$, $2p_y$ and $2p_z$. A carbon atom can be represented by a minimum of five vectors for its five atomic orbitals. The common basis set 6-31g(d) or 6-31G* has one vector, or basis function per atomic orbital.

Once a structure has been solved, normal-mode vibrational frequencies and their magnitude can be derived – giving predictions for infrared and Raman spectra. Free energies can also be calculated, which gives an indication of how stable each conformer is. Together, DFT and IR can be important tools in determining molecular conformation in amorphous structures, where XRD is not useful. One limitation of DFT that it is not easy to account for the interactions of other molecules and packing. Molecules with large dipole moments for example will interact strongly with each

other via the dipole-dipole interaction or hydrogen bonding. Multiple molecules can be modelled but time and computer processing costs will increase and quickly become impractical. DFT will be used to model a single molecule to determine the stability of different conformers, and predictions of IR spectra will be compared to experimental results to determine the structure of TPP molecules in the different phases.

2.10.5.   Liquid-Liquid Transitions

Polymorphism is the ability of a substance to exist in two or more crystal structures – for example $CaCO_3$ can exist as calcite, aragonite and vaterite which belong to the crystal systems trigonal, orthorhombic and hexagonal respectively. It is a phenomenon which is easy to characterise using many of the methods involved in this thesis such as X-ray diffraction and infrared spectroscopy. Polyamorphism is a rarer and more challenging phenomenon to investigate – the ability of a substance to exist as two or more amorphous forms. Amorphous substances can be defined as having no long-range ordering or periodic structures. By elimination this means that local structure is what differentiates polyamorphic phases. The transition between two polyamorphic liquids is often referred to as a liquid-liquid transition (LLT). LLTs have been documented (controversially) in triphenyl phosphite (TPP)[71], n-butanol[72], phosphorus[78], silicon[79], germanium[80], a metal alloy[81] and possibly d-mannitol.[82]

Perhaps the most promising LLT candidate is triphenyl phosphite (TPP), a slightly polar room temperature liquid, which will be used in all the experiments in this chapter. The extensive literature surrounding the LLT in TPP will now be summarised.

2.10.6.   Triphenyl Phosphite

Unusual behaviour in supercooled TPP was first noted by Kivelson and co-workers in a brief paper in 1996[83], which was followed up with a more detailed investigation using X-Ray scattering, calorimetry and light scattering.[84] The authors observed that when supercooled below its melting point at 297 K to 245 K, TPP crystallised as expected. When quenched (rapidly cooled) to $213 < T_Q < 225$ K however, crystallisation did not occur, yet it was well above T_G at 204 K. Instead, TPP went through a slow transition to an apparently amorphous phase which they termed *glacial*. The salient fact of their first paper was that the cold-crystallisation temperature of the glacial phase was 10 K higher than that of the untransformed

liquid. This phase was therefore different from the 'normal' liquid phase, and the crystal. The follow up paper made several key observations. The glacial phase, which will be referred to as liquid 2 or L2 from here on, is denser than liquid 1 (L1) or the crystal. DSC experiments show a latent heat and therefore indicate a first order phase transition, X-ray diffraction patterns show broad peaks very similar to both liquid 1 and liquid 1 as a glass – no sharp peaks like the crystal. Light scattering experiments indicated the existence of *Fischer clusters* on the scale of hundreds of nanometres, which are now known to be growing droplets of L2.[85] The authors tentatively claim that both the nucleation and growth rates of the clusters decrease with decreasing temperature. Kivelson concludes that their observations fit within the theory of *frustration limited domains*[86], which involves locally favoured structures of a few molecules, which cannot tile space and therefore geometrically frustrate the formation of the more thermodynamically stable crystal (See 1.3.3 for a description of geometric frustration). Below the temperature of a hypothetical critical point T*, locally favoured structures form and cause strain. Two length scales emerge below T*: one corresponding to the size of domains consisting of locally favoured structures (which will now be referred to as LFS), and the other associated with the size of density fluctuations in the untransformed liquid. Kivelson suggests the domains may align themselves periodically, to form what he refers to as a defect-ordered crystal. Kivelson paints a thorough and convincing picture, but his studies have spawned decades of research with conflicting conclusions. For ease of reading, the following abbreviations defined again here:

Liquid 1 (L1)	The untransformed liquid which is stable at room temperature.
Liquid 2 (L2)	The transformed liquid which forms between 204 < T < 226 K, often referred to in most literature as the glacial phase.
Crystal 1 (C1)	The crystal which results from crystallisation at high temperature $T_Q \sim$ > 245 K, also referred to as monoclinic or mon.
Crystal 2 (C2)	The crystal which results from crystallisation at low temperature $T_Q \sim$ < 245 K, often referred to as rhombohedral, hexagonal or hex.
Crystal 3 (C3)	The monoclinic crystal which has previously formed in an ionic liquid solvent[87], and in a beaker at 253 K in a freezer in this study.
Glass 1 (G1)	The glass which results from quenching liquid 1 to T_Q < 204 K
Glass 2 (G2)	The glass which corresponds to liquid 2 – liquid 2 is defined by some to be a glass, but others contest this – the latter will be used.
NG	The nucleation and growth regime between 215.5 ≤ T_Q < 226 K
SD	The spinodal decomposition regime between 204 < T_Q < 215.5 K
FLD	Frustration limited domain
LFS	Locally favoured structures
LLT	Liquid-liquid transition

Table 4 – Definitions of abbreviations used to refer to different phases of TPP and others.

Rossler and co-workers used ^{31}P nuclear magnetic resonance (NMR), dielectric spectroscopy and Brillouin scattering to show that the glacial phase is distinct from the crystal.[88] Brillouin scattering indicated that L2 is isotropic on the length scale of phonons, i.e. atomic length scales and the Brillouin shift for L2 is distinct from L1 and crystal – a combination of L1 and crystal was not observed. Dielectric spectroscopy showed slower molecular motion in L1 than L2. ^{31}P NMR, as well as dielectric spectroscopy showed that *considerable collective motion takes place*, so the authors suggest a transition from a fragile to strong liquid. Puzzlingly, the authors state in the conclusion that the LLT was not observed in DSC yet assert the opposite in the results section – the endotherm of the LLT occurs at 224 K, followed by cold-crystallisation at 237 K (Figure 52).
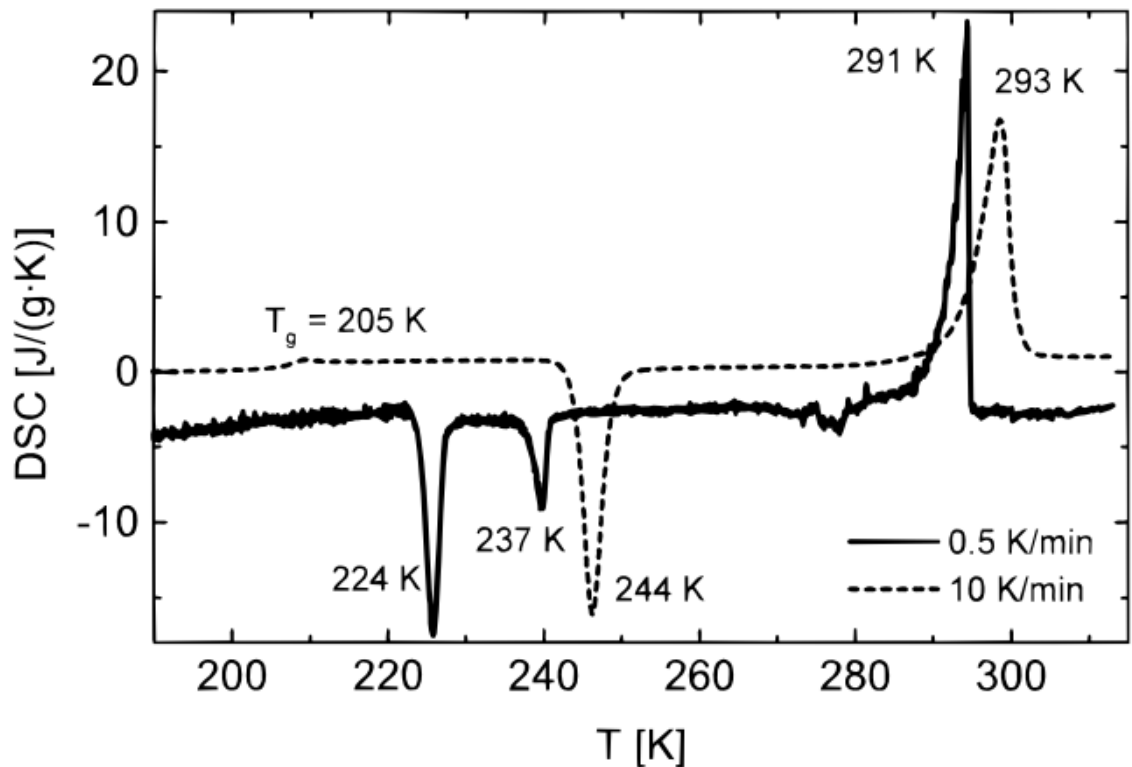
Figure 52 – DSC traces by Rossler and co-workers at different heating rates. For the slow heating rate, which is represented by the solid line, the LLT is visible at 224 K. The fast heating rate does not allow for sufficient time for the LLT to take place, so the endotherm at 224 K is not visible[88].

Alain Hédoux published two articles in 1998/99 which came to the opposite conclusion of Rossler and Kivelson. He based his argument on low-frequency Raman spectroscopy[89] and X-ray diffraction (XRD).[75] Phonons are quantised collective lattice vibrations, which can be detected using Raman spectroscopy at low frequencies. In a long-range ordered structure like a crystal, Raman phonon peaks are sharp, but in a liquid are broad and overlap. The L2 spectrum shows broad liquid-like peaks which differ from L1. Hédoux fits the L2 spectrum using the wavenumbers of some of peaks from the crystal spectrum, and states that the L2 spectrum acts as *the perfect envelope of the phonon peaks observed in the crystal.* He concludes by saying that his observations agree with that of Kivelson in terms of L2 being a defect-ordered crystal, but that the LFS may simply be crystalline. Powder XRD at a number of quench temperatures (T_Q) showed varying degrees of sharpness, but were generally broad and liquid-like.[75] The powder pattern was used to incorrectly assign a monoclinic unit cell – it was subsequently shown by Hédoux himself that six units with monoclinic symmetry make up a larger plate-like rhombohedral cell[90] with unit cell dimensions a, b = 37.8 Å c = 5.7 Å. The Debye-Scherrer equation was used to calculate the crystallite size in L2 at different T_Q –

size was shown to decrease with decreasing T_Q, dropping to below two of the unit cell dimension sizes at 30 Å. The Debye-Scherrer equation relates the broadening of XRD peaks to crystallite size. Despite acknowledging that this is problematic, the conclusion is drawn that Kivelson's LFS are simply nanocrystals and *abortive crystallisation* means that crystal nuclei stop growing due to *competition with volume and area forces*. One more important take-away from these papers is that the length scale of structures seems to increase with temperature when $T_Q > 215$ K (Figure 53), although there are too few data points to draw a reliable conclusion.
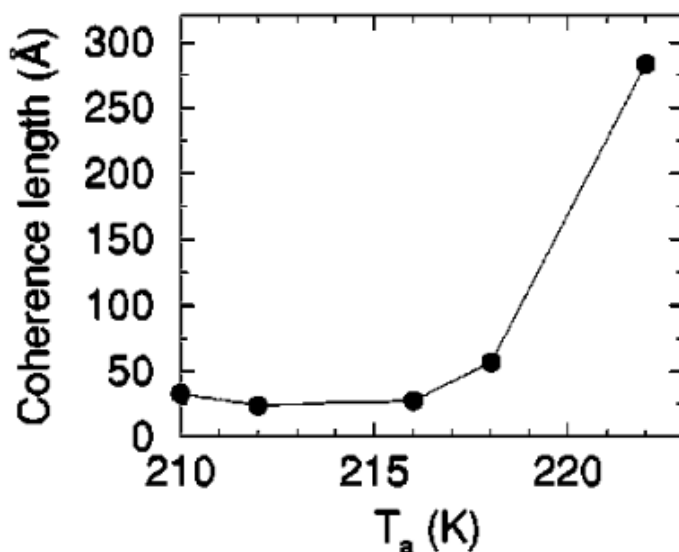
Figure 53 – Crystallite size calculations as a function of the aging (quench) temperature using the Scherrer equation and powder XRD patterns[75].

Johari and Ferrari suggested that L2 is a plastic crystal or liquid crystal[91], which ties in with the Ostwald step rule. L2 could be an intermediate between the normal L1 and the crystal. Oguni used dielectric relaxation spectroscopy to show that higher T_Q means a larger LFS/crystallite size and a more ordered state – indicating that L2 may not be one defined phase, but a series of metastable states which depends on the history of the sample.[92] Two small angle neutron scattering (SANS) studies were carried out by Tarjus[93] and Yarger[94] in 2000 and 2001 which contained information about structure sizes. Scattering patterns by Tarjus indicated '*structural organisation on a mesoscopic scale (~ 80 Å) and we have shown that no sign (sic) of aborted crystallization to the normal crystalline phase*'. This conclusion is based on a shoulder on a curve at $Q = 0.1$ Å^{-1} which only appears at 225 K, but not at 218 K. Yarger concluded that small clusters of 16 Å form at 210 K, which grow in size at higher temperature and agglomerate to a maximum cluster size of 60 Å on heating.

Hédoux carried out XRD at a synchrotron and used Rietveld refinement to resolve a rhombohedral crystal structure and molecular conformation which almost had mirror plane symmetry.[90] He concludes that TPP stacks along the short c axis through weak hydrogen-bonding. In 2004, Tanaka and co-workers visualised the LLT using phase contrast (PC) microscopy for the first time.[95] It was clear that the LLT had two kinetic regimes: nucleation and growth (NG) where 215.5 K < T_Q < 223 K and spinodal decomposition 205 K < T_Q < 215.5 K. This confirms part of FLD theory – the existence of a narrowly missed critical point. The authors showed using rheological measurements that at 220 K and 213 K at least, L2 is in a glassy state, whereas the untransformed L1 is a highly viscous liquid in that range of temperatures. During the LLT there is a jump of orders of magnitude in G', the real part of the complex shear modulus. This points to the existence of a different, higher T_G for L2, which ties in with the higher cold-crystallisation temperature observed by Kivelson. Based on kinks in graphs of nucleation and growth rates with respect to T_Q at 223 K, the authors estimate $T_{Binodal}$ to be 230 K by extrapolation. Above 223 K, both nucleation and growth rates of the crystal outstrip that of L2 and below 223 K the opposite is true, although it is important to note L2 is still more favourable than L1 in the range 223 K < T < 230 K. Calorimetric measurements show that when T_Q ≥ 228 K, the crystal forms rather than L2, which agrees with the binodal estimate. Tanaka published a follow up paper in the same year which used PC microscopy quantitatively to prove the existence of L2, and calculate structure factors.[74] He has subsequently admitted that the structure factored were calculated incorrectly.[96] Tanaka proposes the phase diagram shown in Figure 54, where the x-axis is the order parameter S - the local fraction of LFS.
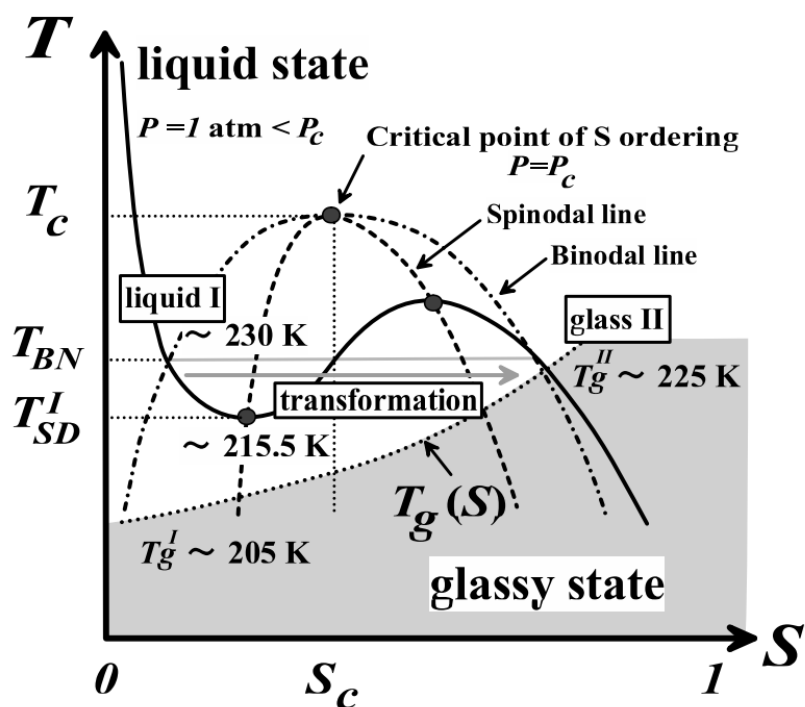
Figure 54 – Phase diagram proposed by Tanaka and co-workers where the order parameter S is the local fraction of locally favoured structures[95].

Senker carried out ^{1}H and ^{31}P NMR which indicated micro or nanocrystalline material forming only when T_Q > 223 K.[97] ^{31}P radio-frequency-driven spin-diffusion exchange spectroscopy indicated small clusters of 'a few' parallel aligned molecules (30-40 Å) which is the order of magnitude of the LFS.

Golovanov made the first observation of a second monoclinic crystal of TPP, which he crystallised in bulk in an ionic liquid solvent.[87] Single crystal XRD revealed unit cells dimensions a = 11.8, b = 9.9 and c = 13.5 which are distinct from both the rhombohedral crystal 2 (C2) and the incorrectly assigned monoclinic crystal by Hédoux. The molecular conformation of monoclinic TPP (C3) appears similar to that of C2, but with a change in the torsion angle O-P-O-C, as is illustrated in Figure 55.
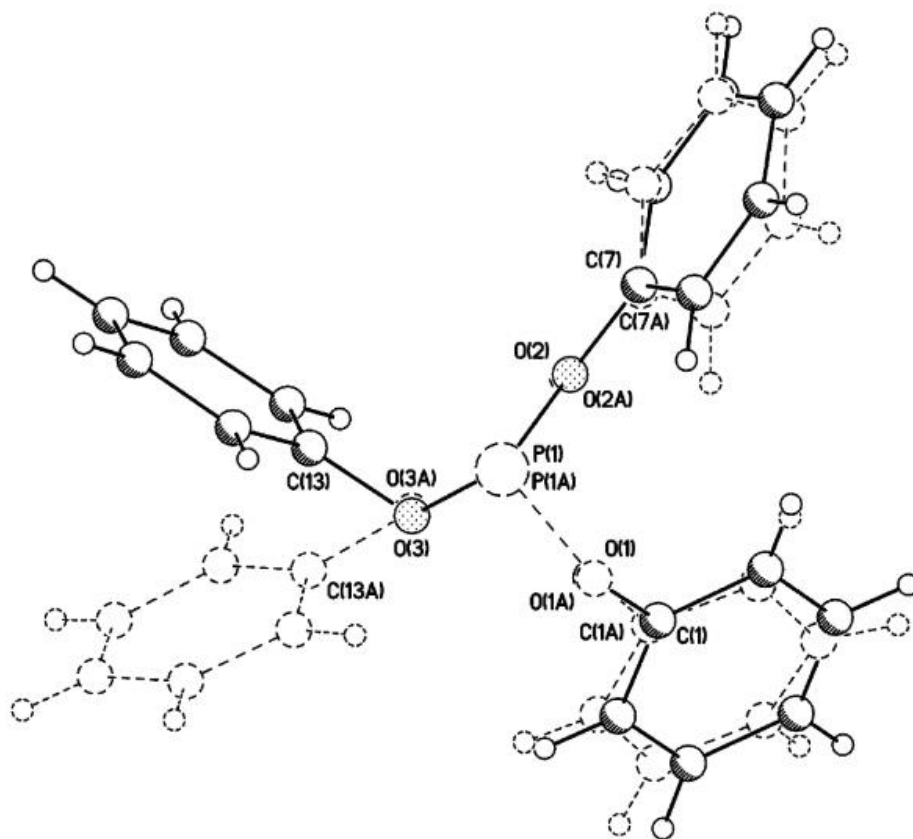
Figure 55 – Mon (solid lines) and hex (dashed lines) conformations of TPP, in the former case calculated by single crystal XRD by Golovanov and co-workers[87].

Hédoux published another article which included Raman spectroscopy and XRD in 2006, adding microscopy to his data.[98] The micrographs, which were taken at T_Q = 214, 220 K look very different from that of Tanaka, and the microscopy images which are displayed in the results section. Hexagonal plate-like crystallites are clearly visible in the 220 K image, despite the fact that the crystal grows needle-like crystals spherulitically, and at 220 K it grows radially to form discs/spheres. The Raman and XRD data do not add anything new. Alain Hédoux's final major contribution to the subject of the LLT in TPP took the form of density functional theory (DFT) calculations to make a start at determining the conformation of TPP in the liquid phase. Two degrees of freedom were allowed by rotating two torsion angles and made an energy surface plot of those conformers. This resulted in three stable conformers, with C_3, C_1 and C_S symmetry.[99] The differences in energy between the conformers are likely within error, owing to DFT being performed as a single molecule at absolute zero, not taking packing into account. However, two and three molecules are simulated as rods, which are connected by weak hydrogen bonds, which may be trimers of the rod/needle like structures in C2. He concludes that the study was difficult and maintains his thesis that L2 is simply a mixture of L1 and C2.

After a gap of a few years, interest in TPP revived in 2014 with a paper by Drozd and co-workers who identified a new polymorph of TPP[100] which will be termed C1. It was not clear at the time whether it was the monoclinic form (C3) previously identified by Golovanov[87] and it is shown in the results section that it is indeed not C3. Drozd showed that by quenching to 243 K, holding for 15 mins, then heating to 270 K, the C1 form could be crystallised in a reliably large proportion. DSC revealed a different melting point of 291.6 K, compared to 299.1 K of C2. IR spectroscopy was carried out, showing the intervals 840 – 910 cm^{-1}, 1050 – 1100 cm^{-1} and 1570 – 1620 cm^{-1}. It is clear from their data (an example is shown in Figure 56) that the two crystals have unique spectra – the C1 form which they refer to as metastable, having more and arguably sharper peaks.
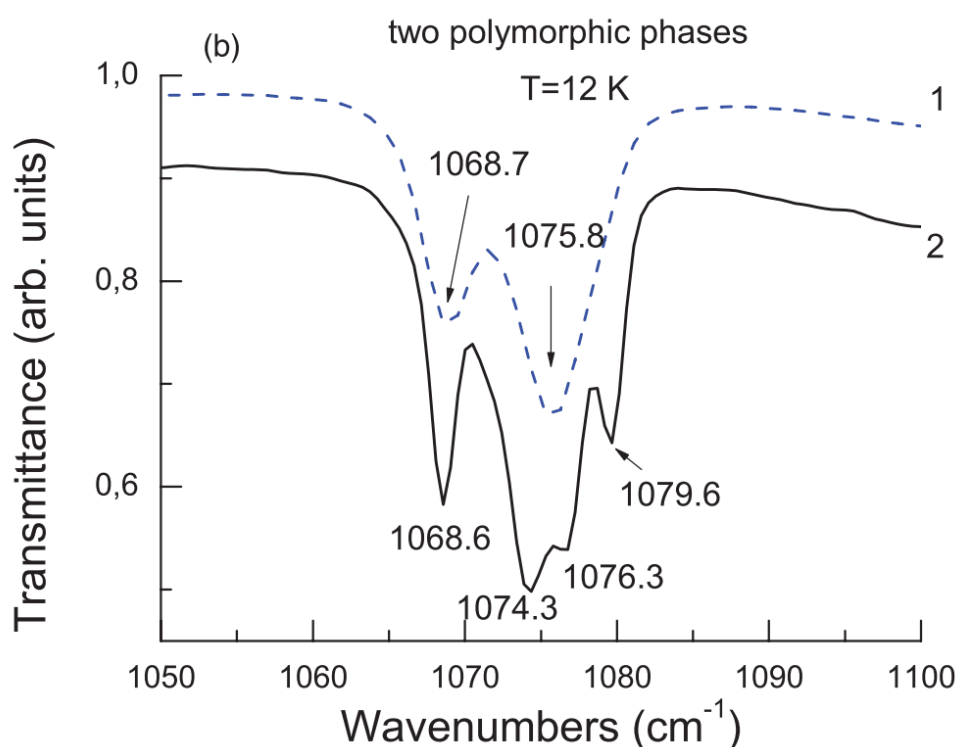
Figure 56 – IR data from Drozd and co-workers[100] of the two crystal polymorphs of TPP: 1 – 'stable' rhombohedral C2 crystal, 2 – 'metastable' C1 crystal. The two are clearly distinct, with 2 having extra peaks at 1074.3 and 1079.6 cm^{-1}.

In the same month, Tanaka and co-workers published a depolarised visible light scattering study of the LLT in TPP.[96] The transient VV (vertical vertical) scattering patterns shown in Figure 57 agrees with previous measurements of viscosity. The permanent nature of the Maltese crosses in the VH (vertical horizontal) patterns indicate birefringent structure on the order of 10^{-7} m. The intensity of the cross increases with T_Q and is practically zero where $T_Q < 213.5$ K – which the authors suggest as is the spinodal temperature T_{SD}. This leads Tanaka to a conclusion which

is a bit of an olive branch to Hédoux – nanocrystals are embedded in L2, and the processes proceed independently.
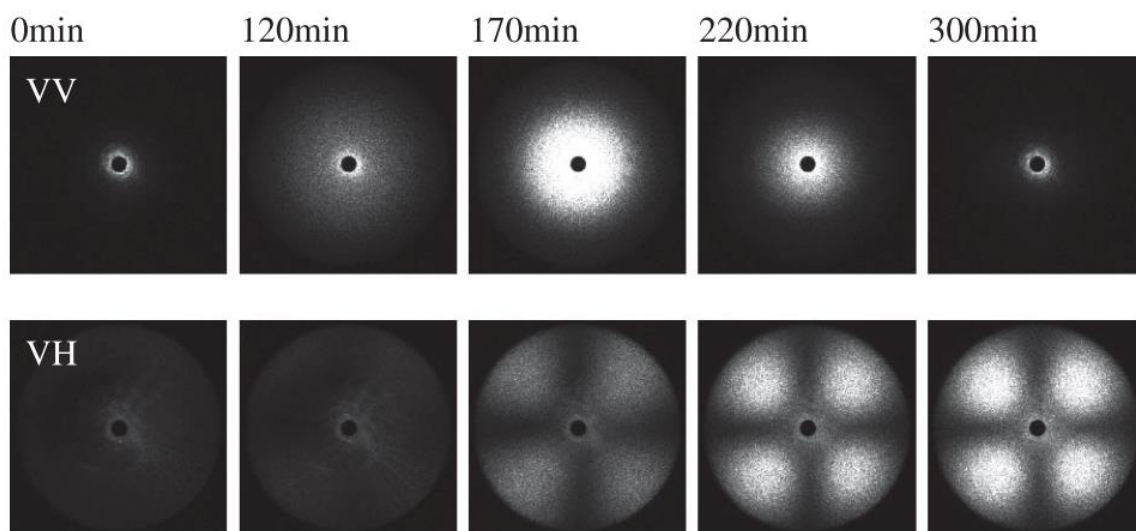
Figure 57 – Depolarised visible light scattering patterns of the LLT in TPP over time at $T_Q = 215$ K. VV agrees with increases in viscosity during the LLT. Maltese crosses seen in VH show permanent birefringent structure in L2[96].

Wynne and co-workers used fluorescence lifetime imaging to analyse the LLT, using two environmentally sensitive dyes - perylene and coumarin 153.[71] They observed a change in fluorescence lifetime during the LLT, which was larger at higher T_Q. Interestingly, they observe contrasting lifetimes for two different crystal forms. The second crystal form gives rise to a longer fluorescence lifetime in coumarin 153, which indicates a more polar structure, which ties in with the more polar monoclinic C3 polymorph observed by Golovanov. They conclude that the transition to L2 is associated with conformational change involving a twist of a phenoxy ring and the LFS suggested by Kivelson. The two liquid phases can be thought of as *echoes* of the crystal polymorphs.

Tanaka published again in 2015, with an X-ray scattering study where he reiterates that the order parameter of the LLT is the number density of locally favoured structures, whose size is a few nanometres.[15] However, he proposes that the LLT in fact has two order parameters, as there are two independent processes taking place: the growth of L2, and 'microcrystals' forming at the interface which are frozen in to the highly viscous or glassy L2. He claims that you can see evidence of microcrystals only in the NG regime. The SAXS data in Figure 58 show two separate features – a power law (a straight line on a logarithmic y-axis in Figure 58) which varies inversely with q (nm^{-1}) in the Porod regime (0.08 < q < 0.3) and a static bump

at q = 0.7 nm^{-1} (Tanaka denotes this is 0.4 nm^{-1}). It should be noted here that the parameter q used by Tanaka appears to have been divided by 2π, which is not consistent with other literature. So, the Porod regime corresponds to sizes 13 < d < 3 nm) and 3 nm for the LFS. The slope of the line in the Porod regime can indicate the surface area. A gradient of -4 indicates a sphere, -3 to -4 indicates a rough ball and < -3 others shapes such as rods. The slope of samples where T_Q > 213 K is clearly around -4, but spherical particles of this size would be impossible to form. The objects are roughly 3-13 nm in size, which is far too small for an even vaguely spherical spherulite of C2 to form. C2 TPP has unit cell has dimensions a,b = 3.8 nm and c = 0.6 nm. Data from Senker[97] and Hédoux[98] has shown that TPP in C2 stacks to form anti-parallel rods along the c-axis. The rods therefore have cross sectional dimensions of 3.8 by 3.8 nm, which could not form a 3-13 nm spherulite. If the particles are indeed roughly spherical, it is more likely that they are just larger LFS, which Tanaka concludes have a radius of gyration of 3.3 nm in the interval 212-218 K. In addition, an increase in the intensity in the Porod regime could mean either an increase in surface area S, indicating rough structures, or indeed the q^{-4} line indicating spheres. In summary, the SAXS data in the Porod regime are not convincing proof of the larger structures being either LFS or crystalline material.
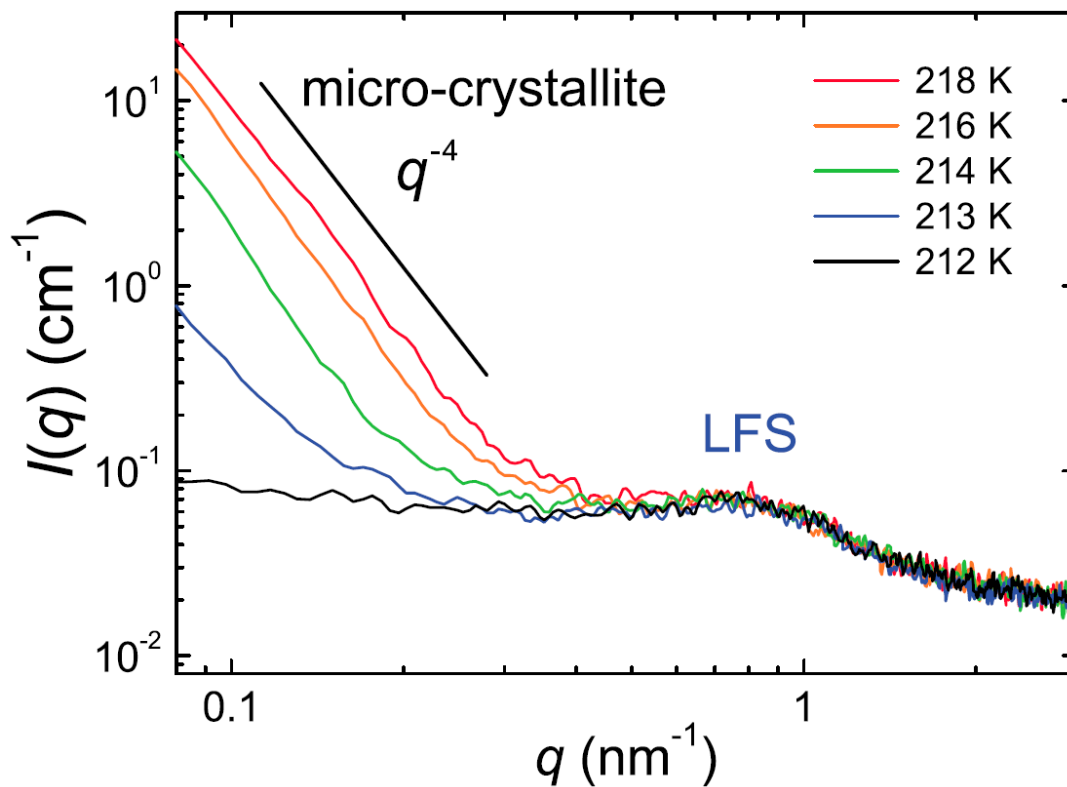
Figure 58 – SAXS data taken by Tanaka and co-workers which indicates smooth spherical micro-crystallites in the Porod regime (the -4 gradient indicates smooth spheres) and locally favoured structures at 0.8 nm^{-1} which appear between 212 – 233 K.[15]

In 2016 Tanaka published a thorough study of the LLT using flash DSC, with a very high heating rate of 1000 Ks^{-1} and a small sample mass of 20-50 ng. From the offset, this method presents two main problems: firstly, the position of transitions in DSC shift with heating rate and secondly, the small sample size could introduce confinement effects. The high heating rate allows the reverse LLT to be elucidated however by bypassing crystallisation. Tanaka identifies the two liquid phases using their distinct T_G (which the authors acknowledge are shifted drastically). The authors annealed countless samples at 216 K over ten hours, then the samples are heated to some temperature T_{RC} before being quenched to 173 K. The samples are then measured in the DSC. By increasing T_{RC} from 222 K to 262 K the higher temperature glass transition of L2 disappears, while the L1 glass transition increases to the point that there is no L2 left. Although the paper provides strong evidence for L2, the results will be taken with a pinch of salt because of the extreme heating rate and potential confinement effects. The following year Tarnaka and Kaminski published a paper which was critical of the confinement effects in Tanaka's paper[101], and agreed instead with the thesis of Hédoux. Their critique has two of its own problems, however. The authors confine TPP in pores which are 35 and 150 nm in size, which was orders of magnitude smaller than that of Tanaka. A sphere of 50 ng of TPP would have a diameter of 43 μm. Secondly, the authors observe no LLT in their confined TPP, but also see no LLT in their bulk TPP which should act as a control. This points to a significant problem with their sample and/or methods, so their results are too unreliable to be considered.

The final contributions to-date of TPP literature are two papers by Babkov and co-workers who carried out IR spectroscopy and used DFT to try to identify the conformer(s) present in the liquids and crystals.[102,103] The 2017 paper was only available in Russian[103], so Google Translate has been used as an aid. The 2016 paper focussed on part of the mid infrared region (700-920 cm^{-1}) and recorded a degree of peak sharpening and a change from five to seven distinct peaks during the LLT at 225 K. They also carry out crystallisation at 240 K from the glacial phase and see further degree of peak sharpening. The authors showed that the spectra of the glacial phase and C2 do not change significantly over a broad range of temperatures (12 – 225 K for the former, 12 – 300 K for the latter). The data in Figure 99 (Appendix 5.7) show that this is the same with L1 in the T range 211 – 300 K. The 2017 paper also features IR spectra, but over a broader range with three predicted conformers and their predicted spectra. There is a single graph of the

region 1150-1250 cm^{-1} which is the region that will be focused on in the results section of this chapter. The predicted spectra show either a single peak or a single peak with a shoulder in the interval. The experimental data show what appears to be a peak with a shoulder splitting in to two more distinct peaks – not simply sharpening. What could have been two very informative and useful studies for the DFT calculations in this chapter are sadly lacking. The authors note the existence of six torsion angles, about the P-O and O-C bonds on each of the three phenoxy arms. Unfortunately the authors only consider the O-C torsions (red in Figure 59), which correspond to the phenyl rings twisting about the O-C bond. Due to two lone pairs on the oxygens, the P-O-C angles are ~120 °. This means a change in the P-O torsion of 180 ° amounts to a flip of the whole phenoxy ring like the depiction in Figure 55. The lack of reference to the P-O torsion angle, or whether it was a constant or a variable, makes their conclusions about conformations of little value. As will be discussed later, a change in one of the P-O torsion angles is a key finding in the DFT and IR results.
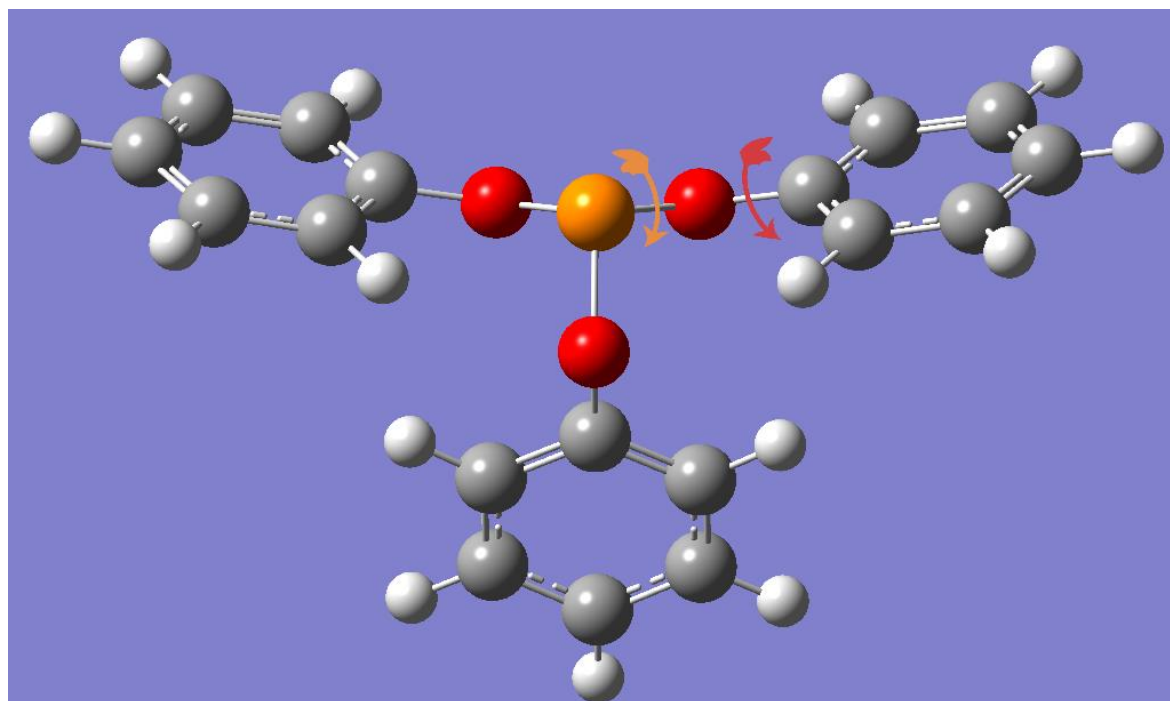
Figure 59 – TPP molecule in the rhombohedral (C2) conformation showing the two torsion types where lp is lone pair: lp-P-O-C (orange) and P-O-C-C (red). The lone pair not pictured, but would extend out of the page and upwards from the P atom, completing the tetrahedral geometry.

TPP can be seen through the lens of two competing theories – Tanaka vs. Hédoux – a second liquid state composed of locally favoured structures vs. nanocrystals in untransformed liquid respectively. It is possible that the two arguments may be two sides of the same coin. The full scope of the literature surrounding TPP, alongside

new results reported here, will be used to consolidate it all into a single coherent theory about the nature of the liquid-liquid transition in triphenyl phosphite.

2.11. Methods

Mid-IR data was obtained using a Bruker Vertex 70 FTIR spectrometer equipped with a globar lamp, a DLaTGS detector and KBr beamsplitter. Data was taken with either 2 cm^{-1} or 4 cm^{-1} resolution between 400 and 4000 cm^{-1} in transmission mode. Samples were housed in and temperature controlled using a liquid N_2 cooled Oxford Instruments cryostat. The sample, inner and outer windows were made of CaF, ZnS and KRS-5 respectively. No spacer was used between the CaF sample windows due to detector saturation with thicker samples.

Infrared imaging was carried out at the beamline B22 multimode infrared imaging and microspectroscopy (MIRIAM) at the Diamond Light Source synchrotron in Didcot, Oxford. Mid-IR imaging data were recorded using a Bruker Vertex 80 which was combined with a Hyperion 3000 optical microscope which had an automated, translating sample stage. Mid-IR imaging samples were housed in a liquid N_2 cooled Linkam THMS600 stage with 0.1 K temperature control and sandwiched between BaF_2 windows with no spacer.

Microscopy was carried out using an Olympus BX53 microscope with PC and polarisation capabilities. For microscopy, samples were also housed in the same Linkam stage, but with 11 µm glass spacer beads (Whitehouse Scientific) and borosilicate glass slides (VWR).

X-ray diffraction data were collected using a Bruker D8 Venture geometry diffractometer equipped with a Photon-II CPAD detector and dual (Copper and Molybdenum) ImS 3.0 microfocus sources. Samples were kept cold using an Oxford Cryosystem n-Helix low temperature device which flowed cool N_2 over the sample. Data were collected at 150 K. Samples were housed in an open 100 µm diameter capillary for powder patterns and mounted on a needle for single crystal diffraction. Single crystals of C1 were obtained using the Linkam stage used for microscopy, but with 155 µm spacer beads, in order to produce large enough single crystals. Single crystals of C2 and C3 were obtained by crystallising TPP in a large sealed flask in a domestic freezer at -19 °C. Glass slides for the Linkam stage were cleaned with the procedure: wash in acetone, isopropyl alcohol, distilled water, blow dry with

N_2 gas then oven for 30 mins at 150 °C. IR windows were cleaned in the same way but without acetone.

Triphenyl phosphite (99% Sigma-Aldrich) was filtered using 0.2 μm hydrophilic polytetrafluoroethylene filters (Millipore) to remove dust particles. The standard procedure for IR, Microscopy and XRD was to quench samples from 300 K at the maximum cooling rates of the Linkam stage (150 K min^{-1}) and cryostat (ca. 10 K min^{-1}) to the desired temperature in range 211 – 250 K.

Density functional theory calculations were performed (by a collaborator, Dr Hans Senn) by first optimising using a force field calculation on Avogadro, then Gaussian using the method/basis set M06-2X/def2-TZVP. Data were analysed using Gaussview for DFT, Mercury for XRD, ImageJ for microscopy and Opus and Igor for IR/IR imaging.

2.12.   Results

The following results section is broken down by technique rather than being in chronological order, although where possible, it will be chronological. The chapter will begin with infrared spectroscopy data, followed by infrared imaging, density functional theory calculations, optical microscopy and finally XRD.

2.12.1.   Infrared Spectroscopy

Infrared spectroscopy in the entire mid region (400 - 4000 cm^{-1}) was carried out on TPP – as only select bands had been reported thus far.[102,103] Substantial changes during the LLT in the 1150-1250 cm^{-1} region were observed, which had only briefly been reported once and glossed over.[103] Figure 60 shows a dynamic experiment where the quench temperature was T_Q = 219 K and the sample was left for several hours to transform from L1 (red) to L2 (blue). The vibrations in this region correspond to antisymmetric C-O stretches and a degree of in plane bending of the phenyl rings (From DFT calculations in Table 8). For reference, Figure 62 shows the molecular structure of TPP in the conformation found in C2 by Hédoux and co-workers, from the Cambridge Structural Database(Deposition No. 214221).[104] The two strongest peaks in the region will be referred to as peak A (~1180 cm^{-1}) and peak B (~1200cm^{-1}). The liquid 1 spectrum in this region consists of a strong peak (B) with a shoulder (A) at lower wavenumber. There is also a peak with roughly half the absorbance at 1160cm^{-1}. There are a number of isosbestic points – points which do not vary in absorbance throughout the transition – the most obvious of which is at 1170 cm^{-1} in

these data. A full assignment of all strongly absorbing bands in the range 945-4000 cm^{-1} based on existing IR tables and DFT can be found in the appendix (5.6). If indeed L2 is a liquid state with no long-range ordering, the strong, repeatable changes in this region of the IR spectrum suggest either a change in molecular conformation (conformer), local ordering or both.
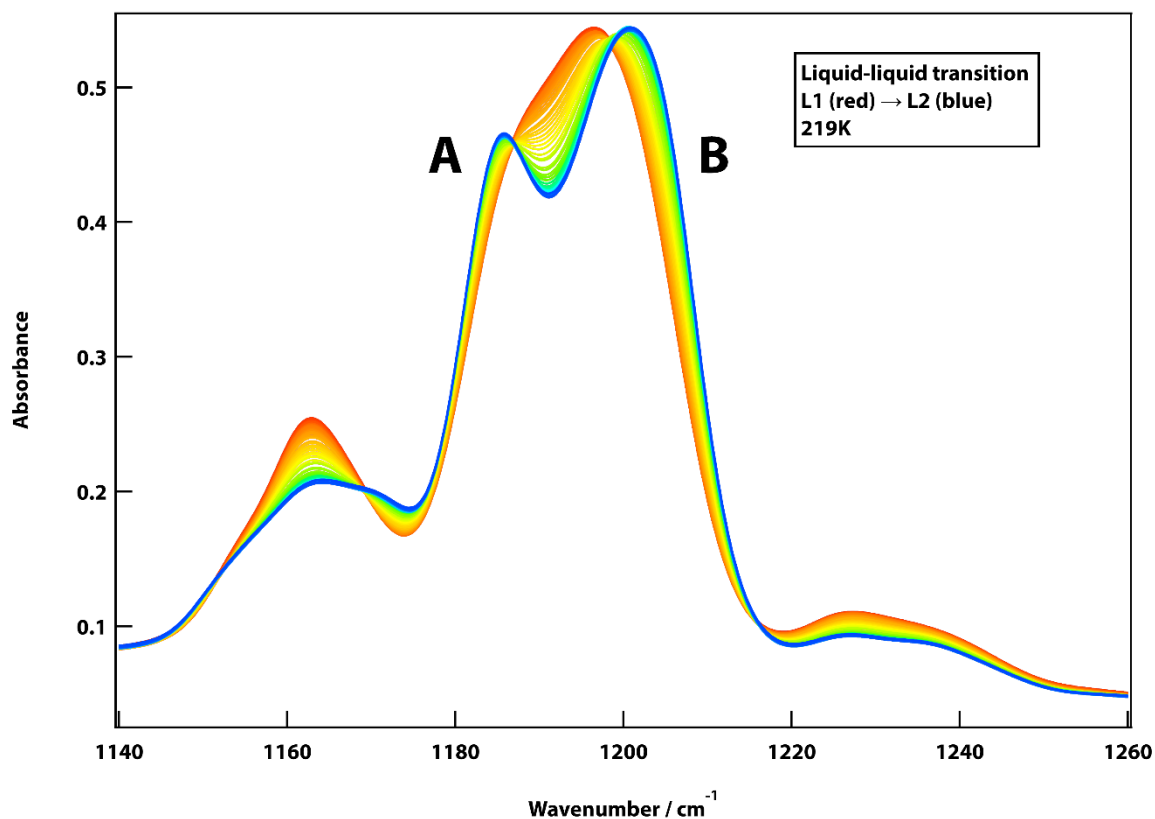
Figure 60 – The LLT at T$_Q$ = 219 K from L1 (red) to L2 (blue) over two hours. The region corresponds to combinations bands of antisymmetric C-O stretches and in plane-bending in the phenyl rings. The two strongest absorbing peaks with be referred to as peak A (~1185 cm^{-1}) and peak B (~1205 cm^{-1}), which correspond to double and triple simultaneous asymmetric C-O stretches (Mode 70 and 71 in Table 8 respectively).

The transition from L1 to crystal (which will be shown later to be C2) shows more pronounced changes than the LLT, in particular a big change in the position of peak B (Figure 61). Again, a number of isosbestic points can be seen, and appear in different locations to those in the LLT at 219 K.
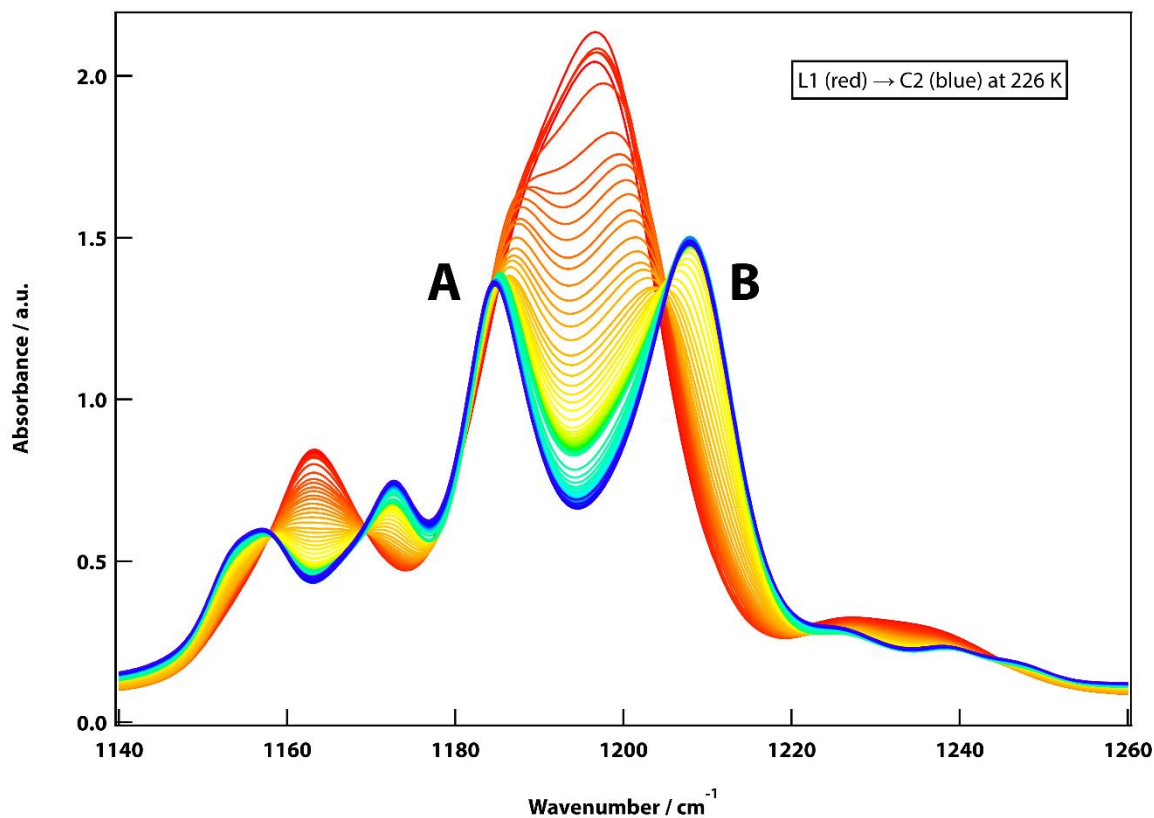
Figure 61 – Transition between liquid 1 (L1) and the crystal at $T_Q = 226$ K over two hours, which will be identified by microscopy and XRD as C2.
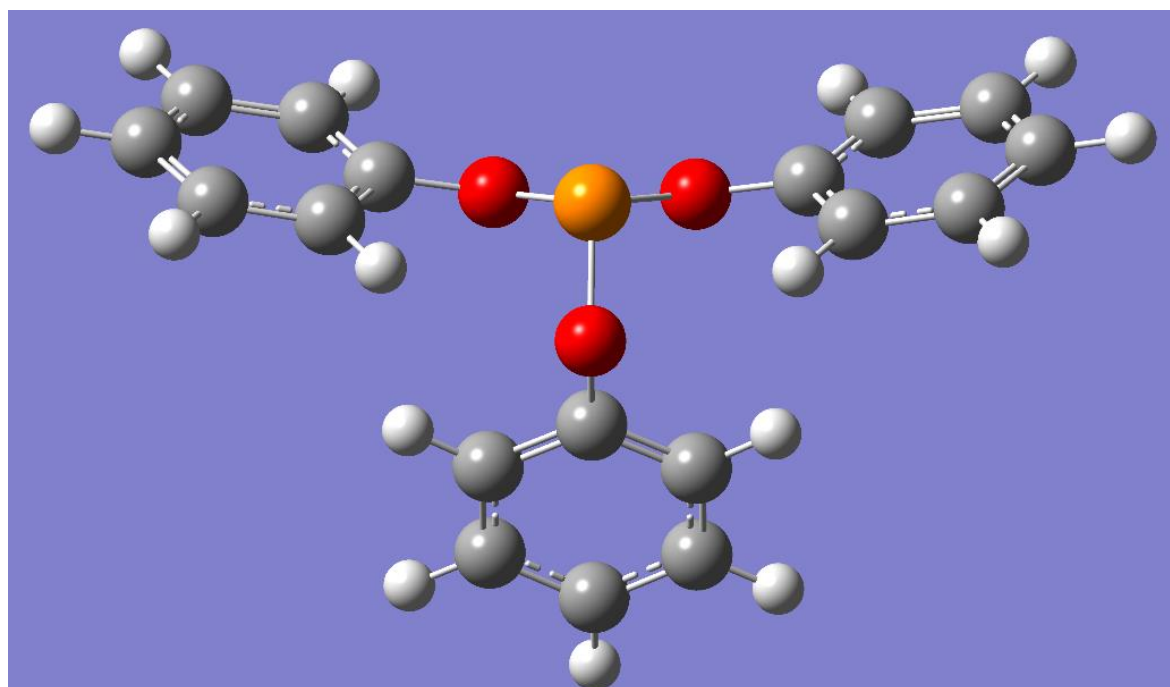
Figure 62 – The molecular structure of TPP in the conformation present in the stable crystal C2. The central phosphorous (orange) is bonded to three phenoxy rings. The molecule has six key degrees of freedom: three rotations of the phenoxy arms around the torsions of the form lp-P-O-C and three phenyl ring rotations around the P-O-C-C torsions. If the oxygens (red) point downwards with respect to the phosphorous, the phenoxy rings tend to point 'up up down (uud)' in C2. There is almost a mirror plane, so the molecule approximately belongs to the C_S point group. Carbons are coloured grey and hydrogens white.

Peak A does not show a significant shift in wavenumber during the LLT, but peak B does. The higher the quench temperature T_Q, the more significant the shift is. Figure 63 shows the spectrum of L2/C2 at various quench temperatures and L1 for comparison.

A number of different samples were used to collect the data, which have a range of sample thicknesses. The smallest spacer thicknesses which were accessible proved too thick, as the detector saturated several strong bands. As such, the TPP sample was sandwiched between CaF windows with no spacer, so sample thickness was not well controlled. The result is variability in absorbance between samples, so the data have been scaled so that peak A has a constant absorbance. There is clustering of peak B around ~1201cm^{-1} at lower T_Q and above 219 K the peak shifts to higher wavenumber.
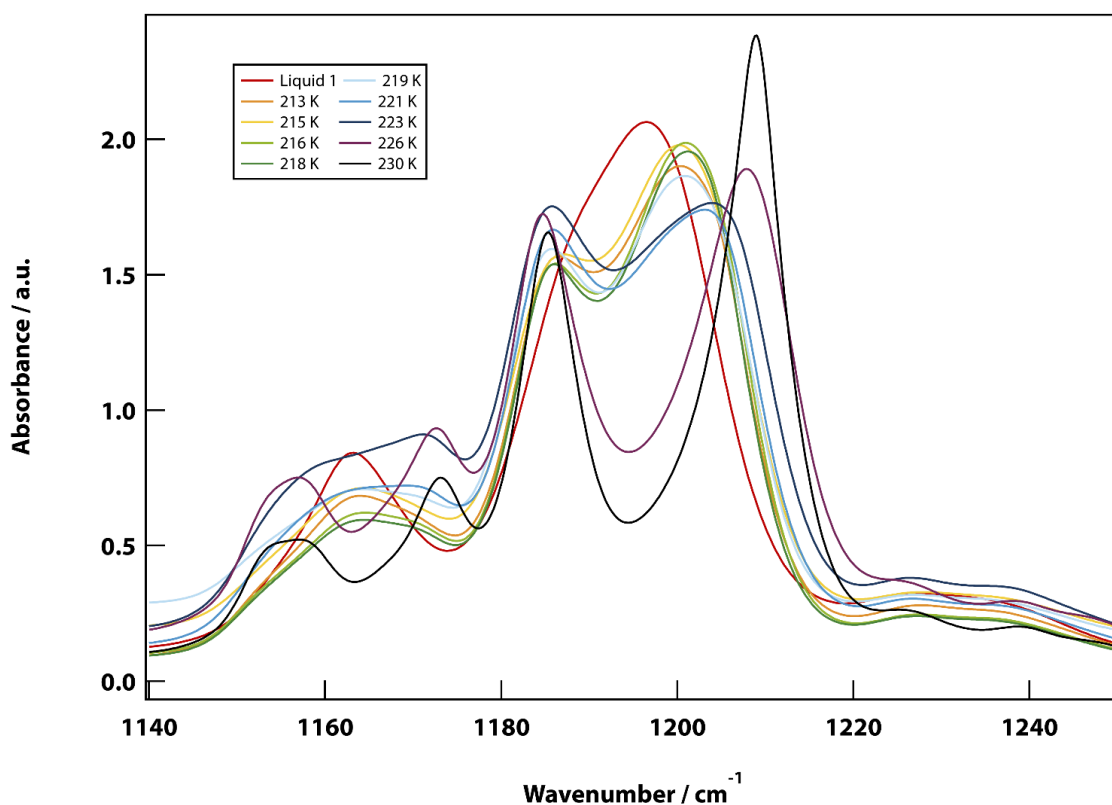
Figure 63 – L2 spectra at different quench temperatures T_Q. There is an inverse relationship between the shift of the strongest 1150-1250 cm^{-1} peak and T_Q, or rather a direct relationship between the peak position and T_Q. The absorbance values on the y-axis have been scaled to make comparison easier – samples needed to be extremely thin to prevent detector saturation, which made controlling sample thickness difficult. L1 and C2 (230 K) example spectra have been included for reference.

Figure 64 shows a plot of the final position (wavenumber) of peak B as a function of quench temperature. The peak position in C2 and in the isotropic L1 (which does

not have a quench temperature) have been included for reference. The position of peak B in L1 is constant across the range of temperatures that are involved in experiments (213 – 300 K). L1 spectra as a function of temperature are given in the appendix (5.7). Firstly, during these experiments, each sample was cold-crystallised by heating. All with T_Q < 226 K cold-crystallised, but at 226 K the spectrum did not change, indicating that it is essentially C2. There is a roughly linear relationship between the position and T_Q in the interval 220 < T_Q < 226 K, but the peak position flattens out as the temperature drops < 220 K. Overall the data follows a sigmoidal curve. One interpretation of this data would be that > 220 K there is some crystalline character to L2. Another would be there is a distinct metastable state associated with each T_Q, which could mean differences in local ordering. The latter picture agrees with the conclusions of Oguni and co-workers[92], that an increase in T_Q means an increase in average *cluster size*, increase in ordering within the cluster (not inter-cluster ordering) and a corresponding increase in glass transition temperature T_G of L2. As will be discussed later, this could also indicate the proportion of multiple conformers of TPP.
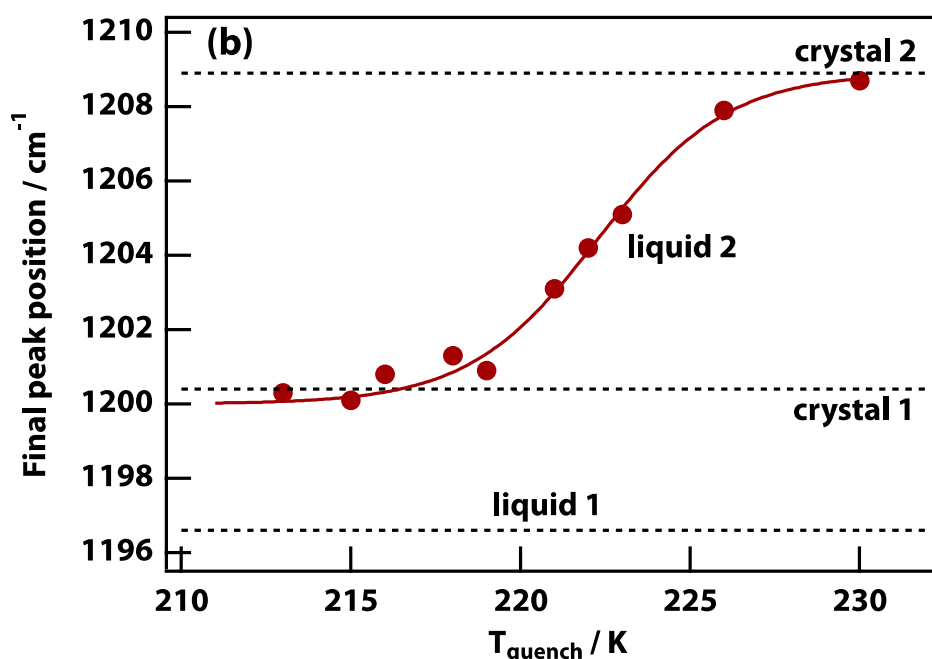
Figure 64 – The position of the strongest peak in the 1150 - 1250cm^{-1} region with respect to quench temperature T_Q. The peak position in untransformed L1 at 222 K (although it does not appreciably shift with temperature) and crystal 2 at T_Q = 230 K have been includes as reference points. The peak position decreases with decreasing temperature but levels off at T_Q < 220 K. It can be interpreted that this means there is some proportion of crystal when T_Q > 220 K as the nucleation rates of L2 and C2 become similar. When T_Q < 220 K, the L2 shift is fairly constant, and distinct from L1.

As mentioned earlier, several isosbestic points occur in the infrared spectra during the LLT from L1-L2. Since isosbestic points indicate specific transitions or reactions, the Hédoux hypothesis that L2 is simply a mixture of L1 and crystal can be tested, as the isosbestic points should match between L1-L2 and L1-crystal. Figure 65 shows the LLT occurring at $T_Q = 220$ K with the isosbestic points marked with orange lines to zero. Also shown is a transition using the same sample from L1 to what is now known to be C2, with isosbestic points marked with purple lines to zero. The isosbestic points clearly lie in different locations across the region, which refutes the hypothesis. The data support the Tanaka hypothesis that L2 is a distinct, second liquid state.
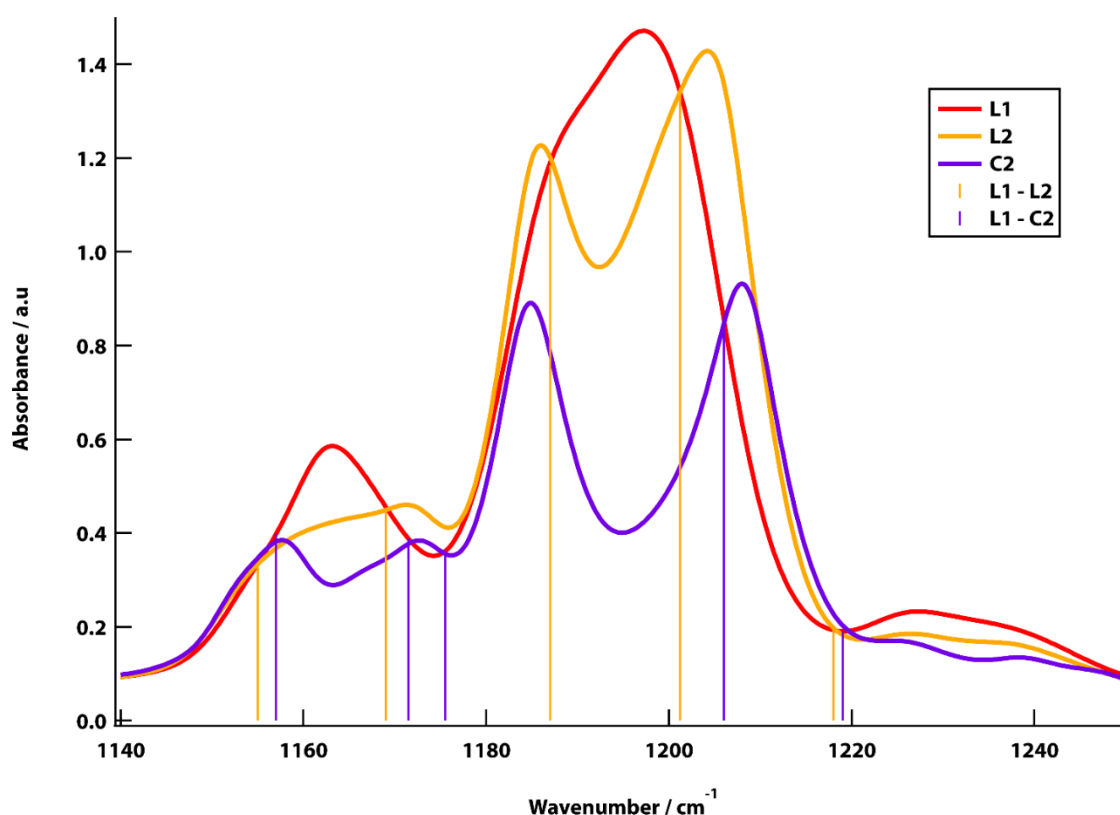
Figure 65 – Graph showing isosbestic points during two transitions: L1-L2 at $T_Q = 220$ K and L1-C2 at 230 K. Since the position of isosbestic points in wavenumber indicate a specific transition, the fact that they occur in different places indicates that there are separate transitions and L2 is a distinct state. The Hédoux hypothesis would predict that the points would stay in the same place – since the glacial phase is simply a mixture of L1 and crystal.

A full list of the dynamic spectra of the LLT in TPP occurring at different T_Q can be found in the appendix (5.4).

Motivated by the work of Drozd and co-workers[100], a different crystal polymorph was crystallised at higher temperature, which will be termed crystal 1 or C1. The authors recommended quenching to 243 K, holding for 15 minutes then heating to 270 K.

However, when crystallised between glass slides at least, C1 can be readily crystallised at a wide range of temperatures with no specific holding time. After quenching, samples for experiments were held for ten minutes for consistency. The infrared spectrum of C1 is different to that of C2 in the region 1150-1250 cm^{-1}, as can be seen in Figure 66. In C1 at T_Q = 250 K, peak A and B shift less than in the transition to C2, unlike when TPP is converted to C2, but a change to higher wavenumber is seen in the smaller peak at 1160cm^{-1}. Peak B shifts to 1200.5 cm^{-1}, which is similar to the shifts seen in L2 below T_{SD}. It is highly likely that this shift is due to a degree of C2 contamination. A full examination of the sample at T_Q = 250 K revealed that although C1 makes up the majority of the crystals, there is still a significant proportion of C2. However, it also cannot be ruled out completely that peak B in pure C1 would shift. In the conversion to C2, the peak at 1160cm^{-1} splits in to three peaks, one at higher wavenumber like in C1, and two overlapping peaks at lower wavenumber.
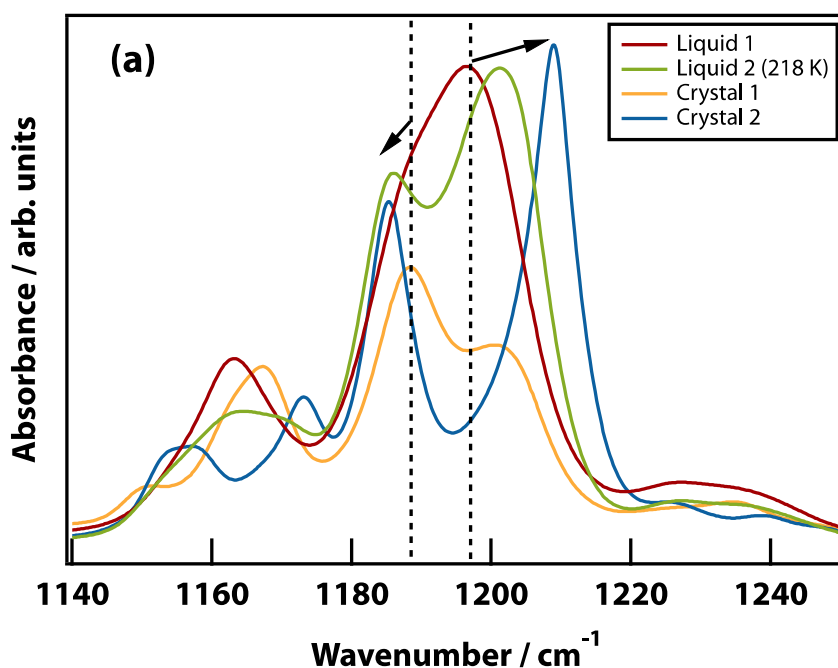
Figure 66 – A comparison between the four classes of states: Liquid 1, Crystal 1, Liquid 2 and Crystal 2. As stated previously the liquid 2 spectrum changes depending on quench temperature T_Q, so 218 K has been chosen as an example. The strong peak at ~1200cm^{-1} shifts during the transition to L2 and shifts further as C2 forms. There is no shift during the L1-C1 transition at 250 K. There is a difference of a couple of wavenumbers which is attributed to a small degree (a few %) of contamination of C2.

The transition from L1 – C1 is shown below in Figure 67. Peak B and to some extent peak A reduce in absorbance and sharpen.
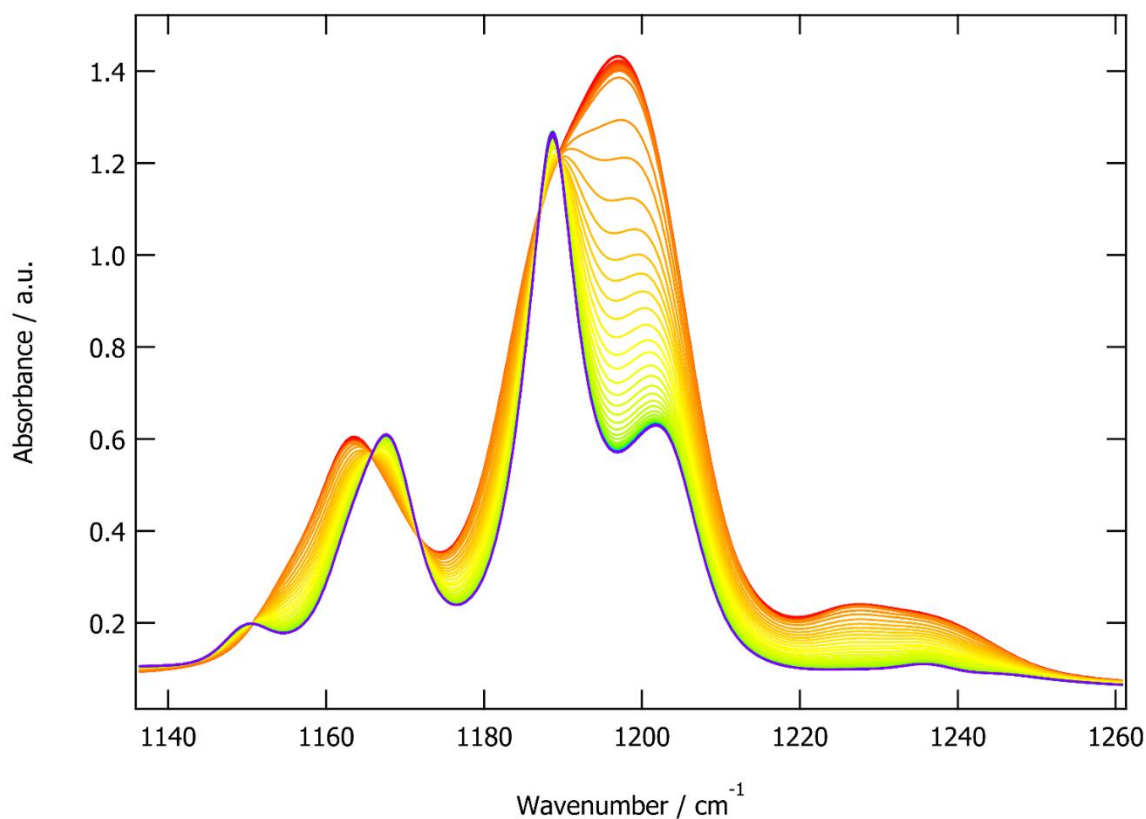
Figure 67 – The spectrum of TPP over 30 minutes at 250 K from L1-C1 (red to blue), inspired by Drozd and co-workers[100]. The shifts in the strongest peaks A and B during the conversion to L2 or C2 are not seen here, they simply drop in absorbance and sharpen to some extent. A small shift to higher wavenumber is seen for smaller 1160cm^{-1} peak. Spectra were recorded at an interval of 30 seconds.

The change in position of peak B in the LLT and L1-C2 and the lack of a shift in L1-C1, indicates that the two liquid states may act as precursors to the two crystal states. In addition, L1 is the stable liquid at high temperature and C1 nucleates preferably at higher temperature. L2 only forms < 226 K and C2 is only nucleates preferentially over C1 at lower temperatures (but above 226 K of course).

Several conclusions can be drawn from the IR data. Firstly, the change in the spectra of L2 as a function of T_Q suggests that L2 is not one phase, but a series of metastable phases at different T_Q. Dielectric relaxation data from Oguni and co-workers showed that there was a direct relationship between T_Q and LFS size[92] – it is possible this is the source of the different spectra. It is also possible that the different metastable states have different proportions of crystal, which is why as T_Q rises, L2 resembles C2 more and more. Above 219 K this may be the case, as the data in Figure 64 show, but not at lower temperatures. The presence of crystal is unlikely because there are different isosbestic points for L1-L2 and L1-C2 transitions. This refutes the hypothesis that L2 is simply L1 and nanocrystals and indicates that L2 is indeed a second liquid state. The split peaks A and B of L2 and

C2 and the lack of splitting in L1 and C1 indicate that the two liquid phases may be precursors of the two crystals.

2.12.2. Infrared Imaging

Infrared imaging at beamline B22 at Diamond Light Source was carried out for $T_Q >$ 220 K, which meant that large droplets could form in a reasonable time and could be imaged. In the first instance, point spectra were taken inside and outside of droplets, with a point on the sample which contained no TPP (but still through the ZnSe windows) being used as a background. The point spectra inside and outside of the droplet matched the bulk measurements of L2 and L1 respectively (shown in Figure 68). A shift of peak B can be seen, and no significant shift in peak A. The isosbestic point at 1170 cm^{-1} is also consistent with the bulk IR measurements. These data confirm that above the spinodal decomposition temperature, the L2 phase nucleates droplets in a sea of untransformed L1 – there in no change in the spectrum of the sea of L1 as the transition progresses.
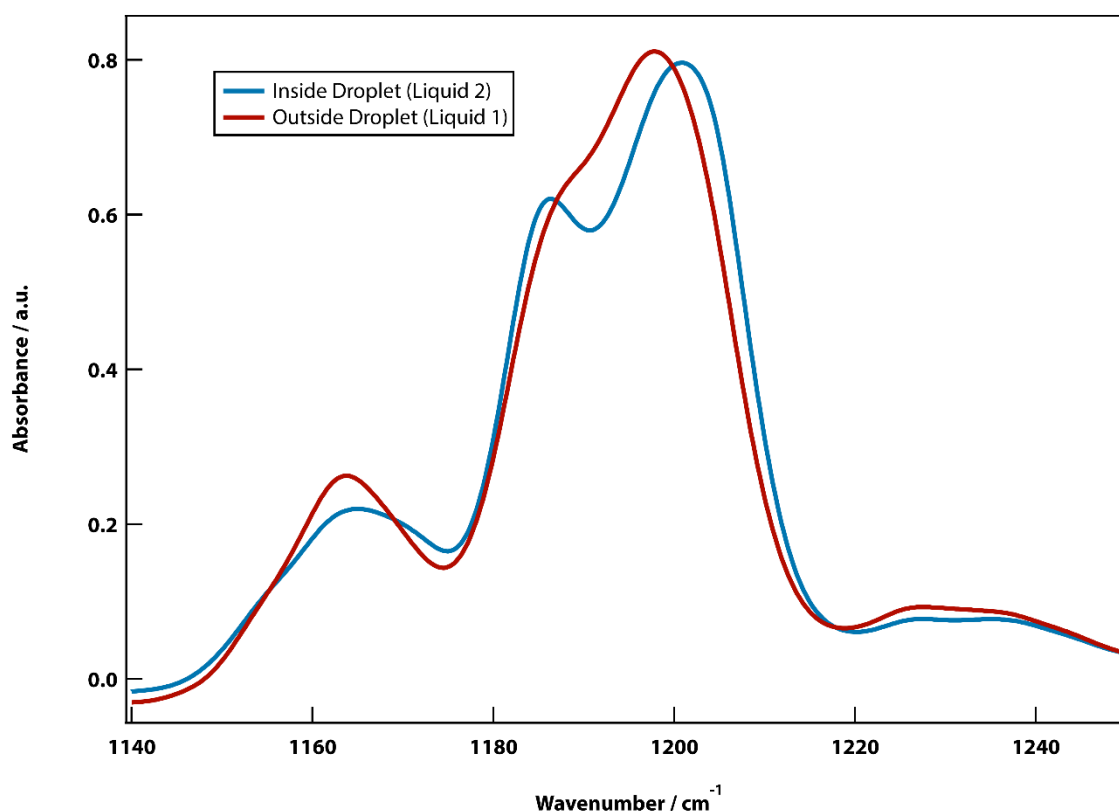
Figure 68 – Infrared spectra of the 1100-1250 cm^{-1} region inside and outside of a droplet of L2 at $T_Q = 224$ K. The two spectra in/out of the droplet match the before/after spectra from the bulk measurements.

Infrared images were typically 11x11 arrays with a slit size of 20x20 μm and a spacing of 10 μm which allowed a degree of overlapping. With slit sizes less than this, the wavelength of the IR light would be of a similar size (e.g. ν = 1200 cm^{-1}

corresponds to λ = 8.3 μm), which causes significant attenuation of the beam which would mandate longer acquisition times and this was not practical.
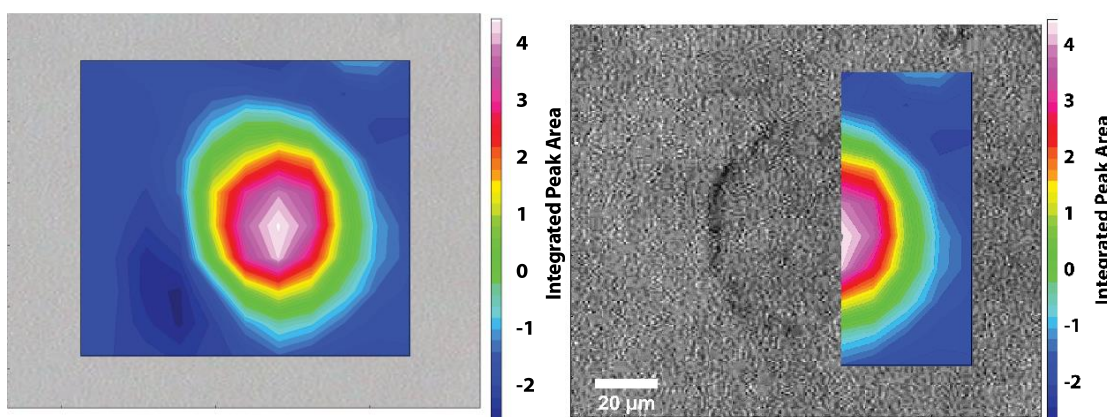
Figure 69 – Bright field microscopy image of a droplet of L2 at T_Q = 224 K with an infrared image overlay. The colour scale corresponds to the integral of the peak area of the interval 1200-1215 cm^{-1}. As the peak in L2 is higher in wavenumber than L1, a high value indicates L2. (left) shows the full 11x11 IR image, which has been smoothed with contours. (right) shows a contrast enhanced bright field image of the droplet, with half the IR image overlaid.

2.12.3.   Density Functional Theory

DFT calculations which were carried out by a collaborator Dr Hans Senn, were run in two sessions. The first session involved *ab initio* calculations, i.e. with no starting molecular conformation. The second used the C1, C2 and C3 conformers which were calculated using the XRD data from ourselves, Hédoux(CSD Refcode PUXLUP01)[105] and Golovanov(CSD Refcode PUXLUP04)[87] respectively. Structures were pre-optimised using a Merck molecular force field calculation (MMFF94s) on Avogadro. They were then were optimised with Gaussian using the M06-2X hybrid functional and def2-TZVP basis set. The calculations do not take packing into account, so are effectively in the gas phase at 0 K.

The ab initio calculation minimised three conformers, which have been termed up up up (uuu), up up down 1 (uud1) and up up down 2 (uud2). The up and down descriptors correspond to the lp-P-O-C torsion angle, where angles between -90 < $\theta_{lp-P-O-C}$ < 90 ° are up and 90 < $\theta_{lp-P-O-C}$ < 270 ° are down. Lp is an abbreviation for lone-pair (of electrons). To illustrate, Figure 70 shows typical uuu and uud conformers where one phenoxy ring has been flipped from an up to down position. The structural co-ordinates can be found in the appendix (Table 9,Table 10 and Table 11).

The predicted IR spectrum from the Uuu conformer shows a peak with a shoulder which looks remarkably similar to peak A and B in L1, factoring in the 0.946 scaling factor which is specific to the functional and basis set used. Both uud conformers show a splitting of peak A and B, which is reminiscent of L2. There is a lack of the fairly strong band at 1160 cm^{-1}, but there are some weak bands at higher wavenumber, like in L1/L2. The two uud conformers show different degrees of peak splitting, so in principle L1 and L2 could different forms of uud, but this is less likely. These predicted spectra suggest that there may be a change in conformation associated with the LLT, which is largely a rotation in the lp-P-O-C torsion from an uuu configuration to uud.
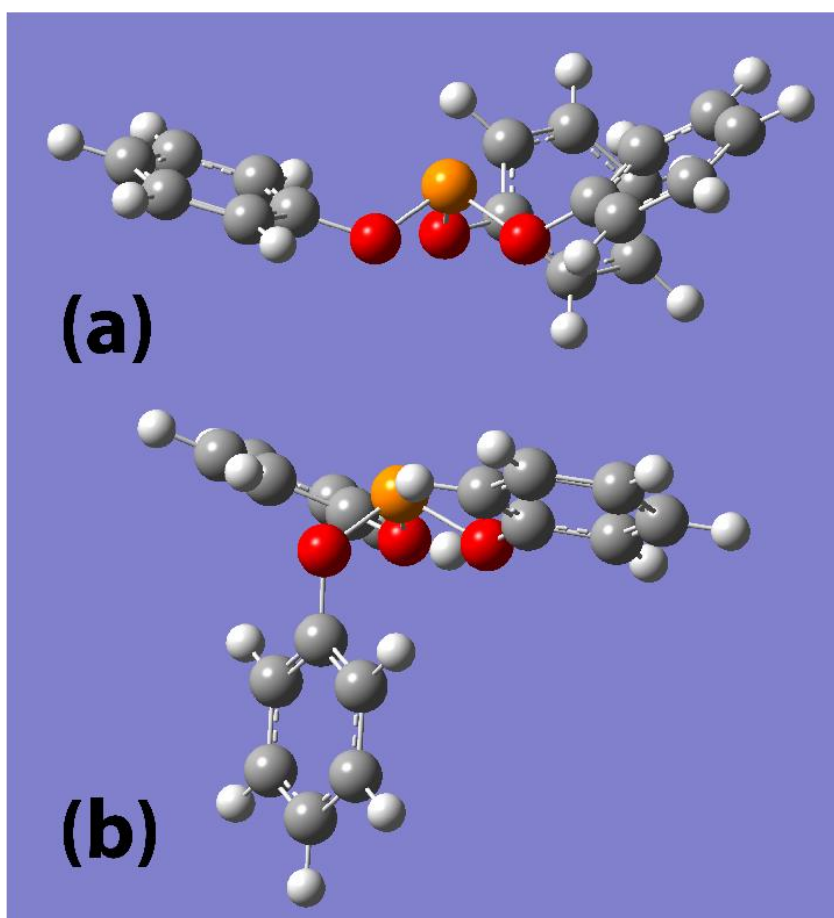
Figure 70 – TPP molecules in typical (a) up up up (uuu) and (b) up up down (uud) conformation categories. 'Up' is where the lp-P-O-C torsion is between 270 and 90 ° and 'down' is between 90 and 270 °.
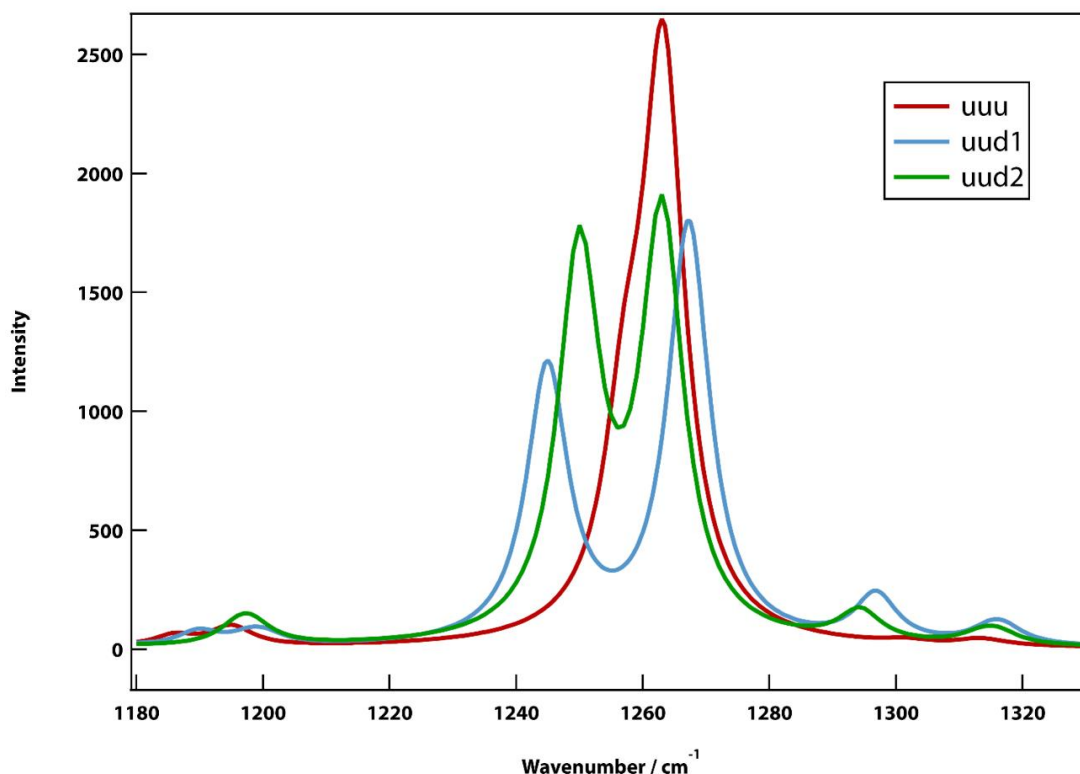
Figure 71 – The predicted IR spectrum of the three conformers initially predicted by DFT. 'uuu' (red) shows a peak and shoulder like L1 (the peak and shoulder are reversed in terms of wavenumber), and both 'uud1' and 'uud2' like L2, shows a splitting of the two strong peaks but to different extents. Neither show the fairly strong band(s) at ~1160 cm^{-1}, although there are some weak peaks in uud1 and uud2 at higher wavenumber, like L1 and L2. The peak similarity to the L1/L2 in these spectra suggests that there is a conformational change in TPP from L1 to L2. The change is likely uuu to one of the uud conformers.

As part of the second run of DFT, the three conformations which were observed from single crystal x-ray diffraction (see 2.12.5) were used as starting points. All three of the conformations from XRD were of the uud family, and changed very little upon optimisation with DFT. The IR spectra from normal mode calculations are shown in Figure 72, along with an uuu conformer. All three show substantial splitting of the two main peaks. C2 shows peak B to be stronger than peak A, just like in experimental L2 and C2 spectra. The uuu conformer again shows peak A & B to be overlapping, just like in the first round of calculations and L1. This supports the hypothesis that L1 has a high proportion of a conformer with an 'up up up' type geometry.

The peak splitting differs between the C1 and C2 spectra – they are approximately 23 and 18 wavenumbers respectively. This is similar to the lesser peak splitting in the experimental IR spectrum of C1 relative to C2, which can be seen in Figure 66.
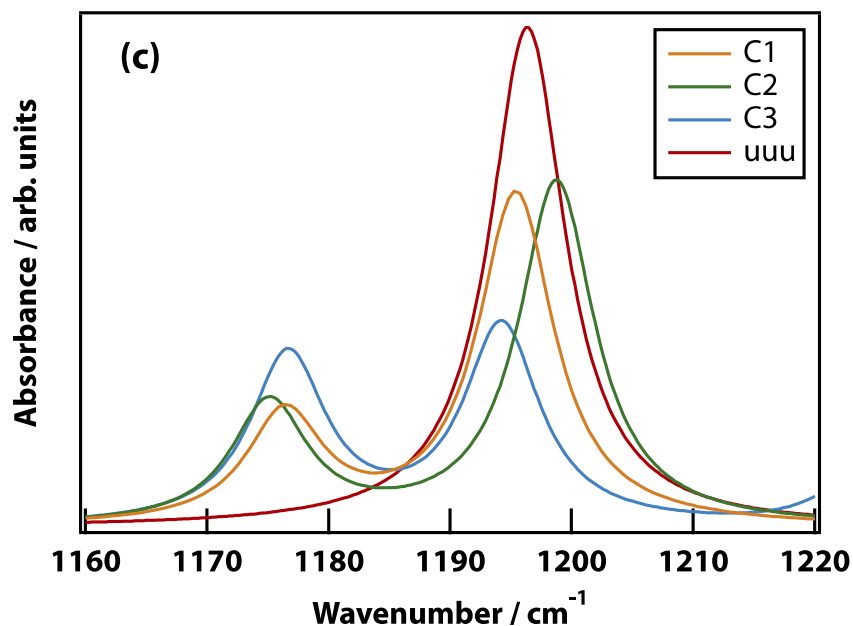
Figure 72 – Predicted IR spectra from DFT calculations. The data have been scaled in terms of wavenumber by a method/basis specific factor of 0.946. The Mon (C3) and Hex (C2) spectra used the conformers predicted by using XRD data from the CSD for the monoclinic and rhombohedral (hexagonal) polymorphs respectively. The uuu2 spectrum (mislabelled as uuu here), like the uuu spectrum in Figure 71, features two strong, overlapping peaks which are reminiscent of the L1 spectrum.

Table 5 is a summary of all the TPP conformations which were minimised during DFT. The uud conformations have similar free energies (within 3.5 kJ mol^{-1}) and are consistently lower than the two uuu conformations (7.8 and 9 kJ mol^{-1}). Notably, conformer 7, which almost belongs to the C3 point group (has a threefold rotational symmetry), is 8 kJ mol^{-1} higher than the minimum and has been considered in a previous DFT study of the LLT in TPP[99].

Conformer No.	Conformation	ΔE/ kJ mol^{-1}	ΔG$_{Corr}$ / kJ mol^{-1}(*)	|μ| / D
1 (C2)	uud	0.0	0.0	0.395
2 (C3)	uud	1.5	0.9	1.482
3	uud	1.4	1.3	1.137
4	uud	1.7	1.6	1.137
5 (C1)	uud	3.0	3.0	0.440
6	uud	3.8	3.5	1.057
7 (Run 1)	uuu	8.7	7.8	1.402
8	uuu	10.0	9.0	1.671
(*) ΔG$_{Corr}$ is calculated for T = 298.15 K and P = 101.325 by scaling by 0.971				

Table 5 – A summary of the conformations of TPP generated after two runs of DFT optimisations. Relative electronic energies (ΔE), Gibbs free energies (ΔG) and dipole moments (\|μ\|) have been calculated. Packing is not taken into account so the results are equivalent to the gas phase.

The calculated IR spectra of the three conformers which were generated by Babkov and co-workers DFT calculations[103] resemble the uuu and uuu2 conformers from DFT in the 1150-1250 cm^{-1} region of the mid-IR. They have overlapping (or single) peaks which suggests that their undefined P-O torsion angles were between -90° and 90° like the uuu conformers.

The DFT data presented in this work indicate that L1 is composed in a large part of some form of uuu conformer, and L2 a form of uud. Therefore, the LLT is at least in some part, associated with an inversion of a phenoxy arm, rotating around one of the lp-P-O-C torsion angles. Additionally, the lesser splitting of the main peaks in the C1 derived conformer relative to the C2 derived conformer agrees with the IR data which is laid out in 2.12.1.

2.12.4.   Polarisation Microscopy

3.4.4.1 Polyamorphs

Polarisation microscopy was carried out to observe the LLT at different T_Q and compare L2 droplets to the different crystal polymorphs to gain insight in their crystalline character. In the nucleation and growth (NG) regime, the LLT is visible using PC, polarisation and to a lesser extent normal BF microscopy (Figure 73). It is easiest to visualise the LLT using the former two, as better contrast is achieved between the nucleating droplets of L2 and the untransformed L1. PC gives amplitude contrast between the two phases in smaller droplets but due to shade off effect, only interfaces are enhanced in larger droplets. Polarisation microscopy, or rather crossed polarisers (CP), can reveal whether a sample possesses optical activity or birefringence. Optically active materials like quartz (which can be left or right handed) can rotate the angle of incident linearly polarised light such that a there is a perpendicular component which can pass through the second polariser (analyser). Birefringent materials like calcite on the other hand, possess different refractive indices depending on polarisation angle of the incident light. This leads to the phenomenon of *double refraction* where different polarisations of the incident light split in to two beams and refract at different angles. Like many non-cubic crystals, TPP (which has been shown to have monoclinic and rhombohedral polymorphs) is birefringent. When, for example, a vertically (linearly) polarised beam is normal to a birefringent crystal, the *slow* axis experiences a phase delay relative to the *fast* axis. The result is elliptically polarised light where the phase delay $0 < \varphi$

$< \lambda/4$ or if the thickness of the crystal is chosen correctly, fully circularly polarised light for $\varphi = \lambda/4$.
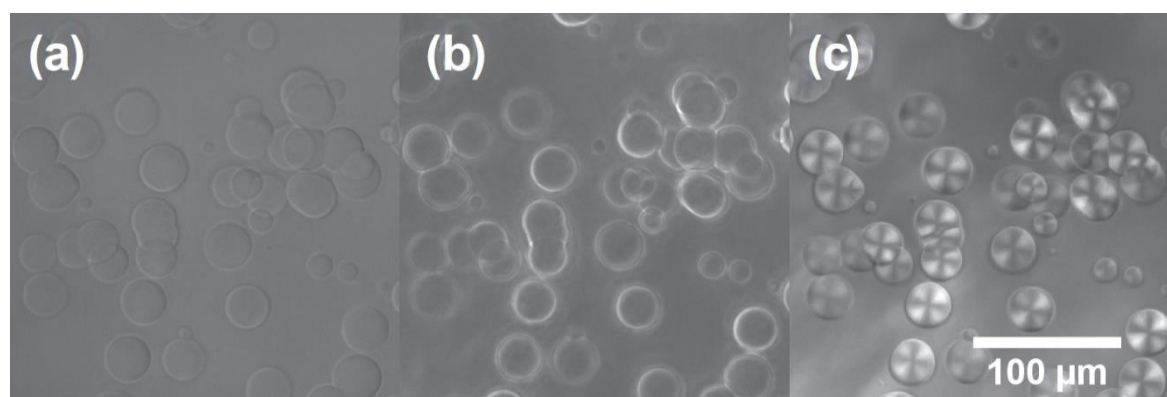
Figure 73 – TPP undergoing the LLT at $T_Q = 221$ K, viewing using an optical microscope in (a) bright field (BF), (b) phase contrast (PC) and (c) crossed polariser (CP, polarisation) modes. PC enhances droplet edges and tells us that L2 has a higher density than L1 at 221 K.

When TPP nucleates in the NG regime between 226 K > T_Q > 215.5 K, droplets grow radially (Figure 74). There is an inverse relationship between T_Q and the nucleation probability/density of droplets. In PC mode, an increase in brightness corresponds to a phase delay, which means a higher refractive index and generally speaking, density. For the lowest temperatures above T_{SD} (215 – 217 K), individual droplets can be resolved, but they are too small to see any structure within them with the highest magnification lens available (50x) as they bump in to other droplets at a maximum of ~5 µm in diameter at 217 K. At 218 K (Figure 74 (c)), faint *Maltese* crosses can be seen when CPs are used. Maltese crosses appear when birefringent samples which have radial ordering are viewed with CP.[106] The linearly polarised light that comes from the first polariser is rotated by the sample in either clockwise or anti-clockwise; this could either be more parallel with, or more perpendicular to the second polariser (analyser), generating a difference in brightness. Maltese crosses are often associated with liquid crystals, polymers and other macromolecules which align radially.[72] From 217 – 223 K the Maltese crosses are only slightly brighter than their surroundings, but this begins to change at higher T_Q. In Figure 74(j) for example at 224 K, the droplet appears rougher than at low T_Q, and the cross is brighter than the background. By 226 K the droplet is much brighter than the background, but is disordered, which suggests multiple nucleation sites, and probably crystal content. Above 226 K, droplets (which should now be called spherulites) are fully crystalline based on IR data which is illustrated in Figure 65. They have bright, clean Maltese crosses as shown in Figure 76 and grow with needle-like crystals which are larger at higher temperatures.
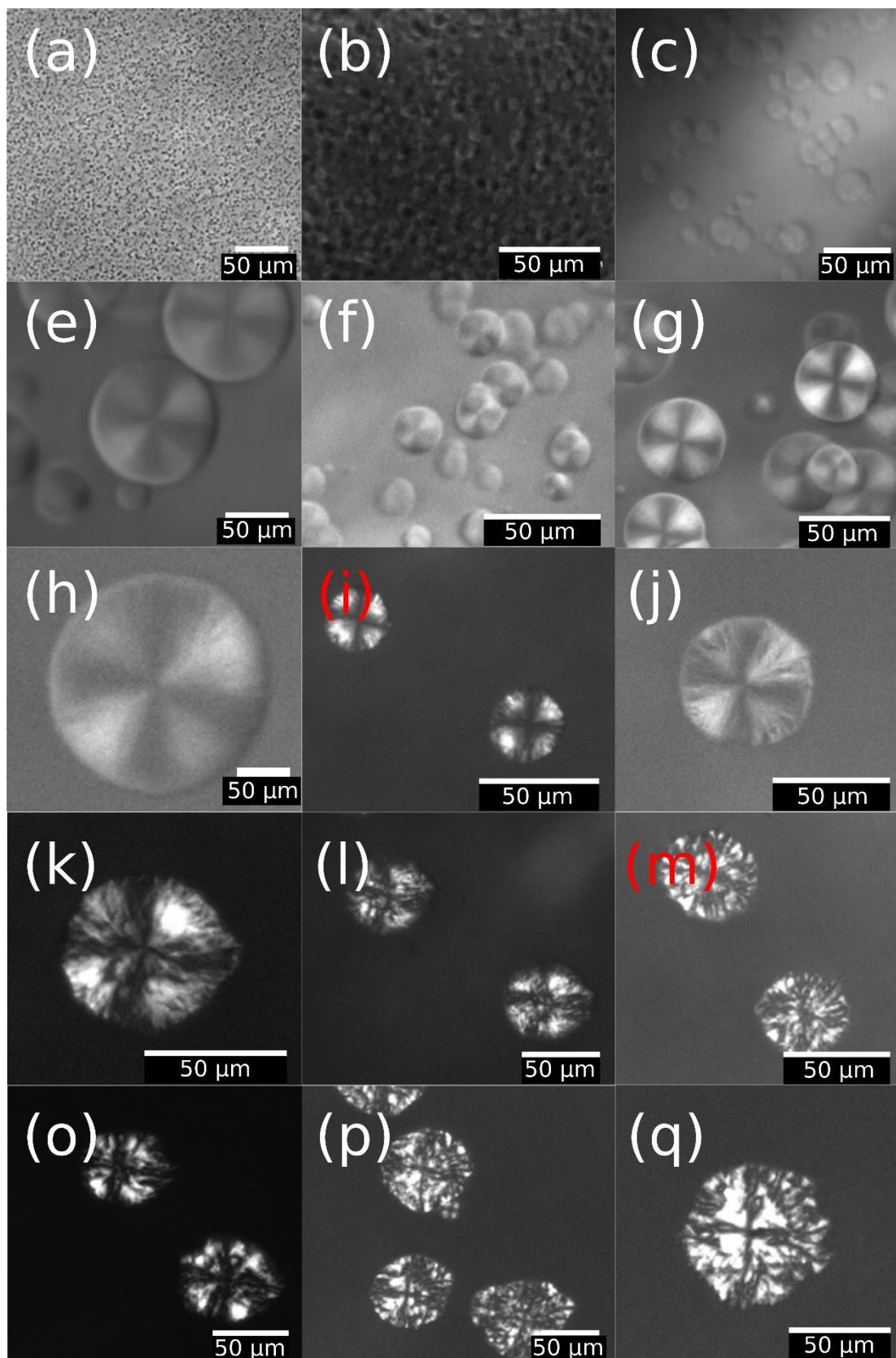
Figure 74 – Polarisation microscopy images of L2 TPP at T_Q = (a) 215 (b) 217 (c) 218 (d) 219 (e) 220 (f) 221 (g) 222 (h) 223 (i) 224 (j) 224.7 (k) 224.9 (l) 225 (m) 225.5 (n) 225.8 (o) 226 K. The nucleation probability and the density of L2 droplets varies inversely with temperature, as is predicted by Gibbs theory. The images here agree with previous assertions that the LLT proceeds by spinodal decomposition below ~215.5 K. Image (a) at 215 K shows very small nuclei which grow, so T_{SD} may be lower, but this cannot be said with confidence due to potential confinement effects. Some lettering is coloured for easy reading.

The long-range ordering, or crystallinity, of droplets/spherulites at different T_Q is plotted in Figure 75, and was calculated using the average brightness of the Maltese crosses, with the brightness of the background of each image and a crystal at 273 K as references. With the exception of an outlier at 223 K, the crystallinity remains < 1% of the maximum when T_Q < 224 K. At 226 K there is a large jump to > 80 % which indicates it now crystalline. The polarisation microscopy measure of crystallinity corroborates the figure of T_Q ≥ 226 K from IR, where TPP is crystalline.
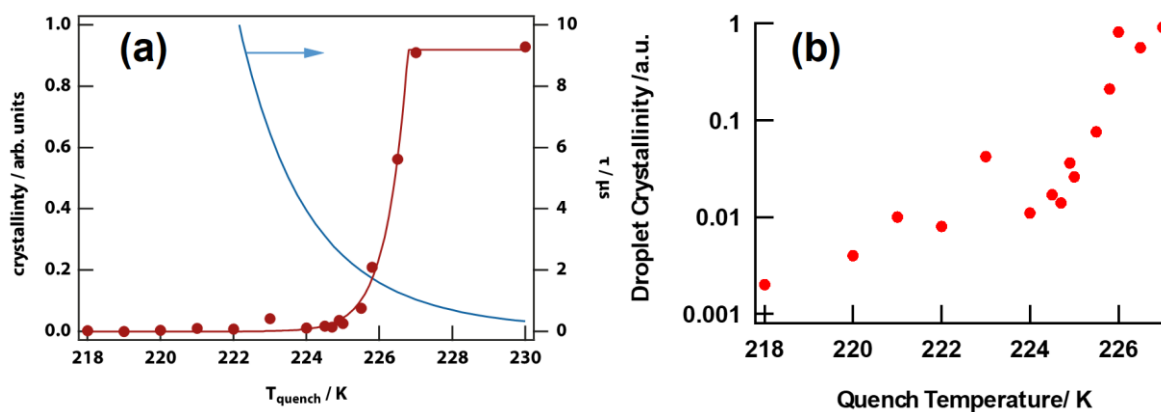
Figure 75 – Droplet Crystallinity as a function of quench temperature T_Q on a (a) linear scale and (b) log scale. L2 droplets show vague Maltese crosses, indicating weak long-range radial ordering. As T_Q edges over 226 K there is a drastic increase in droplet brightness, indicating that the droplets are essentially crystalline spherulites. (a) also shows a blue line which is a fit of viscosity data[107] for TPP as a function of temperature.

3.4.4.2   Polymorphs

The C1 polymorph of TPP was crystallised first at T_Q = 243 K using the method described by Drozd and co-workers, however it was found that simply quenching to a range of temperatures from 230-250 K was all that was necessary. The C1 polymorph nucleates alongside the C2 polymorph at 243K but has a remarkably different appearance. C1 is bright under CP but does not show a strong Maltese cross like C2, indicating less ordering directed radially, but still crystallinity (Figure 76). It has a rough, multi-coloured appearance under CP and appears to incorporate impurities into the spherulite as opposed to expelling them like C2 does. The photograph illustrates that C2 grows faster than C1 at 243 K. Had they grown at the same rate, the interface between them would be a vertical line, but it curves towards C1 instead.
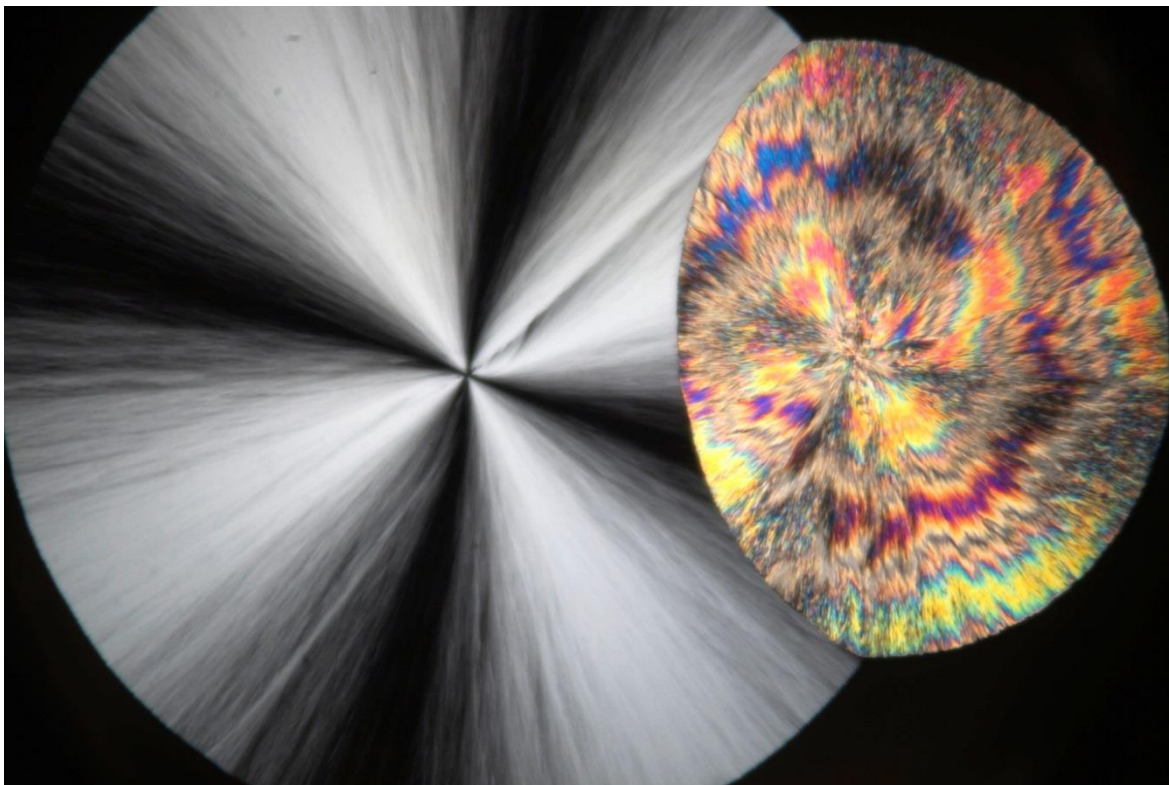
Figure 76 – Polarisation microscopy image taken using a Sony A5000 mirrorless photography camera with no lens attached. Despite growing radially like C2, C1 shows only a vague Maltese cross, suggesting little radial ordering. The colourful appearance of C1 suggests a disordered, polycrystalline state.

If the two crystal forms are heated close to their melting points at 283 K, they grow rapidly but once again differ in appearance. C2 has dense, needle-like shards whereas C1 has more plate-like crystallites.
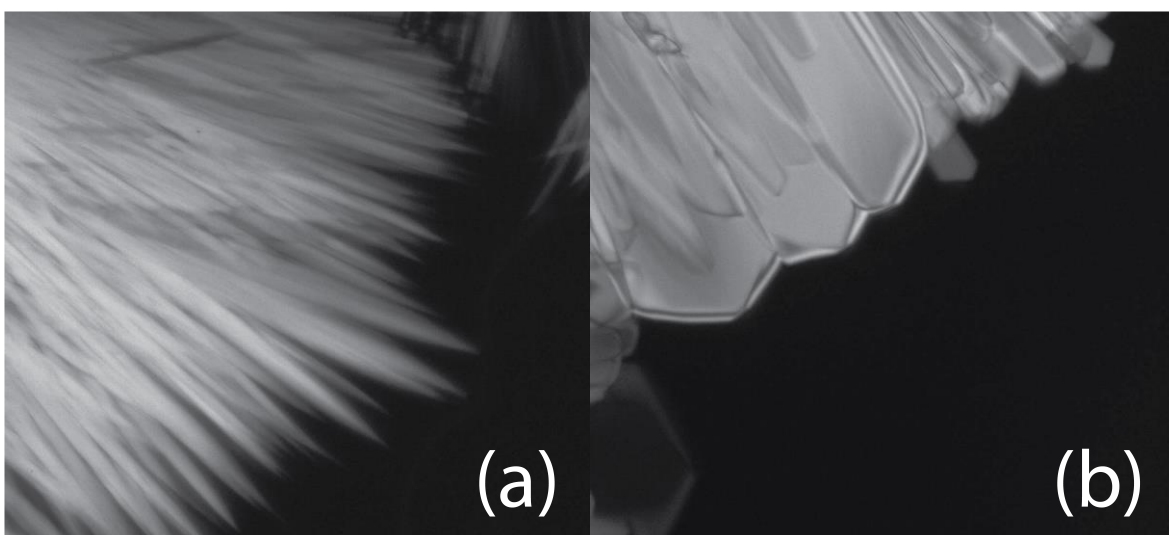
Figure 77 – Comparison between the appearance of (a) C2 and (b) C1 crystals at 283 K. C2 shows dense needle-like shards and C1 has wider, plate like crystals.

Figure 78 shows C1 (left) and C2 (right) crystals side by side during melting. Drozd reports melting points of 299.1 K and 291.6 K for C2 and C1 respectively.
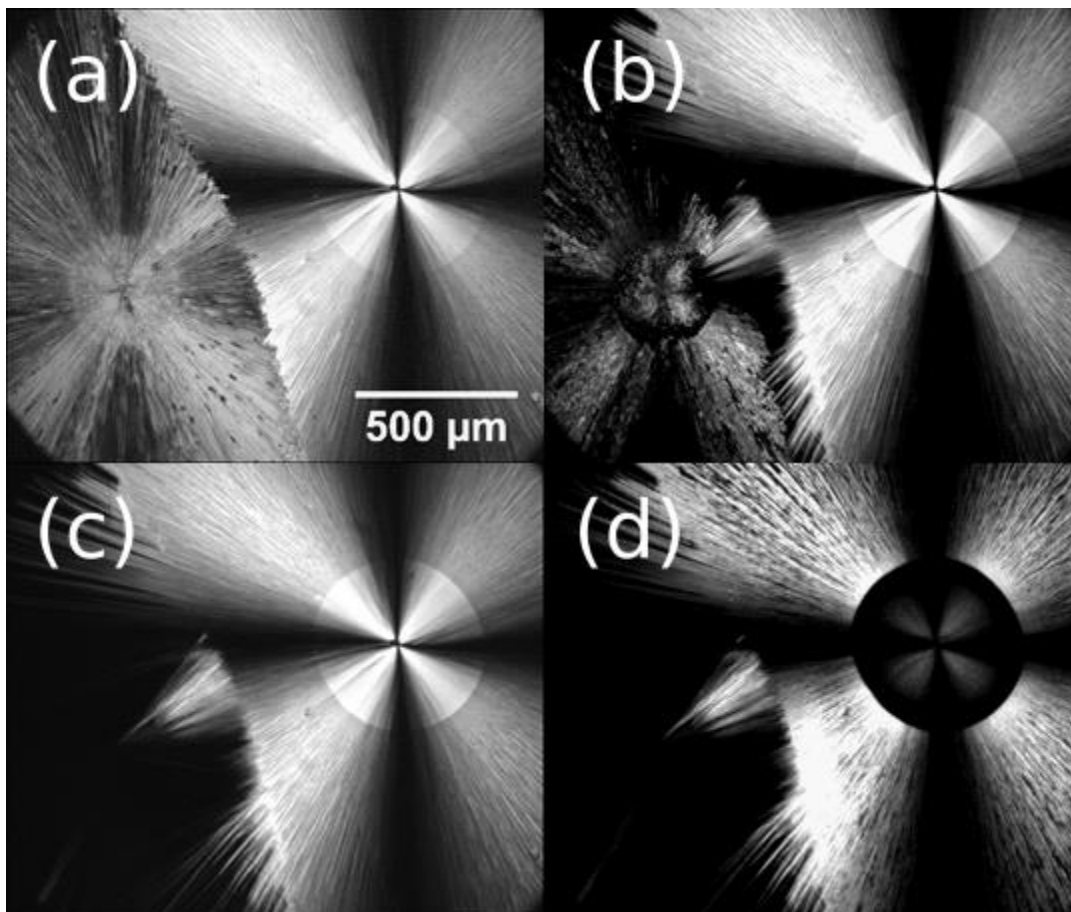
Figure 78 – Four panel image illustrating the different melting points of the two crystal polymorphs C1 (on the left of each image) and C2 (on the right-hand side of each image). The temperatures that each image was taken at were 287 (top left), 290 (top right), 293 (bottom left) and 297 K (bottom right).

Drozd made the claim that the more stable C2 polymorph nucleates preferentially below 233 K. TPP samples were crystallised between 230 and 250 K at 1 K intervals and all experiments were repeated three times. The proportion of nucleation sites within the same camera frame was noted and the data is graphed in Figure 79. The data indicate that C2 nucleates preferentially <239 K and C1 >239 K. Nucleation sites were counted within a single camera frame for consistency and to reduce human error, but this does mean that the majority of the sample is not included. Even at 250 K, there were some C2 spherulites over the whole 201 mm^2 sample but were too sparse to appear reliably in the 1.78 mm^2 camera frame.
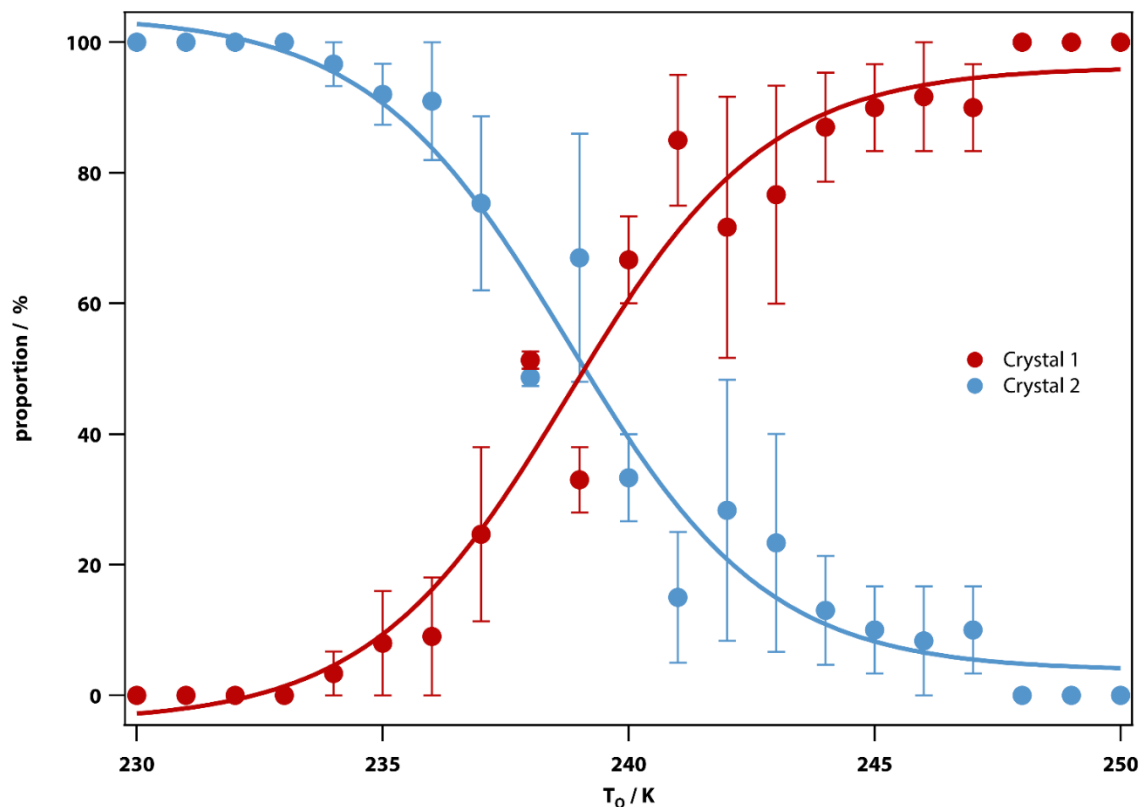
Figure 79 – The proportion of nucleation sites which gave rise to C1 and C2 crystals. The data clearly show that C1 is favourable at high temperature like L1, and C2 is favourable at low temperature like L2. The data displayed here was collected, processed and graphed by undergraduate project student Ewen McEwen, under supervision.

PC microscopy of growing TPP droplets confirms that L2 has a higher density than L1 at 221 K. Polarisation microscopy has been used to measure the long-range ordering, or crystallinity of L2 droplets. The plot as a function of T_Q shows that the Maltese crosses of the L2 droplets are mostly < 1 % of the brightness of C2 spherulites. The long-range ordering could be caused by crystals, liquid-crystal or partial ordering of LFS. The novel C1 polymorph was surprisingly easy to crystallise alongside C2, and preferentially nucleates above 239 K. It has a disordered, multi-coloured appearance and does not shows as strong as Maltese cross as C2. The C1 polymorph spherulites incorporate impurities into its structure, but C2 spherulites expel them. The C1 polymorph grows more slowly than C2 and has a lower melting point range of 289.6 - 291.3 K compared to 296.6 - 298.5 K. These figures broadly agree with existing melting point data obtained from DSC.

Figure 80 shows C2 nucleating from C1 after a C1 spherulite was grown at 250 K, then cooled to 230 K. The converse process does not occur – C1 does not nucleate from C2 spherulites at high temperatures like 250 K. Along with melting point data,

this indicates that C2 is the thermodynamically more stable polymorph not just below the 239 K crossover temperature but above it too at 250 K.
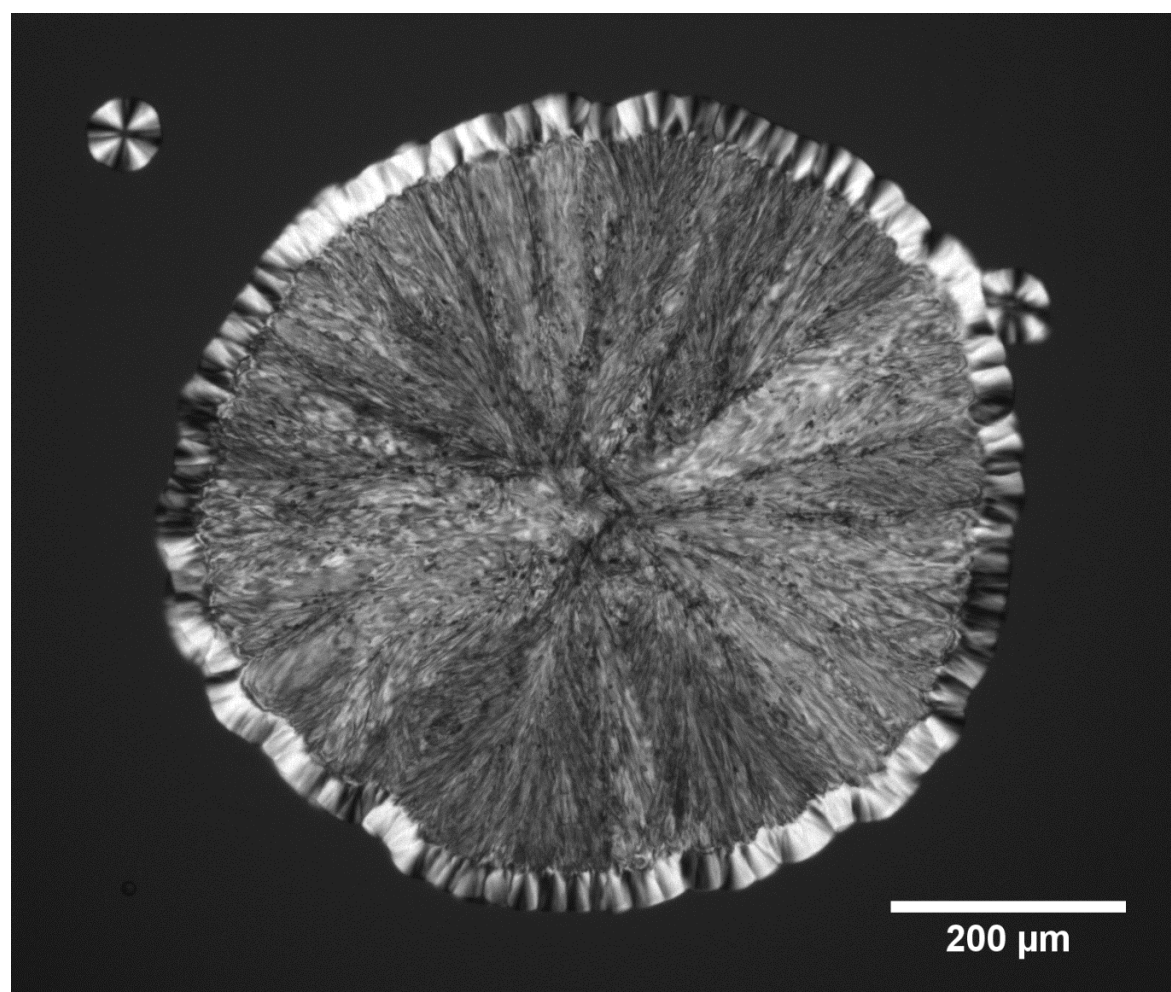
Figure 80 – The sample was quenched to 250 K and C1 spherulites are allowed grow, followed by cooling to 230 K, where C2 can be seen nucleating from the C1 growth front. The converse does not occur, i.e. C1 does not nucleate from C2.

2.12.5.   X-Ray Diffraction

Drozd and co-workers discovered a new polymorph of TPP (C1) with a different melting point, and different infrared spectrum.[100] Polarisation microscopy in Figure 76 reveals C1 to be more disordered and highly colourful under CP, with a melting point which agreed with Drozd and was distinct from the melting point of C2. The method used by Drozd to nucleate and grow C1 was unnecessarily complex and it is shown in this work that C1 could be preferentially nucleated when $T_Q > 239$ K. XRD was carried out to ascertain once and for all that C1 is a different polymorph with a unique diffraction pattern and unit cell parameters.

TPP crystals grow as spherulites and as has been documented before, growing and collecting single crystal was a difficult task which required much trial and error. In the meantime, powder patterns were taken first.

2.12.6.   Powder Diffraction

Crystals were grown in glass capillaries using the same recipes as were used in microscopy and IR spectroscopy – quenching to a high temperature for C1 and low for C2. Quenching to 253 K yielded C1, with a pattern shown in red in Figure 82 which was distinct from that of C2 and C3 (taken from Cambridge Structural Database, blue and green respectively). It was also distinct from the pattern taken by Hédoux of C2 which was erroneously assigned as monoclinic[75]. Quenching to 230 K gave C2, which matches data from the CSD.
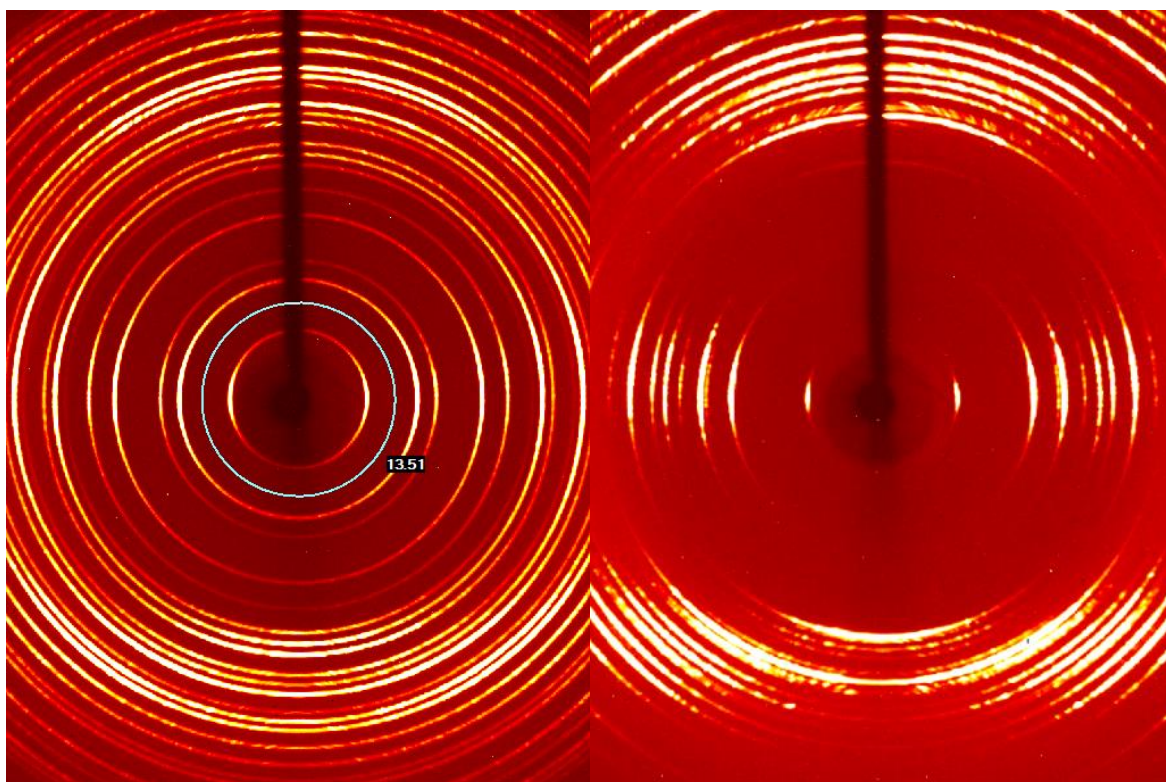
Figure 81 – Powder diffraction patterns of (left) C2 and (right) C1. The C2 pattern matches the d-spacings from the CSD, but C1 is different from all known patterns for TPP. Both shown a degree of anisotropy, but it is more pronounced in C1 - this is likely due to the growth of crystals along the capillary. C1 also shows some spotting, rather than just homogenous lines. This suggests larger crystallites than C2, which bodes well for future attempts at single crystal XRD.
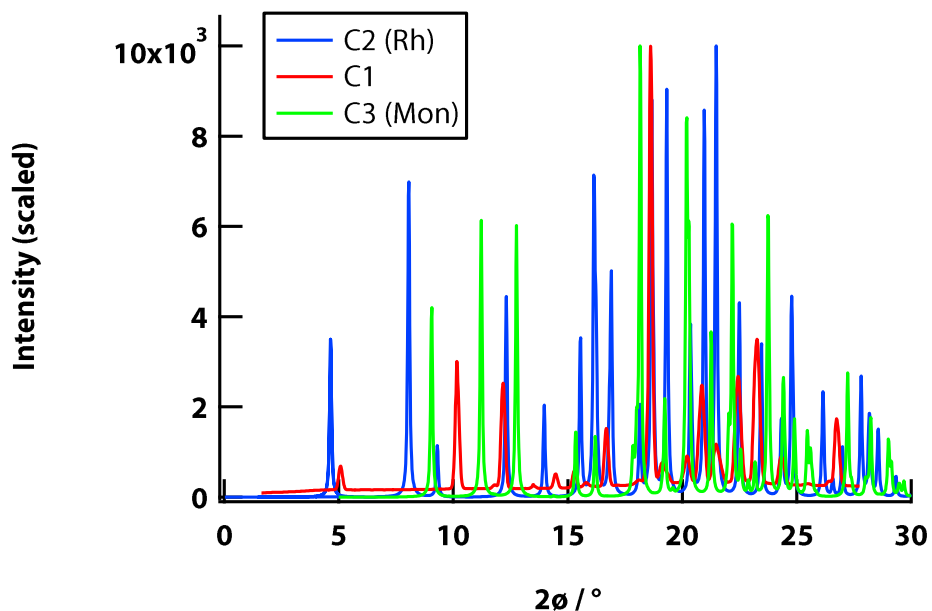
Figure 82 – Powder diffraction patterns as a function of 2θ of three distinct crystal forms: C2 (the common rhombohedral or hexagonal form which forms preferentially < 239 K), C3 (the monoclinic form, first measured by Golovanov[87]) and a hitherto unmeasured polymorph which forms preferentially >239 K).

The Bragg equation (3.4) can convert 2θ to d-spacings, which are listed in Table 6

Peak no.	2θ / °	d-spacing / Å	Intensity / a.u.
1	5.08	17.40	690
2	10.16	8.71	3000
3	12.18	7.27	2530
4	13.49	6.57	270
5	14.48	6.12	510
6	15.30	5.79	580
7	15.80	5.61	320
8	16.68	5.31	1520
9	18.62	4.77	10000
10	19.12	4.64	760
11	20.22	4.39	910
12	20.86	4.26	2480
13	21.48	4.14	1170
14	22.44	3.96	2680
15	23.26	3.82	3500
16	24.32	3.66	890
17	26.74	3.33	1230

Table 6 – 2θ values and d-spacings of the C1 polymorph.

Based on powder diffraction data (although technically a polycrystalline sample in a capillary in a single crystal diffractometer), C1 is a new polymorph of TPP which is distinct from the already characterised C2 and C3 forms.

2.12.7.   Single Crystal Diffraction

Single crystals of all three polymorphs of TPP have been successfully isolated. Single crystals of C3 have been characterised previously in the literature (after crystallisation from an ionic liquid solution), but C1 has only been characterised by powder XRD at a synchrotron. A large single crystal of C1 was successfully isolated by growing a large spherulite between glass slides with 150 µm spacer beads. The glass was then broken, the crystal extracted and characterised by single crystal XRD. At this time the structure is not available in the public domain on the CSD, but it can be requested directly from myself. C3 single crystals were found in a large flask of TPP which was simply put in a domestic freezer at -19 °C. The majority of the crystals in the flask were C2, but one happened to be C3 – it is unknown what proportion of flask was C3, or indeed how to reliably crystallise C3. The unit cell parameters are shown in Table 6 and agree with the data from the CSD in the case of C2 and C3, and the powder patterns in capillaries for C1.

	Space Group	a (Å)	b (Å)	c (Å)	α (°)	β (°)	γ (°)
C1	$P2_1/c$	17.4434(12)	5.8920(3)	14.9985(10)	90	97.462	90
C2	$R\bar{3}$ (148)	37.867(14)	37.867(14)	5.714(2)	90	90	120
C3	$P2_1/n$ (14)	11.8572(16)	9.8747(14)	13.5070(14)	90	102.52	90

Table 7 – Unit cell parameters of the C2 and C3 polymorphs of TPP, retrieved using single crystal XRD

The conformers present in the single crystal samples were all forms of uud – the main differences coming from two torsion rotations. The C3 conformer was the most distinct, showing a rotation in the torsion angle lp-P-O-C (the torsion responsible for a flip from uuu to uud). The C2 conformer practically has mirror plane symmetry, which can be seen in Figure 84. C2 and C3 have no other obvious symmetry elements. The C1 and C2 conformers differ by a rotation of the P-O-C-C torsion on one of the 'up' arms, i.e. a rotation of the phenyl ring along. If it is the case that L1 and L2 act as precursors for C1 and C2, then it can be deduced that the LLT is associated with a P-O-C-C torsion rotation. The single crystal XRD data reveals that C1 possesses a degree of π-π stacking of phenyl rings in a sandwich configuration. The ring-centroid distance is 4.028 Å and centroid to plane distance is 4.744 Å,

which are reasonable for a π-π interaction. The rings have an offset of 1.486 Å and an angle of ~22°. The packing in C2 however showed substantial π-π stacking in a t shaped configuration (rings at roughly right angles), which is depicted in Figure 86. Sherill and Sinnokrot used DFT calculations to show that aromatic rings had lower energy in the T shaped form than sandwich form when either in a dimer or packed.[108] The π-π interaction is therefore an explanation for why C2 is thermodynamically more stable than C1.

These C2 and C3 conformations were used as starting points for the second run of DFT calculations and are shown overlaid with C1 in Figure 83.
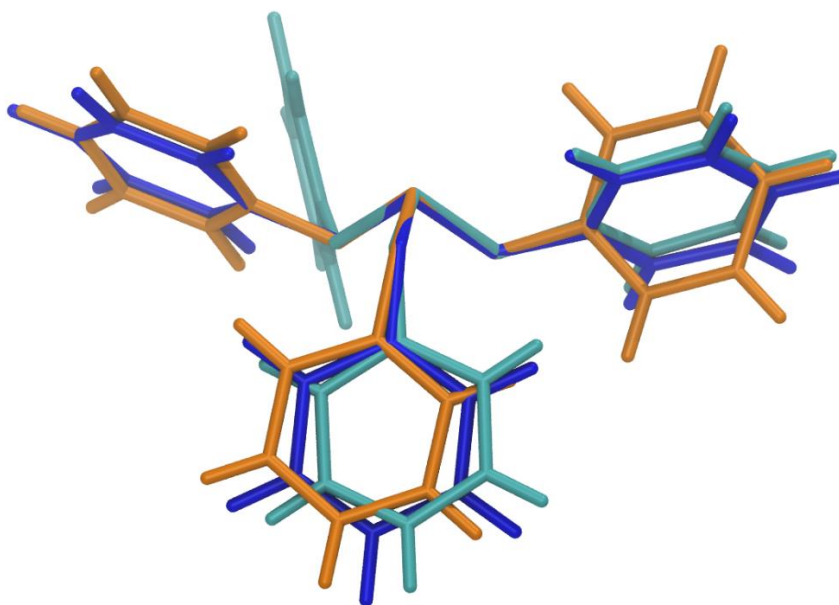
Figure 83 – The three conformations of TPP are overlaid, aligned by the PO_3 group. The chief difference between them is a change in the angle of the lp-P-O-C torsion on one of the 'up' phenoxy rings. C1 (the newly discovered polymorph) is orange, C2 (the common hexagonal polymorph) is dark blue and C3 (The ionic liquid crystallised monoclinic polymorph discovered by Golovanov) is cyan. In terms of conformation, C1 and C2 differ by a ~90° rotation of a phenyl ring along the P-O-O-C torsion. C3 differs from C2 by a smaller ~45° rotation of a different phenoxy arm around a lp-P-O-C torsion.
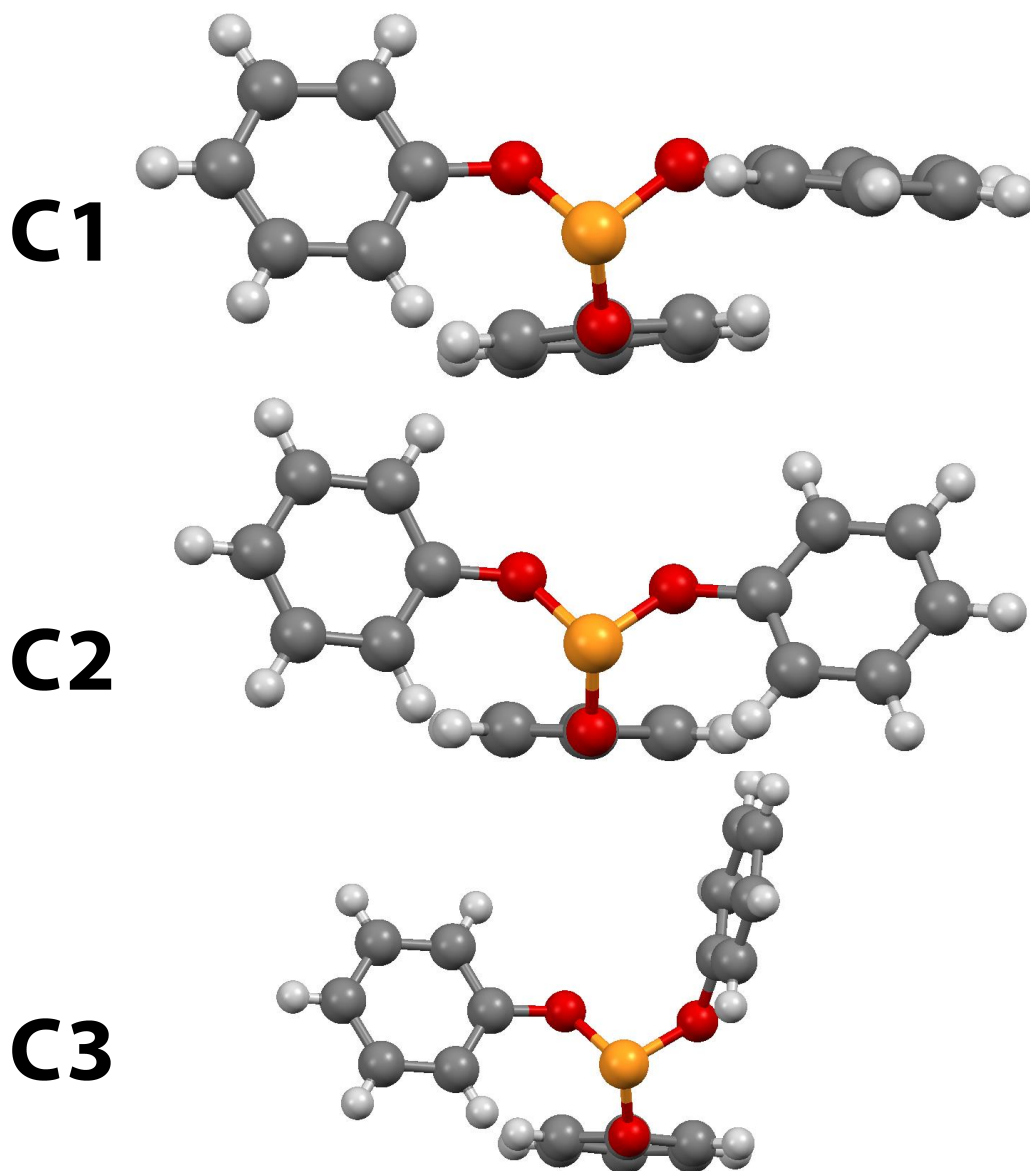
Figure 84 – Ball and stick representations of the three crystal polymorphs of TPP, viewed along the O-C bond axis of the 'down' phenoxy ring. The main difference between C1 and C2 is a rotation along the P-O-C-C torsion on one of the up rights (right hand side on this image).
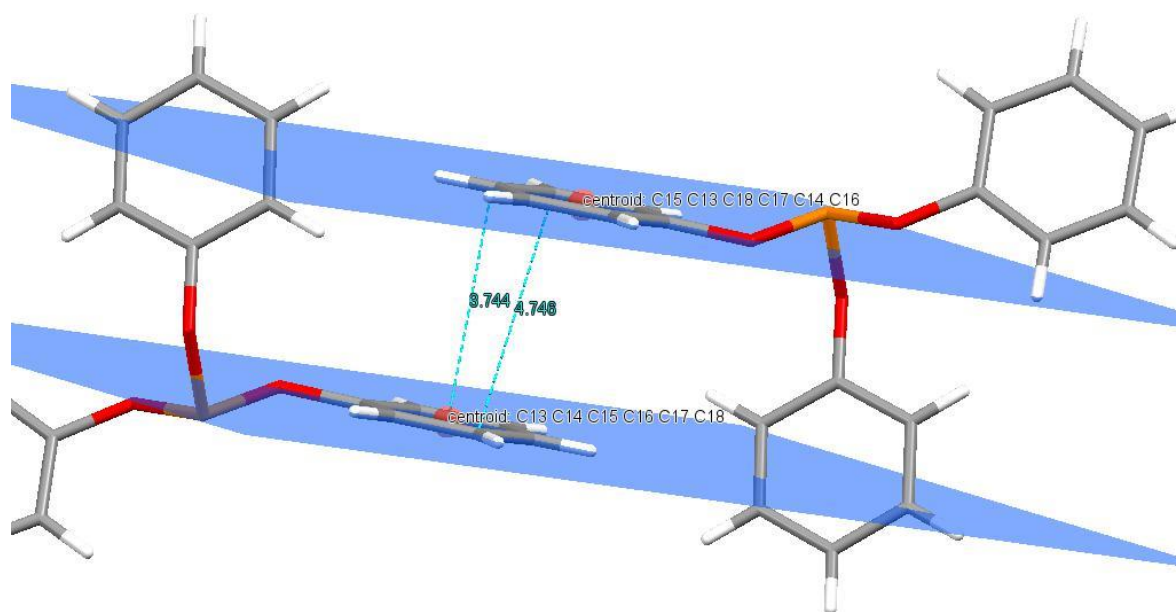
Figure 85 – Figure showing slightly offset 'sandwich' π-π stacking in crystal 1. The ring-centroid centroid distance is 4.028 Å and centroid to plane of the other ring of 3.744 Å. The ring offset is 1.486 Å and the angle is 22 °.
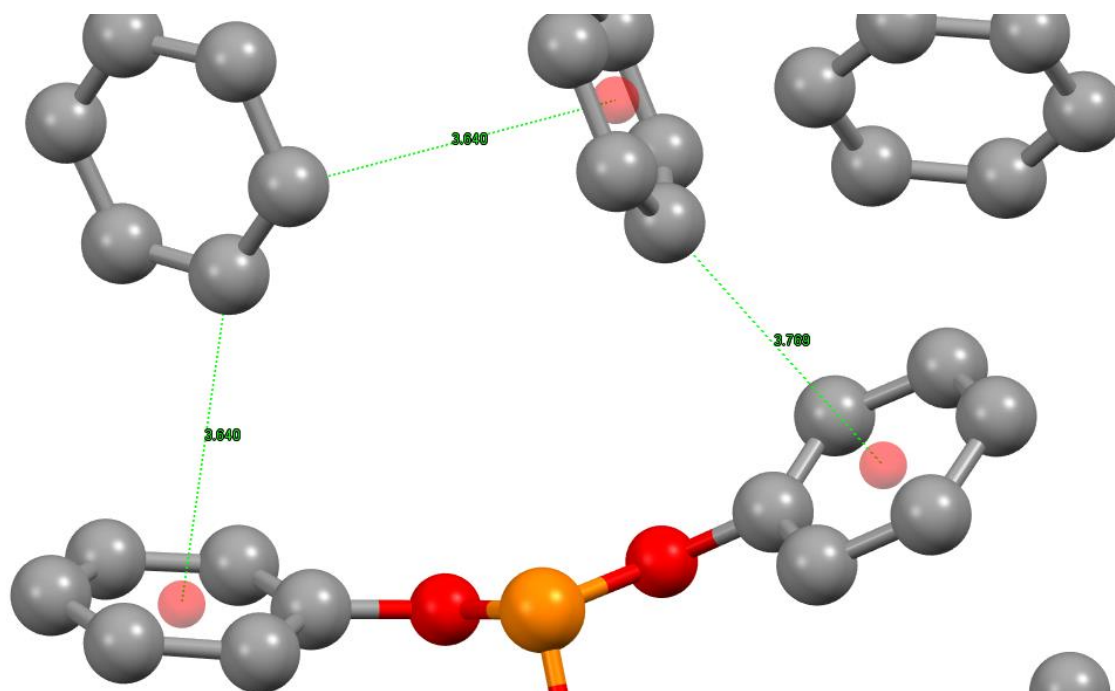
Figure 86 – T shaped π-π interaction between the aromatic rings on neighbouring molecules. The mean centroid to nearest carbon distance is 3.683 Å. Hydrogens are omitted.

Single crystals of C1, C2 and C3 have been successfully isolated for XRD and assigned unit cells and conformers which match the powder pattern for C1, existing refined powder patterns for C2 and single crystal data for C3. All three have an uud type conformation, and this is first single crystal characterisations of C1 and C2. C1 and C2 differ by a rotation of a phenyl ring along the P-O-C-C torsion and a change from parallel 'sandwich' to T-shaped π-π stacking.

2.13.   Discussion

The debate surrounding the LLT in TPP can be summarised as two competing hypotheses. Hédoux – L2 is not a second liquid state but simply a mixture of untransformed L1 and micro/nanocrystals. Tanaka – L2 is a second liquid state which is distinct from the first by local ordering, but nanocrystals form at the interfaces as droplets grow. One of the most obvious questions to ask is why do the nanocrystals not continue to grow? T_G has been shown repeatedly to be 204-205 K, so at 220 K for example, the liquid is not viscous enough to arrest crystal growth. Indeed, the droplets of L2 grow at 220 K, so it is quite a leap to suggest that the more thermodynamically stable crystal would nucleate but stop growing. Hédoux describes the glacial state as '*a heavily nucleated state composed of nanocrystals of the stable crystalline phase embedded in the matrix of non-transformed supercooled liquid*'.[105] If this picture is taken further, a heavily nucleated state in a viscous, but not glassy L1 would lead to randomly oriented grains of nano or micro scale crystals bumping in to each other, leaving only those aligned radially to grow. This leads to a spherulite, which is what can be seen in C2, where T_Q > 226 K. Spherulites show bright Maltese crosses under CP like is clear in C2, but the brightness drops drastically under 226 K by a factor of 100. The Hédoux hypothesis therefore seems highly implausible. The hypothesis favoured by Tanaka is more convincing – L2 has been described by some as a glass in the LLT regime, so it could in principle arrest the growth of crystals which arise from growth front nucleation (GFN). So the question remains: what is causing the long-range ordering which leads to the faint Maltese crosses in L2 droplets? It seems plausible that at say, T_Q = 225 K the droplets contain some crystal contamination as they are rougher and slightly brighter than for say T_Q = 220 K when viewed using polarisation microscopy, not to mention that it is very close to 226 K, where C2 nucleates. Tanaka proposed that the nano/microcrystal and L2 formation are independent processes, based on depolarised light scattering and wide and small angle x-ray scattering (WAXS/SAXS). Tanaka's data which is shown in Figure 58 is fairly

convincing. There are separate features in his SAXS patterns for 3nm clusters which he assigns to be LFS and larger clusters which he assumes to be nearly spherical microcrystallites based on the gradient of the line in the Porod regime. The Porod law is an approximation of an equation describing scattering pattern intensity for objects around 1 – 10 nm in size. The scattering intensity $I(q)$ is proportional to the interfacial surface area of the objects and to the inverse of q to some power n. The former can clearly be used as an indicator of roughness, but so can the second. If the power n is four, the objects are smooth spheres, but if between 3 and 4, are rough spheres. The slope of samples where $T_Q > 213$ K is clearly around four, but spherical particles of this size would be too small to form. The objects are roughly 3-13 nm in size, which is far too small for an even vaguely spherical spherulite of C2 to form. C2 TPP has unit cell dimensions a, b = 3.8 nm and c = 0.6 nm. Data from Senker[97] and Hédoux[98] has shown that TPP in C2 stacks to form anti-parallel rods along the c-axis. The rods therefore have cross sectional dimensions of 3.8 by 3.8 nm, which could not form a 3-13 nm spherulite. These rods likely act as templates for the needle-like crystals that can be seen in the microscopy images. If the particles are indeed roughly spherical, it is more likely that they are just larger LFS, which Tanaka concludes have a radius of gyration of 3.3 nm in the interval 212-218 K. In addition, an increase in the intensity $I(q)$ in the Porod regime could mean an increase in surface area S, indicating *rough or non-spherical* structures, which contradicts the claim that the -4 gradient of the Porod law line indicates smooth spheres. The fact that there are two separate features to the pattern is convincing, but there are several sources of contradictory data – this is not the first time that there has been an attempt to determine the size of structures in L2. The increase in the intensity and steepness of the gradient relates rises with quench temperature – which could be an indication of increasing cluster size. An extensive study by Oguni showed there is a relationship between LFS size and quench temperature.[92] The supposed 3 nm LFS peak that is assigned by Tanaka contradicts this as it does not change scattering angle as a function of T_Q. Similarly, data from Hédoux suggested that clusters (which he assumes are crystals) increase from ~3 nm when $T_Q < 216$ K to 30 nm when $T_Q = 222$ K. A small angle neutron scattering (SANS) experiments by Tarjus and co-workers shows '*structural organisation on a mesoscopic scale (~ 80 Å) and we have shown that no sign (sic) of aborted crystallization to the normal crystalline phase*'. The statement is based on a shoulder at Q = 0.1 Å^{-1} which only appears at $T_Q = 225$ K, but not at 218 K. A similar SANS

study by Yarger concludes that small clusters at 16 Å at 210 K which appear larger at higher temperatures and they surmise that they agglomerate to a maximum of 60 Å on heating.[109] What is clear from polarisation microscopy in this work, and light and x-ray scattering and other techniques from literature is that there definitely is nanoscopic or mesoscopic local structure in L2 that is not present in L1. There are multiple sources which suggest that these local structures, which will be termed locally favoured structures (LFS) increase in size as a function of T_Q. The nanocrystal hypothesis is practically unfalsifiable using many techniques due to their small size and Tanaka's scattering experiments offer weak evidence at best. L2 certainly appears to resemble or echo C2 in terms of Raman and XRD data, which favours the pro-nanocrystal consensus, but it is not conclusive. Both L2 droplets and C2 spherulites show Maltese crosses, although the former are around 1 % as intense under CP when compared to C2 for the most part. Although L2 having some crystalline C2 material within in it first appears a sensible suggestion, the mountain of data which appears to support this has significant flaws as has been outlined above. The Hédoux vs Tanaka (nanocrystal yes/no) dichotomy may be a simple lens with which to view the debate around the LLT in TPP, but it may be that they are looking at two sides of the same coin. 'Nanocrystals' may simply be LFS in L2 and L2 is a higher density, second liquid state which resembles C2. In the liquid-liquid transition in water, high density liquid water becomes a low density liquid whose density and local hydrogen bond structure is closer to, but is still distinct from that of the (hexagonal) ice.[110]

The IR spectrum of L2 resembles C2, with the peak and shoulder of L1 splitting in to two distinct peaks. In addition, the C1 spectrum resembles the L1 spectrum to some extent – the peaks do not shift significantly but sharpen and peak B drops in intensity. The similarities between the IR spectra indicates that the two liquid phases L1 and L2 act as precursors to C1 and C2. It has been suggested before that L2 is thermodynamically favoured over L1 at temperatures above 226 K.[95] The microscopy data indicate that C2 nucleates preferentially at relatively high temperatures (~250 K), and is favoured over C1 at <239 K. It can be deduced therefore that the LLT occurs at higher temperatures, but L2 immediately converts to C2. The reason that L2 droplets can be seen when T_Q < 226 K is that 226 K is the T_G temperature of L2.[95]

While understanding packing into different crystals/LFS is critical, changes in molecular conformation must also be considered to complete the picture of the LLT

in TPP. DFT calculations have produced two distinct conformations which have an uuu structure (Figure 71, Figure 72) and both feature the strong peaks A & B (corresponding to C-O stretching) in the 1150-1250 cm^{-1} interval *merged*. There are numerous uud conformations, which all have separated peaks A & B to different extents. The IR spectra of L1 and L2 show merged and separated peaks respectively. It is therefore likely that a flip of one of the phenoxy arms around the lp-P-O-C torsion is associated with the liquid-liquid transition.

Single crystal XRD shows that the molecules in all three crystals are in the uud conformation. The main difference between the conformations of C1 and C2 is a rotation of one of the P-O-C-C torsions, causing a switch in packing from sandwich to T-shaped π-π stacking respectively. The nucleation fraction data in Figure 79 and the IR spectra in Figure 66 show that there is mirroring between the liquids and crystals. Therefore, it can be deduced that there is also a change from sandwich to T-shaped π-π stacking during the LLT. The change is a suitable order parameter for the LLT.

There is strong evidence to suggest that L2 is not one phase, but a series of metastable glassy phases as is depicted in Figure 87. It is well established that the properties of a glass such as its entropy depend on the way it is cooled.[111] The properties of L2 vary significantly with quench temperature, so L2 can be viewed as a series of metastable glassy states L2, L2', L2" and so on. Phases of L2 which form at higher T_Q have more long-range ordering and IR spectra which more closely resembles that of C2. Existing literature data suggest that there is also a direct relationship between T_Q and cluster size, number density of LFS, T_G, cold crystallisation temperature and dielectric relaxation times.
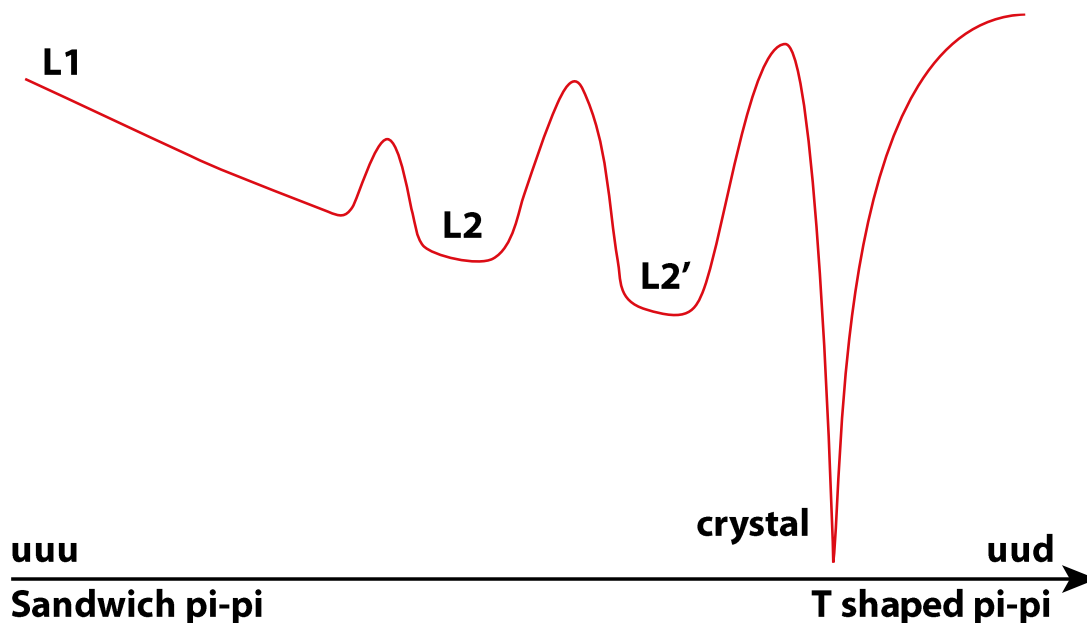
Figure 87 – The properties of L2 vary significantly with quench temperature, so it can be viewed as a series of metastable states rather than a single one. Forms of L2 which form at higher temperatures are closer to the crystal in terms of long-range ordering from microscopy and peaks in the 1150-1250cm^{-1} interval shifting to the uud pattern of C2. Existing data suggests that LFS cluster size and number density increase with temperature also. The diagram is denoted with both uuu/uud and sandwich π-π/T-shaped π-π conformations. The latter is indicated by XRD of C2, but the former cannot be ruled out.

2.14.   Conclusion

The debate surrounding TPP has been raging for decades between two camps which can be represented by Hédoux and Tanaka. Hédoux believes that L2 does not exist and is instead a heavily nucleated mixture of untransformed L1 and C2. Tanaka argues that L2 does exist but contains small nano or micro crystallites forming at the interfaces between L1 and L2. Tanaka has already provided a lot of data which shows L2 to be real and the isosbestic points in the IR spectra presented in this chapter confirm the Hédoux hypothesis to be false. L2 is at the very least, a distinct phase. Tanaka's hypothesis is convincing, but it is argued here that Tanaka and Hédoux are looking at two sides of the same coin. L2 can instead be described as dense state of C2 resembling locally favoured structures, which show faint long-range ordering. Even if there are nanocrystals in TPP, they make up < 1 % of the total material when T_Q < 224 K as evidenced by the polarisation microscopy data presented in this chapter. IR and microscopy data confirm previous observations that the figure of 226 K is the point at which C2 forms rather than L2, and is the glass transition temperature of L2.[95] During the LLT, there is a change from sandwich to T-shaped π-π stacking, which can be deduced from the crystal structures of C1 and C2 as the polyamorphs mirror the polymorphs as evidenced by

IR spectra and nucleation fraction data. This change is a suitable order parameter for the LLT and is used as the x-axis in the cartoon depiction of the behaviour of TPP in Figure 88. There are two conformational change associated with the LLT. Firstly, a flip of one of the phenoxy rings around the lp-P-O-C torsion and secondly a rotation of one of the phenoxy arms around the P-O-C-C. L1 and L2 are precursors of C1 and C2, and L2 is thermodynamically favoured over L1 <239 K. This is reflected in the proportion of crystals which nucleate at a range of temperatures around 239 K. The existence of the NG and SD regimes indicates that there is a narrowly missed critical point, as was predicted by the frustration-limited domain theory, pioneered by Kivelson. L2 shows substantial variations with quench temperature T_Q, which includes peak splitting in the 1150-1250 cm^{-1} region of the IR spectrum and crystallinity from polarisation microscopy. This indicates that a picture of L2 as a series of metastable glassy states which exhibit hysteresis is more appropriate than as a single phase.

TPP undergoes an LLT prior to the nucleation of C2, but the intermediate L2 state is too transient to be observable at higher temperatures. The higher T_G of L2 causes nucleation of C2 to be arrested below 226 K. The window between the two glass transition temperatures (204 K and 226 K) permits analysis of the so-called glacial phase. Although the ability to study this phase is uncommon among molecular liquids, it is reasonable to assume that the existence of multiple liquid phases is common.

As a fragile glass forming molecular liquid, triphenyl phosphite is ideal for studying the properties of supercooled liquids and the enigmatic phenomenon that is the liquid-liquid transition. IR, IR imaging, XRD, microscopy and DFT calculations have been used to elucidate a clearer picture of the properties of triphenyl phosphite.
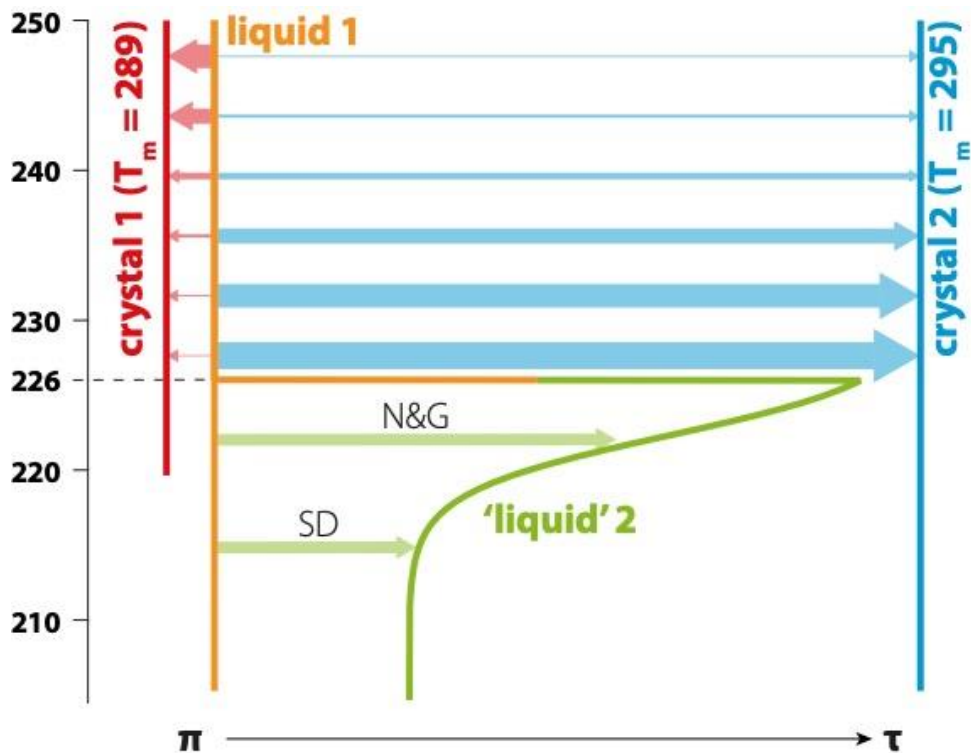
Figure 88 – Cartoon depicting the order parameter of the LLT and crystallisation in TPP. The horizontal axis is the order parameter, which goes from parallel 'sandwich' π-stacking of the phenoxy rings on neighbouring molecules on the left (π) to T-shaped stacking on the right (τ). The vertical axis represents the quench temperature T_Q. Solid lines show the four relevant forms of TPP (liquid 1, liquid 2, crystal 1, and crystal 2) and arrows the transitions between them, with the thickness of the arrow indicating the relative probability of a transition. Liquid 2 is formed from liquid 1 through nucleation and growth (N&G), and spinodal decomposition (SD).

3. General Conclusion

Two specific nucleation phenomena – non-photochemical laser-induced nucleation (NPLIN) and the liquid-liquid transition (LLT) in triphenyl phosphite (TPP) have been studied. It was found that the fundamental mechanism behind NPLIN is what has been termed here as laser-induced phase separation and nucleation (LIPSaN). The strong concentration fluctuations around critical points can be harnessed by the electric potential generated by a laser, to attract high refractive components to the focus and increase the probability of forming a critical nucleus. Using a broad range of spectroscopic and microscopic techniques, it has been concluded that the LLT in TPP does occur and nano- or micro-crystals do not play a role in the process. The LLT forms a second liquid phase which has locally favoured structures of a few molecules at low temperatures. The size of the LFS rises with quench temperature. There is also a subtle conformational change which involves the rotation of phenyl rings to give T π-π stacking rather than the less favourable sandwich π-π stacking. It is also possible that the conformational change involves a phenoxy ring flip from an 'up up up' type state to an 'up up down' type state. The crystal polymorphs of TPP have been fully characterised with single crystal X-ray diffraction and the two liquid phases have been shown to act as precursors to two of those polymorphs.

Research into nucleation has made limited progress in terms of a unifying theory since the work of Josiah Willard Gibbs, who formed much of the basis of classical nucleation theory. This thesis presents a detailed mechanistic understanding of two somewhat esoteric nucleation phenomena which have broader implications. Hidden critical points like those in NPLIN and the LLT in TPP likely play an important and poorly understood role in nucleation rates and routes. The challenge remains to fully understand their influence on the intricate phenomenon of nucleation.

4. Bibliography

1. Atkins, P. & De Paula, J. *Atkin's Physical Chemistry*. (Oxford University Press, 2010).

2. Fisher, M. E. & Widom, B. Decay of Correlations in Linear Systems. *J. Chem. Phys.* **50**, 3756 (1969).

3. Vehkamaki, H. *Classical Nucleation Theory in Multicomponent Systems. Springer* (Springer, 2006). doi:10.1017/CBO9781107415324.004

4. Jena, A. & Chaturvedi, M. *Phase Transformations in Materials*. (Prentice Hall, 1992).

5. Sanz, E. *et al.* Homogeneous ice nucleation at moderate supercooling from molecular simulation. *J. Am. Chem. Soc.* **135**, 15008–15017 (2013).

6. Gebauer, D., Raiteri, P., Gale, J. D. & Cölfen, H. On classical and non-classical views on nucleation. *Am. J. Sci.* **318**, 969–988 (2018).

7. Onuma, K. & Ito, A. Cluster Growth Model for Hydroxyapatite. *Chem. Mater.* **10**, 3346–3351 (1998).

8. Gebauer, Denis. Völkel, Antje. Cölfen, H. Stable Prenucleation Calcium Carbonate Clusters. *Science (80-.).* **322**, 1819–1822 (2008).

9. Scheck, J. *et al.* The Molecular Mechanism of Iron(III) Oxide Nucleation. *J. Phys. Chem. Lett.* **7**, 3123–3130 (2016).

10. Kellermeier, M. *et al.* Amino acids form prenucleation clusters: ESI-MS as a fast detection method in comparison to analytical ultracentrifugation. *Faraday Discuss.* **159**, 23–45 (2012).

11. Smeets, P. J. M. *et al.* A classical view on nonclassical nucleation. *Proc. Natl. Acad. Sci.* **114**, E7882–E7890 (2017).

12. Kléman, M. & Sadoc, J. F. A tentative description of the crystallography of amorphous solids. *J. Phys. Lettres* **40**, 569–574 (1979).

13. Graham, U. M. & Ohmoto, H. Experimental study of formation mechanisms of hydrothermal pyrite. *Geochim. Cosmochim. Acta* **58**, 2187–2202 (1994).

14. Frank, F. C. Supercooling of liquids. 165–183 (1952).

15. Murata, K. & Tanaka, H. Microscopic identification of the order parameter governing liquid–liquid transition in a molecular liquid. *Proc. Natl. Acad. Sci.* **112**, 5956–5961 (2015).

16. ten Wolde, P. R. & Frenkel, D. Enhancement of protein crystal nucleation by critical density fluctuations. *Science* **277**, 1975–1978 (1997).

17. Young, H. D. & Freedman, R. A. *University Physics with Modern Physics*. (Pearson, 2015).

18. Shanmugaraju, S., Joshi, S. A. & Mukherjee, P. S. Fluorescence and visual sensing of nitroaromatic explosives using electron rich discrete fluorophores. *J. Mater. Chem.* **21**, 9130–9138 (2011).

19. Pertot, Y. *et al.* Streaking of 43-attosecond soft-X-ray pulses generated by a passively CEP-stable mid-infrared driver. *Opt. Express* **25**, 27506 (2017).

20. Soare, A. *et al.* Crystal nucleation by laser-induced cavitation. *Cryst. Growth Des.* **11**, 2311–2316 (2011).

21. Ehrlich, D. J., Rothschild, M. & Black, J. G. Laser photochemical reactions. *Ultramicroscopy* **23**, 283–290 (1987).

22. Garetz, B. A., Aber, J. E., Goddard, N. L., Young, R. G. & Myerson, A. S. Nonphotochemical , Polarization-Dependent , Laser-Induced Nucleation in Supersaturated Aqueous Urea Solutions. *Phys. Rev. Lett.* **77**, 3475–3476 (1996).

23. Polynkin, P. & Kolesik, M. Critical power for self-focusing in the case of ultrashort laser pulses. *Phys. Rev. A* **87**, 053829 (2013).

24. Zaccaro, J., Matic, J., Myerson, A. S. & Garetz, B. a. Nonphotochemical, Laser-Induced Nucleation of Supersaturated Aqueous Glycine Produces Unexpected γ-Polymorph. *Cryst. Growth Des.* **1**, 5–8 (2000).

25. Srinivasan, K. Crystal growth of α and γ glycine polymorphs and their polymorphic phase transformations. *J. Cryst. Growth* **311**, 156–162 (2008).

26. Garetz, B. A., Matic, J. & Myerson, A. S. Polarization Switching of Crystal Structure in the Nonphotochemical Light-Induced Nucleation of Supersaturated Aqueous Glycine Solutions. *Phys. Rev. Lett.* **89**, 175501 (2002).

27. Yuyama, K. I., Sugiyama, T. & Masuhara, H. Laser Trapping and crystallization dynamics of l-phenylalanine at solution surface. *J. Phys. Chem. Lett.* **4**, 2436–2440 (2013).

28. Lee, I. S. *et al.* Nonphotochemical Laser Induced Nucleation of Hen Egg White Lysozyme Crystals †. *Cryst. Growth Des.* **8**, 4255–4261 (2008).

29. Knott, B. C., Larue, J. L., Wodtke, A. M., Doherty, M. F. & Peters, B. Communication: Bubbles, crystals, and laser-induced nucleation. *J. Chem. Phys.* **134**, (2011).

30. Ward, M. R., Jamieson, W. J., Leckey, C. A. & Alexander, A. J. Laser-induced nucleation of carbon dioxide bubbles. *J. Chem. Phys.* **142**, (2015).

31. Duffus, C., Camp, P. J. & Alexander, A. J. Spatial control of crystal nucleation in agarose gel. *J. Am. Chem. Soc.* **131**, 11676–11677 (2009).

32. Ward, M. R., Copeland, G. W. & Alexander, A. J. Chiral hide-and-seek: Retention of enantiomorphism in laser-induced nucleation of molten sodium chlorate. *J. Chem. Phys.* **135**, (2011).

33. Li, W. *et al.* Non-Photochemical Laser-Induced Nucleation of Sulfathiazole in a Water/Ethanol Mixture. *Cryst. Growth Des.* **16**, 2514–2526 (2016).

34. Ikni, A. *et al.* Experimental demonstration of the carbamazepine crystallization from non-photochemical laser-induced nucleation in acetonitrile and methanol. *Cryst. Growth Des.* **14**, 3286–3299 (2014).

35. Ward, M. R., McHugh, S. & Alexander, A. J. Non-photochemical laser-induced nucleation of supercooled glacial acetic acid. *Phys. Chem. Chem. Phys.* **14**, 90–93 (2012).

36. Sun, X., Garetz, B. a., Moreira, M. F. & Palffy-Muhoray, P. Nonphotochemical laser-induced nucleation of nematic phase and alignment of nematic director

from a supercooled thermotropic liquid crystal. *Phys. Rev. E* **79**, 021701 (2009).

37. Knott, B. C., Doherty, M. F. & Peters, B. A simulation test of the optical Kerr mechanism for laser-induced nucleation. *J. Chem. Phys.* **134**, (2011).

38. Liu, Y., Ward, M. R. & Alexander, A. J. Polarization independence of laser-induced nucleation in supersaturated aqueous urea solutions. *Phys. Chem. Chem. Phys.* **19**, 3464 (2017).

39. Liu, Y., van den Berg, M. H. & Alexander, A. J. Supersaturation dependence of glycine polymorphism using laser-induced nucleation, sonocrystallization and nucleation by mechanical shock. *Phys. Chem. Chem. Phys.* **19**, 19386–19392 (2017).

40. Clair, B. *et al.* A new experimental setup for high-throughput controlled non-photochemical laser-induced nucleation: Application to glycine crystallization. *J. Appl. Crystallogr.* **47**, 1252–1260 (2014).

41. Kacker, R. *et al.* Multiparameter Investigation of Laser-Induced Nucleation of Supersaturated Aqueous KCl Solutions. *Cryst. Growth Des.* **18**, 312–317 (2018).

42. Alexander, A. J. & Camp, P. J. Non-photochemical laser-induced nucleation. *J. Chem. Phys.* **150**, (2019).

43. Yuyama, K. I., Rungsimanon, T., Sugiyama, T. & Masuhara, H. Selective fabrication of α- And γ-polymorphs of glycine by intense polarized continuous wave laser beams. *Cryst. Growth Des.* **12**, 2427–2434 (2012).

44. Bartkiewicz, S. & Miniewicz, A. Whirl-enhanced continuous wave laser trapping of particles. *Phys. Chem. Chem. Phys.* **17**, 1077–1083 (2015).

45. Knott, B. C., Duff, N., Doherty, M. F. & Peters, B. Estimating diffusivity along a reaction coordinate in the high friction limit: Insights on pulse times in laser-induced nucleation. *J. Chem. Phys.* **131**, (2009).

46. Debye, P. & Kleboth, K. Electrical field effect on the critical opalescence. *J. Chem. Phys.* **42**, 3155–3162 (1965).

47. Ziolo, J. The Critical Exponent for Nitrobenzene-Hexane Mixtures Determined by the Nonlinear Dielectric Method*. *Chem. Phys. Lett.* **64**, 570–572 (1979).

48. Walton, F. & Wynne, K. Control over phase separation and nucleation using a laser-tweezing potential. *Nat. Chem.* **10**, 506–510 (2018).

49. Walton, F. & Wynne, K. Control over phase separation and nucleation using a optical-tweezing potential. *Proc. SPIE* **10723**, 107230O (2018).

50. Walton, F. & Wynne, K. Using optical tweezing to control phase separation and nucleation near a liquid–liquid critical point. *Soft Matter* **15**, 8279–8289 (2019).

51. Jones, R. A. L. *Soft Condensed Matter. Oxford master series in condensed matter physics* (Oxford University Press, 2002). doi:10.1080/09362835.2017.1283622

52. Taslc, A., Djordjevlč, B. D., Grozdanlč, D. K. & Radojkovlč, M. Use of Mixing Rules In Predicting Refractive Indexes and Specific Refractivities for Some Binary Liquid Mixtures. *J. Chem. Eng. Data* **37**, 310–313 (1992).

53. Aminabhavi, T. M. Use of Mixing Rules in the Analysis of Data for Binary Liquid Mixtures. *J. Chem. Eng. Data* **29**, 54–55 (1984).

54. Walker, G. C., Åkesson, E., Johnson, A. E., Levinger, N. E. & Barbara, P. F. Interplay of solvent motion and vibrational excitation in electron-transfer kinetics: Experiment and theory. *J. Phys. Chem.* **96**, 3728–3736 (1992).

55. Benitez, M. Thermal diffusivity measurement using the mode- mismatched photothermal lens method. **48**, 1–8 (2018).

56. Peterman, E. J. G., Gittes, F. & Schmidt, C. F. Laser-induced heating in optical traps. *Biophys. J.* **84**, 1308–16 (2003).

57. Rozier Cannon, J. The One-Dimensional Heat Equation. in *Encyclopedia of Mathematics and its Applications* (Campbridge University Press, 1984).

58. Wiegand, S. Thermal diffusion in liquid mixtures and polymer solutions. *J. Phys. Condens. Matter* **16**, R357–R379 (2004).

59. Méndez-Castro, P., Troncoso, J., Peleteiro, J. & Romaní, L. Heat capacity singularity of binary liquid mixtures at the liquid-liquid critical point. *Phys Rev E* **88**, 42107 (2013).

60. Gelb, L. D., Gubbins, K. E., Radhakrishnan, R. & Sliwinska-Bartkowiak, M. Phase separation in confined systems. *Reports Prog. Phys.* **62**, 1573–1659 (1999).

61. Meaney, M. S. & McGuffin, V. L. Investigation of common fluorophores for the detection of nitrated explosives by fluorescence quenching. *Anal. Chim. Acta* **610**, 57–67 (2008).

62. Wang, J. The Nature of Asymmetry in Fluid Criticality. *Thesis, Univ. Maryl.* (2006).

63. Cerdeiriña, C. A., Tovar, C. A., González, D., Carballo, E. & Romaní, L. Thermodynamics of the nitromethane + 1-butanol system near the upper critical point. *Fluid Phase Equilib.* **179**, 101–115 (2001).

64. Rebillot, P. F. & Jacobs, D. T. Heat capacity anomaly near the critical point of aniline-cyclohexane. *J. Chem. Phys.* **109**, 4009–4014 (1998).

65. Yuyama, K., George, J., Thomas, K. G., Sugiyama, T. & Masuhara, H. Two-Dimensional Growth Rate Control of <scp>l</scp> -Phenylalanine Crystal by Laser Trapping in Unsaturated Aqueous Solution. *Cryst. Growth Des.* **16**, 953–960 (2016).

66. Mukai, S. *et al.* Liquid / liquid dynamic phase separation induced by a focused laser. **83**, 2557 (2003).

67. Crauste-thibierge, C., Petrosyan, A. & Ciliberto, S. Phase-transition oscillations induced by a strongly focused laser beam. **052312**, 1–6 (2015).

68. Bunkin, N. F., Lobeev, A. V, Lyakhov, G. A. & Svirko, Y. P. Local light-induced phase separation of binary liquid solutions. *Kvantovaya Elektron.* **23**, 62–66 (1996).

69. Osborne, M. A., Balasubramanian, S., Furey, W. S. & Klenerman, D. Optically Biased Diffusion of Single Molecules Studied by Confocal Fluorescence Microscopy. **5647**, 3160–3167 (1998).

70. Woerdemann, M. Introduction to Optical Trapping BT - Structured Light Fields: Applications in Optical Trapping, Manipulation, and Organisation. in *Structured Light Fields* (ed. Wördemann, M.) 5–26 (Springer Berlin Heidelberg, 2012). doi:10.1007/978-3-642-29323-8_2

71. Mosses, J., Syme, C. D. & Wynne, K. Order Parameter of the Liquid − Liquid Transition in a Molecular Liquid. *J. Phys. Chem. Lett.* **6**, 38–43 (2014).

72. Syme, C. D. *et al.* Frustration of crystallisation by a liquid-crystal phase. *Sci. Rep.* **7**, 42437 (2017).

73. Zhu, M., Wang, J. Q., Perepezko, J. H. & Yu, L. Possible existence of two amorphous phases of d -mannitol related by a first-order transition. *J. Chem. Phys.* **142**, 244504 (2015).

74. Kurita, R. & Tanaka, H. Critical-like phenomena associated with liquid-liquid transition in a molecular liquid. *Science* **306**, 845–848 (2004).

75. Hédoux, A., Hernandez, O., Lefèbvre, J., Guinet, Y. & Descamps, M. Mesoscopic description of the glacial state in triphenyl phosphite from an x-ray diffraction experiment. *Phys. Rev. B - Condens. Matter Mater. Phys.* **60**, 9390–9395 (1999).

76. Atkins, P. & Friedman, R. *Molecular Quantum Mechanics.* (Oxford University Press, 2005).

77. Cinque, G. *et al.* Synchrotron-Based Infrared Spectral Imaging at the MIRIAM Beamline of Diamond Light Source. *Synchrotron Radiat. News* **30**, 11–16 (2017).

78. Katayama, Y. *et al.* A first-order liquid-liquid phase transition in phosphorus. *Nature* **403**, 170–173 (2000).

79. Mcmillan, P. F., Wilson, M., Daisenberger, D. & Machon, D. A density-driven phase transition between semiconducting and metallic polyamorphs of silicon. *Nat. Mater.* **4**, 680–684 (2005).

80. Bhat, M. H. *et al.* Vitrification of a monatomic metallic liquid. *Nature* **448**, 787–790 (2007).

81. Xu, W. *et al.* Evidence of liquid-liquid transition in glass-forming La50Al35Ni15melt above liquidus temperature. *Nat. Commun.* **6**, 1–9 (2015).

82. Zhu, M. & Yu, L. Polyamorphism of D-mannitol. *J. Chem. Phys.* **146**, 244503 (2017).

83. Ha, A., Cohen, I., Zhao, X., Lee, M. & Kivelson, D. Supercooled Liquids and Polyamorphism [†]. *J. Phys. Chem.* **100**, 1–4 (1996).

84. Cohen, I. *et al.* A low-temperature amorphous phase in a fragile glass-forming substance. *J. Phys. Chem.* **100**, 8518–8526 (1996).

85. Fischer, E. W. Light scattering and dielectric studies on glass forming liquids. **201**, 183–206 (1993).

86. Debenedetti, P. G. & Stillinger, F. H. Supercooled Liquids and the Glass Transition. *Nature* **410**, 259–267 (2001).

87. Golovanov, D. G. *et al.* Long-awaited polymorphic modification of triphenyl phosphite. *CrystEngComm* **7**, 465–468 (2005).

88. Wiedersich, J. *et al.* On Polyamorphism of Triphenyl Phosphite. *J Phys Chem B* **101**, 5800–5803 (1997).

89. Guinet, Y. & Descamps, M. Raman signature of polyamorphism in triphenyl phosphite. *Phys. Rev. B - Condens. Matter Mater. Phys.* **58**, 31–34 (1998).

90. Lefebvre, J., Guinet, Y., Hernandez, O. & He, A. research papers Ab initio structure determination of triphenyl phosphite by powder synchrotron X-ray diffraction research papers. 212–219 (2001). doi:10.1107/S0021889802000511

91. Johari, G. P. & Ferrari, C. Calorimetric and Dielectric Investigations of the Phase Transformations and Glass Transition of Triphenyl Phosphite. *J. Phys. Chem. B* **101**, 10191–10197 (1997).

92. Mizukami, M., Kobashi, K., Hanaya, M. & Oguni, M. Presence of Two Freezing-In Processes Concerning α-Glass Transition in the New Liquid Phase of Triphenyl Phosphite and Its Consistency with "Cluster Structure" and "Intracluster Rearrangement for α Process" Models. *J. Phys. Chem. B* **103**, 4078–4088 (1999).

93. Alba-Simionesco, C. & Tarjus, G. Experimental evidence of mesoscopic order in the apparently amorphous glacial phase of the fragile glass former triphenylphosphite. *Europhys. Lett.* **52**, 297–303 (2000).

94. Yarger, J. L., Schwickert, B. E., Kline, S. R., Zimmermann, H. & Lantzky, K. M. Early stages of glacial clustering in supercooled triphenyl phosphite. *Phys. Rev. B - Condens. Matter Mater. Phys.* **64**, 045410 (2001).

95. Tanaka, H., Kurita, R. & Mataki, H. Liquid-Liquid Transition in the Molecular Liquid Triphenyl Phosphite. *Phys. Rev. Lett.* **92**, 4 (2004).

96. Shimizu, R., Kobayashi, M. & Tanaka, H. Evidence of liquid-liquid transition in triphenyl phosphite from time-resolved light scattering experiments. *Phys. Rev. Lett.* **112**, 125702 (2014).

97. Senker, J., Sehnert, J. & Correll, S. Microscopic description of the polyamorphic phases of triphenyl phosphite by means of multidimensional solid-state NMR spectroscopy. *J. Am. Chem. Soc.* **127**, 337–349 (2005).

98. Guinet, Y. *et al.* Micro-structural investigations in the glacial state of triphenyl phosphite. *J. Non. Cryst. Solids* **352**, 4994–5000 (2006).

99. Hernandez, O. J., Boucekkine, A., Rennes, F.- & He, A. Density Functional Theory Study of Triphenyl Phosphite : Molecular Flexibility and Weak Intermolecular Hydrogen Bonding. *J. Phys. Chem. A* **111**, 6952–6958 (2007).

100. Baran, J., Davydova, N. A. & Drozd, M. Polymorphism of triphenyl phosphite. *J. Chem. Phys.* **140**, 104512 (2014).

101. Tarnacka, M. *et al.* Is There a Liquid-Liquid Phase Transition in Confined Triphenyl Phosphite? *J. Phys. Chem. C* **121**, 19442–19450 (2017).

102. Babkov, L. M. *et al.* Infrared spectra of triphenyl phosphite and their interpretation on the basis of quantum chemistry calculation. *Ukr. J. Phys.* **61**, 471–477 (2016).

103. Babkov, L. M., Davydova, N. A. & Ivlieva, I. V. IR Spectra of Triphenyl Phosphite and Their Interpretation by Molecular Modeling. *Ser. Phys.* **17**, 11–

19 (2017).

104. Groom, C. R., Bruno, I. J., Lightfoot, M. P. & Ward, S. C. The Cambridge structural database. *Acta Crystallogr. Sect. B Struct. Sci. Cryst. Eng. Mater.* **72**, 171–179 (2016).

105. Guinet, Y. *et al.* A contribution to the understanding of the polyamorphism situation in triphenyl phosphite. *Phys. Chem. Chem. Phys.* **6**, 3192–3199 (2004).

106. BeMiller, J. & Whistler, R. *Starch: Chemistry and Technology*. (Academic Press, 2009).

107. Schiener, B., Loidl, A., Chamberlin, R. V. & Böhmer, R. Dielectric study of supercooled triphenylphosphite and butyronitrile: Comparison with a mesoscopic model. *J. Mol. Liq.* **69**, 243–251 (1996).

108. Sinnokrot, M. O. & Sherrill, C. D. High-accuracy quantum mechanical studies of π-π interactions in benzene dimers. *J. Phys. Chem. A* **110**, 10656–10668 (2006).

109. Yarger, J. L., Schwickert, B. E., Kline, S. R., Zimmermann, H. & Lantzky, K. M. Early stages of glacial clustering in supercooled triphenyl phosphite. *Phys. Rev. B - Condens. Matter Mater. Phys.* **64**, (2001).

110. Palmer, J. C. *et al.* Metastable liquid-liquid transition in a molecular model of water. *Nature* **510**, 385–388 (2014).

111. Ediger, M. D., Angell, C. A. & Nagel, S. R. Supercooled Liquids and Glasses. *J. Phys. Chem.* **100**, 13200–13212 (1996).

5. Appendix

5.1. Calculation of the refractive index and composition of a LIPS droplet

The LIPS droplet composition can be estimated by calculating the changes in refractive index as measured on the edge of phase-separated nitrobenzene droplets. From the cross sections of PC images shown in Figure 89, the droplet edges have intensities of 1820 and the LIPS droplet a central amplitude of 110 (relative to the background). These values vary linearly with the difference in refractive index Δn between the droplets and the bulk. Using the lever rule in the phase diagram in Figure 31, the nitrobenzene-rich droplet and surrounding decane-rich region can be calculated to have mole fractions of 0.68 and 0.45 respectively. Under the reasonable assumption that the refractive index varies linearly with mole fraction, mole fractions of 0.68 and 0.45 correspond to refractive indices of 1.505 and 1.473 respectively. Therefore, $\Delta n = 0.032$ for the separated case, and the ratio 110/1820 can be used to calculate $\Delta n = 0.002$ for the LIPS droplet. Therefore $n = 1.493$ in the LIPS droplet compared to $n = 1.491$ in the bulk. This means that the mole fraction of nitrobenzene within the LIPS droplet can be calculated to be 0.589 compared to 0.575 in the bulk.
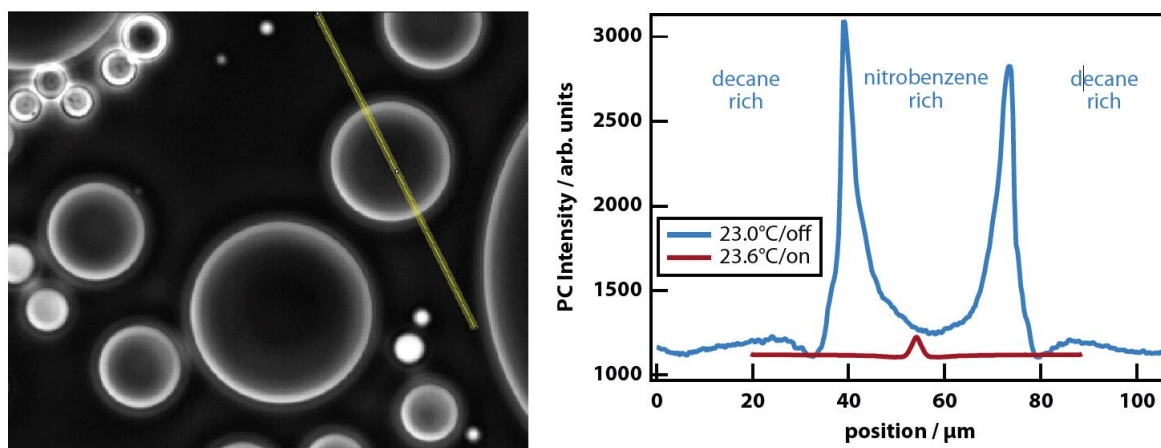
Figure 89 – (left) A PC image of a critical sample of nitrobenzene–decane ($x_C = 0.575$) at a temperature (296.2 K) in a phase separated state. The line dissects a large droplet of nitrobenzene. (right) Phase-contrast intensity (or LIPS Intensity) along the cut line of a nitrobenzene–decane sample at the critical mole fraction at T = 296.2 K (phase separated) and T = 296.8 K (mixed) but in the presence of a LIPS-inducing laser. The curve at 296.2 K clearly shows saturation caused by the shade-off effect 2 inherent in phase-contrast microscopy of larger objects[48].

5.2. Experimental Phase Diagram for a Nitromethane-n-octanol Mixture
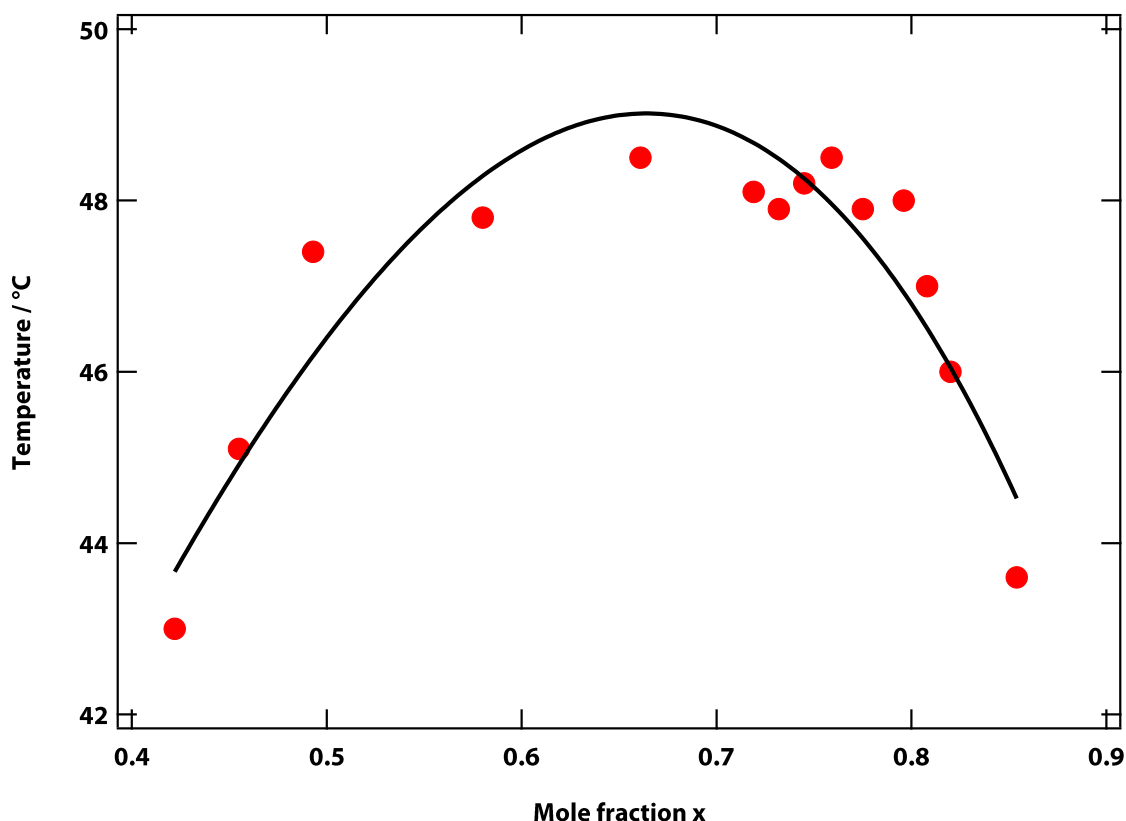
Figure 90 – The critical parameters of nitromethane and n-octanol were determined to $T_C = 49.0$ °C = 322.2 K and $x_0 = 0.664$ by fitting a fourth order polynomial.

5.3. Determination of the Extinction Co-efficient using UV-Vis Spectroscopy

The UV-Vis spectra of nitrobenzene and decane in Figure 91 show no combination or overtone bands at the laser wavelength of 785 nm. Nevertheless, the absorbance can be used as part of a heating calculation, but first subtracting the contribution from the cuvette. Three cuvette path lengths were used (1, 2 and 10 mm) and a line was fitted the absorbances in order to calculate the y-intercept, i.e. the contribution of the cuvette. The calculated cuvette absorbance of 0.0293 was used to calculate the heat term Q in Eq (2.40).
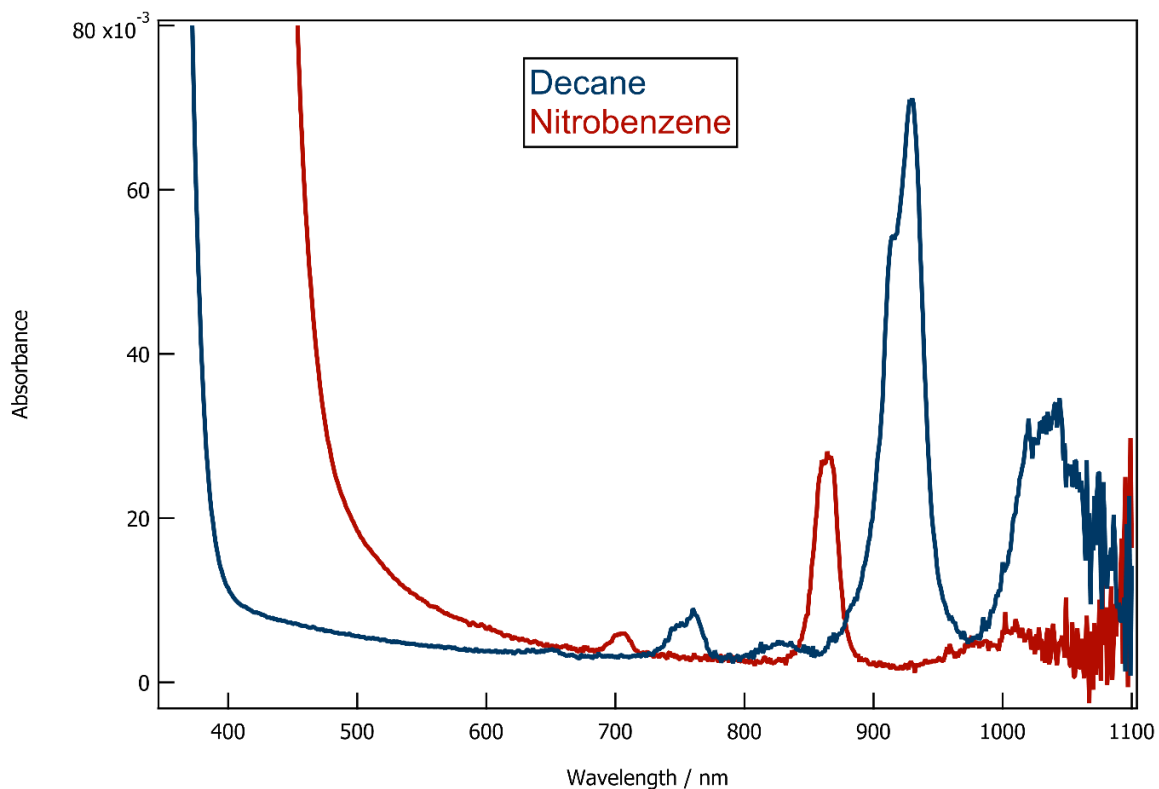
Figure 91 – UV-Vis spectra of nitrobenzene and decane. Both show no combination or overtone bands near 785 nm (the peak wavelength of the laser).
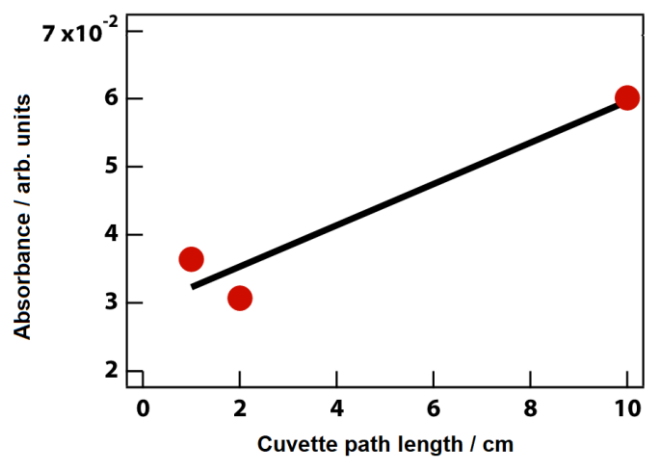
Figure 92 – The contribution of the cuvette glass to the UV-Vis signal was found to be 0.0293.

5.4. Dynamic IR spectra of TPP during the LTT
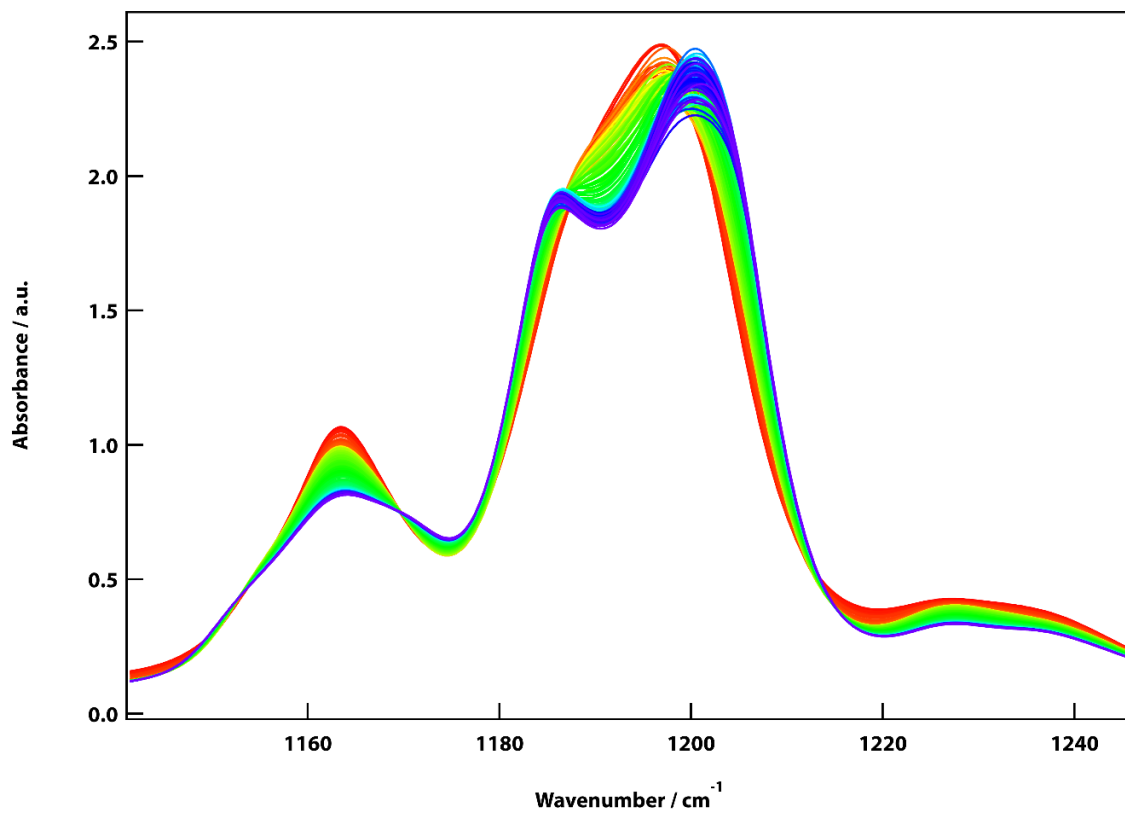
Figure 93 – LLT at $T_Q = 213$ K.
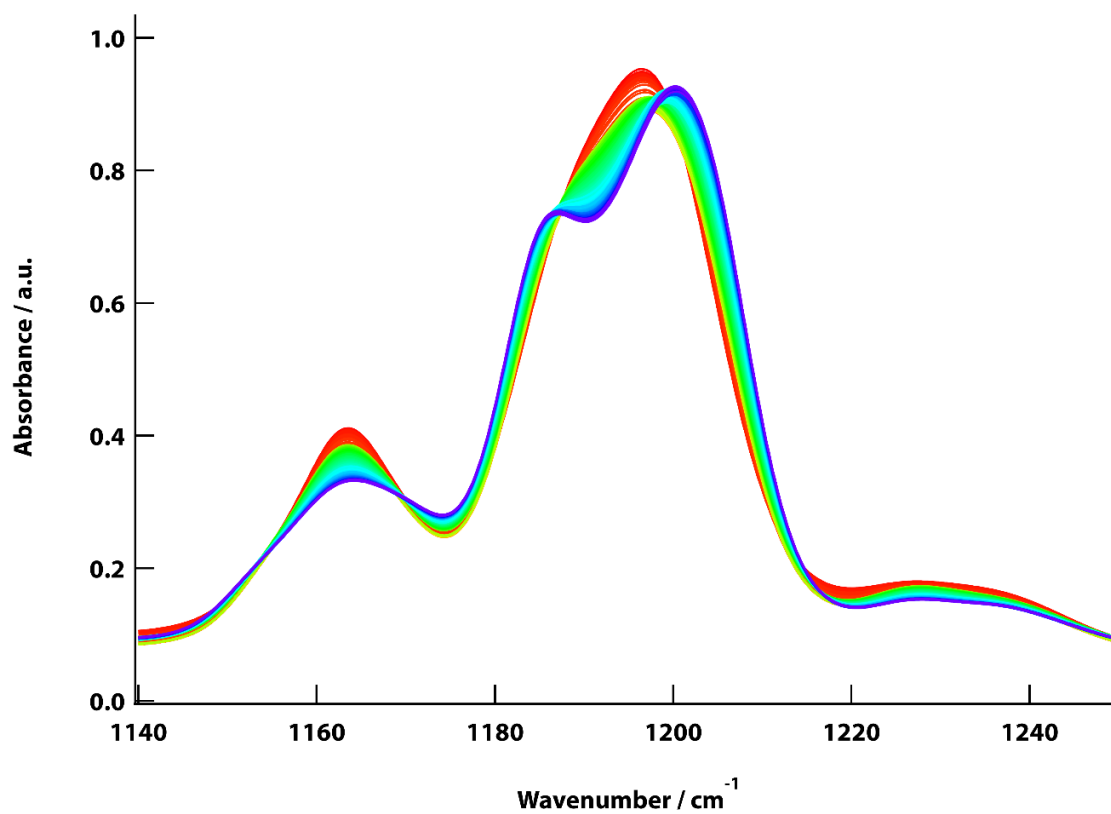
Figure 94 – LLT at $T_Q = 215$ K.
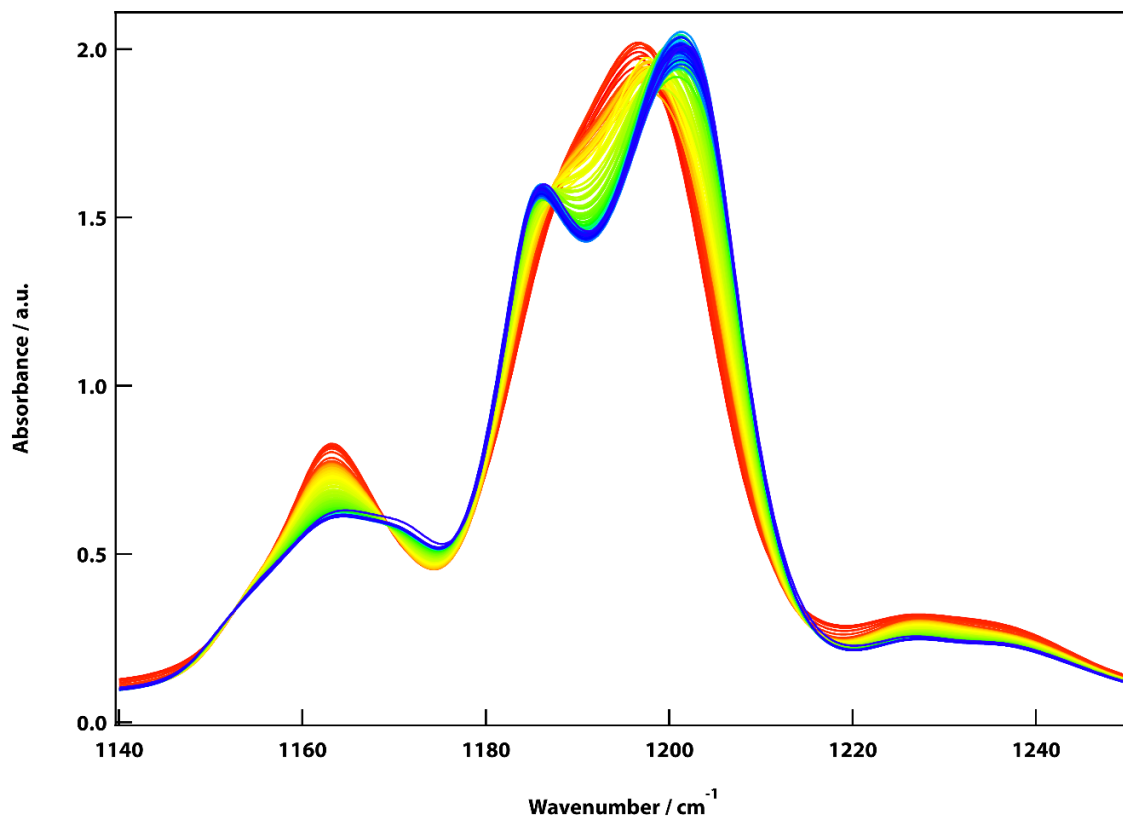
Figure 95 – LLT at TQ = 218 K.
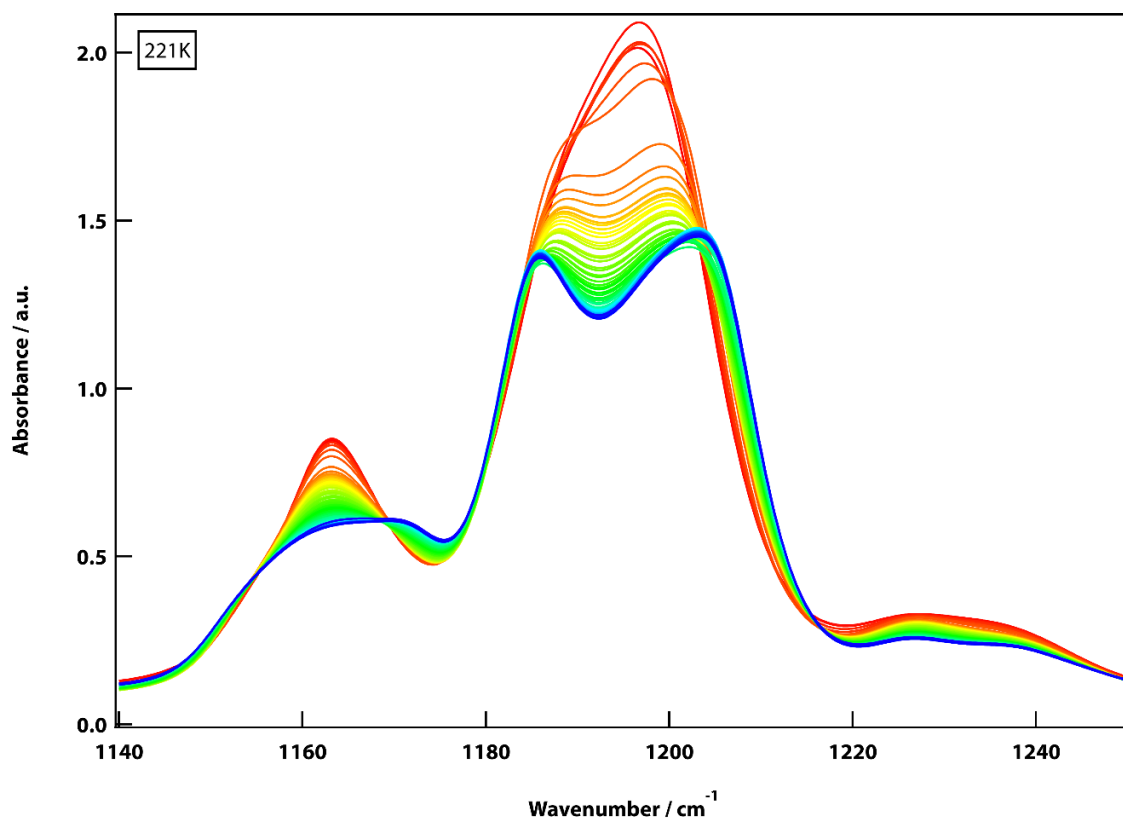
Figure 96 – LLT at TQ = 221 K.

138
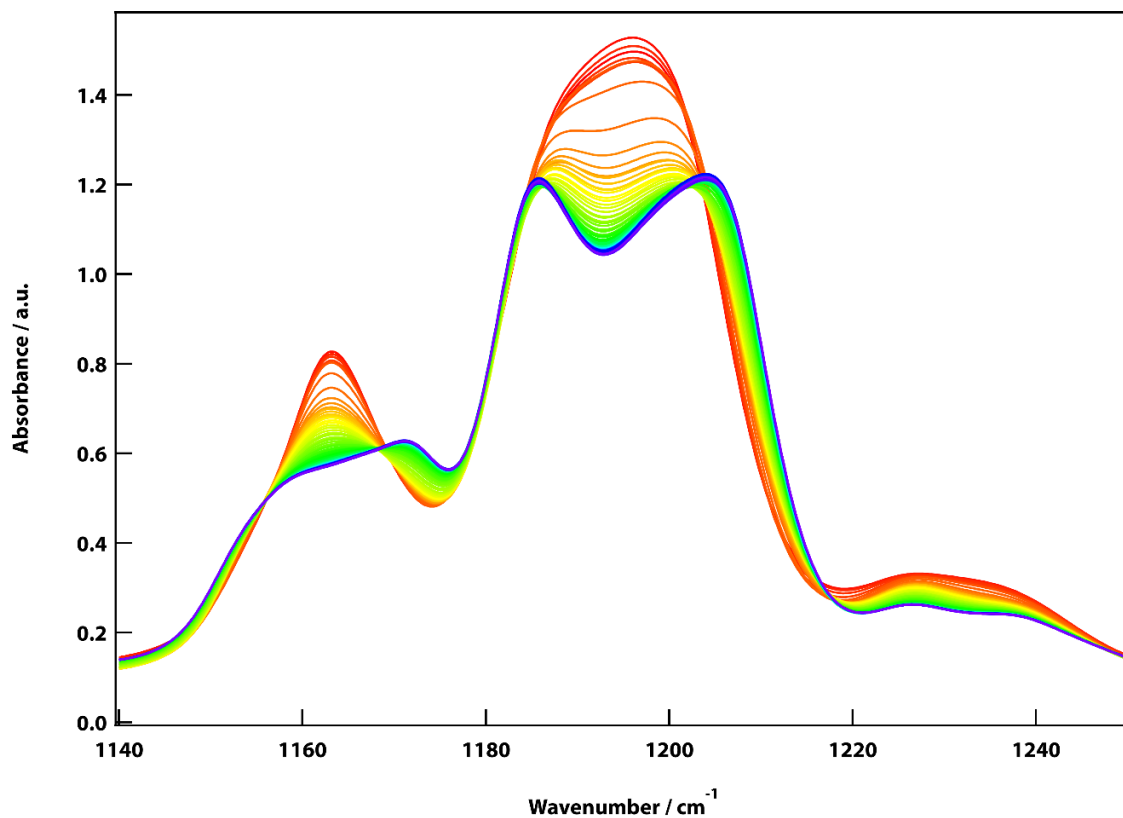
Figure 97 – LLT at TQ = 223 K.

5.5. Full IR spectrum of TPP
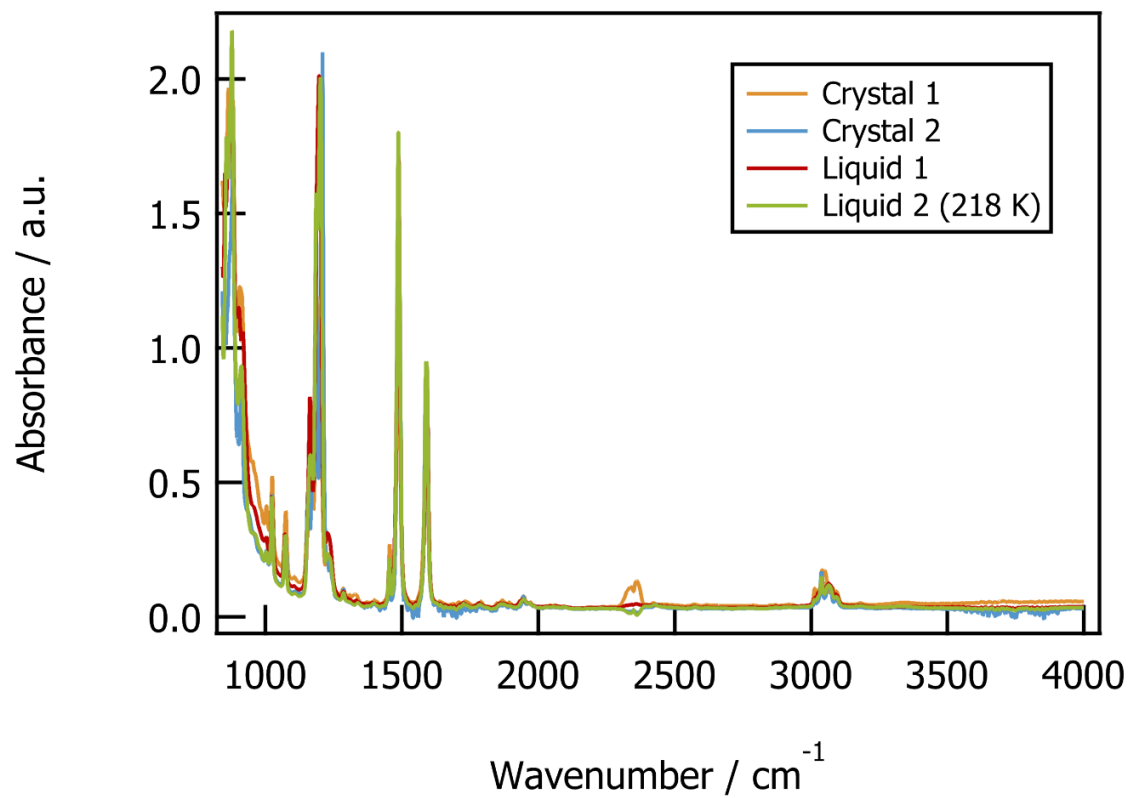
Figure 98 – Full mid-IR spectrum of TPP from 900 - 4000 cm^{-1}. Using CaF windows meant that reliable data could not be collected where $\tilde{v}$ < 900 cm^{-1}.

5.6. IR band assignment from 945 – 4000 cm^{-1} for the uuu conformer from DFT

Mode#	v (cm^{-1})	Amplitude	Description
47	949	35.2	P-O stretch, C-O bend x3 asym, C-H out of plane
48	961	48.6	P-O stretch, C-O bend x3 sym, C-H out of plane
49-57	992-1026	0.1-1.5	C-H out of plane bends
58-66	1056-1176	0.1-17.6	Various C-H in plane bending
67	1186	13.1	C-H in plane bend x1 ring
68	1195	19.3	C-H in plane bend x2 ring #1
69	1196	5.3	C-H in plane bend x2 ring #2
70	**1257**	**211.5**	**C-O stretch P-O bend x2**
71	**1263**	**700.6**	**C-O stretch P-O bend x3**
72	1302	4.2	C-O stretch P-O bend x3 sym
82	1538	118.8	C-C stretch/bend + C-O stretch x3
83	1540	277.5	C-C stretch/bend + C-O stretch x2
88, 89	1670, 1673	130.8, 61.3	C-C stretch/bend
91-105	3204-3236	0.8 – 8.9	C-H stretches

Table 8 – IR band assignment from 945 – 4000 cm^{-1} for the uuu conformer from DFT calculations.

5.7. Liquid 1 as a Function of T_Q
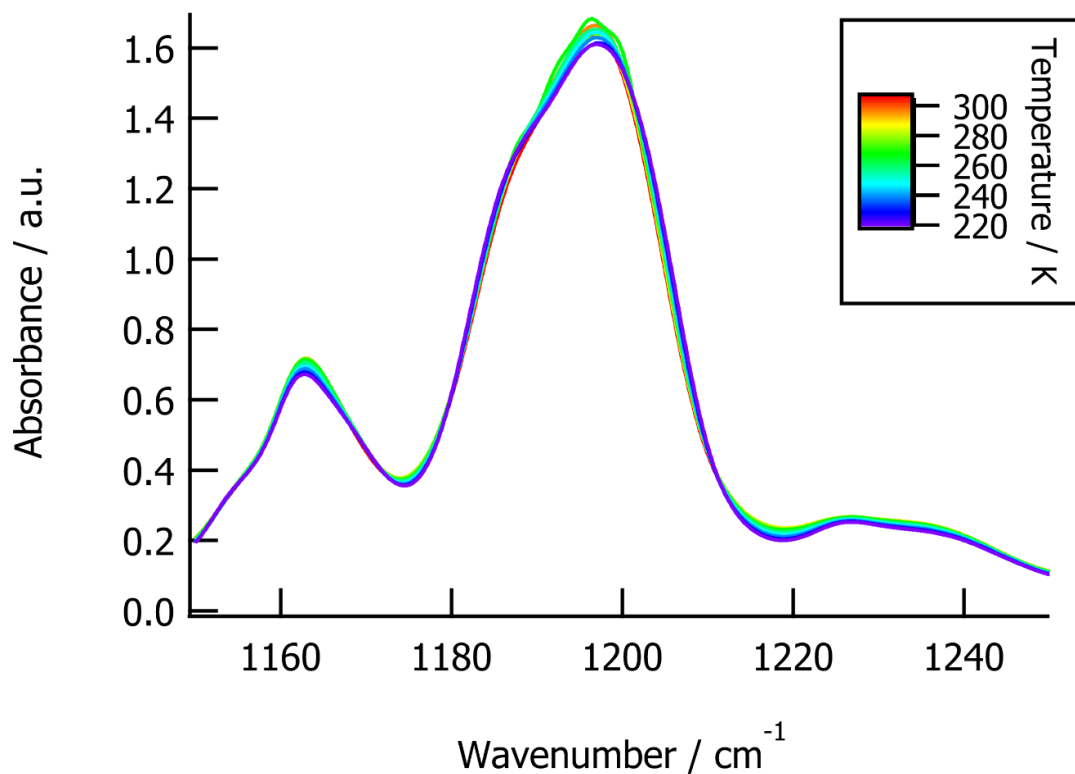
Figure 99 – L1 spectrum as a function of temperature from 220 - 300 K. If anything, there is a small drop in absorbance, but no other changes.a

5.8. C1 Single Crystal Diffraction Parameters

	x	y	z	U_{iso}*/U_{eq}
P1	0.76907 (3)	0.66564 (8)	0.68132 (3)	0.02400 (14)
O1	0.79949 (7)	0.6998 (2)	0.58449 (8)	0.0280 (3)
O2	0.79043 (7)	0.9093 (2)	0.73027 (8)	0.0268 (3)
O3	0.67831 (7)	0.7360 (2)	0.65977 (9)	0.0297 (3)
C1	0.77769 (10)	0.8722 (3)	0.52184 (12)	0.0244 (4)
C2	0.71565 (10)	0.8361 (3)	0.45641 (13)	0.0290 (4)
H2	0.685847	0.701088	0.456312	0.035*
C3	0.69758 (11)	0.9999 (4)	0.39090 (13)	0.0347 (5)
H3	0.654931	0.977487	0.345531	0.042*
C4	0.74130 (12)	1.1967 (4)	0.39102 (14)	0.0361 (5)
H4	0.728879	1.308188	0.345703	0.043*
C5	0.80291 (12)	1.2295 (3)	0.45730 (13)	0.0358 (5)
H5	0.832756	1.364410	0.457578	0.043*

C6	0.82162 (11)	1.0676 (3)	0.52338 (13)	0.0302 (4)
H6	0.863996	1.090418	0.569066	0.036*
C7	0.86285 (9)	0.9322 (3)	0.78138 (11)	0.0217 (4)
C8	0.89190 (10)	0.7693 (3)	0.84295 (12)	0.0253 (4)
H8	0.863402	0.634910	0.850674	0.030*
C9	0.96331 (11)	0.8052 (3)	0.89326 (12)	0.0290 (4)
H9	0.984038	0.693895	0.935503	0.035*
C10	1.00468 (11)	1.0015 (3)	0.88254 (13)	0.0300 (4)
H10	1.053846	1.024229	0.916747	0.036*
C11	0.97407 (11)	1.1639 (3)	0.82185 (12)	0.0286 (4)
H11	1.002061	1.299734	0.814980	0.034*
C12	0.90291 (10)	1.1307 (3)	0.77089 (12)	0.0252 (4)
H12	0.881898	1.242964	0.729248	0.030*
C13	0.62138 (10)	0.5721 (3)	0.63892 (12)	0.0254 (4)
C14	0.63539 (11)	0.3658 (3)	0.60061 (13)	0.0315 (4)
H14	0.685753	0.328679	0.587589	0.038*
C15	0.57493 (12)	0.2136 (4)	0.58138 (15)	0.0392 (5)
H15	0.584146	0.070079	0.555963	0.047*
C16	0.50201 (12)	0.2684 (4)	0.59872 (16)	0.0422 (5)
H16	0.460818	0.163530	0.584868	0.051*
C17	0.48837 (11)	0.4756 (4)	0.63624 (15)	0.0401 (5)
H17	0.437611	0.513355	0.647684	0.048*
C18	0.54810 (11)	0.6294 (3)	0.65744 (13)	0.0319 (4)
H18	0.538933	0.771385	0.684162	0.038*

Table 9 – Fractional atomic co-ordinates and isotropic or equivalent isotropic displacement parameters ($Å^2$)

	U^{11}	U^{22}	U^{33}	U^{12}	U^{13}	U^{23}
P1	0.0209 (2)	0.0217 (2)	0.0285 (3)	-0.00043 (17)	0.00005 (18)	-0.00009 (18)
O1	0.0255 (6)	0.0276 (7)	0.0307 (7)	0.0050 (5)	0.0031 (5)	-0.0015 (5)
O2	0.0235 (6)	0.0241 (6)	0.0316 (7)	0.0015 (5)	-0.0012 (5)	-0.0037 (5)
O3	0.0216 (6)	0.0272 (7)	0.0399 (8)	-0.0022 (5)	0.0024 (5)	-0.0012 (6)
C1	0.0234 (8)	0.0273 (9)	0.0238 (9)	0.0017 (7)	0.0073 (7)	-0.0028 (7)
C2	0.0243 (9)	0.0322 (10)	0.0313 (10)	-0.0049 (7)	0.0063 (8)	-0.0011 (8)
C3	0.0262 (10)	0.0495 (12)	0.0289 (10)	0.0021 (8)	0.0052 (8)	0.0023 (9)
C4	0.0436 (12)	0.0356 (11)	0.0321 (10)	0.0057 (9)	0.0160 (9)	0.0066 (9)
C5	0.0476 (12)	0.0290 (10)	0.0342 (11)	-0.0081 (9)	0.0187 (9)	-0.0061 (8)
C6	0.0311 (10)	0.0349 (10)	0.0257 (9)	-0.0069 (8)	0.0082 (8)	-0.0081 (8)
C7	0.0198 (8)	0.0255 (9)	0.0204 (8)	0.0008 (7)	0.0048 (6)	-0.0041 (7)
C8	0.0289 (9)	0.0230 (9)	0.0249 (9)	-0.0025 (7)	0.0074 (7)	-0.0014 (7)
C9	0.0312 (10)	0.0323 (10)	0.0230 (9)	0.0037 (8)	0.0016 (7)	0.0015 (8)
C10	0.0229 (9)	0.0407 (11)	0.0257 (9)	-0.0025 (8)	0.0011 (7)	-0.0077 (8)
C11	0.0310 (10)	0.0280 (9)	0.0283 (10)	-0.0077 (8)	0.0099 (8)	-0.0064 (8)
C12	0.0305 (9)	0.0223 (9)	0.0236 (9)	0.0007 (7)	0.0067 (7)	-0.0014 (7)
C13	0.0211 (8)	0.0304 (9)	0.0243 (9)	-0.0052 (7)	0.0016 (7)	0.0041 (7)
C14	0.0255 (9)	0.0326 (10)	0.0368 (11)	-0.0022 (8)	0.0060 (8)	-0.0021 (8)
C15	0.0397 (11)	0.0331 (11)	0.0443 (12)	-0.0080 (9)	0.0039 (9)	-0.0061 (9)
C16	0.0302 (11)	0.0445 (13)	0.0510 (13)	-0.0148 (9)	0.0017 (9)	0.0012 (10)
C17	0.0205 (9)	0.0520 (13)	0.0485 (13)	-0.0031 (9)	0.0072 (9)	0.0035 (10)
C18	0.0280 (10)	0.0344 (11)	0.0337 (10)	0.0013 (8)	0.0056 (8)	0.0007 (8)

Table 10 – Atomic Displacement Parameters (Å)

P1—O1	1.6222 (13)	C8—C9	1.386 (3)
P1—O2	1.6333 (13)	C9—H9	0.9500
P1—O3	1.6279 (13)	C9—C10	1.384 (3)
O1—C1	1.402 (2)	C10—H10	0.9500
O2—C7	1.396 (2)	C10—C11	1.380 (3)
O3—C13	1.391 (2)	C11—H11	0.9500
C1—C2	1.380 (3)	C11—C12	1.384 (3)
C1—C6	1.382 (3)	C12—H12	0.9500
C2—H2	0.9500	C13—C14	1.380 (3)
C2—C3	1.384 (3)	C13—C18	1.385 (3)
C3—H3	0.9500	C14—H14	0.9500
C3—C4	1.388 (3)	C14—C15	1.386 (3)
C4—H4	0.9500	C15—H15	0.9500
C4—C5	1.379 (3)	C15—C16	1.370 (3)
C5—H5	0.9500	C16—H16	0.9500
C5—C6	1.384 (3)	C16—C17	1.378 (3)
C6—H6	0.9500	C17—H17	0.9500
C7—C8	1.382 (2)	C17—C18	1.386 (3)
C7—C12	1.382 (2)	C18—H18	0.9500
C8—H8	0.9500		
O1—P1—O2	102.20 (7)	C8—C9—H9	119.7
O1—P1—O3	102.32 (7)	C10—C9—C8	120.63 (18)
O3—P1—O2	91.41 (7)	C10—C9—H9	119.7
C1—O1—P1	126.73 (11)	C9—C10—H10	120.2
C7—O2—P1	117.97 (11)	C11—C10—C9	119.58 (17)
C13—O3—P1	121.02 (12)	C11—C10—H10	120.2
C2—C1—O1	118.97 (16)	C10—C11—H11	119.7
C2—C1—C6	121.50 (18)	C10—C11—C12	120.57 (17)
C6—C1—O1	119.39 (16)	C12—C11—H11	119.7
C1—C2—H2	120.6	C7—C12—C11	119.15 (17)
C1—C2—C3	118.85 (18)	C7—C12—H12	120.4

C3—C2—H2	120.6	C11—C12—H12	120.4
C2—C3—H3	119.8	C14—C13—O3	123.03 (16)
C2—C3—C4	120.48 (19)	C14—C13—C18	121.09 (17)
C4—C3—H3	119.8	C18—C13—O3	115.86 (17)
C3—C4—H4	120.2	C13—C14—H14	120.5
C5—C4—C3	119.65 (19)	C13—C14—C15	119.05 (18)
C5—C4—H4	120.2	C15—C14—H14	120.5
C4—C5—H5	119.7	C14—C15—H15	119.7
C4—C5—C6	120.58 (19)	C16—C15—C14	120.6 (2)
C6—C5—H5	119.7	C16—C15—H15	119.7
C1—C6—C5	118.94 (18)	C15—C16—H16	120.0
C1—C6—H6	120.5	C15—C16—C17	120.02 (19)
C5—C6—H6	120.5	C17—C16—H16	120.0
C8—C7—O2	121.79 (15)	C16—C17—H17	119.7
C8—C7—C12	121.13 (16)	C16—C17—C18	120.56 (19)
C12—C7—O2	117.01 (16)	C18—C17—H17	119.7
C7—C8—H8	120.5	C13—C18—C17	118.71 (19)
C7—C8—C9	118.92 (17)	C13—C18—H18	120.6
C9—C8—H8	120.5	C17—C18—H18	120.6

Table 11 – Geometric Parameters (Å, °))